C.P. No. 745

C.P. No. 745

MINISTRY OF AVIATION

AERONAUTICAL RESEARCH COUNCIL

CURRENT PAPERS

Wind Tunnel Force and Moment Investigation at M = 4.3 into the Application of Various Devices for the Control of a Cone-Cylinder-Flare Configuration

by

B. E. Pecover

LONDON: HER MAJESTY'S STATIONERY OFFICE

1964

PRICE £1 10s 0d NET

U.D.C. No. 533.696.3/4 . 533.694 : 533.6.013.1 . 533.6.011.5

C.P. No. 745

January 1963

WIND TUNNEL FORCE AND MOMENT INVESTIGATION AT M = 4.3 INTO THE APPLICATION OF VARIOUS DEVICES FOR THE CONTROL OF A CONE-CYLINDER-FLARE CONFIGURATION

by

B. E. Pecover

SUMMARY

Measurements have been made in the R.A.E. No.6 (11" x 6") wind tunnel of the six components of force and moment on a basic cone-cylinder-flare configuration fitted individually with ten different devices to produce aerodynamic control. In addition, some measurements of three components of force and moment on a flap on panel in the flare tail are given.

The controls tested consisted of a tilting nose, tilting flare, nose flap, flare flap, eccentric nose disc, eccentric rear disc, tilting spike, swept spoiler, eccentric ring and tilting ring. The measurements were made at M = 4.3 and Reynolds number from 1.4×10^6 to 5×10^6 depending on the configuration.

Results are discussed and compared with simple estimates and finally the controls are compared with each other. No single device had completely acceptable characteristics. Many, including the tilting nose and flare, were quite effective but only the swept spoiler arrangement could eliminate cross coupling.

Replaces R.A.E. Report No. Aero 2673 - A.R.C. 24810.

LIST OF CONTENTS

LIST OF CONTENTS (CONTD)

LIST OF TABLES

LIST OF ILLUSTRATIONS

LIST OF ILLUSTRATIONS (CONTD)

LIST OF ILLUSTRATIONS (CONTD)

LIST OF ILLUSTRATIONS (CONTD)

1 INTRODUCTION

The kinetic heating problem at high speeds makes it desirable to avoid the use of shapes embodying thin sections for vehicles designed to fly in this regime. Bodies of revolution form one class of shapes in which thin sections are easily avoided and they may also generate considerable lift at high speeds. Further, since base drag at these speeds contributes little to the total drag, large base areas may be acceptable and the diverging flare tail is worthy of consideration as a stabilizer. Thus the cone-cylinder-flare is one shape of interest for flight at high Mach numbers.

There may be other advantages to be obtained from the use of an axisymmetric shape. For instance, it is possible to consider the generation of the forces and moments required for manoeuvre directly in the required plane, that is in a polar rather than a cartesian sense. The object of this investigation has been to produce the aerodynamic data from which the effectiveness of devices which may possibly be suitable for this type of manoeuvre could be assessed.

Aerodynamically an ideal control device should produce an increment of moment which is invariant with the attitude of the basic shape to the airstream. It should preferably be linear with control movement, and should be in, or normal to, the direction of movement so that cross-coupling does not occur. This provides a yardstick for comparison. But there are also mechanical considerations, such as the power required to operate, and the structural feasibility, which make a practical comparison impossible at this stage. It should also be borne in mind that such conclusions as may be drawn herein are relevant to a particular basic body, and may not necessarily be generally applicable.

There are three possible ways of expressing control effectiveness. These are in terms of (a) C.P. shift, (b) force increment and (c) moment increment about some point, for a given control movement. (a) involves dependence on the lifting capability of the basic body and it is not so obvious how the ideal control should perform with change of incidence. In practice, (b) involves either taking the difference of two large quantities or using measurements of (c) and making assumptions about the point of application of the force increment. Although (c) makes comparisons dependent on the location of the reference point it has been used herein because, so expressed, the effectiveness can be compared directly with that desired from the ideal control. The moment reference point used is the estimated C.P. of the particular cone-cylinder-flare used in these tests, and this is thought to lead to a fair comparison between the controls. No attempt has been made to standardise the results because of the differing types of control movement although this would be required for a full comparison which would also include mechanical considerations. The effect of introducing a demand moment on the other five forces and moments is investigated.

2 MODEL

The basic body, a blunted-cone-cylinder-flare, had the following alternative controls:-

(i) tilted nose,

(ii) tilted flare,

(iii) nose flaps,

(iv) flare flaps,

(v) eccentric nose disc,

(vi) eccentric rear disc,

(vii) tilted spike,

(viii) swept spoilers,

(ix) eccentric ring,

(x) tilted ring.

A cylindrical rear section was also provided, in place of the flare.

Outline dimensions of the model are given in Fig.1. It was machined from steel to specification D.T.D. 525, and consisted of a centre body to which any of the range of noses and flares could be secured. Attachment was by four screws passing through jig-drilled holes, mutually at 90°, into tapped holes, which were also jig-drilled. Large diameter spigots ensured concentricity. Any nose or flare could thus be attached to the centre body in any one of four positions 90° apart in roll.

The centre body was secured to the balance by two countersunk head screws, and these ensured alignment of model and balance axes.

All the nose controls were tested in the presence of the basic flare, and all the flare controls in the presence of the basic nose.

The tilted nose control had a slightly different profile from the basic in order to accommodate deflections greater than 7.5°. It was therefore necessary to include an undeflected version having this profile.

A hemispherical nosed model was produced after the tests on the spike nosed models were complete by removing the spike from one of these.

Setting of nose and flare flap angles was accomplished by the insertion of wedges between the flap and the nose or flare. The flaps were of such a shape that at the zero setting they formed a continuous part of the adjacent surface.

A rearward facing step was provided on the rear disc control body at the station at which the flare starts on the basic shape. This was with the object of fixing the separation point ahead of the disc. The taper thereafter was to facilitate the disc fixing.

The spoilers used on the swept spoiler control were flat plates, secured to the V-shaped recess at the rear of the flare by two screws. The outer edge was generated by turning in a lathe about the model centreline with the spoiler extended.

The ring control was secured to the after body by screws passing through spacers of 2.6 m/m O.D. hypodermic tubing, and adjustment of the lengths of these spacers, together with some alternative holes, provided the control deflections. The height of the annulas at the front of the ring was determined on the basis that it was to be 1.5 times the estimated boundary layer thickness on the afterbody in the undeflected position.

3 BALANCE

3.1 Six component balance

This balance, which was used in all the tests, was a six-component, internal, strain-gauge balance designed specially for these tests. It was machined from S.96 steel. The balance was made in two parts, the axial force balance and the sting. The former was of the simple twin cantilever type. The model centre body was secured to one of the beams joining the cantilevers and the forked end of the sting to the other. The sting was of the usual cantilever type except that it had a four bar roll cage separating the fore and aft force and moment stations. The 36 Baldwin AB 19 strain gauges were connected so as to reduce interaction terms between the various forces and moments to a minimum. Two thermistors were provided so that sting temperatures could be measured, and corrections made for temperature drifts in the strain gauges. An arrangement drawing of the basic model and six-component balance is shown in Fig.2.

3.2 Three component flare flap balance

The model and six-component balance had already been made when the need for this balance arose, so that the choice of configuration was limited. The arrangement adopted, shown in Fig.3, consisted of two angle pieces machined integrally with a mounting ring at one end and a platform at the other. A segment of the ring was made detachable to enable the balance to be assembled round the six-component balance. The ring was secured to the inside of the flap control flare and one of the wedges and/or the flap could be mounted on the platform, clearances being kept to a minimum. Eight Baldwin AB 19 strain gauges were fixed to the horizontal members, and connected in bridges of four to measure normal force and moment on the flap and wedge. Four Baldwin AB 19 gauges were mounted on the upright members, and connected to measure axial force nearly enough independently of the height at which it was applied.

It was found that the balance responded to sideways loads so that where these were experienced (as in positive flap setting on the side at incidence) it was necessary to arrange the tests so that the direction of the sideload could be reversed, and the effect removed by meaning the results.

The three component balance was used in all the tests with nose controls (measuring the load on a panel of the basic flare), and in the tests of flare flap controls. A photograph of the complete 9 component balance is shown in Fig.4.

4 TEST FACILITY

The tests were made in the No.6 11" x 6", open-jet non-return circuit, continuous, supersonic wind tunnel at a Mach number of 4.3. The Reynolds number could be varied over the range 1.4 to 5 x 10^6 (based on body length) by altering the stagnation pressure. The stagnation temperature was held in the region 35 to 40°C.

Air was drawn through beds of activated alumina before compression, and through beds of silica gel after compression; the water content is believed to have been less than 0.0001 lb/lb air.

The sting was mounted in a quadrant which enabled the angle of incidence and of incidence plane angle to be varied over the desired range from outside the tunnel.

A data recording system exists by means of which instrument readings proportional to loads were obtained on self-balancing potentiometers and were recorded in typewritten and punched card form. Thermistor potentiometer readings, model incidence, incidence plane angle, total head and base-pressures (measured by Midwood manometers) were also recorded in the same operation.

5 CALIBRATION

This was performed by dead weight loading a calibrating bar in lieu of the model. For axial force calibration load was applied along the axis of the undeflected sting and subsequently corrected by the DEUCE data reduction programme[1] to take account of the non-linear interaction and to give axial force along the model axis.

Temperature drift was determined by a controlled variation of the wind tunnel stagnation temperature under operating conditions over a small range. A correlation was thus found between each of the force or moment readings and one or other of the thermistor readings.

Sting deflection under various loadings was determined optically.

6 TEST METHOD

For control movements designed to produce loads in the incidence plane it was necessary to cover both the leeward and windward operation cases. This could be done either by using a particular control setting covering an incidence range symmetrical about zero, or by using a range only from zero to, say, full positive incidence, first with the control deflected on one side of the body and then on the other. The former method was used for the majority of the tests, and the latter for the nose disc and swept spoiler control tests.

Because of mechanical limitations of the support gear negative incidences were achieved by rolling the model and balance 180° and testing with the support set at positive angles.

At the completion of each incidence traverse, which was performed in 1° steps, the air flow was stopped and a balance zero reading taken. In this way any instrument drifts were minimised.

7 CORRECTIONS TO COMPUTED DATA AND PRECISION

The data reduction programme[1] included corrections for temperature drift, tare variation on axial force, and base pressure. The latter affected axial force and the flap control balance measurements. The axial force was corrected to apply free stream static pressure on the base area. The flap measurements were corrected to apply zero pressure to the inner surface and base of the flap. The base pressure was fed to a Midwood manometer by a tube extending into the balance chamber of the model.

After these corrections had been applied the results still showed the following anomalies -

(i) The C_m vs α curves for symmetrical shapes failed to pass through the origin by an amount which changed sign as the model and balance were rolled to achieve negative or positive incidence.

(ii) The C_m vs α curves for shapes asymmetric about the xy plane - see Fig.5 - were made discontinuous at zero incidence by rolling the model and balance through 180°.

(iii) For symmetrical shapes significant values of C_y and C_n were measured, which in the case of C_y increased with incidence.

(iv) Some of the C_z, C_m and C_ℓ vs α curves for models asymmetric about the xz plane which should, on grounds of symmetry, pass through the origin failed to do so by small amounts.

All these effects were repeatable.

In the case of (i) and (ii) a likely explanation is that the free streamlines were curved. On this assumption a crude correction was applied by taking the mean value of C_m at $\alpha = 0°$ for the upright and inverted cases, and adjusting both curves to pass through this value with the slopes unaltered. In cases where values with sting and model rolled through 180° were not available the zero control setting curve was adjusted to pass through the origin and the curves with non-zero control settings moved a similar amount. The size of the correction varied slightly with the configuration but it was of the order of 0.03 in C_m.

In the case of (iii), the discrepancies at zero incidence were considered to be due to a small stream angle. The variations with incidence were probably due to a small error in roll zero during the calibration of the Z interaction on Y. For example an error of 0.2° in this zero would cause an apparent value of C_y of 0.012 for the basic shape at 25° incidence. These effects were

eliminated by subtracting from the computed C_y the value for the zero control setting case at the same incidence, the value so obtained being considered the true C_y. The same procedure was applied to C_n. (iv) is believed to be due to small errors in model manufacture such that the demand plane was not quite normal to the incidence plane. The curves were therefore adjusted to pass through the origin with slopes unaltered.

These effects rather overshadow the measurement precisions based on repeatability and instrument sensitivity; however, these are given below in Table 1.

TABLE 1

Precision of measurement

Component	Precision at $Re \times 10^{-6} = R$				
	R = 5	R = 3.7	R = 3	R = 2.4	R = 1.4
$C_x > -0.4$	±0.008	±0.011	±0.018	±0.017	±0.029
$C_x < -0.4$	±0.011	±0.015	±0.018	±0.023	±0.039
C_y	±0.002	±0.003	±0.003	±0.004	±0.007
C_z	±0.02	±0.03	±0.03	±0.02	±0.04
C_ℓ	±0.0012	±0.0014	±0.0020	±0.0025	±0.0043
C_m	±0.01	±0.01	±0.02	±0.02	±0.04
C_n	±0.002	±0.003	±0.003	±0.004	±0.007
C_x flap		No reliable estimate possible			
C_z flap AVE	±0.004				
C_m flap AVE	±0.002				

Incidence was accurate to ±0.05° and the nozzle calibration shows the variation of Mach number within the working section to be within ±0.03 of 4.30. This implies an uncertainty of ±2% in the local value of q, the kinetic pressure.

8 PRESENTATION OF RESULTS

The six components of force and moment along and about a right hand system of body axes illustrated in Fig.5 have been found for a model with ten different control systems over a range of incidence angles and control settings and the

bulk of the results is presented as plots of these components in coefficient form versus incidence for various control settings.

In comparing increments it is convenient to consider incidence always positive and make corresponding alterations to the signs of the measured increments. Figs.15 and 16 use this method of presentation, as do the plots of C.P. variation.

The six components have been non-dimensionalised on the basis of the cross-sectional area of the centre body and its diameter, as shown in the list of symbols. Reynolds number is based on net overall length. Axial force coefficients have been corrected to free stream static base pressure, moments are quoted about a point 3.89 inches (3.036 body diameters) forward of the base. This was the estimated C.P. for the basic model.

The flap results are presented on the basis of zero pressure on the unexposed surfaces. The values of the coefficients due to free stream static pressure on these faces are indicated. Flap force and moment coefficients are non-dimensionalised on the basis of the flap span x chord and span x $(\text{chord})^2$ respectively. Moments are measured about the point of intersection of the flap upper surface centre line with the leading edge and are considered positive when tending to increase the angle between the flap and the model axis. Fig.5 shows the axes system.

9 DISCUSSION OF RESULTS WITH ZERO CONTROL SETTING

9.1 Basic shape - including Reynolds number effects

Fig.6 shows that the axial force coefficient increases with decrease of Reynolds number but the effect becomes less as incidence increases. An estimate of axial force by Newtonian theory is included and is seen to be generally lower than the measured values, although the trend with incidence is well represented. The estimate includes the effect of the blunt nose, but of course takes no account of skin friction. If transition is assumed to occur at the cone-cylinder junction then data in Ref.2 gives the skin friction axial force coefficient at zero incidence in the range 0.036 to 0.024, depending on heat transfer conditions, at the highest Reynolds number and 0.046 to 0.031 at the lowest. These values are not quite large enough to close the gap between the estimate and the measured values. Fig.6 also includes measurements of axial force on the cone-cylinder resulting from substitution of the plain tail shown in Fig.1 for the flare.

The measured base axial force coefficients are shown in Fig.7. These show little effect of Reynolds number above about 15° incidence. The values at low incidence are known to be influenced by support interference since the wake could be seen from a Schlieren study to reattach onto the roll gear housing, which was only a little smaller in diameter than the model base. As incidence increased the reattachment moved forward onto the sting, and it appeared that by about 8° incidence a more representative base condition had been achieved. This is close to the incidence at which maximum base axial force was measured. Since however, all axial force results have been corrected to refer to zero base axial force, the support interference effects have been removed from them.

Fig.8 shows C_z vs α for the basic shape at various Reynolds numbers and for the cone-cylinder at the highest Reynolds number. The figure also includes estimates for $\partial C_z/\partial\alpha$ at $\alpha = 0^\circ$ by second order shock expansion theory[3]. This overestimates the slope for the cone-cylinder by about 6% but underestimates the increment due to the flare so that the slope for the complete configuration is underestimated by about 4%. It should be appreciated that this theory is really applicable only to sharp nosed bodies. No correction has been applied to allow for the blunting. The value of these estimates, where non-ballistic trajectories are considered, is limited by the non-linear increase of force with incidence, and so estimates covering the full range of incidence, by Newtonian theory and by Allens theory[4], are given for the complete configuration. The estimate by Newtonian theory is pessimistic by 11% to 16%, depending on incidence. The estimate by Allens theory is also pessimistic but only by about 9% throughout the incidence range.

Fig.8 shows that the effect of Reynolds number variation on C_z vs α is small. Reduction of Reynolds number gives a slight increase in force and this is qualitatively consistent with a thicker boundary layer causing a pressure distribution appropriate to a body of slightly larger diameter.

Fig.9 gives the variation of C_m with α for the basic shape at various Reynolds numbers, and for the cone-cylinder at the highest one. Estimates of initial $\partial C_m/\partial\alpha$ by second order shock expansion theory[3] are given. The estimated slopes are greater than the measured ones, so that for the cone-cylinder the estimated C.P. is 0.26 calibres ahead of the measured value and in the case of the cone-cylinder-flare, it is 0.34 calibres ahead of the result at highest Reynolds number, neglecting the "kink" in the experimental curve. An estimate for C_m vs α using Allens theory[4] gives $C_m \approx 0$ throughout the incidence range in the case of the complete configuration. This represents the results quite well and the estimated C.P. at $\alpha = 25^\circ$ is merely 0.075 calibres ahead of the measured value.

The effect of reducing Reynolds numbers at zero incidence is to increase stability, the "kink" in the C_m vs α curve becoming much more pronounced. Fig.10 shows, at the highest Reynolds number, that the thickening of the boundary layer which occurs ahead of the cylinder-flare junction is much reduced on the windward side as incidence increases from 0° to 3°. At $\alpha = 0^\circ$ the projected line of the flare shock intersects the body well forward of the cylinder-flare junction while at $\alpha = 3^\circ$, coinciding with the extremity of the "kink" in the C_m curve, it intersects at the junction and continues to do so for all higher incidences. It is plausible that the forward shock position at $\alpha = 0^\circ$ gives a higher local lift slope on the rear part of the cylinder than with the shock in the rear position at α greater than 3° (at the highest Reynolds number).

The effect of Reynolds number variation at high incidence is small, in terms of C.P. shift, and the trend with reduction of Reynolds number appears to change sign.

9.2 Effects of alterations to basic shape to suit controls

Only the models with nose or flare flaps and those with tilting flare control reduce to the basic shape when the controls are at zero setting. All the other control devices tested required modifications to the basic shape to accommodate them, with consequential changes in force and moment characteristics. The influence on the normal and axial forces, pitching moment and lift/drag ratio for these shapes, with zero control setting is shown in Figs.11 to 14.

9.2.1 Tilting nose model Re $\simeq 5 \times 10^6$

The effect of the small increase in cone angle required on this model is to produce a slight increase in C_x and a slight reduction in stability. Any effect on C_z was too small to be measured. The value of L/D max is slightly reduced.

9.2.2 Nose disc model Re $\simeq 3.7 \times 10^6$

As would be expected, the nose disc causes a large axial force penalty, the value of $-C_x$ at $\alpha = 0^\circ$ being 0.4 greater than for the basic shape. By Newtonian theory one would expect this change to be 0.46. This neglects any change in skin friction. The disc impairs the lifting power of the nose, causing a reduction in $-C_z/\alpha$ and an increased stability for the model, but this effect is reduced as incidence increases. At about 12° incidence there is a loss of stability which coincides with the disappearance of the reattachment shock on the upper surface of the nose - see Fig.70. At high incidence the values of $-C_z/\alpha$ and $\partial C_m/\partial\alpha$ are very close to those of the basic shape.

9.2.3 Rear disc model Re $\simeq 3 \times 10^6$

At $\alpha = 0^\circ$ Fig.81(c) shows the rear disc causing a separation which starts near the cone-cylinder junction and this gives rise to a relatively low value of axial force, Fig.11 (but nevertheless 0.09 greater than the basic shape). Increase of incidence reduces the extent of the separation on the windward side and causes a progressive large increase in axial force.

The rearward facing step was not effective in locating the separation point. At $\alpha = 2^\circ$ Fig.81(b) shows the separation point still well ahead of the step and by $\alpha = 8^\circ$ Fig.81(a) shows the flow on the windward side reattaching after the step and then separating in front of the disc.

The initial value of $-C_z/\alpha$ is indistinguishable from that of the cone-cylinder, as would be expected, but at high incidence it approaches the value for the cone-cylinder flare.

The stability of this model at zero incidence is greater than that of the cone-cylinder-flare, arising from the distribution of pressure on the face of the disc. A shock forms in front of the into-wind face (Fig.81 (b) and (c)) with consequent pressure rise and restoring moment.

9.2.4 Tilting spike model Re ≃ 3.7×10^6

Comparison of the curves of C_x vs α for the spike nosed and hemispherical nosed models (Fig.11) shows that at $\alpha = 0^o$ the spike causes a reduction in axial force to only 35% of its value in the absence of the spike. Application of incidence causes a rapid rise in axial force towards the hemispherical nose value. The Schlieren picture of Fig.91(c) shows that at zero incidence the flow separates near the front of the spike and most of the hemisphere is in the separated region. As incidence increases the separation on the windward side is reduced in extent, causing an increase in axial force. This is very similar to the rear disc model, where the cone-cylinder acts as a spike. Further increase of incidence reduces the separated region on the upper surface of the hemisphere also. By $\alpha = 22^o$ the values of C_x with and without spike are identical and above this the spike causes an increase in axial force.

Fig.12 shows that replacement of the cone by the hemispherical nose reduces the normal force but the presence of a spike gives a large increase in normal force slope only over the first 4^o. This is sufficient to cause the values of $-C_z$ for the spike nosed model to be greater than those for the basic model for incidences up to 7^o. Above 4^o incidence Fig.91(a) shows the upper surface of the hemisphere to be less influenced by the separation induced by the spike and this leads to a loss of lift. Fig.13 emphasises the loss of lift forward of the moment datum which occurs above 4^o.

9.2.5 Swept spoiler model Re ≃ 5×10^6

The modifications required to accept the swept spoiler produce little effect on axial force. The effect on C_z was too small to be measured in these tests, but the C_m vs α curve (Fig.13) indicates a small unfavourable change in stability.

9.2.6 Ring control model Re ≃ 5×10^6

The Schlieren pictures of Fig.121(a) and (d) suggest that flow through the undeflected ring was unchoked.

The value of $-C_x$ at $\alpha = 0^o$ is greater than that of the basic shape, due possibly to the large contribution of the supporting struts, estimated at -0.12. The increase in $-C_x$ with incidence is less for this model than for the basic one.

The initial value of $-C_z/\alpha$ is less than for the basic shape but at high incidence there is little difference. This indicates that the lift effectiveness of the ring tail is less than that of the flare of the same frontal area, and is consistent with the reduced stability shown by the C_m vs α curve. There is no evidence of the "kink" in the C_m vs α curve at $\alpha = 0^o$ which occurs when the flare is mounted.

10 DISCUSSION OF RESULTS WITH DEFLECTED CONTROLS

10.1 Tilting nose control Re $\simeq 5 \times 10^6$

Overall forces and moments are presented in Figs.17 to 25 and centre of pressure variation in Fig.122 for the tilting nose control model.

Fig.15(a) shows that the incremental pitching moment, ΔC_m, due to control deflection is linear with deflection angle, η, at zero incidence, and approximately so but of steeper slope, at incidence. The control power thus improves with body incidence irrespective of the sense of control deflection. This has been traced, through measurement of the flare panel forces (Fig.26), to loads induced on the flare tail by the nose deflection, particularly on the windward panels, and is thus similar in effect to the well-known foreplane-wing interference of canard aircraft.

A Newtonian theory estimate of the pitching moment on the nose only (i.e. without interference) is 10% too low at zero incidence and more so at incidence.

Fig.17 shows the minimum $-C_x$ for this model always occurred at an incidence equal to the nose deflection angle and of such a sense that the nose incidence was zero. Fig.16(a) indicates that only the case of negative, nose down, deflection at positive incidence gives positive values for ΔC_x (which are of course to be desired) and this is not a case of practical significance since it implies a negative static margin. An estimated ΔC_x curve is included in the figure, calculated by the same method as that for ΔC_m, and this also gives an estimate which is about 10% too low. Incidence effects are better represented, the estimate for $\alpha = 10^\circ$, $\eta = -10^\circ$ being +0.029 compared with +0.023 measured.

Fig.18 shows that the increment of force due to control deflection acts in the demand direction so that the induced load on the flare is less than that generated on the nose control.

Lateral deflection of the nose, to meet a change in the demand acceleration plane, can be seen in Figs.21 and 22 to produce only small changes in the normal force and moment in the incidence plane. Fig.23 shows that the side force produced by such a deflection increases with incidence, while Fig.24 shows that the yawing moment does not vary as much. This implies that the additional side force due to incidence acts near the C.G.

Lateral deflection also translates the C.P. of the nose out of the incidence plane and gives rise to a rolling moment which is dependent on incidence, Fig.25. With this control device, as with all except the swept spoiler (Section 10.8), there is no provision for counteracting such a rolling moment, which is then necessarily unfavourable. Its magnitude is therefore of importance. An estimate, using Newtonian theory and taking the nose C.P. at $\frac{1}{3}$ the net nose length forward of the cone-base, is included in the figure for $\eta = 10^\circ 25'$. It is some 25% less than the experimental result.

10.8.1 Individual spoiler performance

Overall force and moment results with a single spoiler extended are given in Figs.93 to 104 and C.P. variations in Figs.130 and 131.

Fig.15(h) shows that spoilers in the top positions lose pitch effectiveness with incidence more rapidly than those in the upper positions, and that those in the bottom position gain effectiveness with incidence while those in the lower positions are affected very little. These conclusions apply equally to rolling and yawing effectiveness.

It is possible to use the results to find the area of the flare subject to induced load if the pressure is assumed uniform over the face of the spoiler and over the area on the flare. Also if the distance of forward propagation of pressure is assumed constant across the spoiler, a value for this distance can be found. The increment in C_x due to spoiler extension is very nearly entirely due to pressure on the face of the spoiler. This increment can be used to obtain that part of the increment in C_m, or C_n, which is due to this, the remaining part being that due to the induced load on the flare. For example, when the spoiler was extended 0.2" in the incidence plane at zero incidence, the mean measured values of ΔC_x and ΔC_m were 0.105 and 0.30. We find that the ΔC_m corresponding to $\Delta C_x = 0.105$ is only 0.08, leaving 0.22 as the contribution of the induced load. The distance of forward propagation can then be computed as 0.14 inches and the pressure coefficient as 1.24. Other components could be used to make the calculation. Using the values of C_y for 0.2 inches extension in and normal to the incidence plane we obtain 0.17 inches and pressure coefficient of 1.33 for the same case. Computations using ΔC_m, ΔC_x and C_n for all spoiler heights and incidences suggest that in most cases the extent of forward propagation is 0.1 to 0.2 inches.

10.8.2 Use as a longitudinal control

The four spoilers used for negative (nose down) control would be bottom port and starboard and port and starboard lower, the other four spoilers providing control in the positive sense. From Figs.97 and 98 it is clear that whatever combinations of extension in the two planes are used, increasing incidence must give increasing negative control power and decreasing positive power. The latter becomes almost non-existent at $\alpha = 25^0$. Figs.93 and 94 provide means of finding the axial force penalty for any combination of extensions and it is evident that ΔC_x is always negative i.e. unfavourable.

From Figs.95 and 96 it may be seen that the increment of force is opposed to the demand direction.

10.8.3 Use as a directional control

The four spoilers giving negative (nose to port) control are top and bottom port and port upper and lower. The other four give positive control. Figs.101 and 102 show that while increasing incidence somewhat reduces the

increases the pressure ratio, bottom to top, it increases the effect, except that the cross flow separation point moving towards the side of the flare would eventually limit the increase. With lateral deflection of the flare the effect on the side deflected to windward would be enhanced and that on the leeward side reduced, giving a net fall in side force with incidence up to a limiting value as described. Increase of incidence also moves the flare nearer to the bow shock, which is becoming stronger with increasing incidence. This gives a tendency for pressures to rise on the sides of the flare and hence the difference from one side to the other also increases. Eventually this effect becomes the predominant one. The results for the rear flap loads, Fig.60, are of similar shape to these and are susceptible to the same explanation.

Control deflection normal to the incidence plane results in the C.P. on the flare being displaced from the centre line of the model and hence in a detrimental incidence dependent rolling moment (as for the tilted nose). Fig.35 shows this and includes an estimated curve, using Newtonian theory, for the 7.5° deflection case. As in the case of the tilted nose, the estimate is too low by about 25%.

10.3 Nose flap control $Re \simeq 5 \times 10^6$

Overall forces and moments are presented in Figs.37 to 45 and C.P. variation in Fig.124.

Fig.15(c) shows the variation of ΔC_m with deflection and incidence. As only positive deflections were possible and only one setting was tested, results for this individually on the windward and leeward sides of the model are plotted in the same figure. The control is noticeably less effective on the leeward side of the nose, and dependent upon the body incidence when on the windward side. From a comparison of the flare panel loads with and without nose flap deflection (Fig.46) it appears that the reduction in control effectiveness near zero incidence is attributable to the loads induced on the flare tail. The same figure shows that deflection of the nose flap to windward when the model is at incidence considerably reduces the load on the windward side of the flare thus accounting for the increased effectiveness then experienced.

Figs.16(c) and 37 show that operation of the control always results in an axial force penalty. At $\alpha = 0°$ the two dimensional linear theory estimate for ΔC_x is 0.019 for $\eta = 7.5°$ and this is less than half the measured value. However base drag of the flap and wedge has been ignored in the estimate.

The force increment is generally in the demand direction, see Fig.38, but this is not so for flap to windward at incidence greater than 15°. This is accounted for by the reduced load on the windward side of the flare discussed above. Evidently for incidences in excess of 15° the interference load on the flare exceeds the direct load on the nose flap.

When the flap is deflected normal to the incidence plane it increases the slopes with changing α of normal force and moment in the incidence plane - Figs.41 and 42 - due to the increased planform area, and produces a forward C.P. shift (c.f. the rearward shift produced by control deflection in the incidence plane - Fig.38).

Figs.43 and 44 show that incidence effects on the directional components are quite large. The kinks in the curves near zero incidence are due to the flap/flare interference already discussed. A probable cause of the reducing side force and increasing yawing moment at incidences up to 15° is the influence of the expansion field from the upper surface of the wedge on the body and flare. Further increase of incidence then moves these into the pressure field from the under surface and reverses the trend.

The deflection of a flap normal to the incidence plane causes a rolling moment which Fig.45 shows increases linearly with incidence. This is due to the control forming a thick delta half wing on the side of the nose. An estimate of rolling moment using linear theory is included in the figure and agrees very well with the experimental curve even up to 25° incidence. A Newtonian estimate which is also included does not agree nearly as well.

There is no provision for counteracting this rolling moment which is therefore an adverse feature of this control.

10.4 Flare flap control $Re \simeq 5 \times 10^6$

Overall forces and moments are presented in Figs.47 to 55, forces and moments on the flap in Figs.56 to 58 and overall C.P. variation in Figs.125 and 126, whilst the flap C.P. variation is shown in Fig.59.

As in the case of the nose flap, the ΔC_m and ΔC_x vs deflection plots - Figs.15(d) and 16(d) - for flap to windward and to leeward have been presented in the same figures. In this case however the deflection, η, could have negative values i.e. the flap surface could be below the surrounding flare surface.

Fig.15(d) shows that the variation of ΔC_m with η is not linear, and is very dependent upon body incidence. With flap to windward effectiveness increases with incidence for both positive and negative η, while with flap to leeward increasing incidence reduces ΔC_m. If the flow were Newtonian, even the largest deflection used would be expected to lose all effect when $\alpha > 7°$, flap to leeward, due to the shadow effect from the forebody. The results show that this is pessimistic at this Mach number and all effect is not lost until about $\alpha = 25°$.

Three methods of estimating the flap effectiveness at $\alpha = 0°$ have been tried and the estimates are included in Fig.15(d). Those using linear theory and the pressure coefficients for cones of semi-angle $7.5° + \eta$ are both based on the assumptions that the appropriate total head is that of the free stream, that the flow direction is initially along the flare surface and that the Mach number is that corresponding to flow along the flare surface. Newtonian theory appears to give the best agreement at low incidence, but overestimates the changes due to incidence.

From the tilting flare results (Section 10.2) one would expect to find some effect of nose shock/flare shock interaction on the results for $\eta = +7.5°$, flap to windward at incidences greater than 22°. This can be seen clearly in Fig.15(d) and in the flap force and moment curves of Figs.57 and 58. In the latter distinct changes of slope are visible, while the former shows a failure of ΔC_m to increase between the $\alpha = 20°$ and the $\alpha = 25°$ value.

Fig.57 shows the variation of $C_{Z_{FLAP}}$ with incidence for various flap settings (note: non-dimensionalised on flap area). The results are referred to zero pressure on the unexposed faces. In use it would be necessary to apply a correction for the pressure actually experienced on these faces and the datum for the case where this is the free stream static pressure is indicated. Estimates by Newtonian theory, modified to be consistent with the measured values by the addition of the amount due to free stream static pressure acting on the exposed surface, are included in the figure. The figure shows that the theory gives reasonable agreement with the measured values only when the flap is to windward. Positive settings, however, produce less force than estimated and the error becomes greater with increase of incidence. This may be due to tip losses, which could only occur at positive settings, but if this is so the overall moment results, as discussed above, suggest that these are not recovered on the adjoining flare surfaces when the incidence is large.

There is a discrepancy between the flap force and moment measurements at $\alpha = 0^{\circ}$ with the flap in the incidence plane and these with it normal to the incidence plane - Figs.57, 58 and 60,61. The discrepancy is largest at positive flap settings, where both increments due to change of flap angle and the total measurements are at variance in the two cases. At negative settings the increments agree closely although the total measurements still differ.

There is thus some doubt about the values at $\alpha = 0^{\circ}$.

Fig.57 shows the variation of flap moment about the leading edge with incidence and deflection. Possibly because of vibration the quality of the $C_{X_{FLAP}}$ measurements was poor; faired curves are shown in Fig.55. However the dependence of centre of pressure of the flap load on $C_{X_{FLAP}}$ is weak compared with that on $C_{Z_{FLAP}}$ and Fig.59 is a reasonably reliable determination. The determination becomes less accurate as the incidence approaches the zero load one for the particular flap deflection and so the curves are broken over a small range of incidence at this condition. It can be seen that the C.P. is never far from the mid-chord point and that it is further aft at negative setting than at zero and further forward at positive setting. This trend is consistent with that which tip effects would be expected to produce.

Fig.16(d) shows that negative flap setting always gives a positive, favourable, increment of C_X and Fig.47 shows that this increases with incidence, flap to windward, and decreases, flap to leeward. Since it is possible to obtain moment increments of either sign with flaps restricted to negative settings, the control can be used so as to give always favourable C_X interaction. The converse applies for positive operation.

Fig. 16(d) includes an estimate for the $\alpha = 10^{\circ}$ flap to windward case using Newtonian theory and this agrees fairly well with the experimental curve. Of course, for flap to leeward at this incidence the estimate is zero for all settings, whereas finite values were measured.

Fig.48 shows that the force increment is in the opposite direction to the demand in all cases. Its size varies with incidence in a similar manner to that of the moment increment.

Fig.51 and 52 shows that both positive and negative settings normal to the incidence plane increase the $-C_z$ vs α and $-C_m$ vs α slopes. This is due to the provision of extra lifting area in both cases, in the form of a thick delta wing for positive settings and an inclined duct at negative flap angles. Since the exposed lifting area of the latter is subject to shadowing by the windward part of the flare it is not so effective as the former.

The effects of incidence on C_y and C_n for deflections normal to the incidence plane are shown in Figs.53 and 54. The effects are generally small, there being a slight increase in effectiveness with incidence for α greater than 12°. The negative settings show a small loss in effectiveness with increasing incidence for α less than 12° which may be caused by the increasing shadow area.

The force on the flap itself, Fig.60, shows a dip at zero incidence. Above about 3° incidence there is a reduction with increasing incidence and finally a rise. As already remarked in the discussion of the results of tests with the tilted flare tail model, the dip may be due to thinning of the boundary layer ahead of the flare as incidence is applied. It is interesting to note that there is no dip in the case of full negative setting, where boundary layer thickening would not be provoked - but in the overall force and moment curves, Figs.53, and 54, this setting is the only one with a dip. Presumably this is due to the effect cancelling on port and starboard sides except in this case.

Fig.55 shows the variation of C_ℓ with α. This rolling moment arises from the extra area exposed by either inwards or outwards flap deflection as already mentioned. It is thus of the same sign for both positive and negative deflection but greater for positive deflections. Estimated curves for the +7.5° setting are included in Fig.55 using linear theory and Newtonian theory. The former gives good agreement up to α = 12° but further increase of incidence brings the measured values nearer to the Newtonian estimate.

10.5 Eccentric nose disc control Re ≈ 3.7×10^6

Overall force and moment results are given in Figs.62 to 68 and C.P. variation in Fig.127.

The control was intended to act not so much by means of the high eccentric axial force of the disc as by causing asymmetric separated regions on the nose. Fig.69 shows that at zero incidence the reattachment shock waves from upper and lower surfaces were symmetrical about the body irrespective of the eccentricity so that the object was not achieved at this incidence.

Fig.15(c) shows that at zero incidence eccentricity of the disc produced very little pitching moment. (Newtonian theory predicts ΔC_m of 0.06 for 0.15" eccentricity.) Control moment, linear with eccentricity, developed with incidence and the greatest effectiveness occurred at about α = 15°, irrespective of the sign of the eccentricity.

It is apparent from Fig.16(e) that eccentricity of the disc has no effect on C_x. Fig.62, however, shows that the presence of the disc causes $-C_x$ to be much larger than that for the basic shape.

Fig.63 shows that the force increment is very small but acts towards the demand direction.

Fig.66 and 67 show that operation normal to the incidence plane gives rise to very small changes in C_z/α and C_m/α.

Fig.68 shows that incidence has some effect on C_y and C_n in this case. Maximum effectiveness again occurs at about $\alpha = 15^\circ$.

No rolling moment is produced by any combination of control setting and incidence tested - see Fig.68.

10.6 Eccentric rear disc control, $Re \simeq 3 \times 10^6$

Overall force and moment results are presented in Figs.71 to 79, and C.P. variation in Fig.128.

The variation of ΔC_m with control deflection is shown in Fig.15(f) and this is linear at zero incidence. Effectiveness increases with incidence for eccentricity in either direction in the incidence plane. Fig.73 shows that the variation of C_m with α is very non-linear and this is reflected in the ΔC_m vs eccentricity curves for certain incidences. Since this control was intended to be a low inertia version of the tilted flare, it is of interest to compare the two. On the basis that the flow will be the same as if there was a solid boundary between the rearward step and the extremity of the disc, the maximum eccentricity (0.2") corresponds to 5.2° of flare deflection, although the shape is not quite the same in the two cases. Fig.80 shows the variation of ΔC_m with α for the two cases and from this it can be seen that the rear disc is less effective than the flare only over the incidence range -7° to $+9^\circ$ for downward deflection i.e. displacement to windward at positive incidence.

Fig.16(f) shows the variation of ΔC_x with deflection and it can be seen that at $\alpha = 10^\circ$ there are much larger changes than at $\alpha = 0^\circ$. Despite the relief to be gained by operating with the disc translated to leeward, comparison of Figs.11, 27 and 71 shows that the axial force penalty is still much greater than for the basic shape and for the tilted flare of the same effectiveness.

The force increment can be seen from Fig.72 to act in the opposite direction to the demand. It increases with incidence for both windward and leeward disc translations.

Figs.75 and 76 show that translation normal to the incidence plane causes little change in C_z/α and C_m/α, the main effect being a small rearward C.P. shift.

Displacements normal to the incidence plane are shown in Figs.77 and 79 to produce C_y and C_n which vary considerably, and non-linearly, with incidence. The C.P. of the sideload, C_y, as given by C_n/C_y, is behind the model base, being 6 calibres aft of the C.G. at $\alpha = 0^\circ$ and 3.8 calibres aft at $\alpha = 25^\circ$. That this C.P. is always off the model is due to the eccentricity of the axial force on the disc itself.

Fig.78 shows that no rolling moment was produced by any combination of displacement with incidence.

10.7 Tilted spike control Re $\simeq 3.7 \times 10^6$

Overall force and moment results are given in Figs.82 to 90 and C.P. variation in Fig.129.

At zero incidence Fig.15(g) shows that there is a much larger $\Delta C_m/\eta$ slope for small η than for η greater than about 3°. This is due to the large lift slope of the nose at small incidence which was described in Section 9.2.4, and is caused by asymmetry of the separation ahead of the hemisphere. The effect is dependent only on the spike attitude so that, for instance, $\eta = 4^\circ$, $\alpha = 0^\circ$ produces the same effect as $\eta = 0^\circ$, $\alpha = 4^\circ$. This also accounts for the large variations in effectiveness at negative η and incidence less than 15°. The variation of C_m with α is shown in Fig.84.

Instability of the shock system of spike-bluff body combinations has been noted elsewhere[6], but in these tests it was observed only over a very small range of incidence, less than 2°, when the spike was inclined at about 11° to the free stream.

Fig.16(g) shows the rapid rise in axial force produced by spike deflection at zero incidence. As in the case of the rear disc, the apparent benefit conferred by negative control deflection at $\alpha = 10^\circ$ still entails a higher value of axial force than for the basic shape, as can be seen from Fig.82. This figure shows that minimum axial force occurs at incidences close to those at which the spike is aligned with the free stream. Fig.92 shows that the separation is symmetrical about the spike at $\eta = -9^\circ 17'$ when $\alpha = 8^\circ$ and this corresponds to minimum axial force.

The variation of C_z with α is shown in Fig.83 and this shows that the force increment due to control deflection acts always in the demand direction. The greatest value of increment seems to occur at the incidence which gives $C_z = 0$ for the particular deflection.

Figs.86 and 87 show the effects on C_z and C_m of spike deflections normal to the incidence plane. The main effect is a rapid loss of the control lift produced on the nose by the asymmetric separation. Fig.85 shows increasing axial force at $\alpha = 0^\circ$ for the same reason.

The effects of incidence on C_y and C_n for the normal deflection case are shown in Figs.88 and 89. The high values at low incidence are again due to the asymmetric separation.

Fig.90 shows the variation of C_ℓ with α. This arises from the translation of the spike C.P. away from the model centre line. An estimate by Newtonian theory is included in the figure and is in fair agreement with the corresponding experimental results. The progressive increase of C_ℓ with incidence contrasts with the almost constant increment in C_z due to the spike. This supports the suggestion that there is interference with the body pressure fields since these cannot produce any rolling moment on the axially symmetric body in question.

10.8 Swept spoiler control Re $\simeq 5 \times 10^6$

A swept spoiler gives increments of force and moment in two ways. Firstly there is the direct load on the spoiler, which can be resolved into components parallel to and normal to the longitudinal axis, and secondly there is an induced load on the flare ahead of the spoiler, which acts through the axis. It is therefore possible to combine spoilers so as to eliminate unwanted components. For example, at zero incidence, pure pitching moment may be achieved by means of an adjacent opposed pair extended in the incidence plane, pure yaw by an adjacent opposed pair normal to the incidence plane and pure roll by an opposed pair extended on opposite sides of the flare. Intermediate pairs could be used to obtain increments of moment about any axis through the C.G. and any number of pairs of spoilers could be used.

The model tested had provision for four pairs of spoilers. In this case there are two pairs of spoilers which yield moments of like sign about any particular one of the three body axes, when the incidence is zero. It will be shown that by suitable combination of the extensions of the two pairs it is possible to alleviate cross-couplings and changes in effectiveness due to incidence.

The tests were performed using only one spoiler and the complete control characteristics are evaluated on the assumption of non-interference between spoilers. This assumption, which has no experimental basis, is somewhat open to question in view of the area of the flare upon which the induced load appears to act.

The spoilers extended parallel to the incidence plane are referred to as top or bottom accordingly as they were to leeward or windward when the model was at positive incidence, and they could then be either on the port or starboard side of the incidence plane. The spoilers extended normal to the incidence plane could be either to port or starboard, and upper or lower accordingly as they were above or below the plane of symmetry normal to the incidence plane. Thus, for example, the term "top port" refers to the spoiler on the leeward side of the flare and to port of the incidence plane.

Three spoiler heights were tested in each of the top and bottom port and port upper and lower positions.

10.8.1 Individual spoiler performance

Overall force and moment results with a single spoiler extended are given in Figs.93 to 104 and C.P. variations in Figs.130 and 131.

Fig.15(h) shows that spoilers in the top positions lose pitch effectiveness with incidence more rapidly than those in the upper positions, and that those in the bottom position gain effectiveness with incidence while those in the lower positions are affected very little. These conclusions apply equally to rolling and yawing effectiveness.

It is possible to use the results to find the area of the flare subject to induced load if the pressure is assumed uniform over the face of the spoiler and over the area on the flare. Also if the distance of forward propagation of pressure is assumed constant across the spoiler, a value for this distance can be found. The increment in C_x due to spoiler extension is very nearly entirely due to pressure on the face of the spoiler. This increment can be used to obtain that part of the increment in C_m, or C_n, which is due to this, the remaining part being that due to the induced load on the flare. For example, when the spoiler was extended 0.2" in the incidence plane at zero incidence, the mean measured values of ΔC_x and ΔC_m were 0.105 and 0.30. We find that the ΔC_m corresponding to $\Delta C_x = 0.105$ is only 0.08, leaving 0.22 as the contribution of the induced load. The distance of forward propagation can then be computed as 0.14 inches and the pressure coefficient as 1.24. Other components could be used to make the calculation. Using the values of C_y for 0.2 inches extension in and normal to the incidence plane we obtain 0.17 inches and pressure coefficient of 1.33 for the same case. Computations using ΔC_m, ΔC_x and C_n for all spoiler heights and incidences suggest that in most cases the extent of forward propagation is 0.1 to 0.2 inches.

10.8.2 Use as a longitudinal control

The four spoilers used for negative (nose down) control would be bottom port and starboard and port and starboard lower, the other four spoilers providing control in the positive sense. From Figs.97 and 98 it is clear that whatever combinations of extension in the two planes are used, increasing incidence must give increasing negative control power and decreasing positive power. The latter becomes almost non-existent at $\alpha = 25^0$. Figs.93 and 94 provide means of finding the axial force penalty for any combination of extensions and it is evident that ΔC_x is always negative i.e. unfavourable.

From Figs.95 and 96 it may be seen that the increment of force is opposed to the demand direction.

10.8.3 Use as a directional control

The four spoilers giving negative (nose to port) control are top and bottom port and port upper and lower. The other four give positive control. Figs.101 and 102 show that while increasing incidence somewhat reduces the

yawing moment from the port upper and lower pair (from C_n = 0.6 at $\alpha = 0^\circ$ to 0.48 at $\alpha = 25^\circ$ for 0.2" height) it increases that from the other pair (from C_n = 0.54 at $\alpha = 0^\circ$ to 0.85 at $\alpha = 25^\circ$, also for 0.2" height). It is thus possible to so arrange the extensions in the two planes as to obtain nearly constant values of C_n throughout the incidence range.

Since the top port and port upper spoilers both lose effectiveness as incidence increases there will be nose down pitch coupling irrespective of the combination of these extensions.

Figs.103 and 104 show that increasing incidence causes the pair of spoilers extended normal to the incidence plane to develop a power in the roll sense which is of opposite sign to the power also developed with incidence by the pair extended in the incidence plane. As the former effect is not so strong as the latter, roll coupling can be avoided if a suitably greater extension of spoilers normal to the incidence plane than in it is used. This arrangement is also of the correct sense to reduce, though it cannot eliminate, the pitch coupling.

10.8.4 Use as a lateral control

The swept spoiler is the only control of those tested to provide any means of lateral control and as such might conceivably be used as supplementary to the other devices considered. The combination of spoilers giving negative rolling moment is bottom starboard, port lower, top port and starboard upper - the remaining four giving positive roll control. Figs.103 and 104 show (reversing signs as required) that it is possible to combine the extensions so as maintain uniform roll effectiveness throughout the incidence range. The arrangement required is that the spoilers operated normal to the incidence plane should be extended about twice as far as those operated in the incidence plane. Figs.101 and 102 show that this arrangement also gives near minimal yaw coupling. There is however, a large nose down pitch coupling.

10.9 Eccentric ring control Re $\simeq 5 \times 10^6$

Overall forces and moments for the model fitted with this control are given in Figs.105 to 111, and the C.P. variation is given in Fig.132.

Fig.15(j) and Fig.107 show that at zero incidence 0.1" eccentricity in the incidence plane caused no measurable pitching moment, but as incidence increased there was an increase in restoring moment due to eccentricity which was irrespective of sign. This is a surprising result inasmuch as except for a basic shape which is unstable at zero incidence this control cannot be used to trim at non-zero incidence. In this latter case where, due to a non-linear pitching moment, there is a stable trim attitude at some non-zero incidence (e.g. 24° in Fig.107), then the device may be used to reduce this trim incidence but the plane in which this occurs is arbitrary.

Fig.105 shows the variation of C_x with incidence. There is a small increase in axial force with eccentricity, which is greatest when the eccentricity is to windward at high incidence. It then amounts to an increase of about 18% at 25° incidence.

Fig.106 shows that the variation of force is consistent with the pitching moment trends already described.

Figs.109 and 110 show that the effect of eccentricity normal to the incidence plane is to increase slightly the lift contribution of the control.

Fig.111 shows that variation of the directional components with incidence is very small.

Translation normal to the incidence plane gives rise to an incidence dependent rolling moment, due to the product of ring C_z and eccentricity, and this is shown in Fig.111.

10.10 Tilting ring control $Re \simeq 5 \times 10^6$

The overall forces and moments on the model with this control operative are presented in Figs.112 to 120 and the variation of C.P. with incidence and deflection in the incidence plane in Fig.133.

Fig.15(k) shows that this control is powerful but gives a non-linear variation of ΔC_m with deflection. Increasing incidence causes increasing increments, irrespective of sign of deflection. Generally the value of ΔC_m varies in a similar manner to that for the tilting flare control.

Fig.16(k) shows the variation of ΔC_x with deflection at $\alpha = 0^\circ$ and $\alpha = 10^\circ$, the variation of C_x with α being shown in Fig.112. The value of ΔC_x at zero incidence and $\eta = 9^\circ 8'$ appears rather large and the question arises as to whether the flow through the ring was choked in this case. Fig.121 presents Schlieren photographs of the deflected and undeflected control and in all cases the control leading edge shock waves appear to be attached, indicating that the flow was unchoked. The increase in C_x is probably due to the component of force normal to the ring, the other component of which gives the increment in pitching moment which also increases non-linearly with deflection.

Fig.113 shows that the force increment is opposed to the demand direction.

Figs.116 and 117 show the effect of deflection normal to the incidence plane on the longitudinal components. From these curves it may be deduced that the ring and rear body normal force is increased by deflection in this direction.

The variation of C_y and C_n with incidence for deflections normal to the incidence plane is shown in Figs.118 and 119. There is quite a large increase of effectiveness with incidence, at $\alpha = 25^\circ$ the values are about 50% greater than at $\alpha = 0^\circ$. The gain is greater then for the tilting flare.

Fig.120 shows the variation of C_ℓ with incidence when the deflections are normal to the incidence plane. This arises from the lift on the ring acting at a point off the model axis. An estimate by Newtonian theory of C_ℓ for a corresponding solid cylinder is included in Fig.120 and this gives less than half the measured value, which indicates the important contribution of the internal flow.

11 COMPARISONS AND CONCLUDING REMARKS

It is not possible here to provide a complete assessment of the efficiency of the various control devices tested since they vary so widely in inertia and probably in requirements of force to operate. It is possible however to examine how closely they approach the ideal aerodynamic output, ignoring the mechanical difficulties involved in achieving the control movements which produce it. Ideally, a control should provide a moment which is invariant with incidence of the basic body, linear with control deflection and in, or normal to, the plane containing the longitudinal axis and the deflection. Furthermore, it is advantageous if it provides an increment of force in the direction in which it is desired to accelerate the body. It is also advantageous if it gives an increment of axial force in the thrust sense.

Table 2 gives a simplified summary of the control characteristics over the range of incidence from zero to 25°. Some of the characteristics are particularly referred to $\alpha = 10°$, as a possible cruising incidence of the basic cone-cylinder-flare.

An important point to consider in any practical application is that only the swept spoilers provide means of roll control. If one of the other controls is used on a body of revolution or other body having no stable attitude in roll then some additional means of roll control would be needed and its power would be dependent on the roll coupling of the main control. An indication of this coupling is given in Table 2, in terms of C_ℓ/C_n arising when answering a demand normal to the incidence plane, with the basic body at the assumed cruise attitude.

From Table 2 it may be concluded that the swept spoilers provide the only self-contained control system, but lose effectiveness rapidly at positive incidence, and suffer from yaw/pitch coupling at incidence. Of the others, the best is the tilting nose. The tilting flare suffers larger incidence effects and has an adverse force increment. The nose flap suffers prohibitively large incidence effects, which are due to interference with the body and flare lift. The main disadvantage of the pair of flare flaps is the large increase in longitudinal static margin with the flaps operated to provide yawing moment. The nose disc is ineffective at zero incidence and has a large axial force penalty. The rear disc effectiveness is very incidence dependent, and is also achieved at the cost of a large axial force penalty. The tilting spike effectiveness is highly non-linear, due to the separation phenomenon ahead of the hemisphere, and also incurs a large axial force penalty. The eccentric ring has no power at zero incidence. Where trim is possible (Section 10.9) eccentricity, of whatever sense, merely reduces the incidence at which this

occurs. The tilting ring is a very effective control although somewhat inferior to the tilting flare in many characteristics, and because of the use of thin sections would suffer in common with the eccentric ring difficulties in dissipating kinetic heat in practice.

LIST OF SYMBOLS

$Ox_oy_oz_o$ right hand system of axes fixed in tunnel with Ox_o along the direction of relative wind

$Oxyz$ right hand system of axes fixed in model

α angle of incidence, angle between Ox and Ox_o

η control deflection parameter

X component of force along Ox

Y component of force along Oy

Z component of force along Oz

L moment about Ox

M moment about Oy

N moment about Oz

Force coefficients $C_x = \frac{X}{qS}$, etc

Moment coefficients $C_\ell = \frac{L}{qSd}$, etc

$S = \pi d^2/4$ sq in.

d = body diameter = 1.28 in.

X_{FLAP} component of force on flap along Ox

Z_{FLAP} component of force on flap normal to Ox and in either the xz or xy planes. Positive towards Ox axis

M_{FLAP} moment about flap leading edge, positive tending to increase η

Flap force coefficients $C_{x_{FLAP}} = \frac{X_{FLAP}}{qS}$, etc

LIST OF SYMBOLS (CONTD)

Flap moment coefficient $C_{m_{FLAP}} = \frac{M_{FLAP}}{qS'\ell'}$

S' = flap span x chord sq in.

ℓ' = flap chord in.

q = kinetic pressure = $\frac{1}{2}\rho V^2$

p_s = free stream static pressure

M = Mach number

R_e = Reynolds number based on net overall length

ΔC_m = C_m (control deflected) $-C_m$ (control undeflected) similarly ΔC_x and ΔC_z

---

LIST OF REFERENCES

No.	Author(s)	Title, etc.
1	Cork, G.	A D.E.U.C.E. programme for processing supersonic wind tunnel data. Unpublished N.G.A. Report.
2	Monaghan, R.J.	Formulae and approximations for aerodynamic heating rates in high speed flight. A.R.C. C.P. 360. October, 1955.
3	Syvertson, C.A. Dennis, D.H.	A second order shock expansion method applicable to bodies of revolution near zero lift. N.A.C.A. Report 1328. 1957.
4	Allen, H.J.	Estimation of the forces and moments acting on inclined bodies of revolution of high fineness ratio. N.A.C.A. RM A9I26, N.A.C.A. TIB 2289. November 1946.
5	Hunt, G.K.	Supersonic wind tunnel study of reducing the drag of a bluff body at incidence by means of a spike. Unpublished N.G.A. Report.

TABLE 2

Summary of control characteristics

Control	Answering demand in incidence plane				Answering demand normal to incidence plane			Remarks
	Linearity	Incidence effects	X force penalty	Size and dirn. of ΔZ	Incidence effects	Effects on C_m	Effects on C_ℓ	
	Approx. max. % deviation from linear $\Delta C_m/\eta$ all α	Approx. Max. % variation in ΔC_m (η = max) from val. at $\alpha = 0^\circ$	$\frac{C_X - C_X \text{ (basic shape)}}{\lvert\Delta C_m\rvert}$ at $\alpha = 10^\circ$	Approx. max. value of $\Delta C_z/\Delta C_m$ at $\alpha = 10^\circ$	Approx. % variation of $\lvert C_n\rvert$ from $\alpha = 0^\circ$ value	$\frac{\Delta C_m}{\lvert C_n\rvert}$ at $\alpha = 10^\circ$, η = max.	C_ℓ/C_n at $\alpha = 10^\circ$ η = max.	
Tilting nose	15	+50	+0.006 ΔC_m -VE -0.17 ΔC_m +VE	-0.34	±7	+0.12	-0.098	Very effective control $\lvert\Delta C_m\rvert/\eta^\circ = 0.095$ at $\alpha = 0^\circ$
Tilting flare	15	+100	-0.17 ΔC_m -VE +0.03 ΔC_m +VE	+0.37	±12	-0.12	-0.084	Very effective control $\lvert\Delta C_m\rvert/\eta^\circ = 0.102$ at $\alpha = 0^\circ$
Nose flap	?	+1600	-0.31 ΔC_m -VE -0.34 ΔC_m +VE	-0.2	+500	+0.33	+0.08	Not very effective except at high α, flap to windward. $\lvert\Delta C_m\rvert/\eta^\circ = 0.003$ at $\alpha = 0^\circ$
Flare flaps (a pair, one +VEη one -VE)	10	+20, ΔC_m +VE +10, ΔC_m -VE	-0.12 ΔC_m -VE +0.03 ΔC_m +VE	+0.48	+18	-0.82	-0.065	Effective control $\lvert\Delta C_m\rvert/\eta^\circ = 0.047$ at $\alpha = 0^\circ$
Nose disc	5	$+\infty$ Only effective at high incidence	-3.6 ΔC_m -VE -2.6 ΔC_m +VE	-0.28	∞	0	0	Ineffective and high drag $\lvert\Delta C_m\rvert/\eta$min. = 0 at $\alpha = 0^\circ$
Rear disc	20	+260	-1.5 ΔC_m -VE -0.7 ΔC_m +VE	+0 25	+330	-0.18	0	Large rise in effectiveness and drag at high incidence $\lvert\Delta C_m\rvert/\eta$in. = 1.07 at $\alpha = 0^\circ$
Tilting spike	100	-90 to +60 large changes in ΔC_m for small changes in α	-5 ΔC_m -VE -10 ΔC_m +VE	-0.26	-63	+0.28	-0.04	High drag, large non-linear variations with η and α $\lvert\Delta C_m\rvert/\eta^\circ = 0.041$, $\alpha = 0$, $\eta = 9^\circ$-17'
4 swept spoilers	15	+200 ΔC_m -VE -90 ΔC_m +VE	-0.46 ΔC_m -VE -0.40 ΔC_m +VE	+0.3	+16 equal extn. can be made 0 by diffl. extn.	-0.36	+0.054 equal extn. can be made 0 by diffl. extn.	Provides roll control. Loses + VE power at incidence $\lvert\Delta C_m\rvert/\eta$in. = 6.3 at $\alpha = 0^\circ$
Eccentric ring	?	∞ Only effective at inc. and ΔC_m always -VE	-0.86 to windward -1.27 to leeward	+0.5	$C_n \doteq 0$ at all α	∞	∞	Eccentricity only produces $\partial C_m/\partial\alpha$ change. No ΔC_m ($\alpha = 0$)$\eta\perp$ incidence plane gives C_ℓ
Tilting ring	30	+90	-0.21 ΔC_m -VE -0.13 ΔC_m +VE	+0.43	+47	-0.25	-0.033	Very effective control $\lvert\Delta C_m\rvert/\eta^\circ = 0.11$, $\alpha = 0$, $\eta = 9^\circ$-8'
Ideal	0	0	+VE	-VE	0	0	0	Requires a large value for $\lvert\Delta C_m\rvert/\eta^\circ$

Printed in England for Her Majesty's Stationery Office by the Royal Aircraft Establishment, Farnborough. 4.P.60.K.4

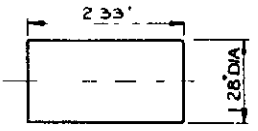

PLAIN TAIL

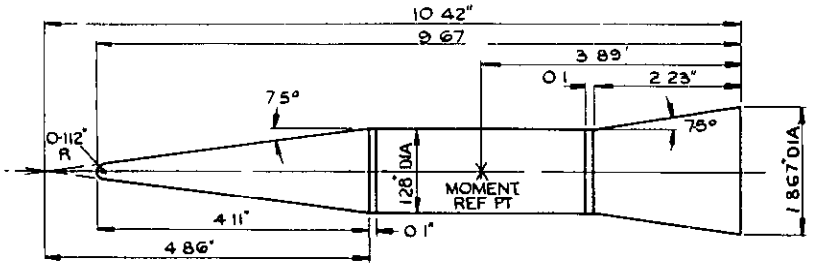

BASIC CONE-CYLINDER-FLARE

NOSE N°	ANGLE A
2	0°
3	1°- 35
4	3°- 8'
5	4°-35
6	7°-36
7	10°-25

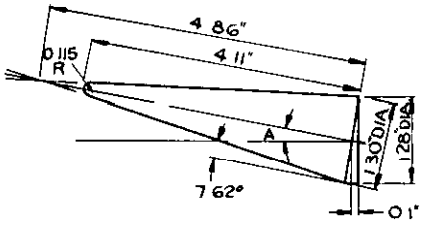

TILTING NOSE CONTROL

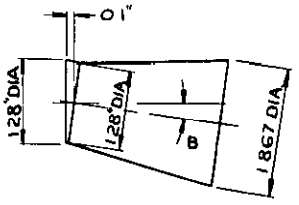

FLARE N°	ANGLE B
3	2°- 30'
4	5°
5	7°- 30

TILTING FLARE CONTROL

WEDGE N°	ANGLE C
	0°
1	7 5°

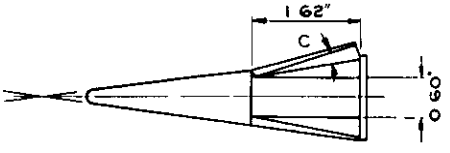

NOSE FLAP CONTROL

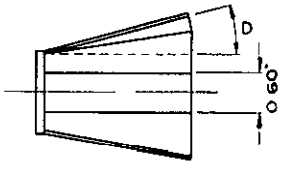

WEDGE N°	ANGLE D
	0°
2	3 75°
3	7 5°
4	11 25°
5	15°

FLARE FLAP CONTROL

DISC N°	DIM E
1	0"
2	0 05"
3	0 10"
4	0 15"

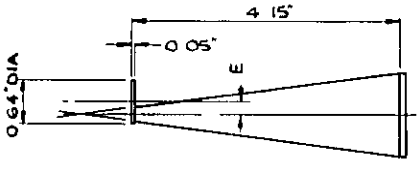

ECCENTRIC NOSE DISC CONTROL

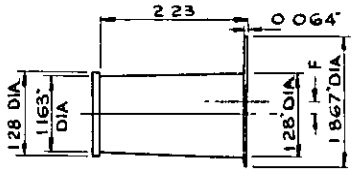

DISC N°	DIM F
5	0"
6	0 1
7	0 15
8	0 2"

ECCENTRIC REAR DISC CONTROL

NOSE N°	ANGLE G
10	0°
11	3°-8'
12	5°-56
13	9° 17

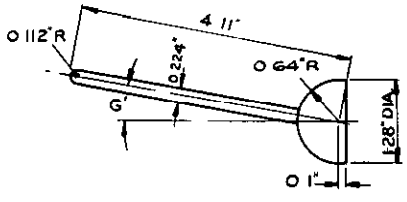

TILTING SPIKE CONTROL

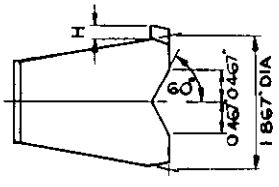

SPOILER N°	DIM H
	0
1	0 1"
2	0 15
3	0 2

SWEPT SPOILER CONTROL

DIM J
0
0 1"

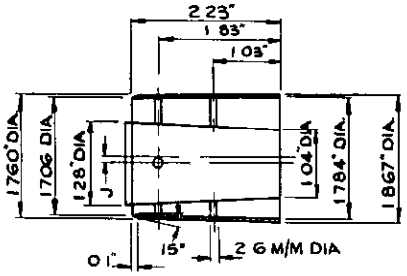

ECCENTRIC RING CONTROL

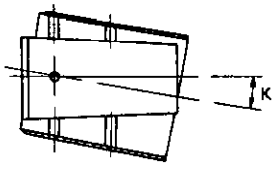

ANGLE K
0°
4°- 43
9°- 17'

TILTING RING CONTROL

FIG. I. DETAILS OF MODELS

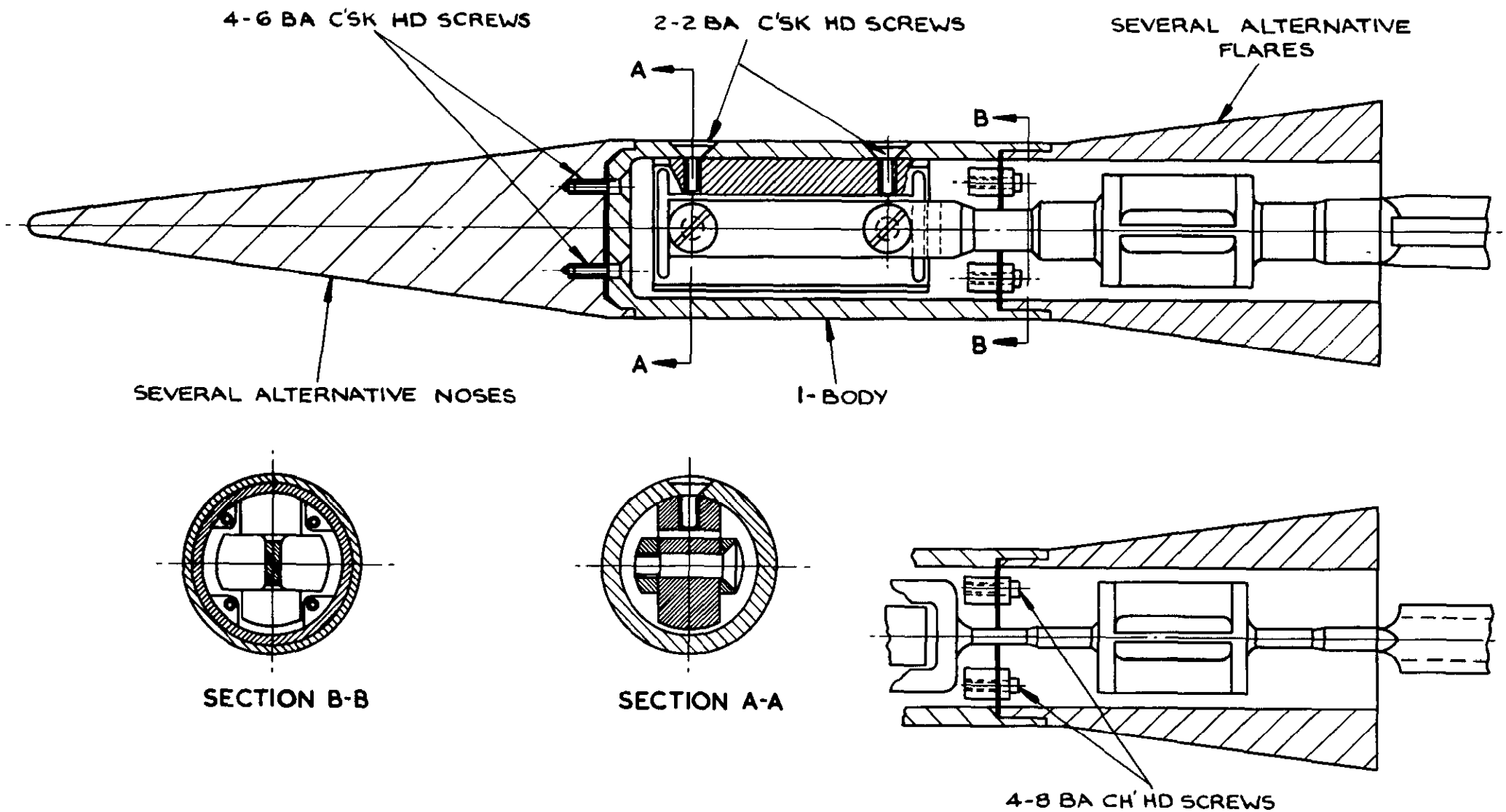

FIG. 2. ARRANGEMENT OF 6-COMPONENT BALANCE AND BASIC MODEL.

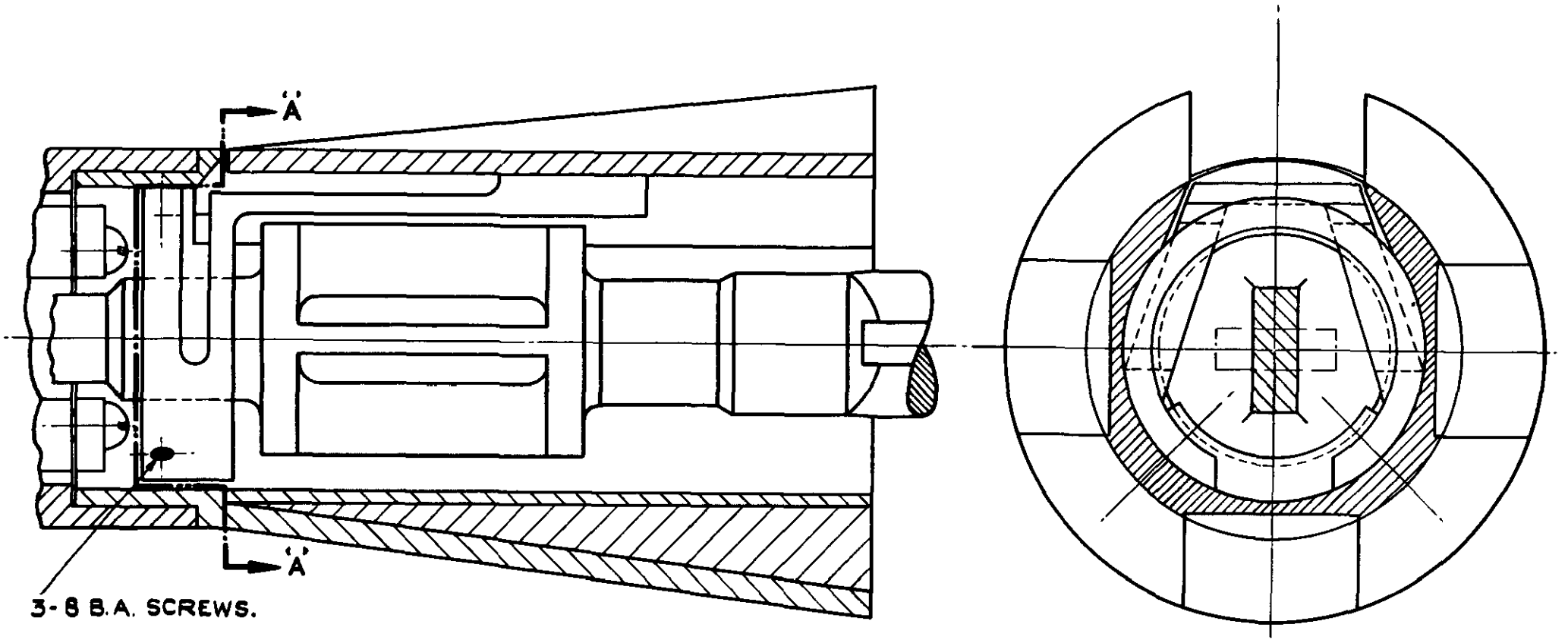

SECTION THROUGH MODEL.

SECTION 'A A'.

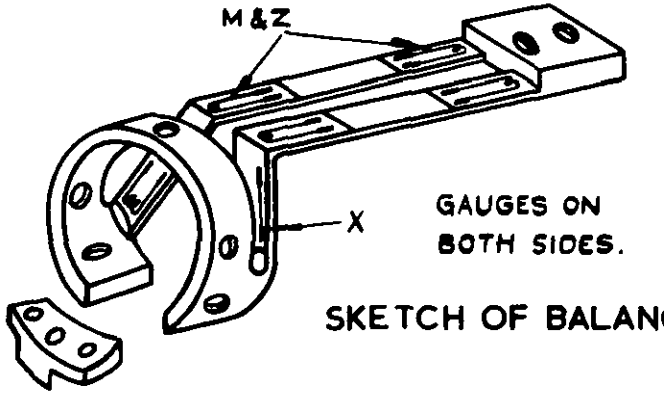

SKETCH OF BALANCE.

FIG. 3. ARRANGEMENT OF REAR FLAP CONTROL BALANCE.

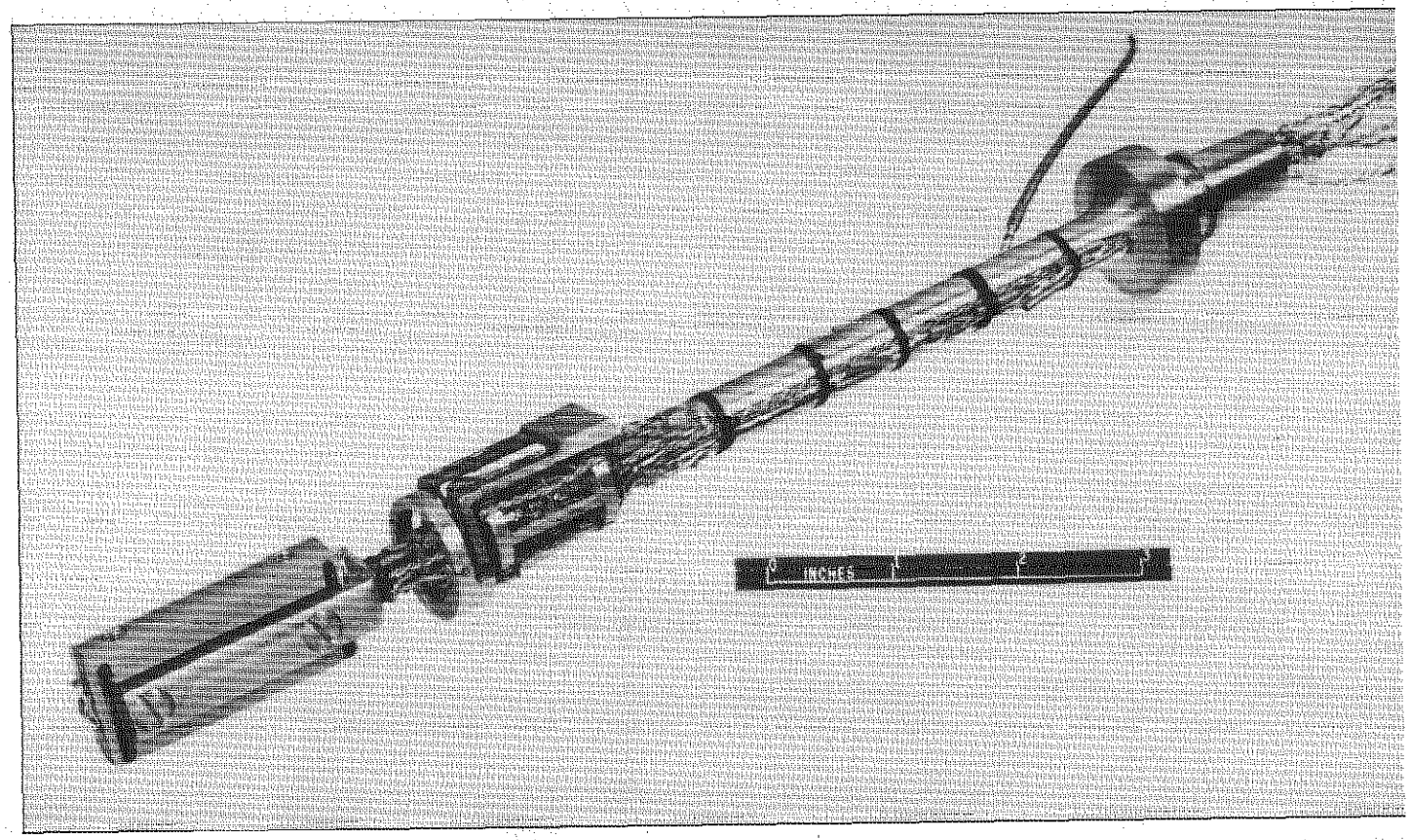

FIG. 4 BALANCES

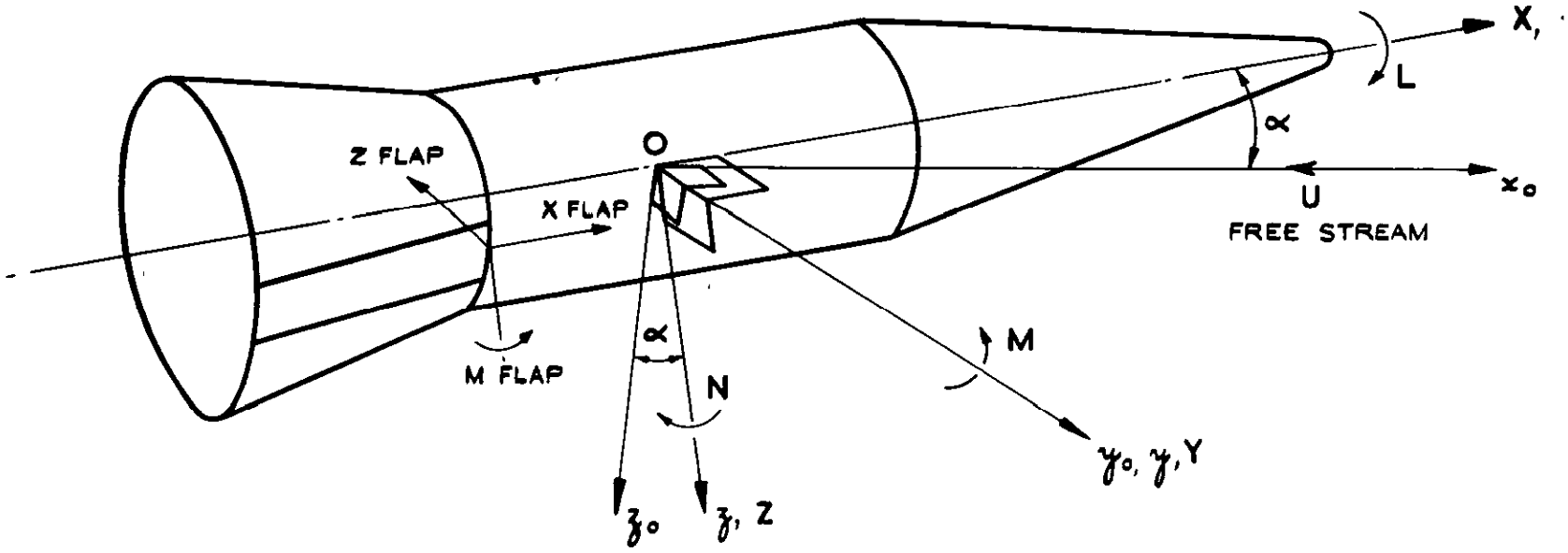

SUFFICES 0 DENOTE TUNNEL AXES.

FLAP X AXIS IS $\parallel \ell$ TO MODEL X AXIS FOR ALL SETTINGS.

Z FLAP IS POSITIVE TOWARDS Ox WHETHER FLAP IS IN O, x, y PLANE OR O, x, z PLANE.

FIG. 5. DIAGRAM SHOWING MODEL AND TUNNEL AXES.

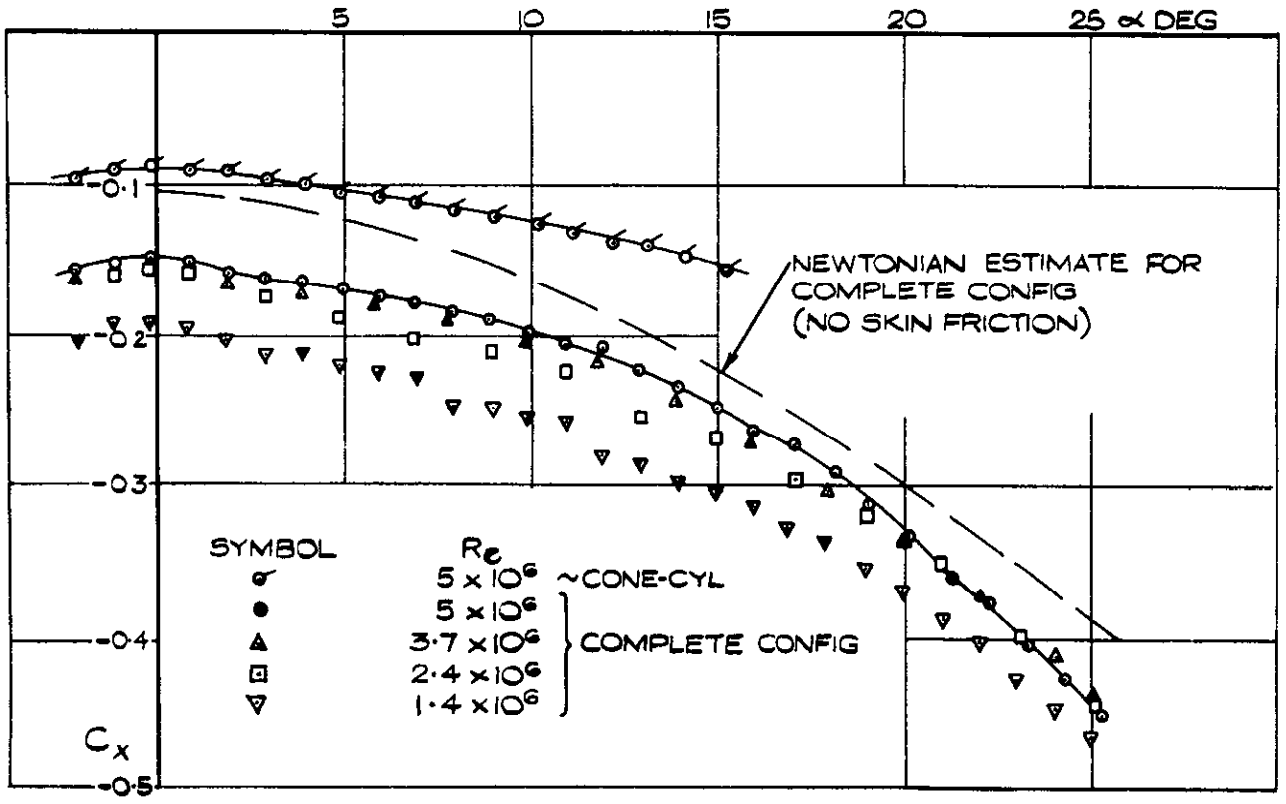

FIG 6. EFFECT OF REYNOLDS NUMBER ON C_x vs α FOR BASIC SHAPE.

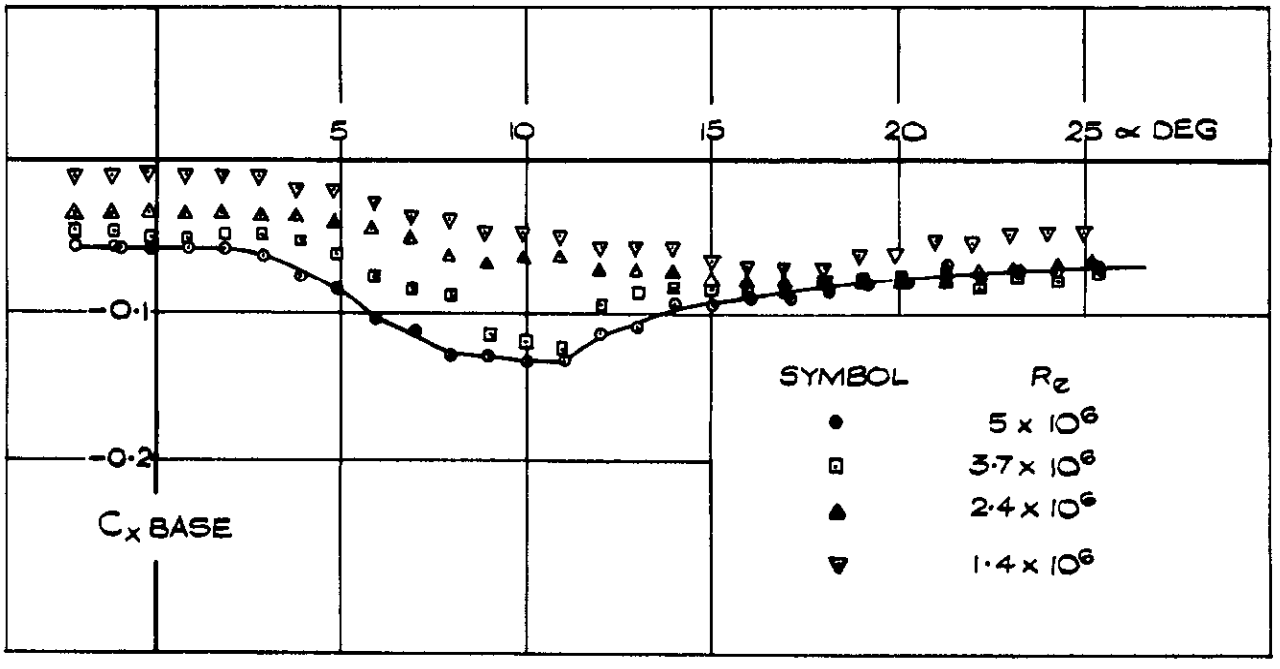

FIG 7 EFFECT OF REYNOLDS NUMBER ON MEASURED BASE AXIAL FORCE FOR BASIC SHAPE.

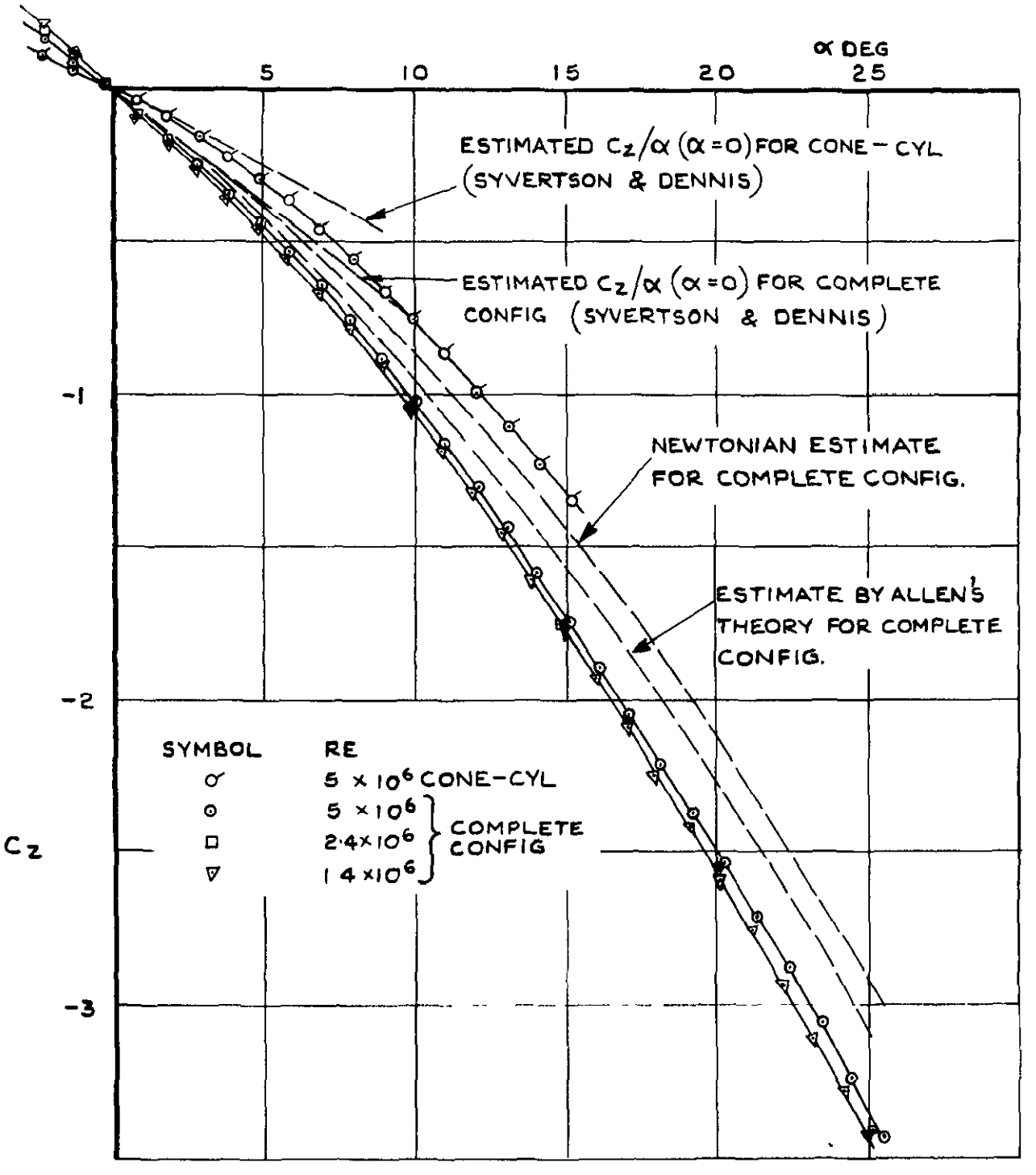

FIG. 8 EFFECT OF REYNOLDS NUMBER ON C_z vs α FOR BASIC SHAPE

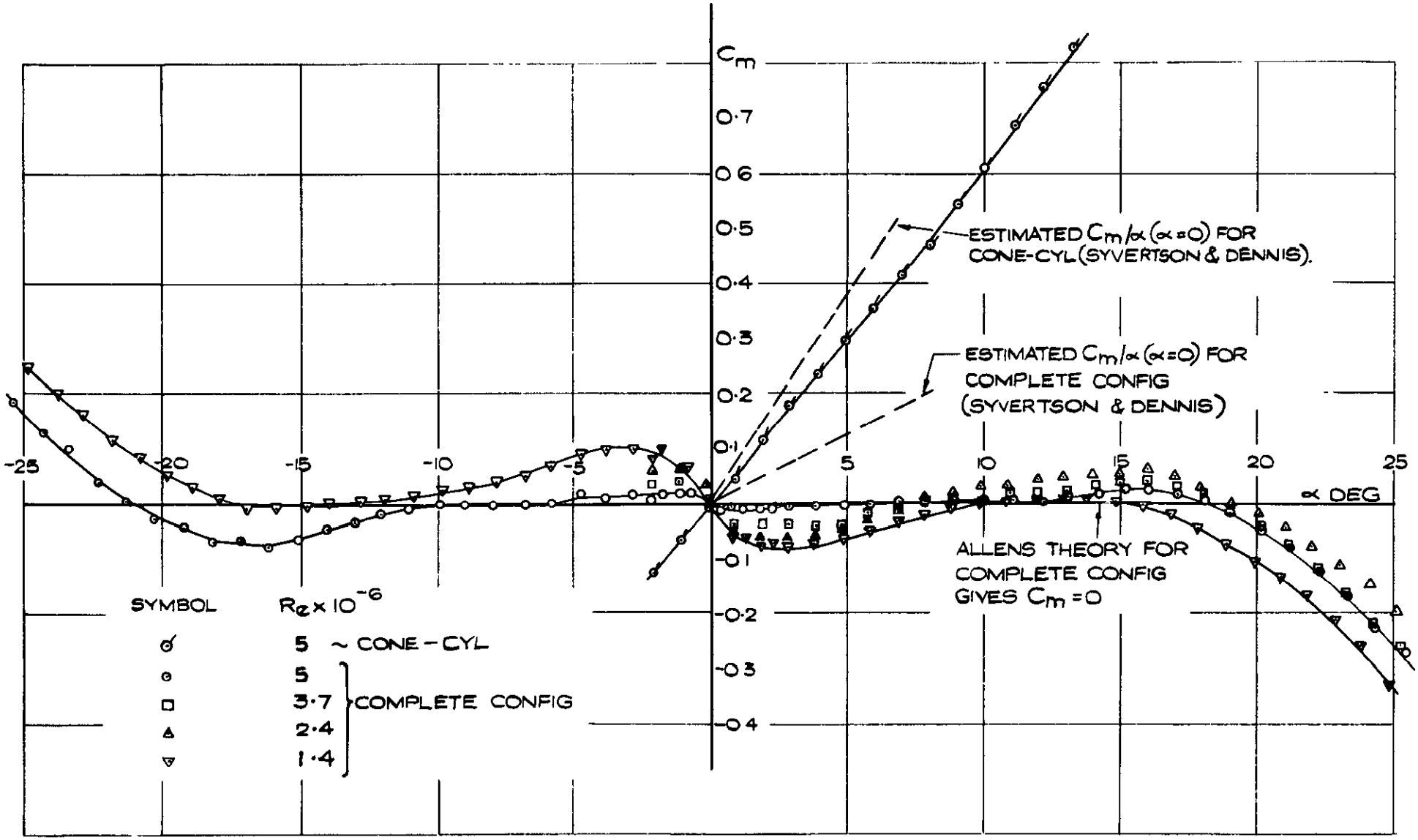

FIG 9 EFFECT OF REYNOLDS NUMBER ON C_m vs α FOR BASIC SHAPE.

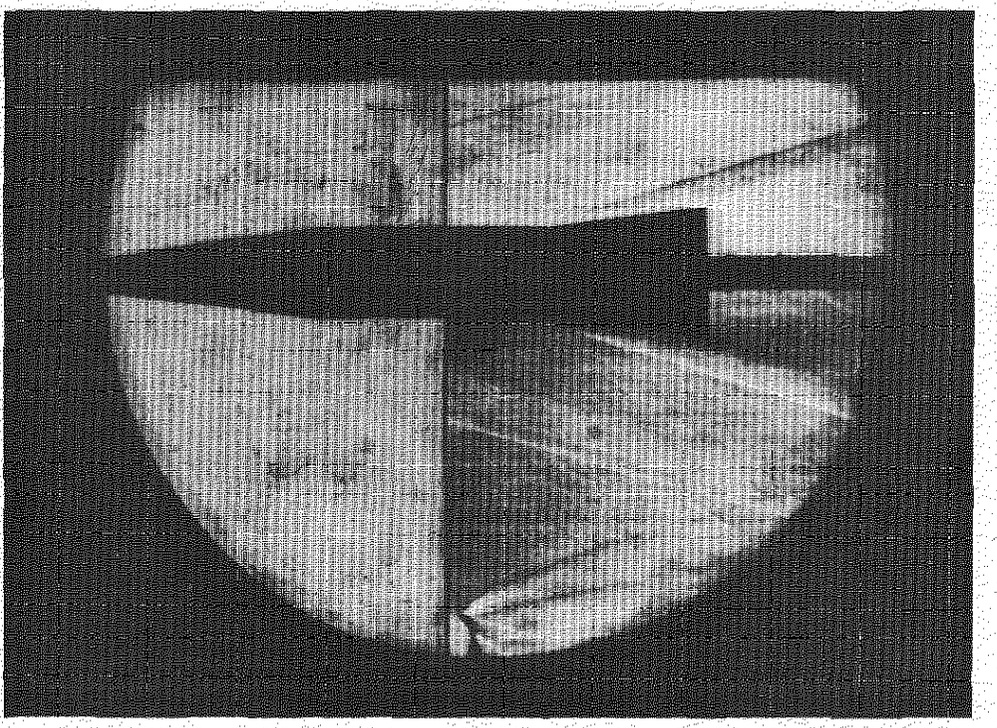

(a) $\alpha = 0^{\circ}$

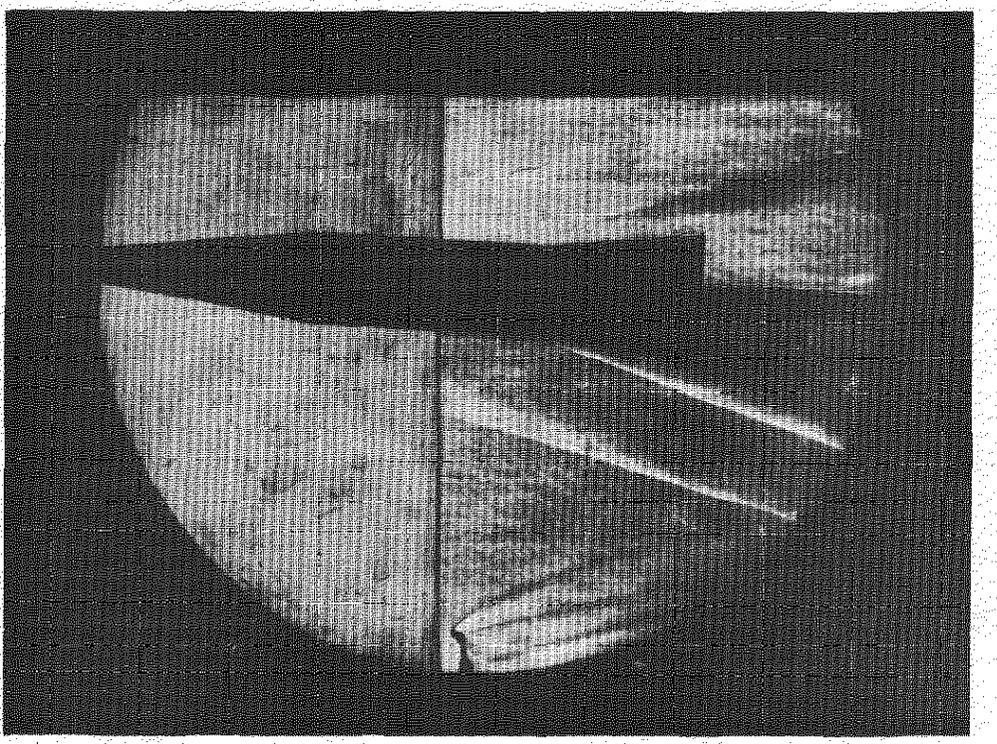

(b) $\alpha = 3^{\circ}$

FIG.10 SCHLIEREN PHOTOGRAPHS OF BASIC MODEL AT $\alpha = 0^{\circ}$ AND 3°. $R_e \simeq 5 \times 10^6$

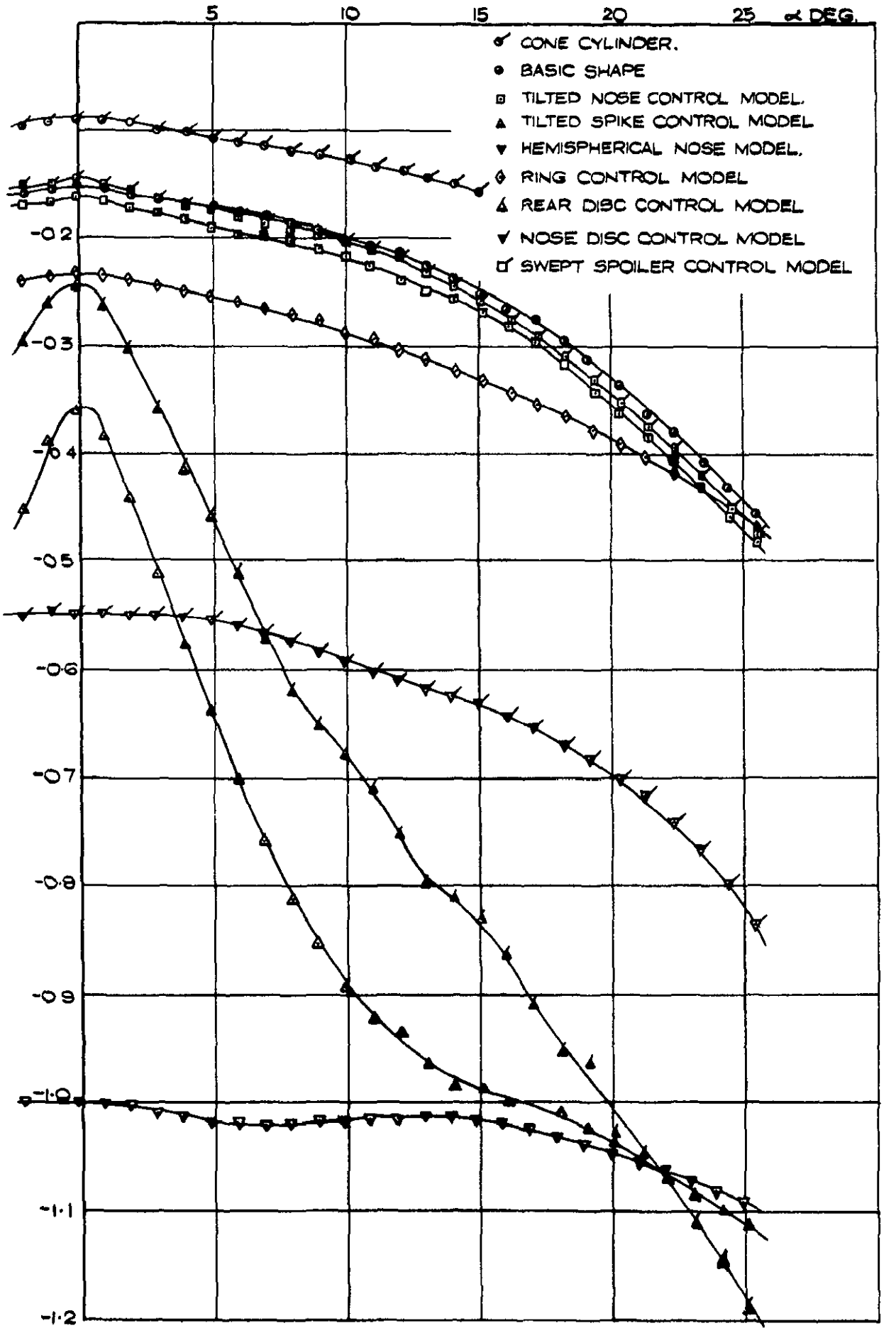

FIG.11. C_x vs α FOR MODELS WITH UNDEFLECTED CONTROLS.

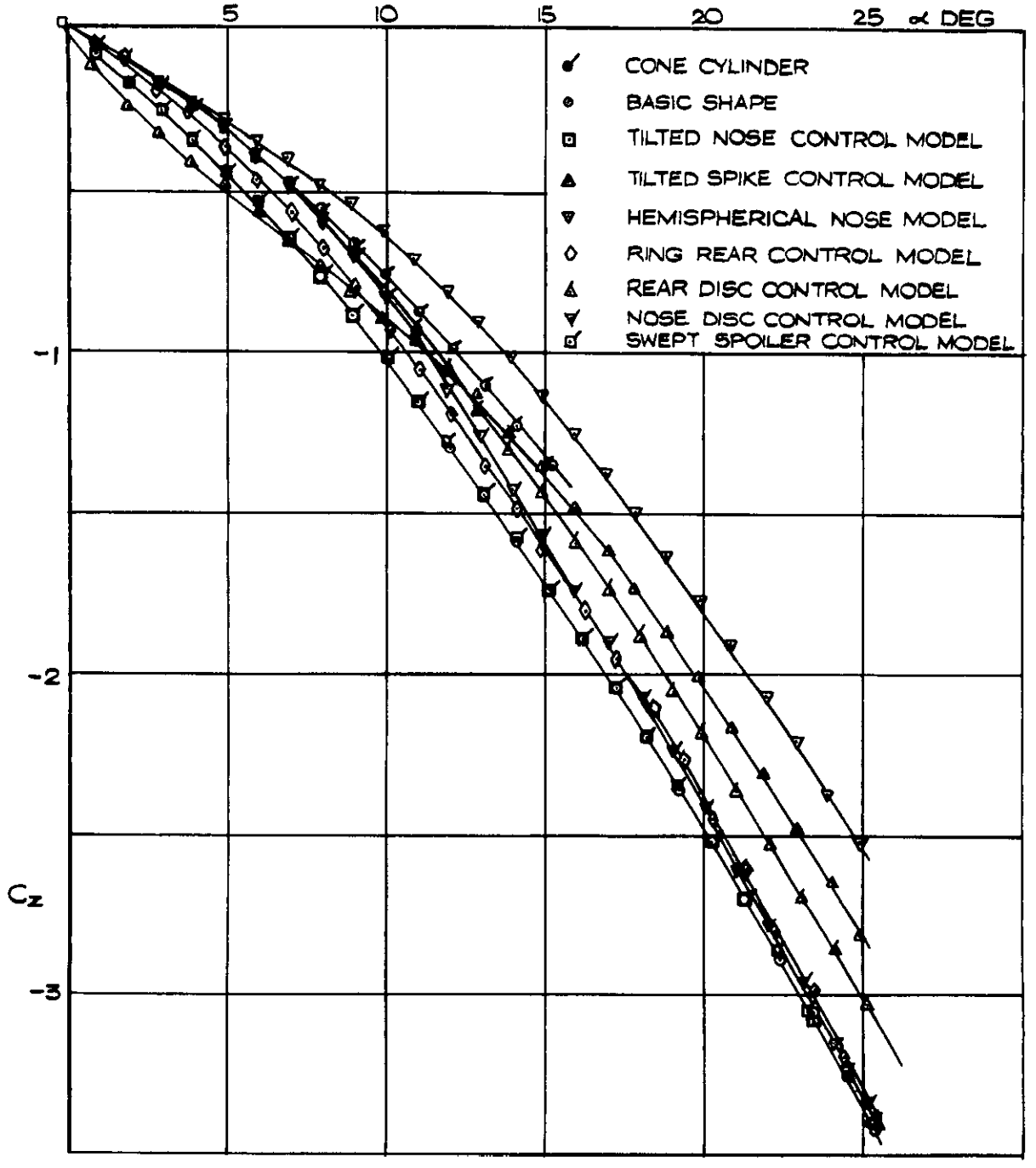

FIG 12. C_{z_v} ∝ FOR MODELS WITH UNDEFLECTED CONTROLS.

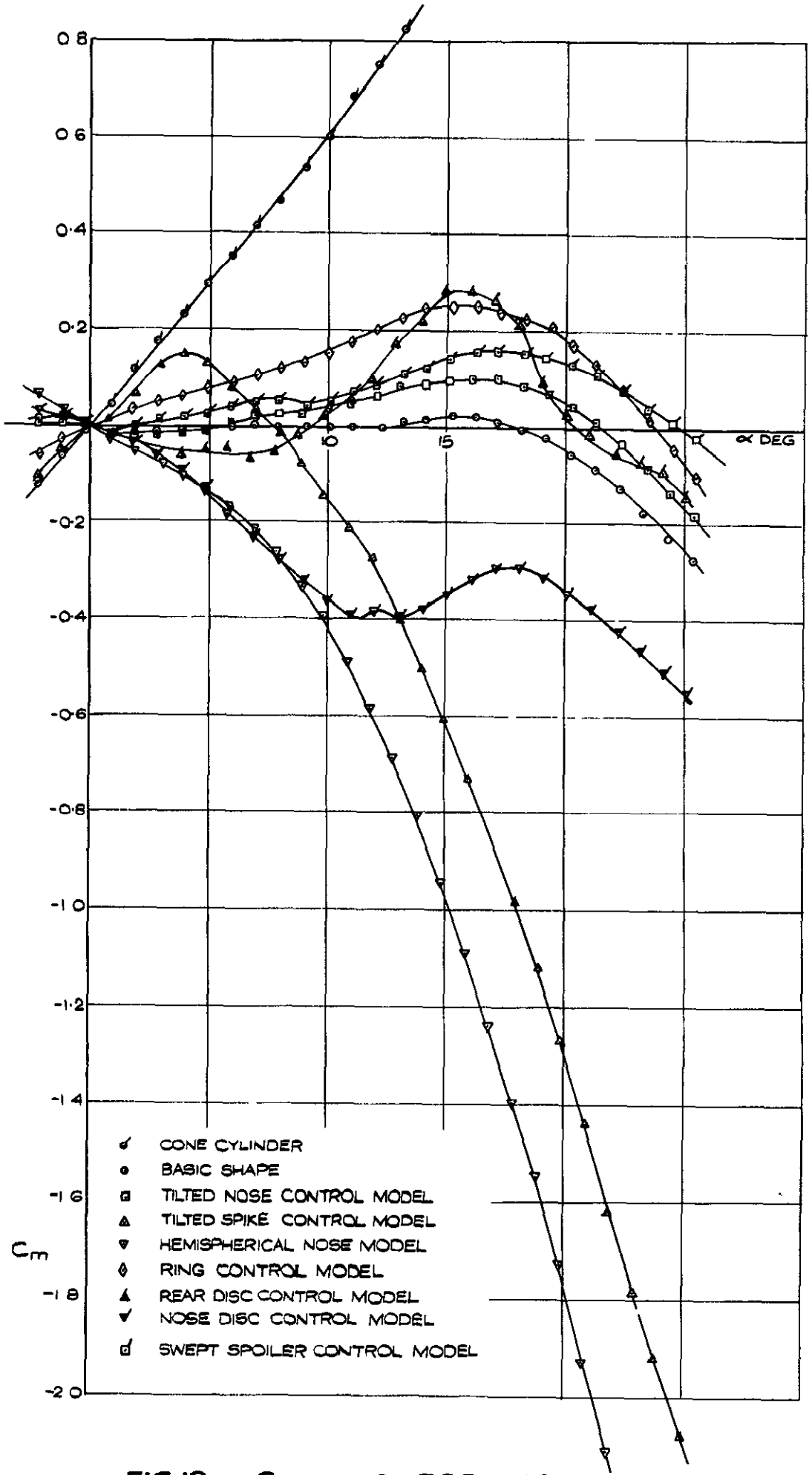

FIG.13. C_m vs α FOR MODELS WITH UNDEFLECTED CONTROLS.

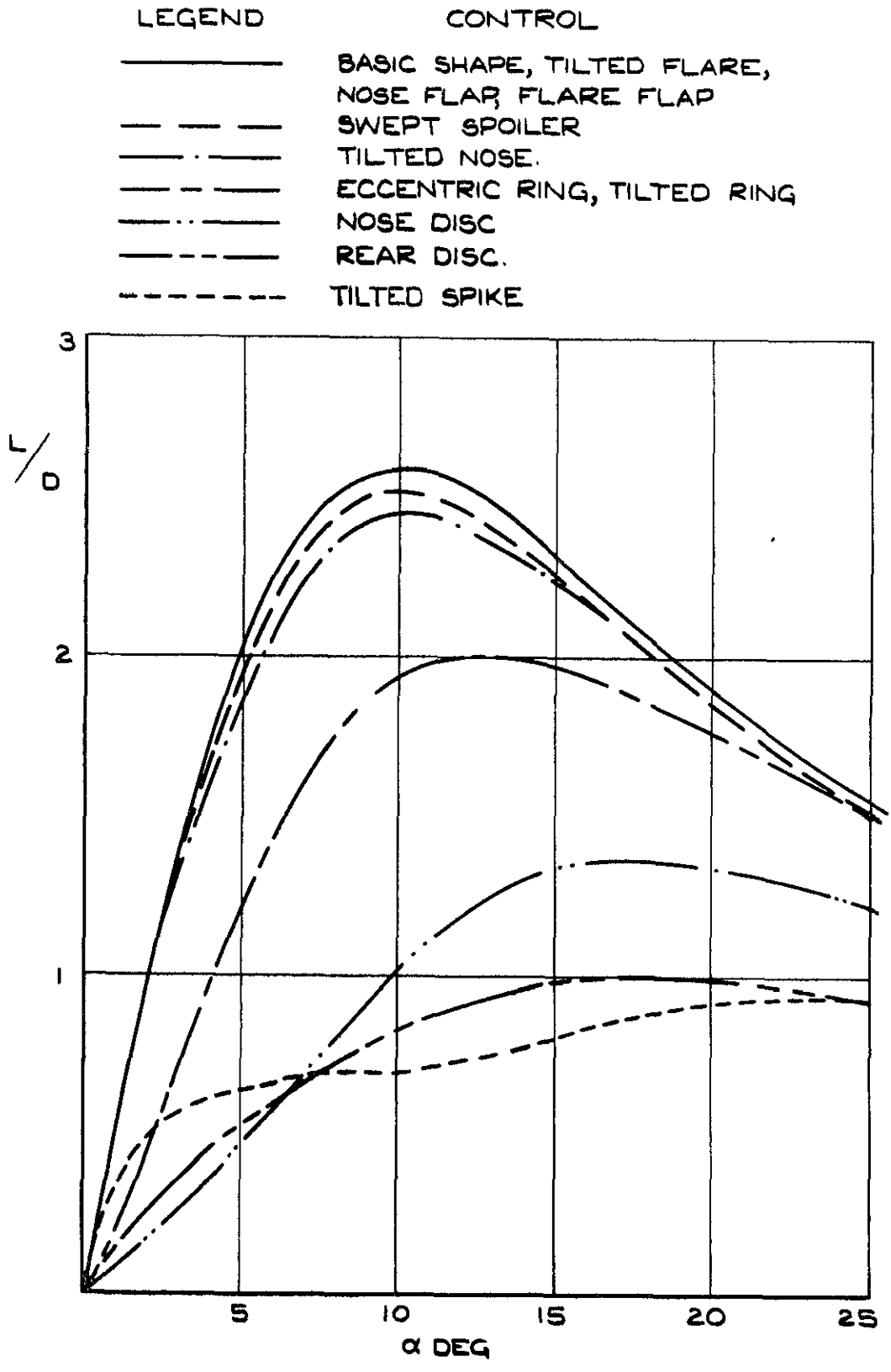

FIG. 14. VARIATION OF LIFT/DRAG RATIO WITH INCIDENCE FOR MODELS WITH UNDEFLECTED CONTROLS

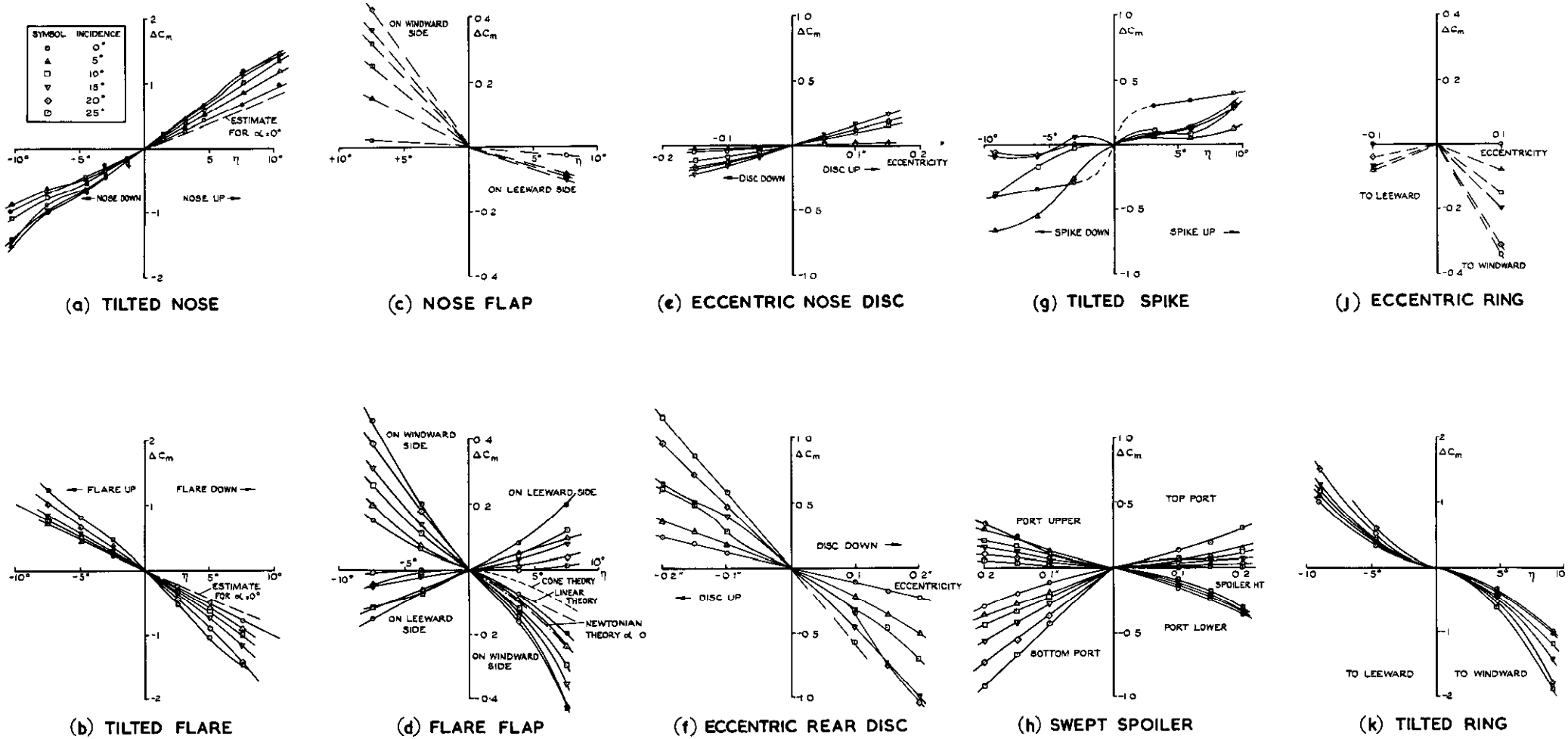

(a) TILTED NOSE (c) NOSE FLAP (e) ECCENTRIC NOSE DISC (g) TILTED SPIKE (j) ECCENTRIC RING

(b) TILTED FLARE (d) FLARE FLAP (f) ECCENTRIC REAR DISC (h) SWEPT SPOILER (k) TILTED RING

FIG. 15. ΔC_m vs DEFLECTION AT VARIOUS α FOR ALL CONTROLS ACTING IN THE INCIDENCE PLANE.

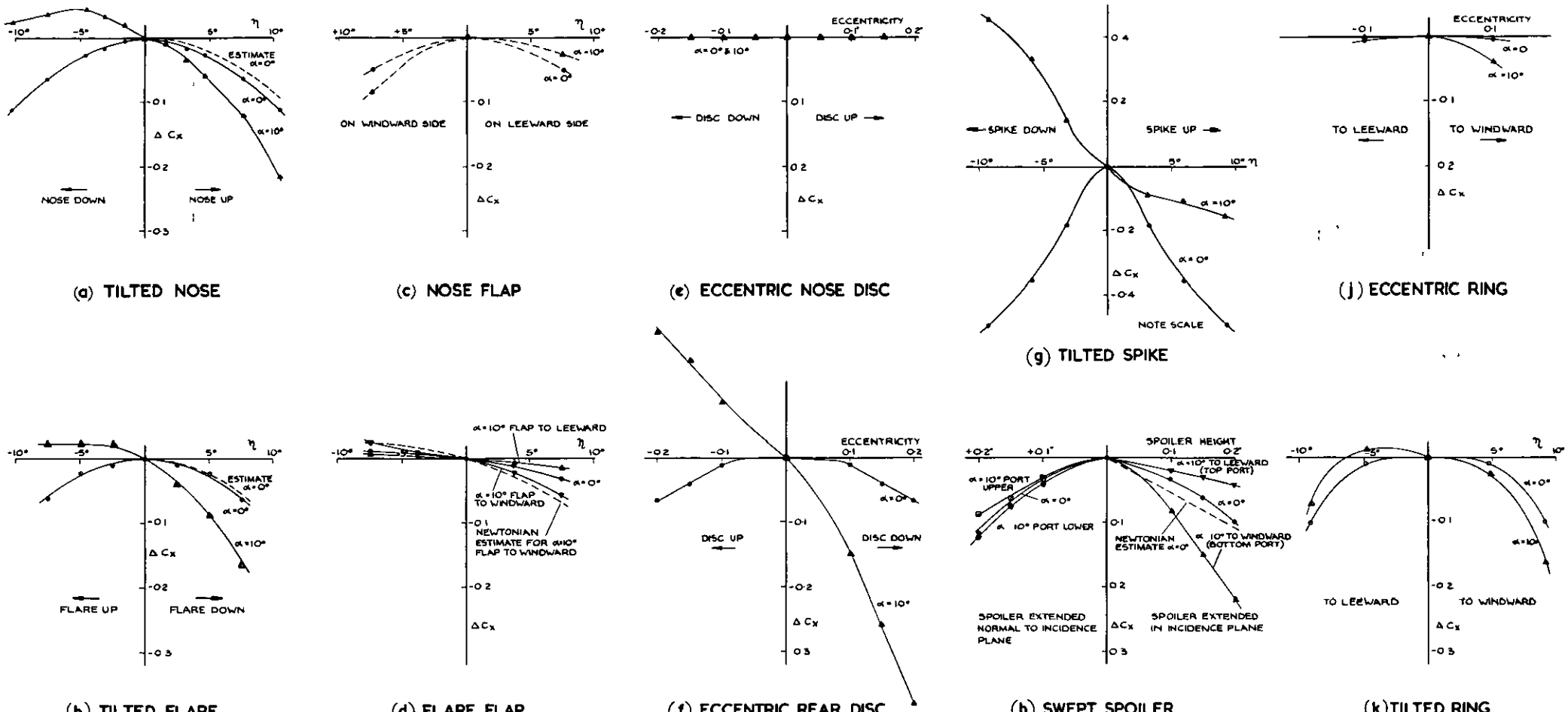

FIG. 16. ΔC_X vs DEFLECTION AT $\alpha = 0°$ & $10°$ OR ALL CONTROLS ACTING IN INCIDENCE PLANE.

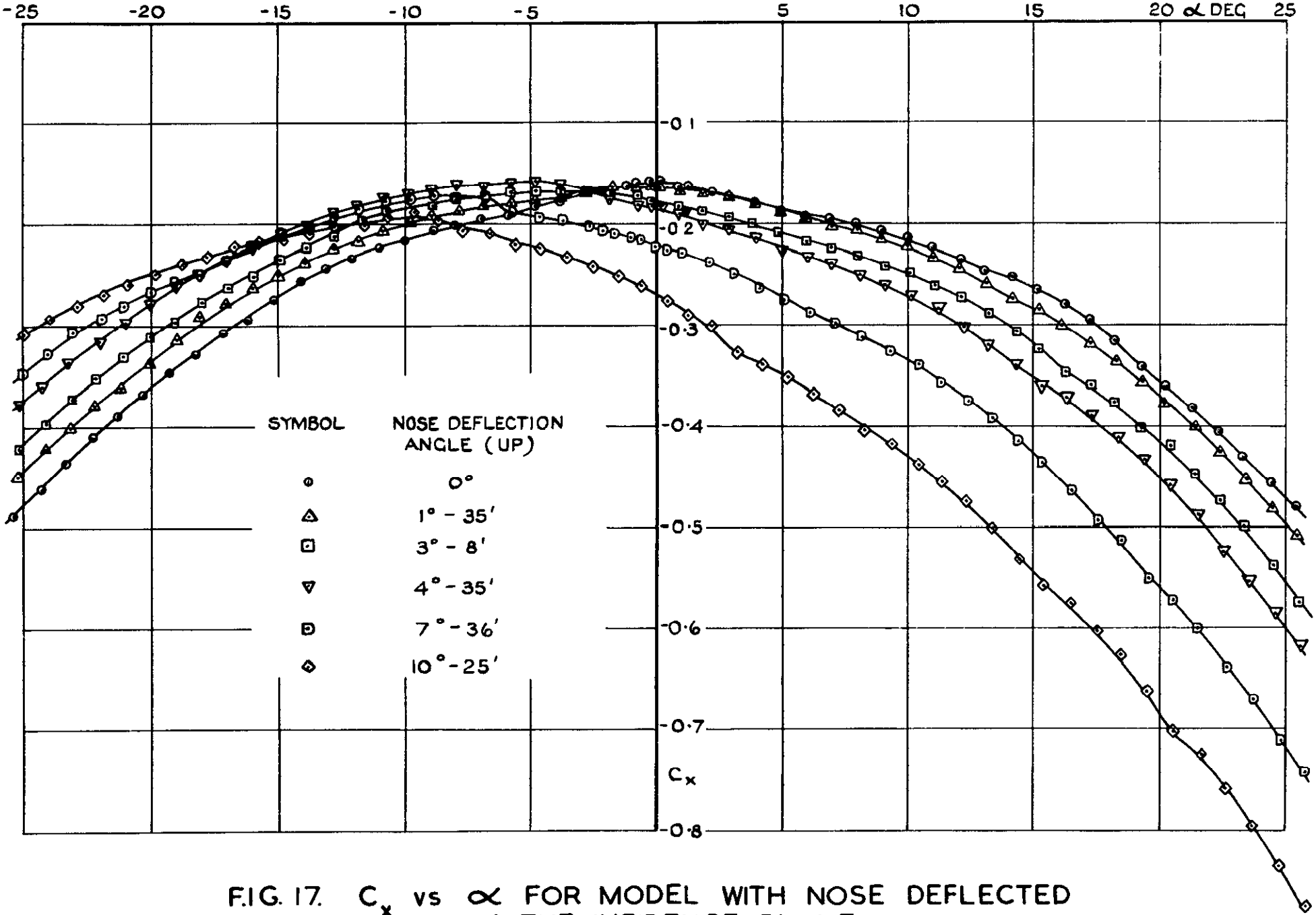

FIG. 17. C_x vs α FOR MODEL WITH NOSE DEFLECTED IN THE INCIDENCE PLANE.

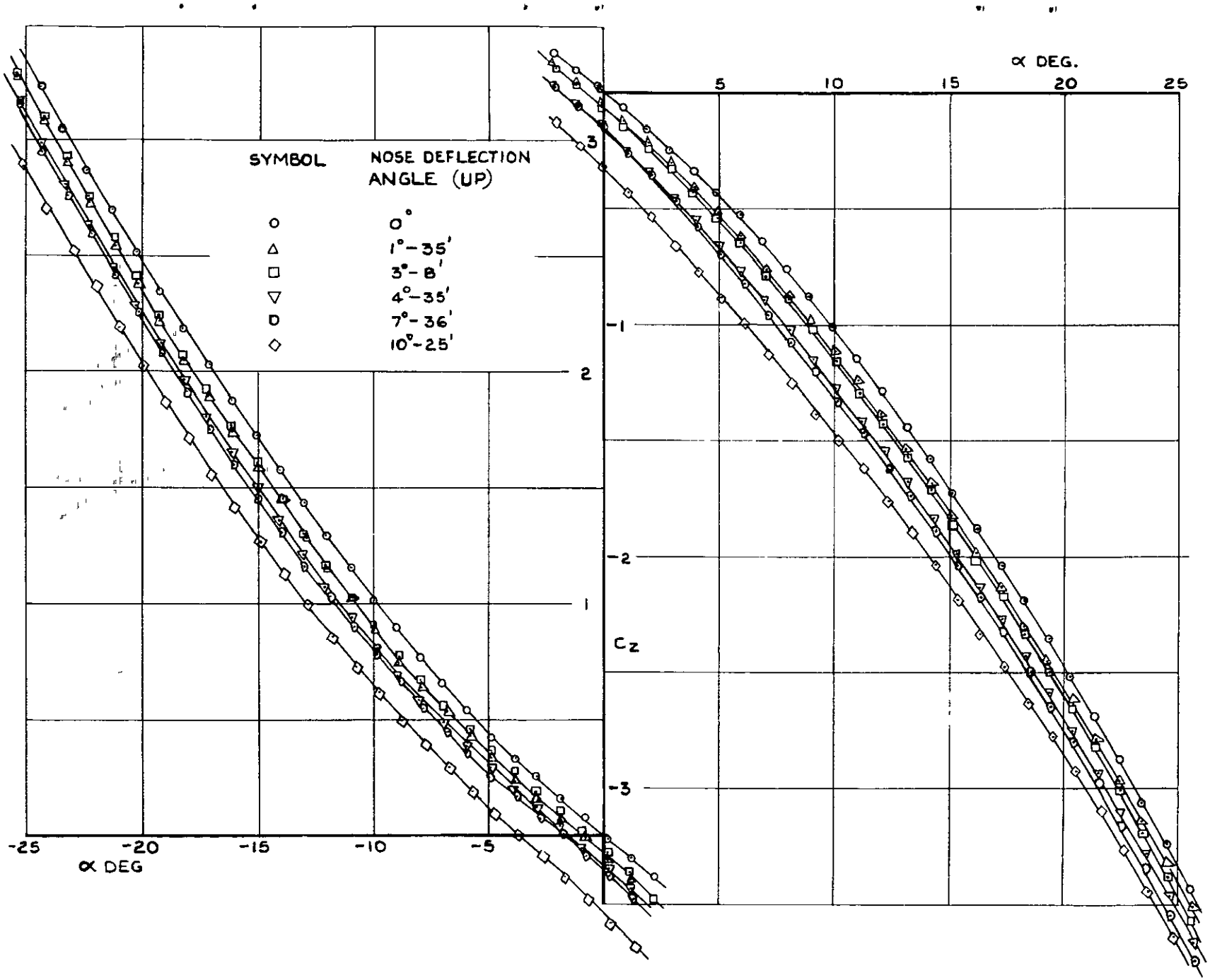

FIG. 18. C_z vs $\propto$ FOR MODEL WITH NOSE DEFLECTED IN THE INCIDENCE PLANE

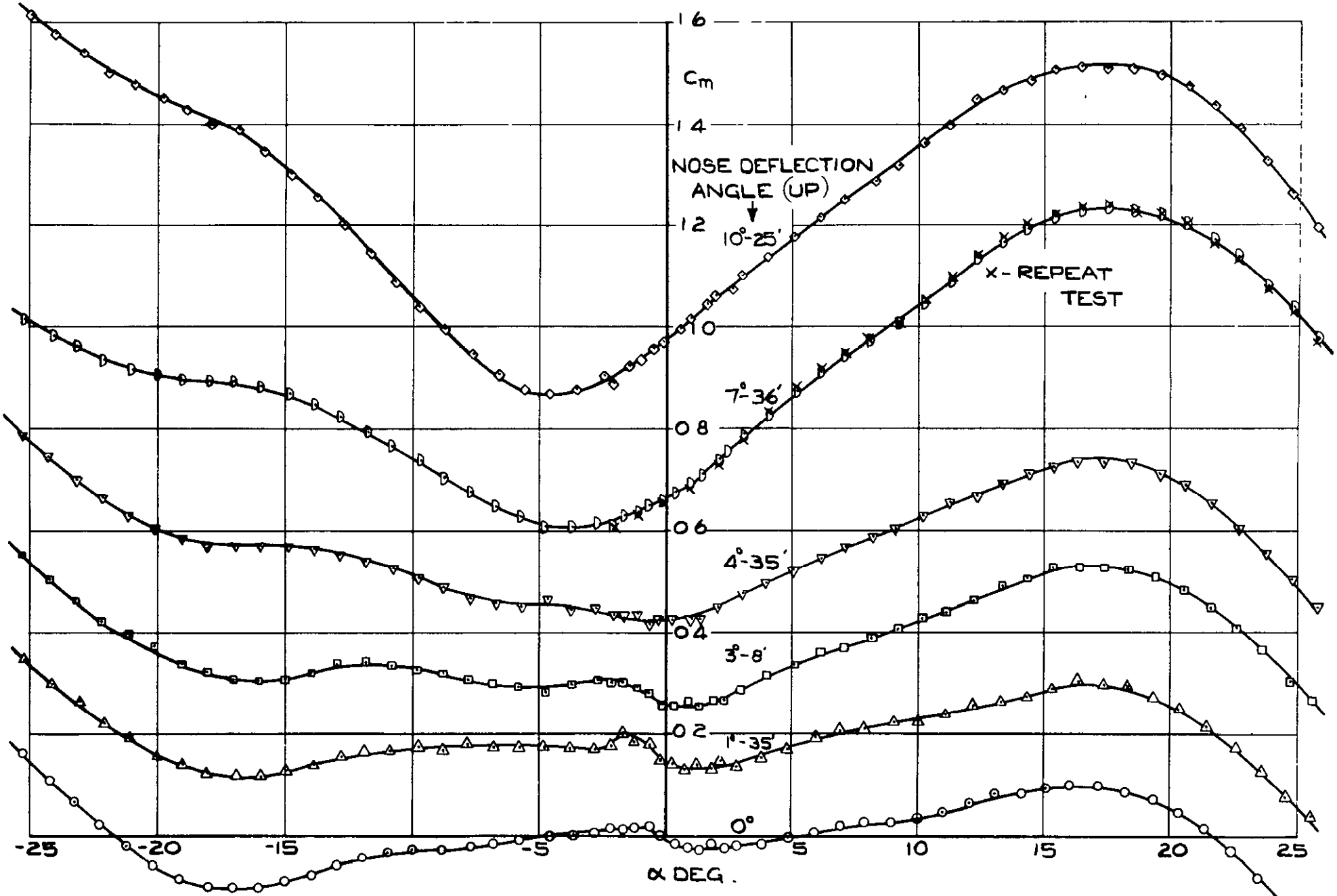

FIG.19. Cm vs α FOR MODEL WITH NOSE DEFLECTED IN THE INCIDENCE PLANE.

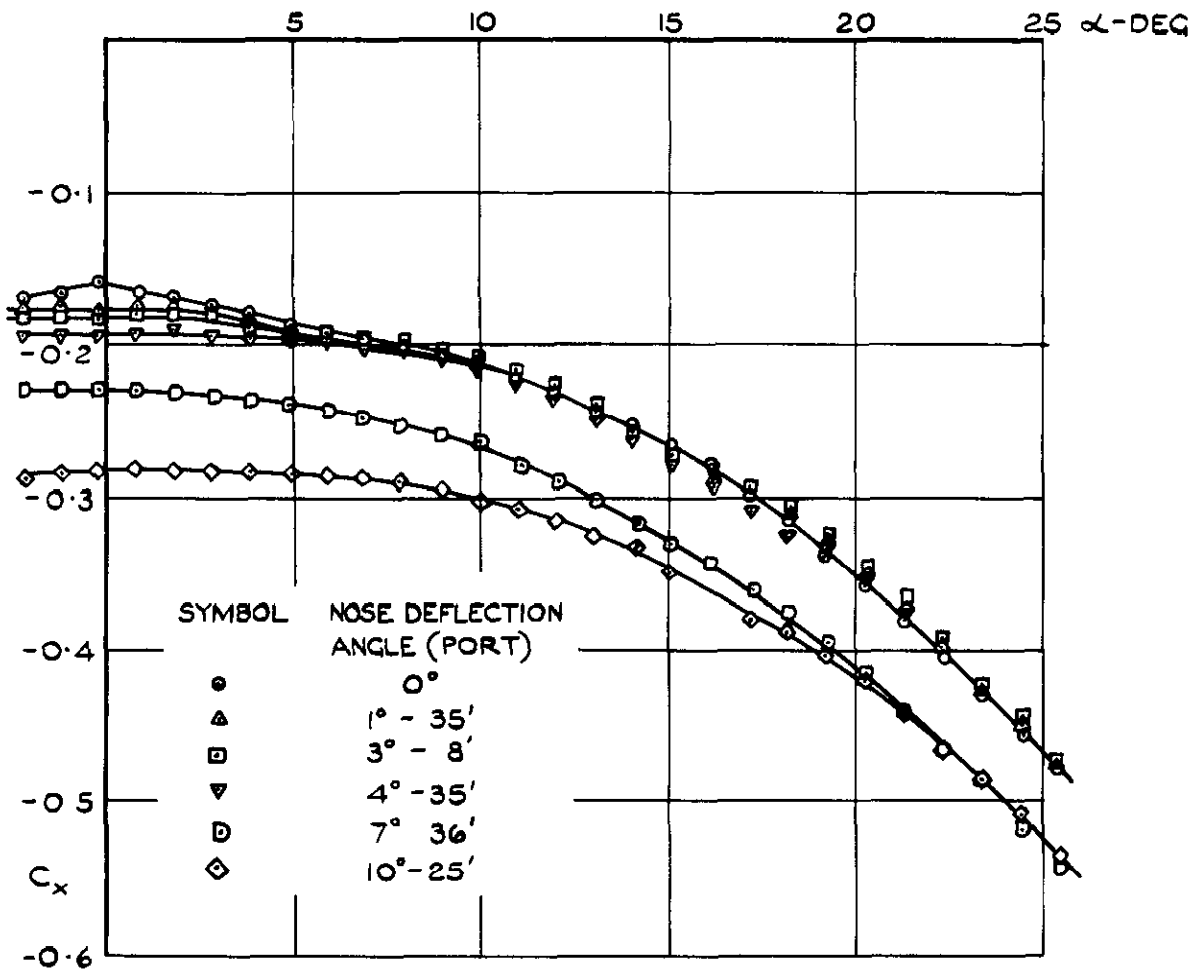

FIG. 20. C_x vs α FOR MODEL WITH NOSE DEFLECTED NORMAL TO THE INCIDENCE PLANE.

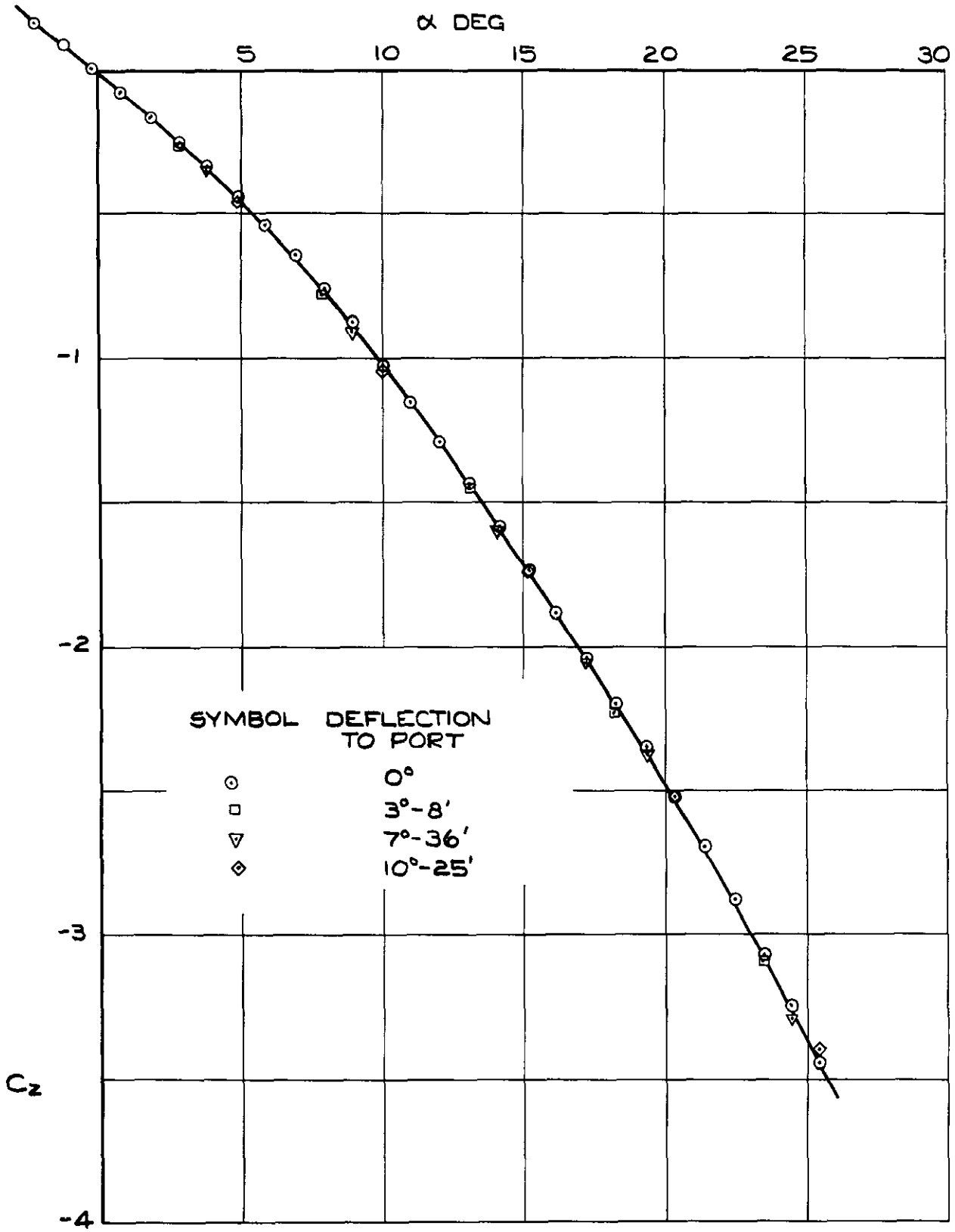

FIG.21. C_z vs α FOR MODEL WITH NOSE DEFLECTED NORMAL TO INCIDENCE PLANE

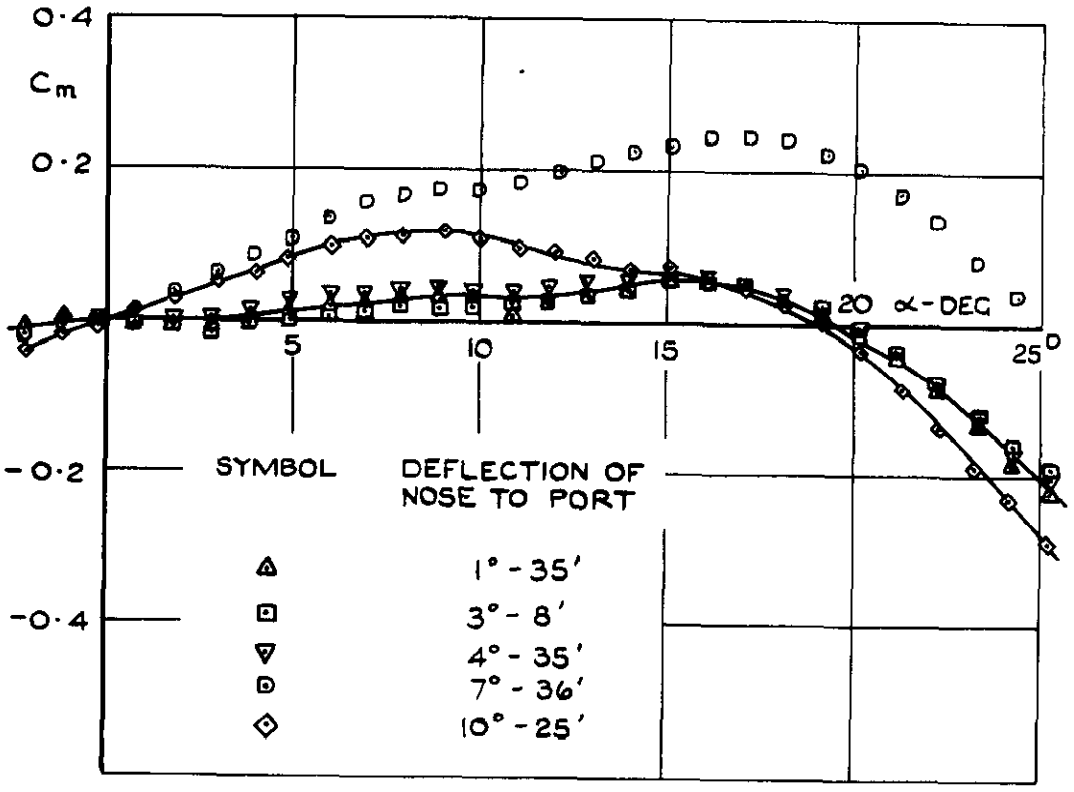

FIG. 22. C_m vs α FOR MODEL WITH NOSE DEFLECTED NORMAL TO INCIDENCE PLANE.

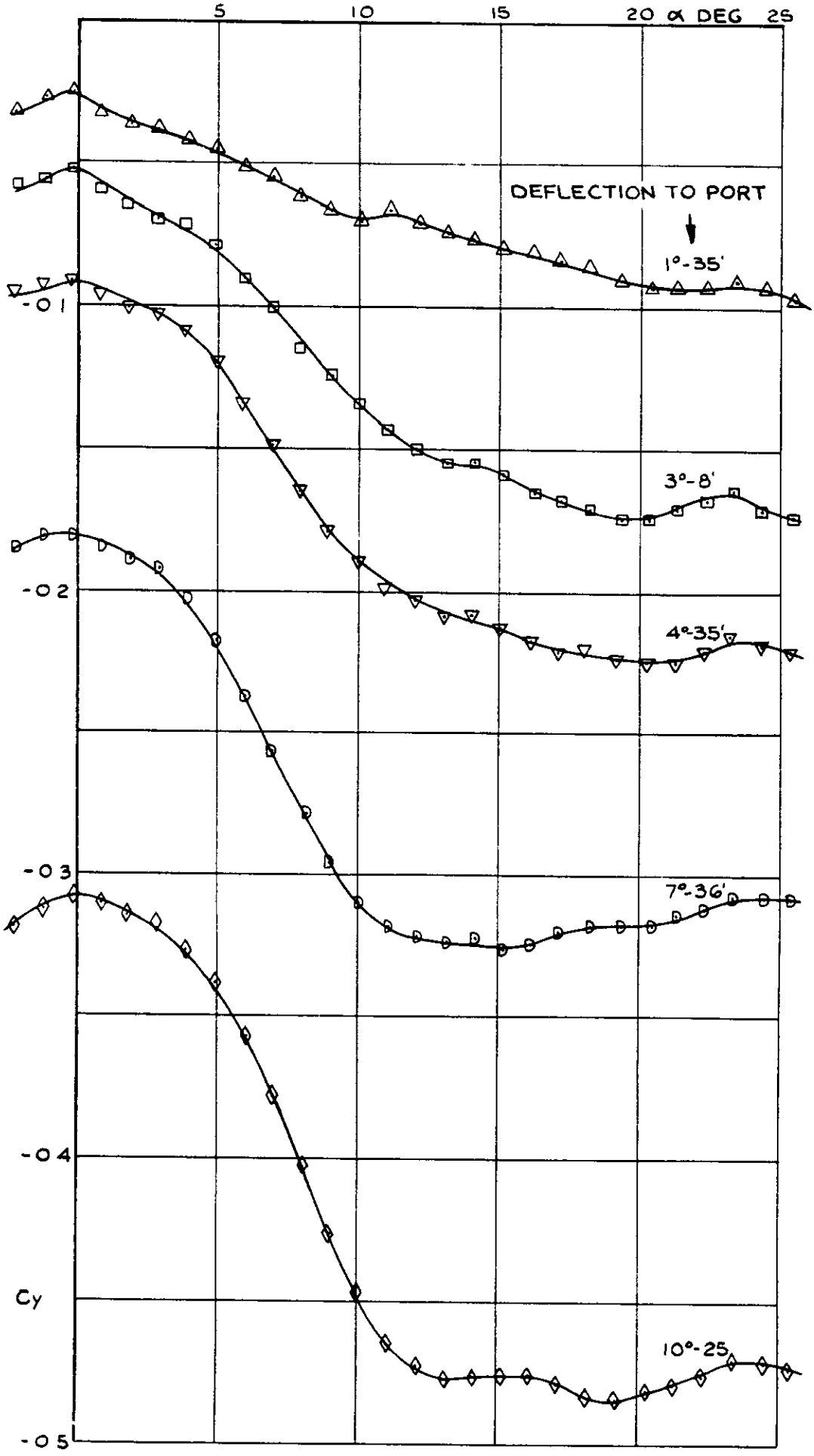

FIG. 23 Cy vs α FOR MODEL WITH NOSE DEFLECTED NORMAL TO INCIDENCE PLANE.

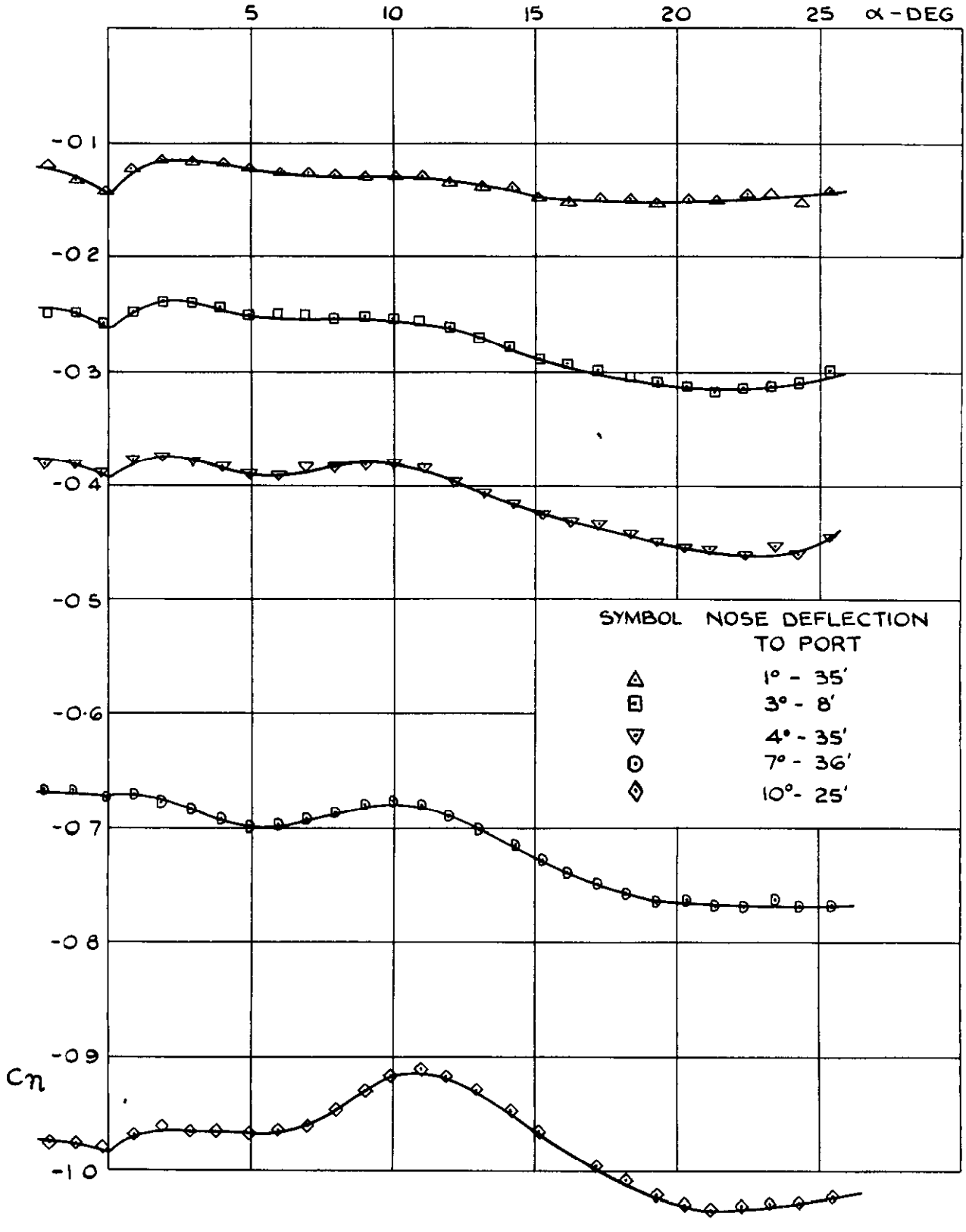

FIG. 24. C_n vs α FOR MODEL WITH NOSE DEFLECTED NORMAL TO INCIDENCE PLANE.

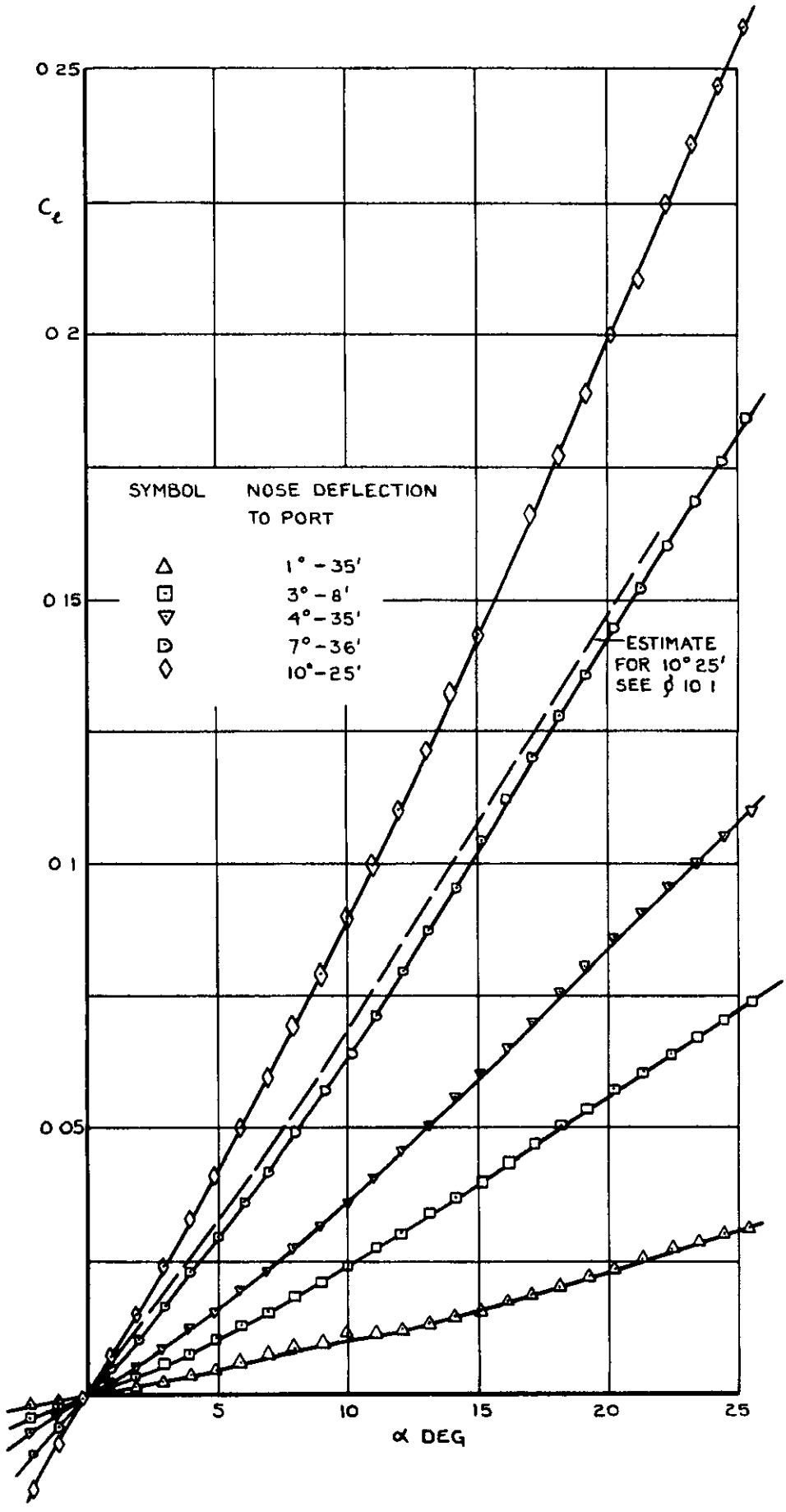

FIG. 25. C_ℓ vs $\propto$ FOR MODEL WITH NOSE DEFLECTED NORMAL TO THE INCIDENCE PLANE.

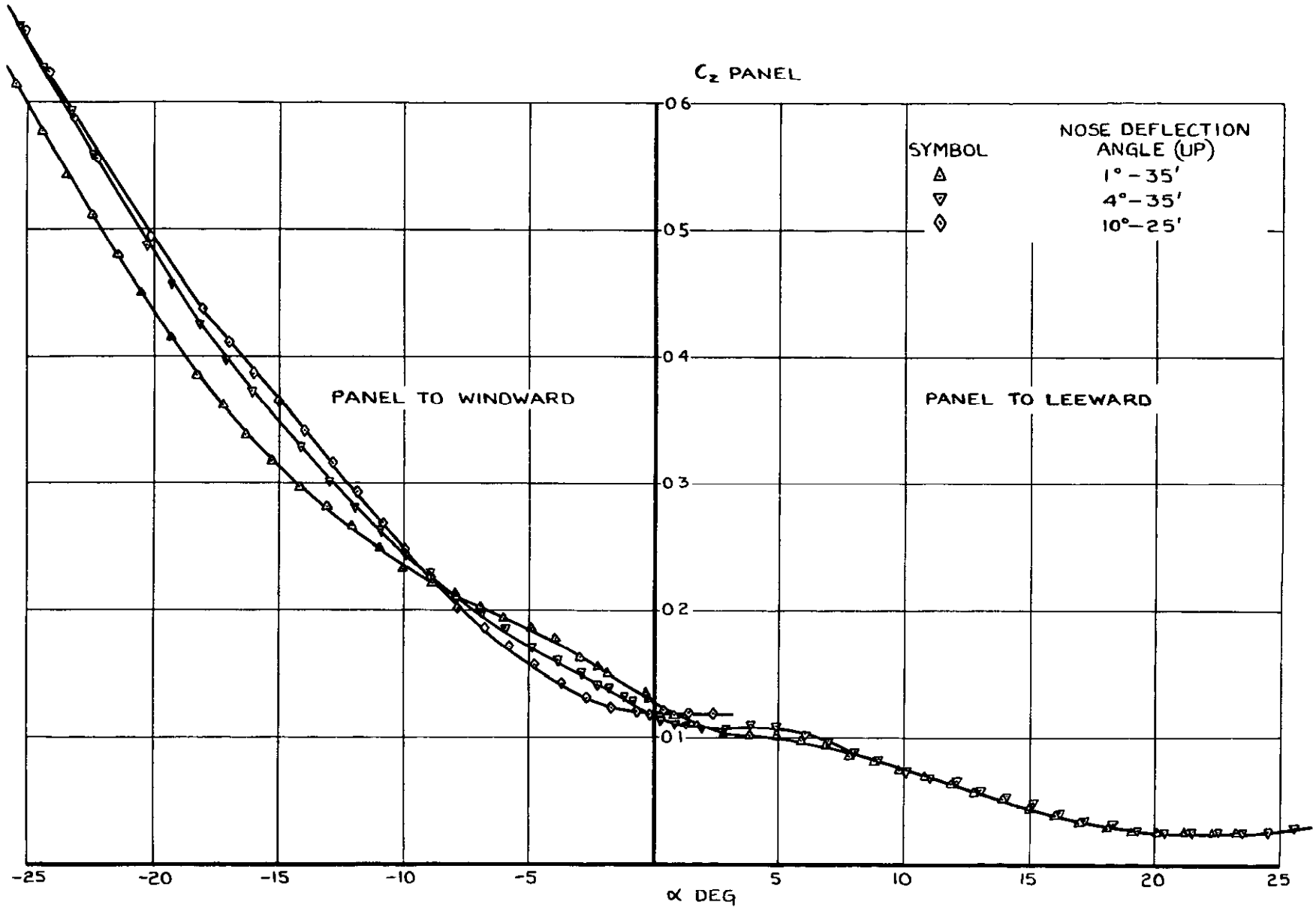

FIG. 26. VARIATION OF FLARE PANEL Z FORCE COEFFICIENT WITH ∝ FOR VARIOUS NOSE DEFLECTIONS.

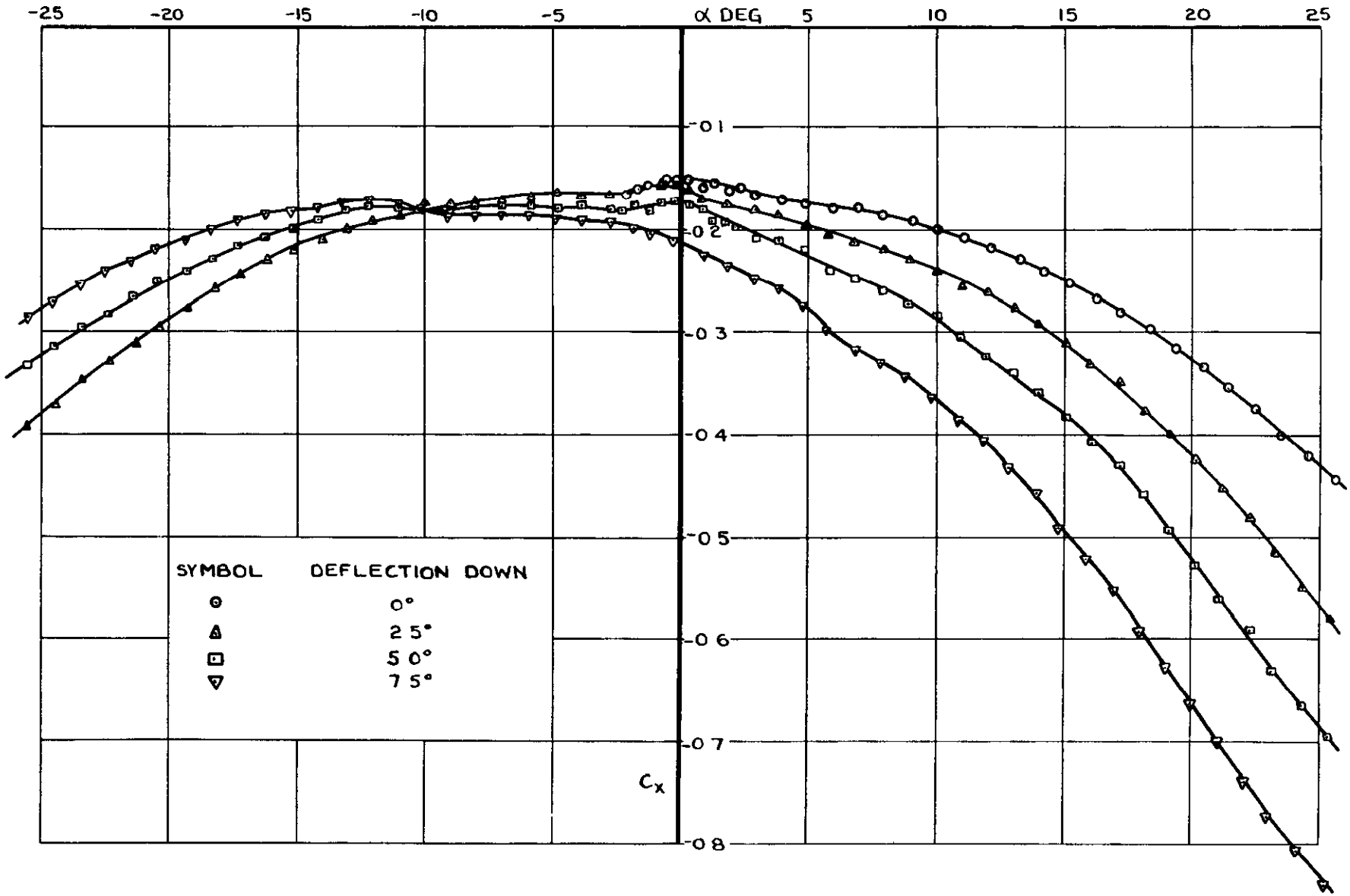

FIG. 27. C_x vs α FOR MODEL WITH FLARE DEFLECTED IN INCIDENCE PLANE.

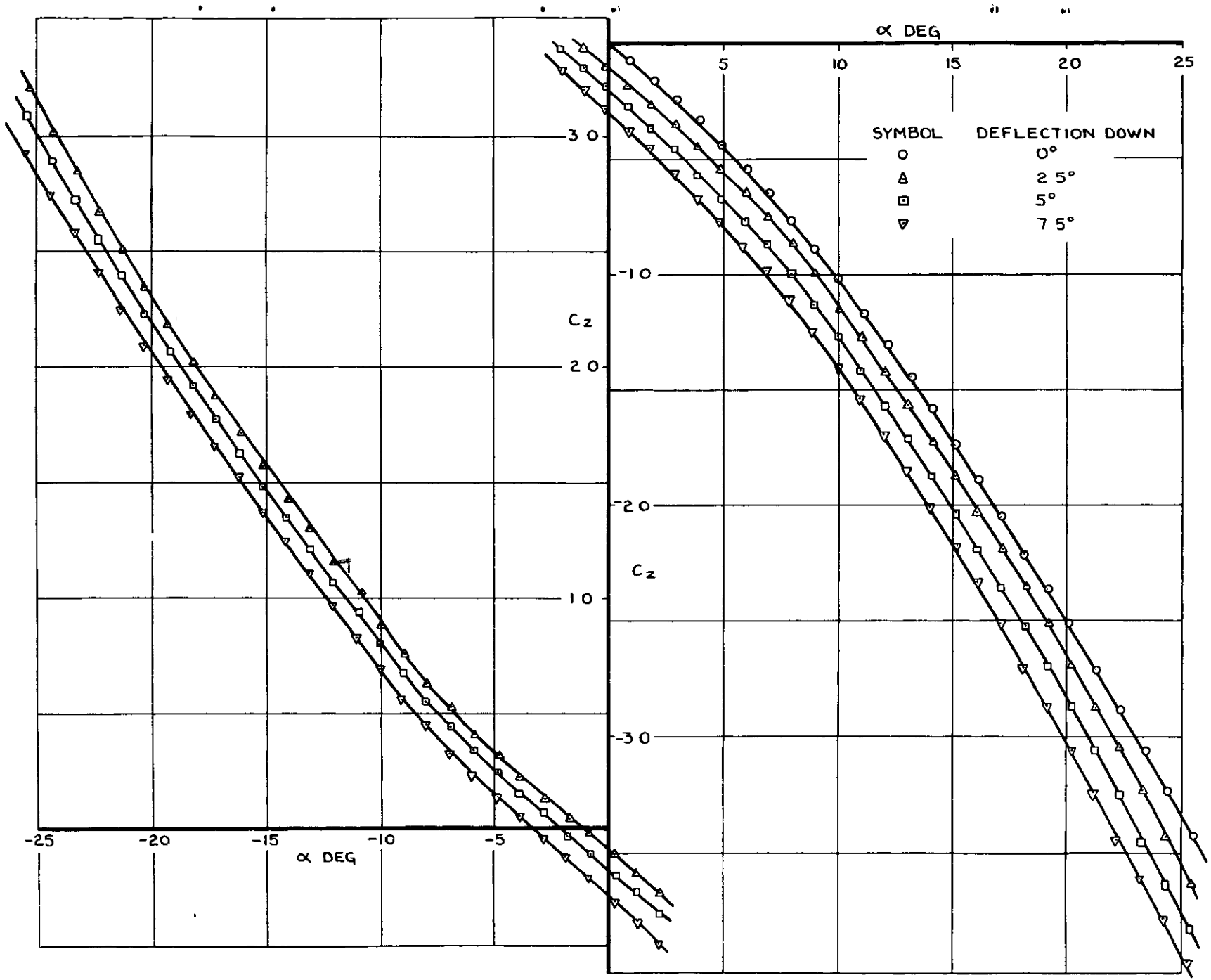

FIG. 28. C_z vs α FOR MODEL WITH FLARE DEFLECTED IN INCIDENCE PLANE.

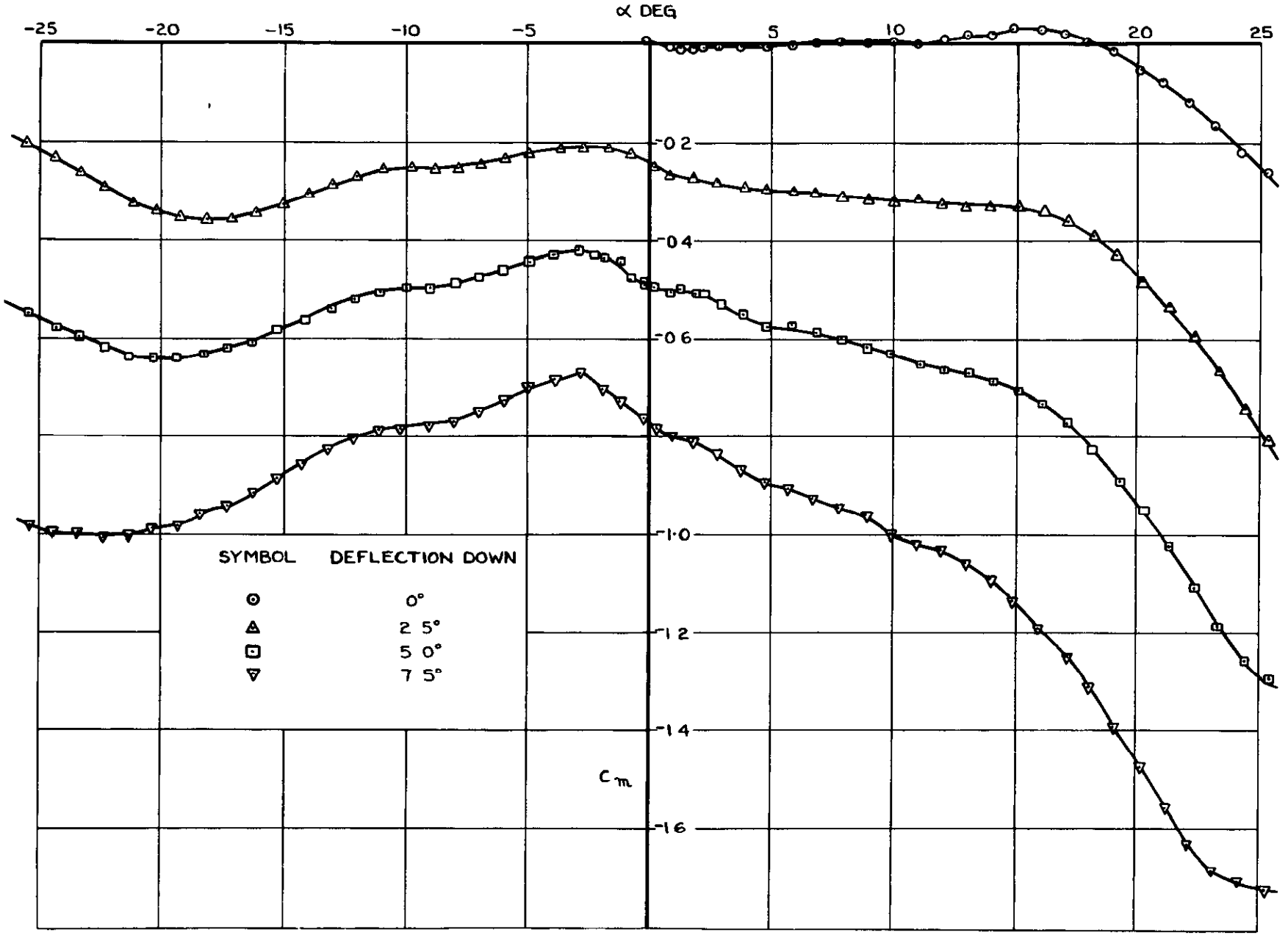

FIG. 29. C_m vs α FOR MODEL WITH FLARE DEFLECTED IN INCIDENCE PLANE.

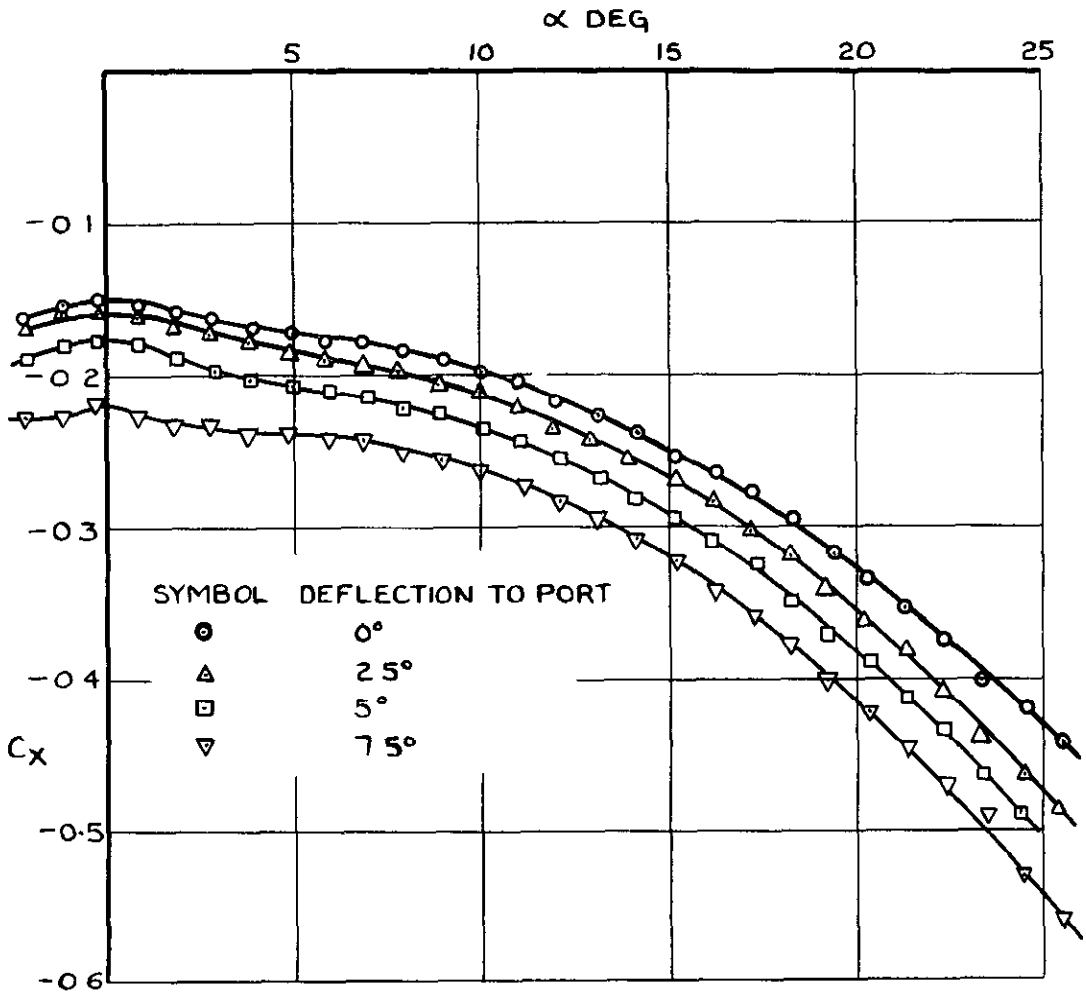

FIG. 30. C_x vs α FOR MODEL WITH FLARE DEFLECTED NORMAL TO INCIDENCE PLANE.

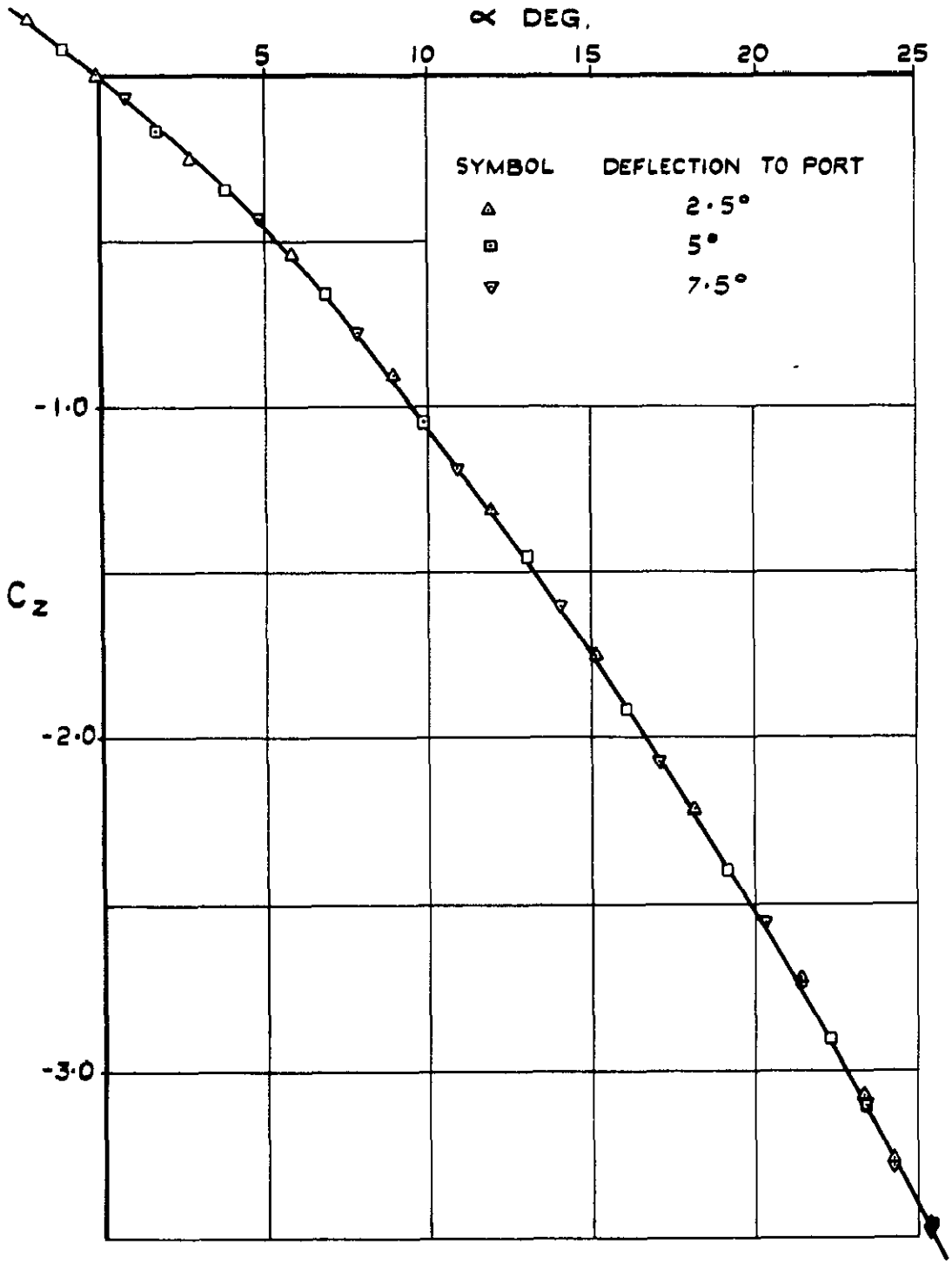

FIG. 31. C_z vs α FOR MODEL WITH FLARE DEFLECTED NORMAL TO INCIDENCE PLANE.

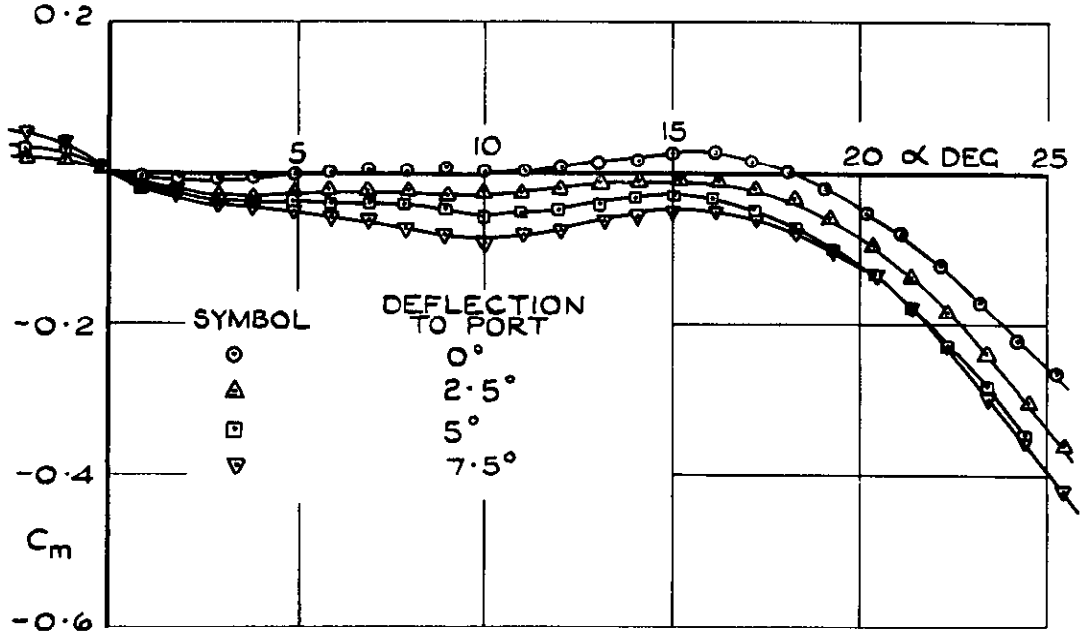

FIG. 32. C_m vs ∝ FOR MODEL WITH FLARE DEFLECTED NORMAL TO INCIDENCE PLANE.

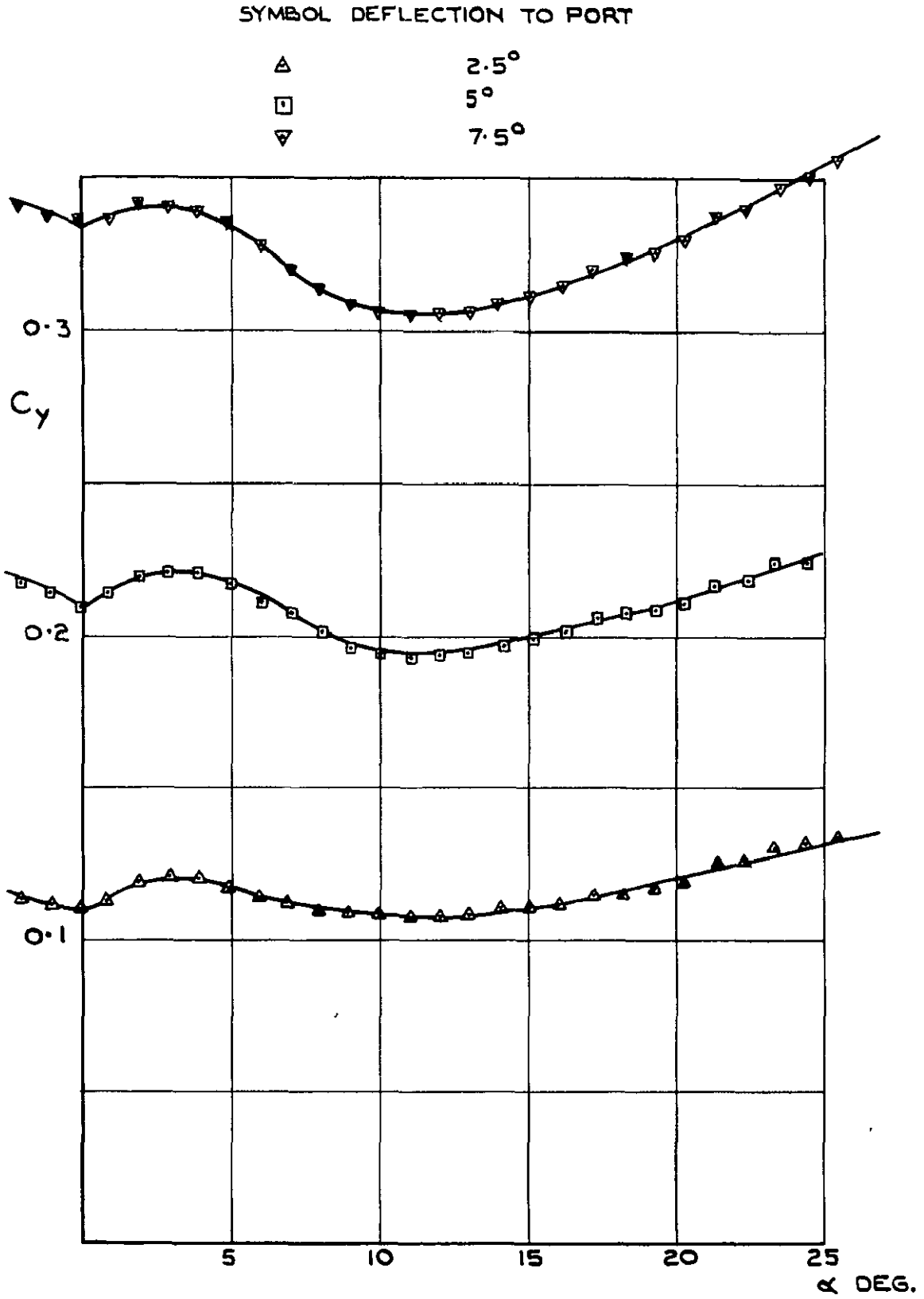

FIG. 33. C_y vs α FOR MODEL WITH FLARE DEFLECTED NORMAL TO INCIDENCE PLANE

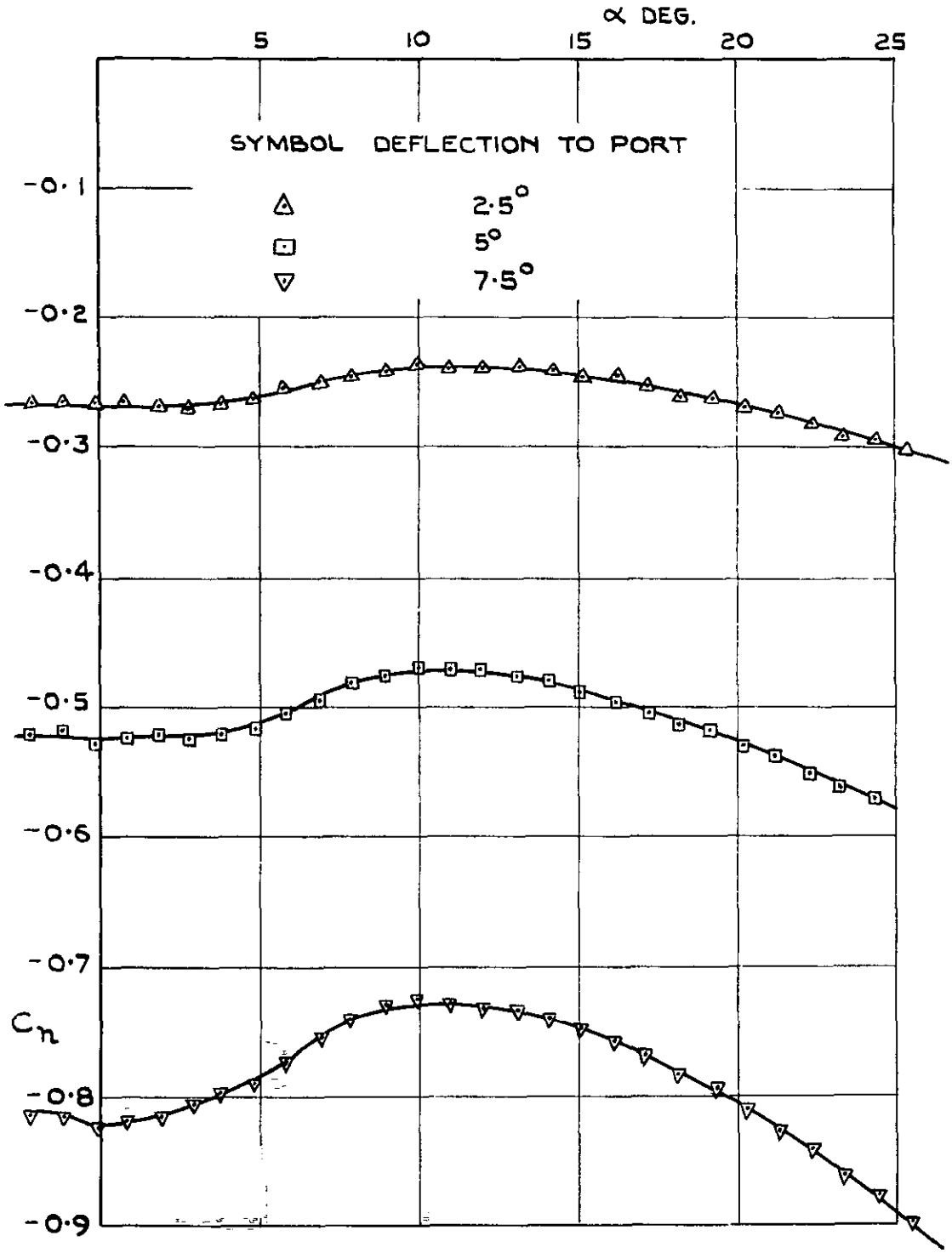

FIG.34 C_n vs α FOR MODEL WITH FLARE DEFLECTED NORMAL TO INCIDENCE PLANE

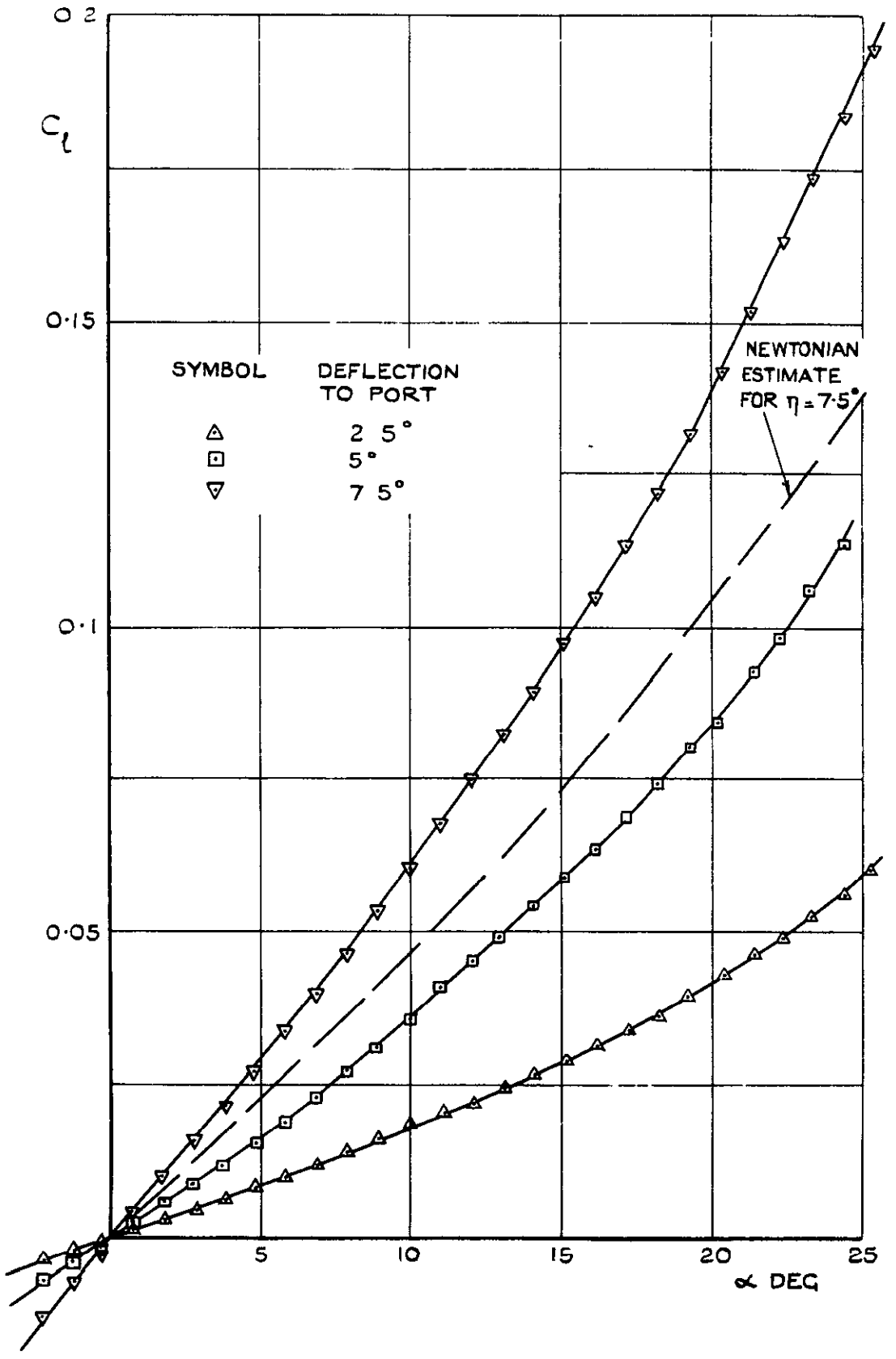

FIG. 35. C_l vs α FOR MODEL WITH FLARE DEFLECTED NORMAL TO INCIDENCE PLANE.

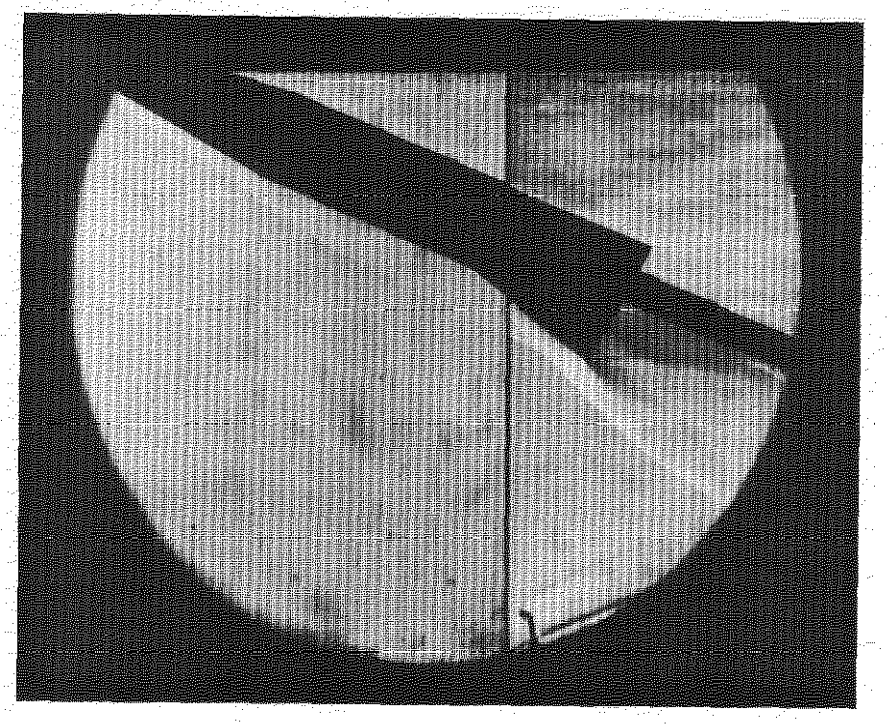

(a) $\alpha = 22^{\circ}$

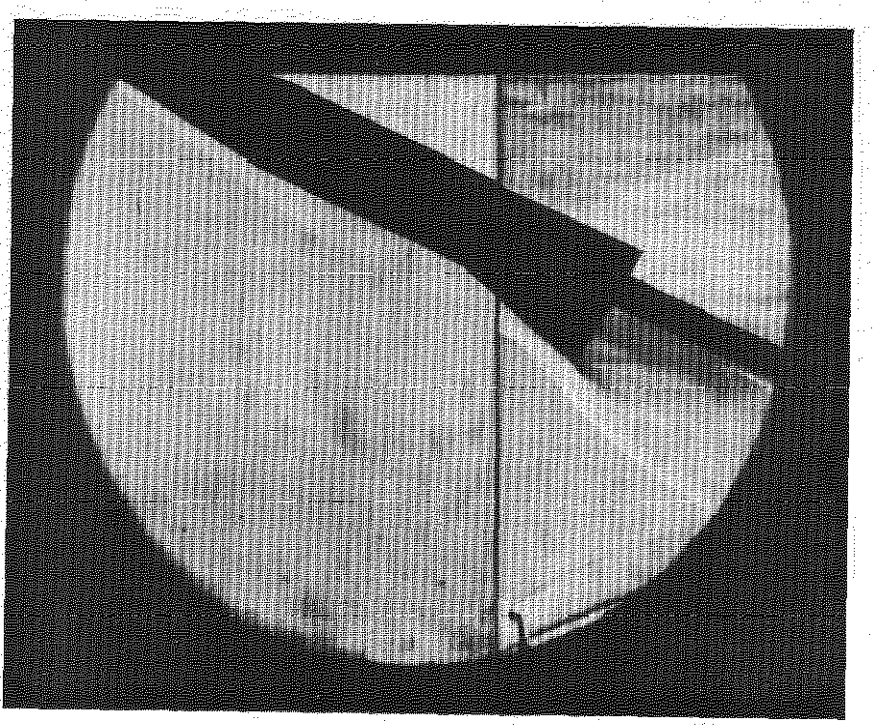

(b) $\alpha = 24^{\circ}$

FIG. 36 SCHLIEREN PHOTOGRAPHS OF MODEL WITH FLARE DEFLECTED, SHOWING NOSE SHOCK/FLARE SHOCK INTERACTION

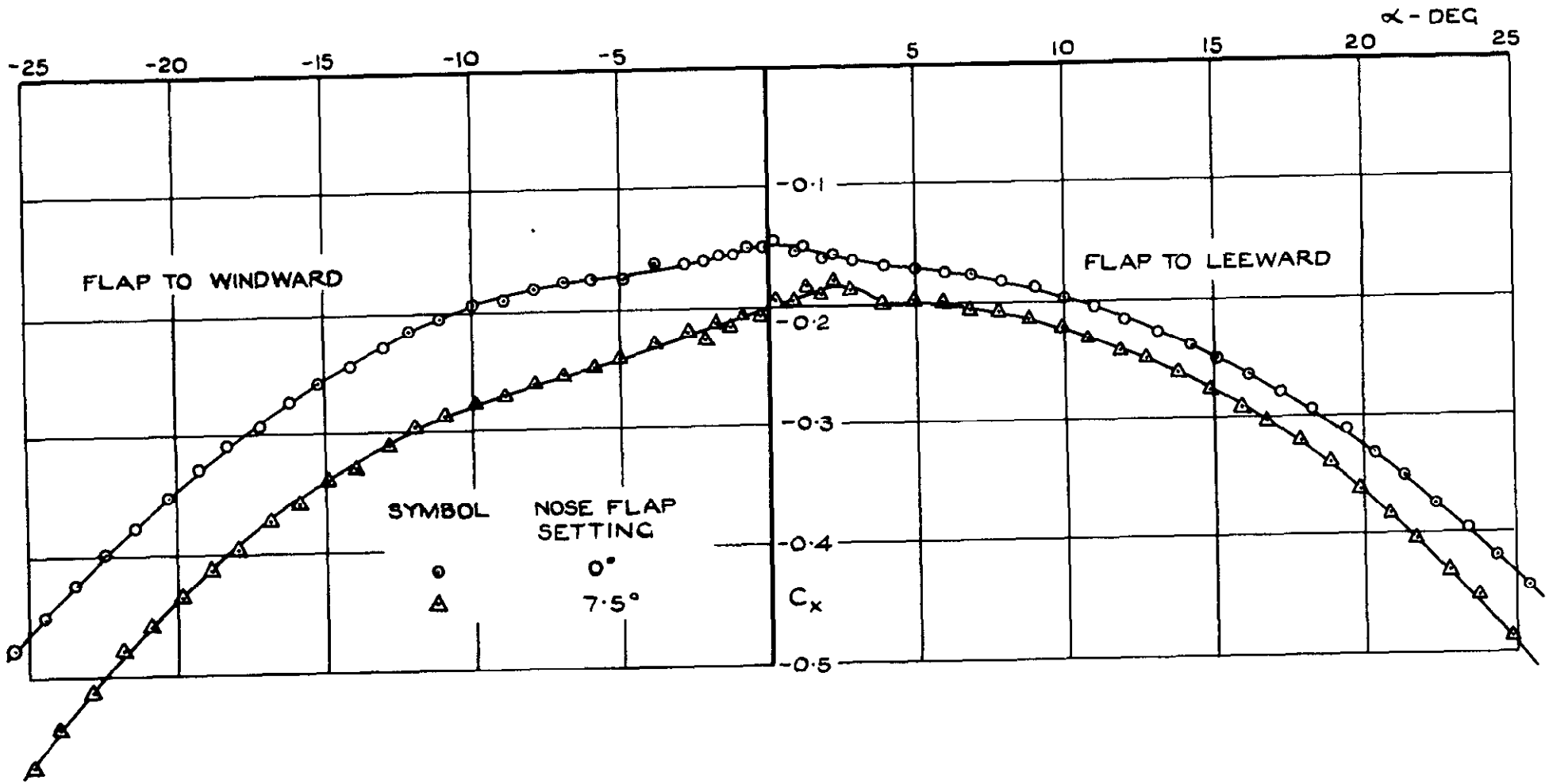

FIG. 37. C_x vs α FOR MODEL WITH NOSE FLAP EXTENDED IN INCIDENCE PLANE.

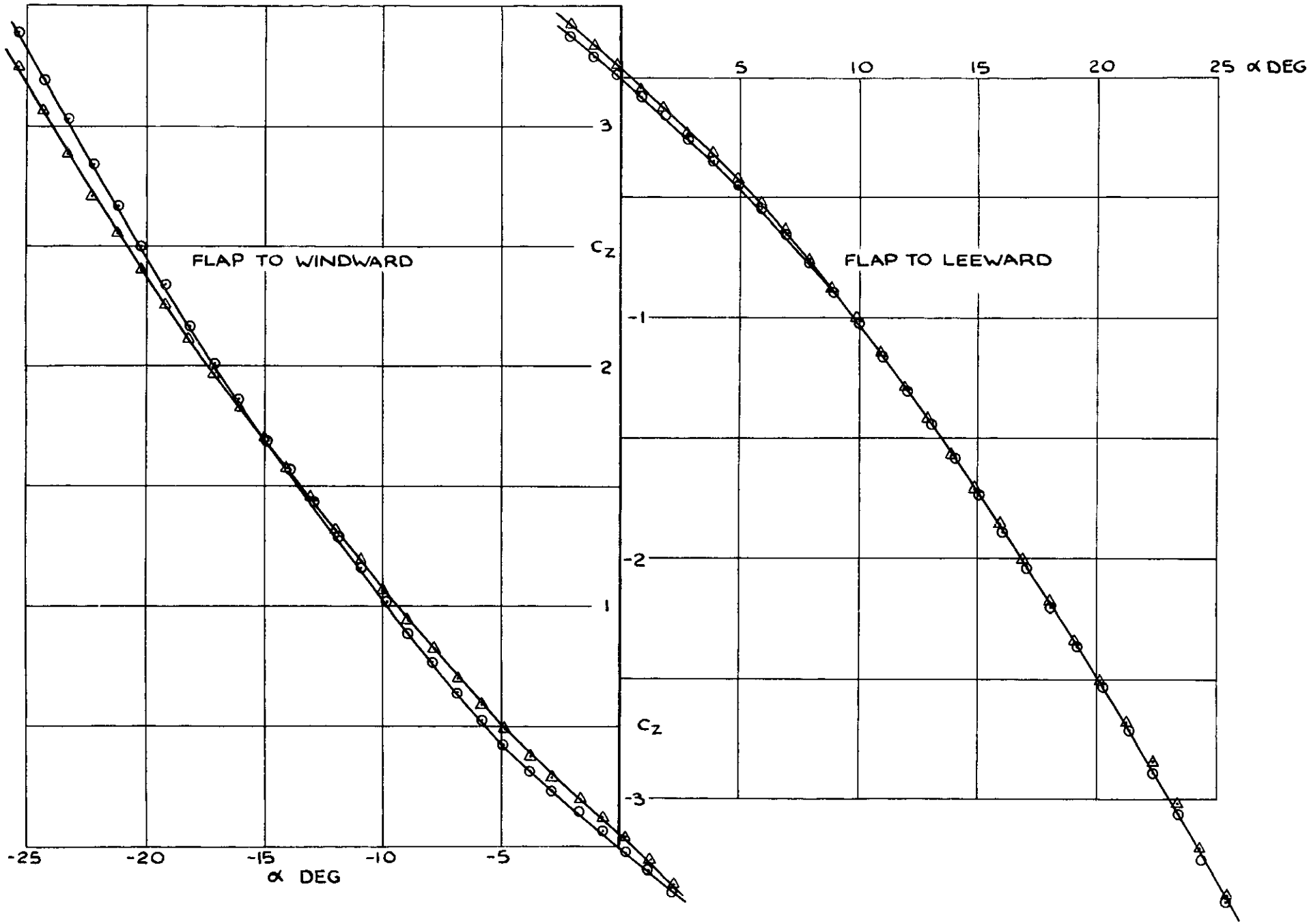

FIG. 38 C_z vs α FOR MODEL WITH NOSE FLAP EXTENDED IN INCIDENCE PLANE

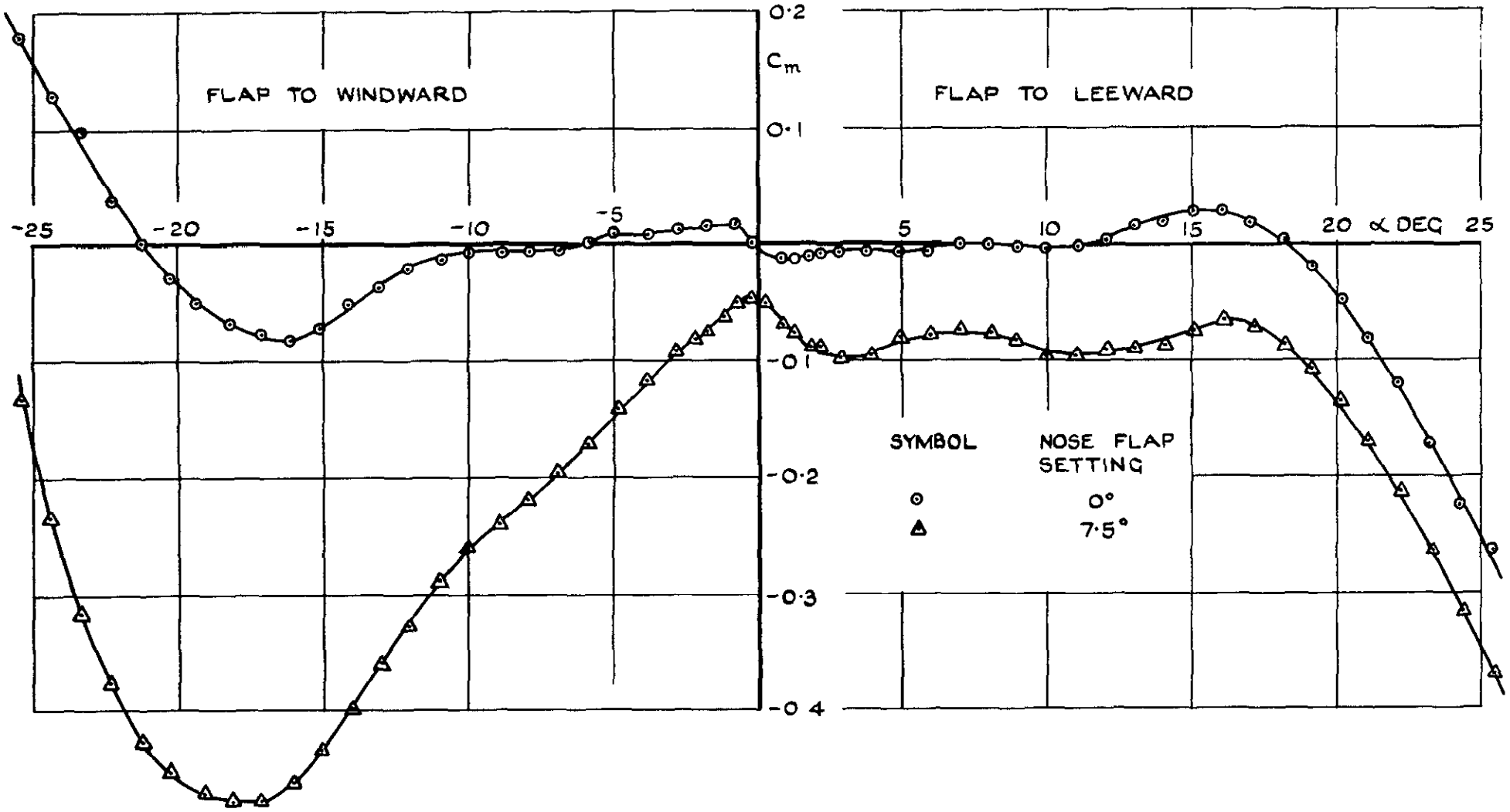

FIG. 39. C_m vs α FOR MODEL WITH FLAP EXTENDED IN INCIDENCE PLANE

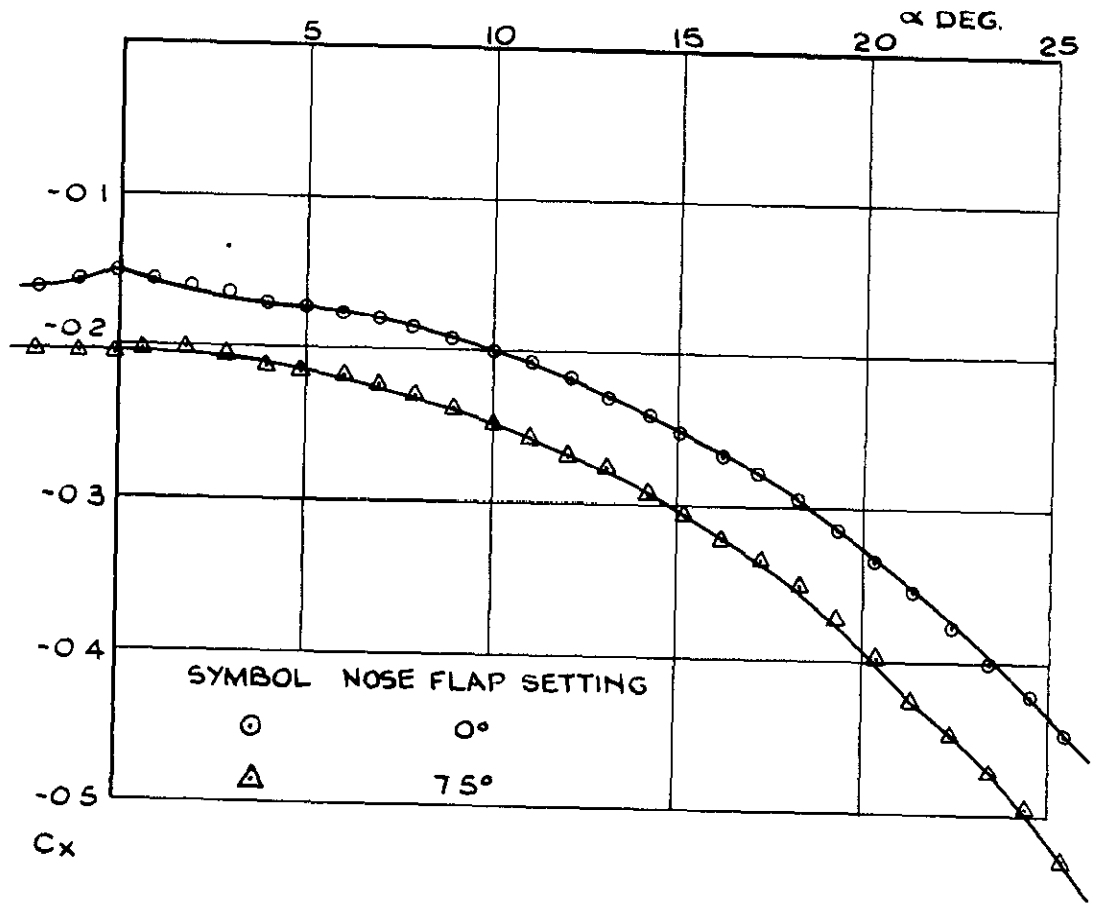

FIG. 40 C_x vs α FOR MODEL WITH NOSE FLAP EXTENDED NORMAL TO INCIDENCE PLANE.

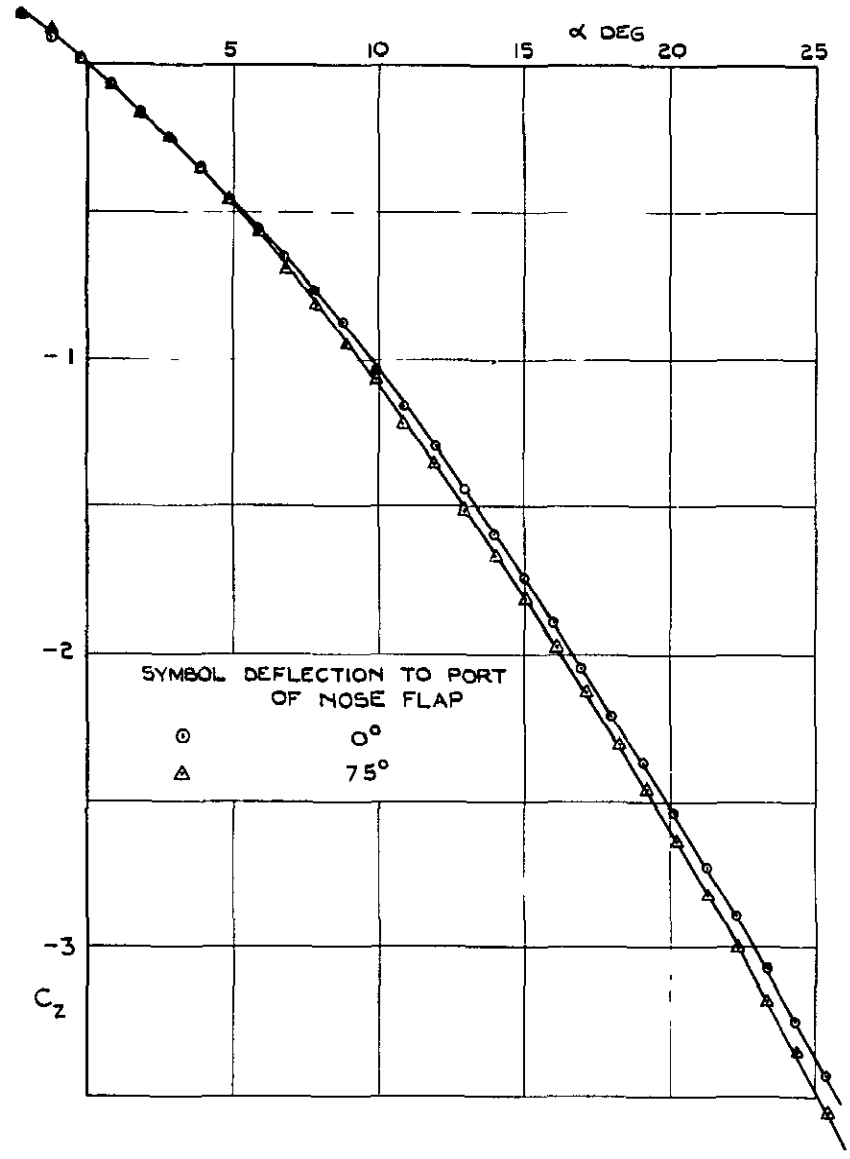

FIG. 41. C_z vs α FOR MODEL WITH NOSE FLAP EXTENDED NORMAL TO INCIDENCE PLANE

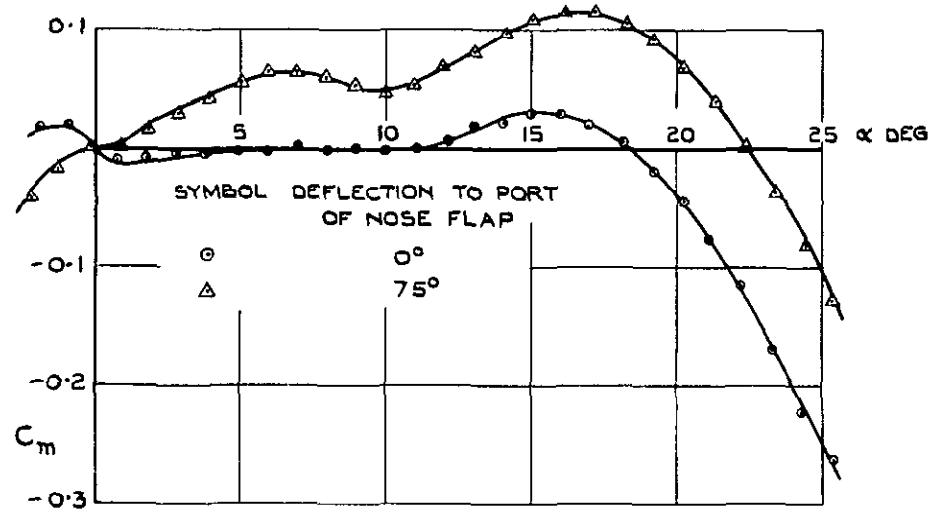

FIG. 42. C_m vs α FOR MODEL WITH NOSE FLAP EXTENDED NORMAL TO INCIDENCE PLANE

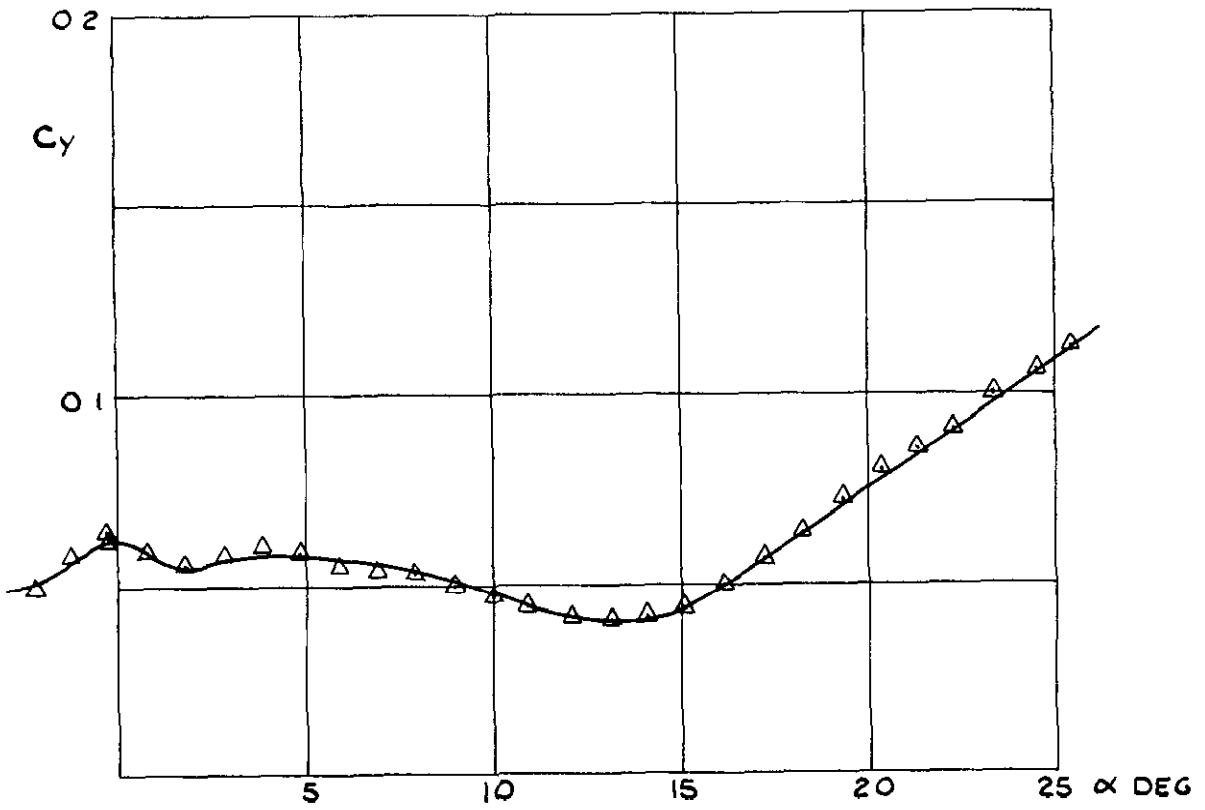

FIG 43 Cy vs ∝ FOR MODEL WITH NOSE FLAP EXTENDED NORMAL TO INCIDENCE PLANE.

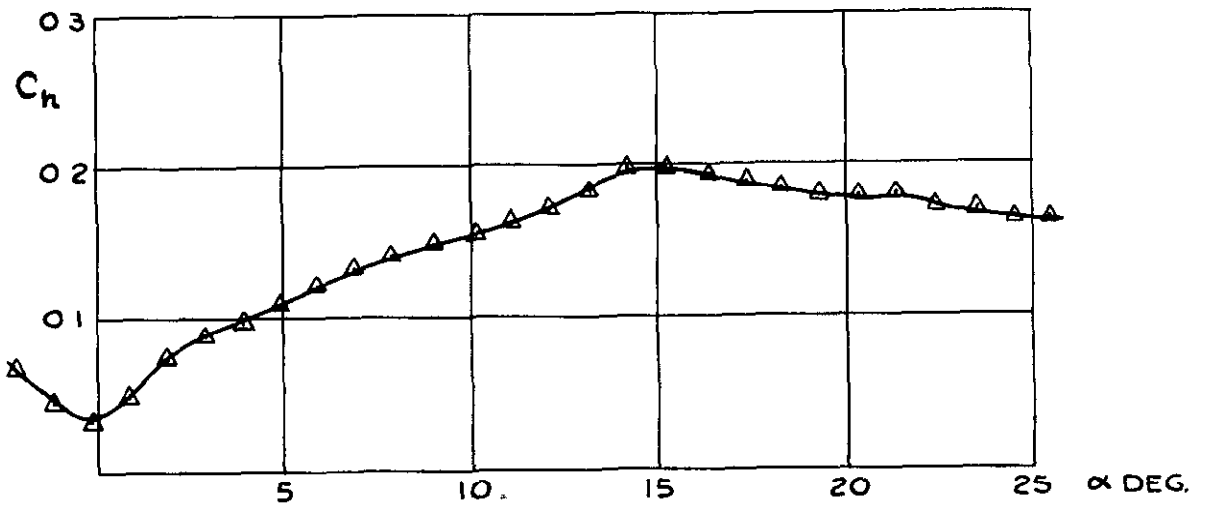

FIG. 44 Cn vs ∝ FOR MODEL WITH NOSE FLAP EXTENDED NORMAL TO INCIDENCE PLANE.

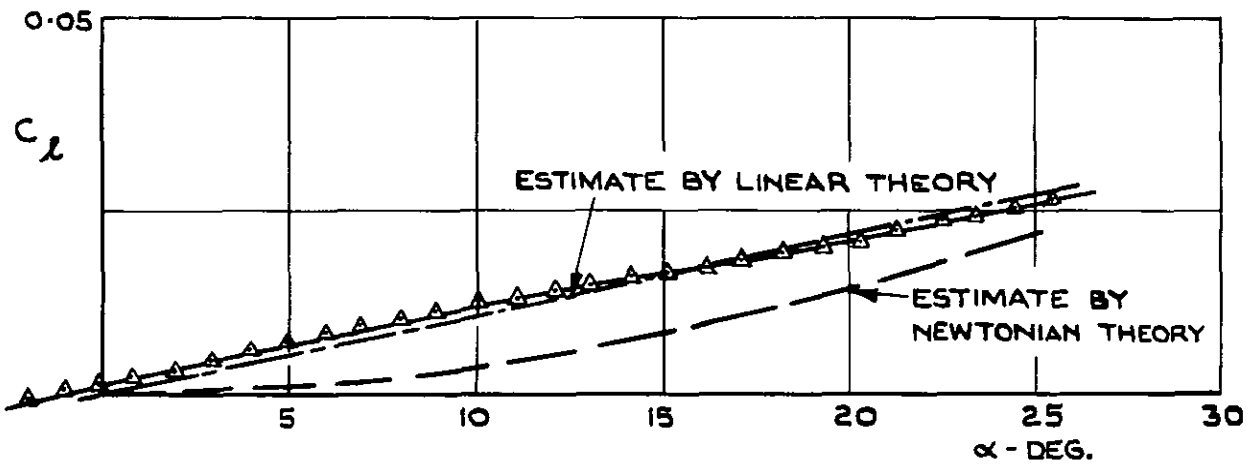

FIG. 45 C_l vs α FOR MODEL WITH NOSE FLAP EXTENDED NORMAL TO INCIDENCE PLANE

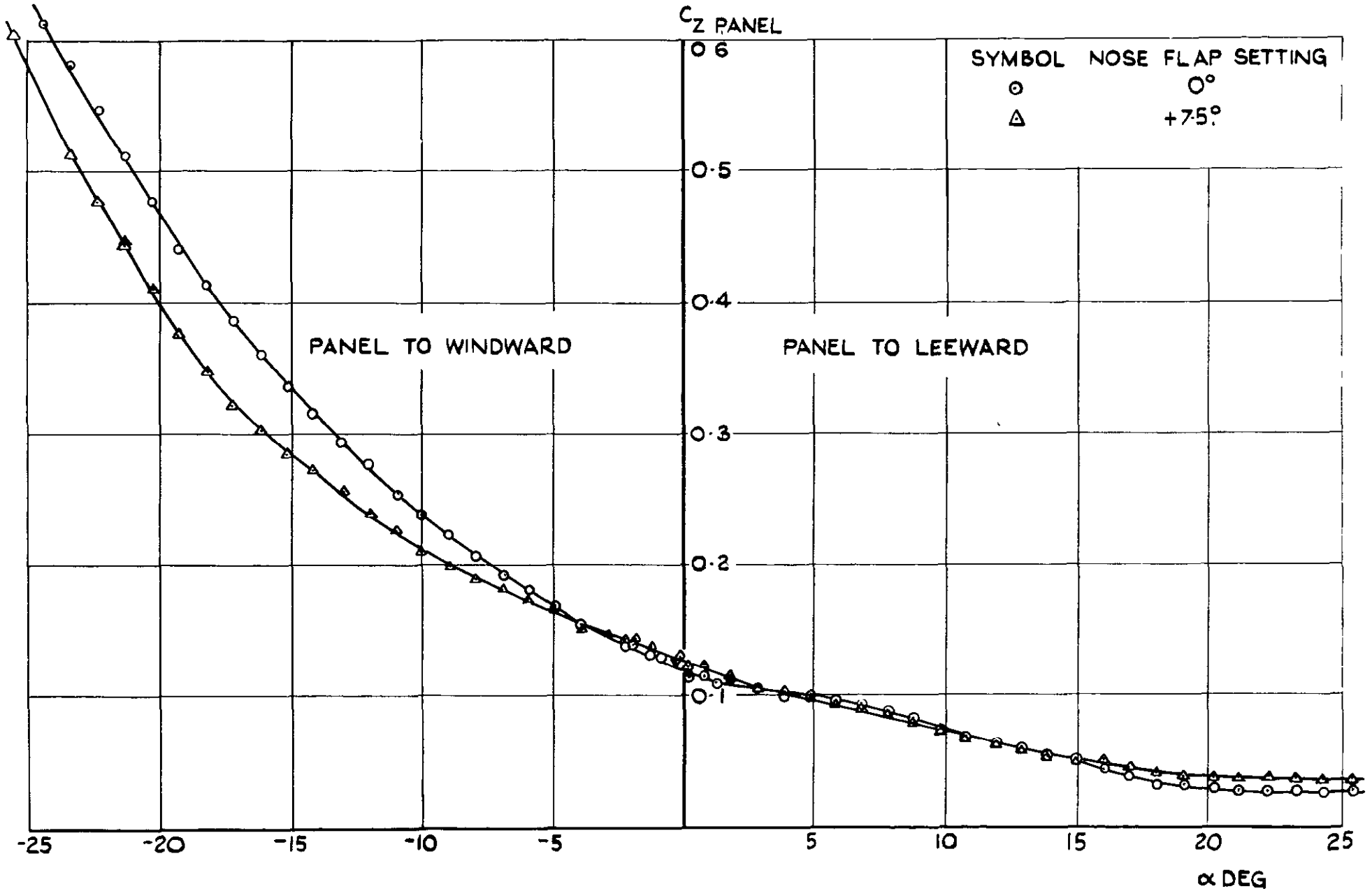

FIG. 46. COMPARISON OF FLARE PANEL Z FORCE COEFFICENTS AT VARIOUS INCIDENCES WITH AND WITHOUT NOSE FLAP.

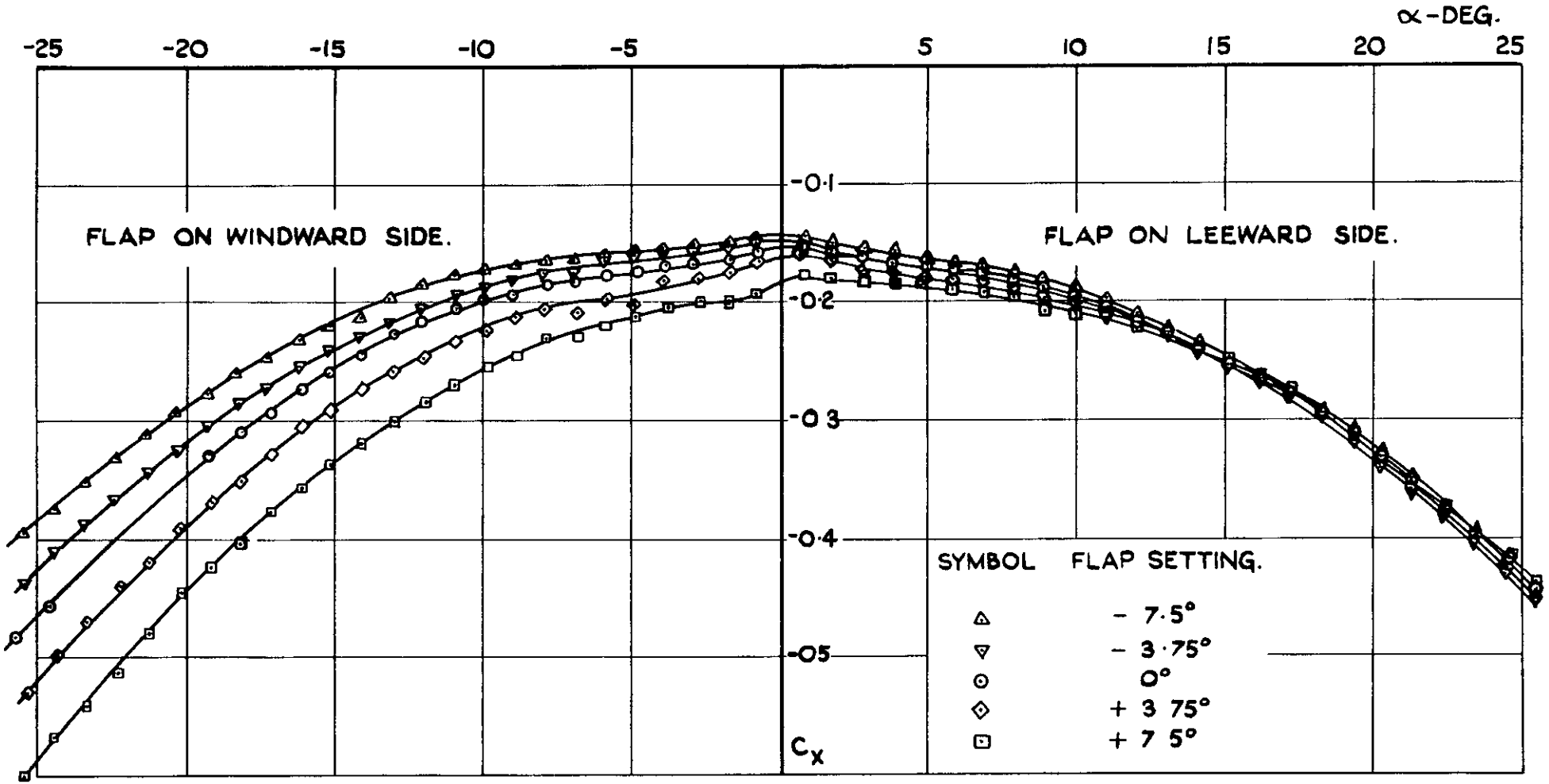

FIG. 47. C_X vs α FOR MODEL WITH FLARE FLAP ACTING IN THE INCIDENCE PLANE (TO WINDWARD AT -VE α)

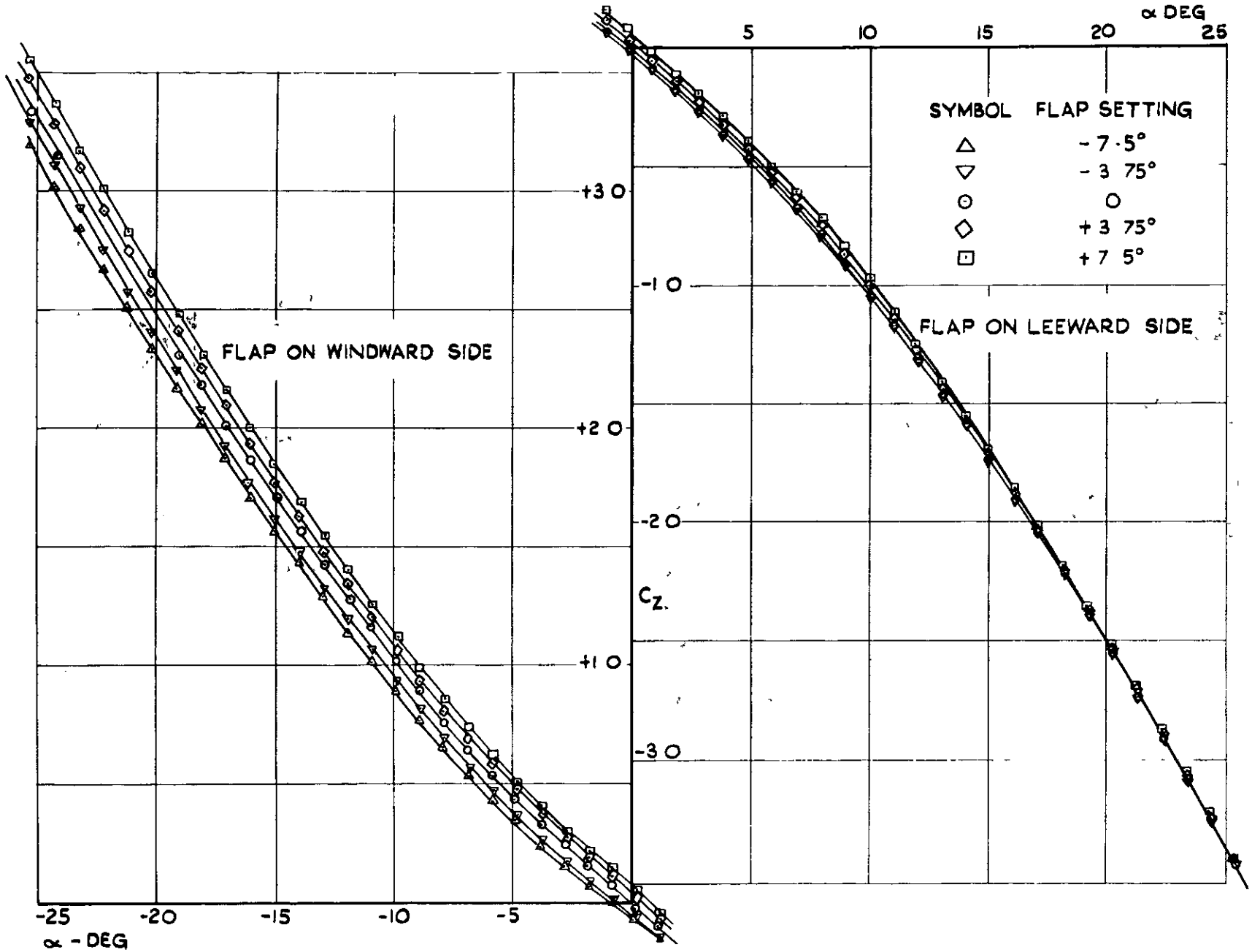

FIG. 48. C_z vs α FOR MODEL WITH FLARE FLAP ACTING IN INCIDENCE PLANE.

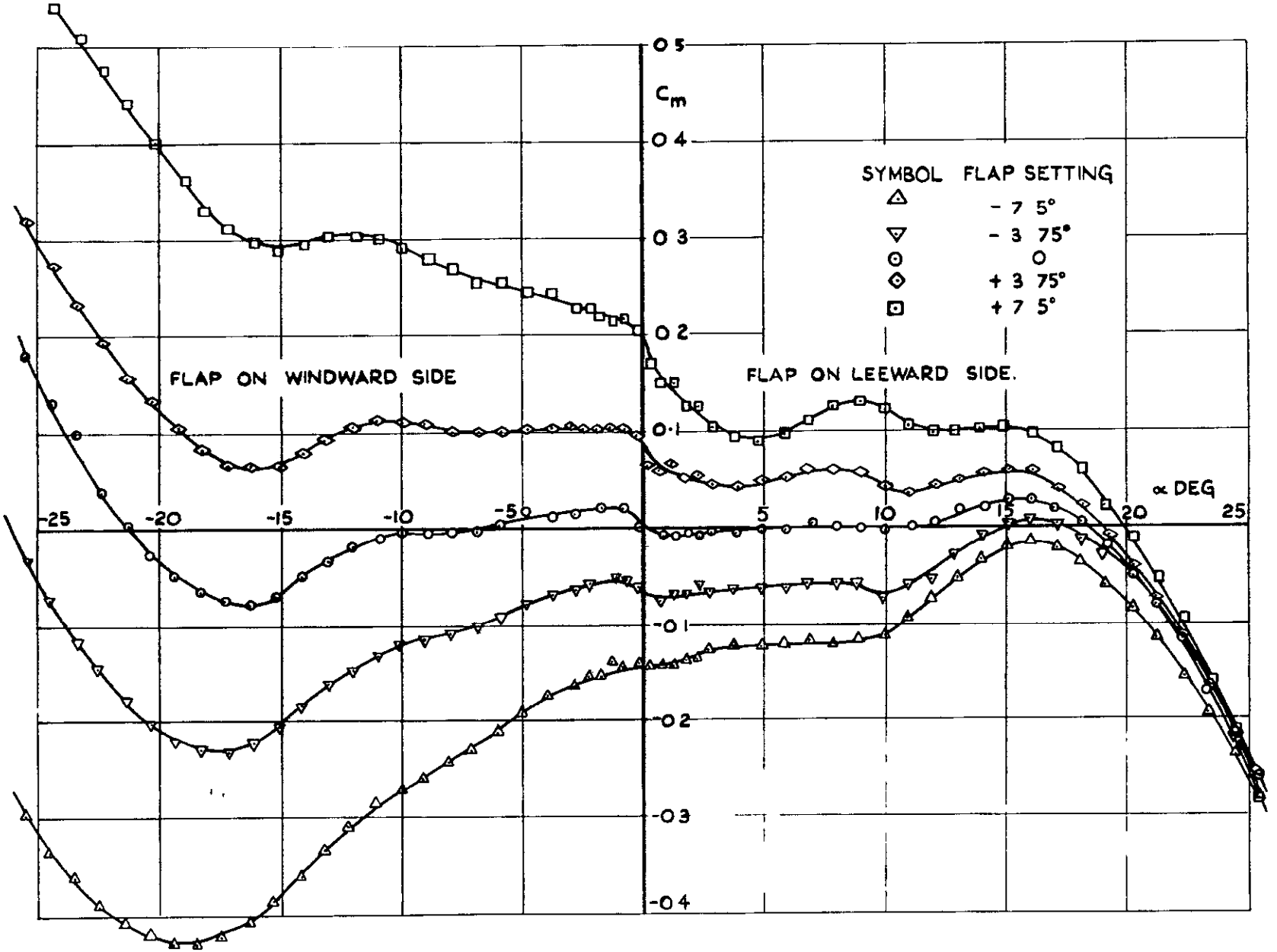

FIG. 49. C_m vs α FOR MODEL WITH FLARE FLAP ACTING IN INCIDENCE PLANE.

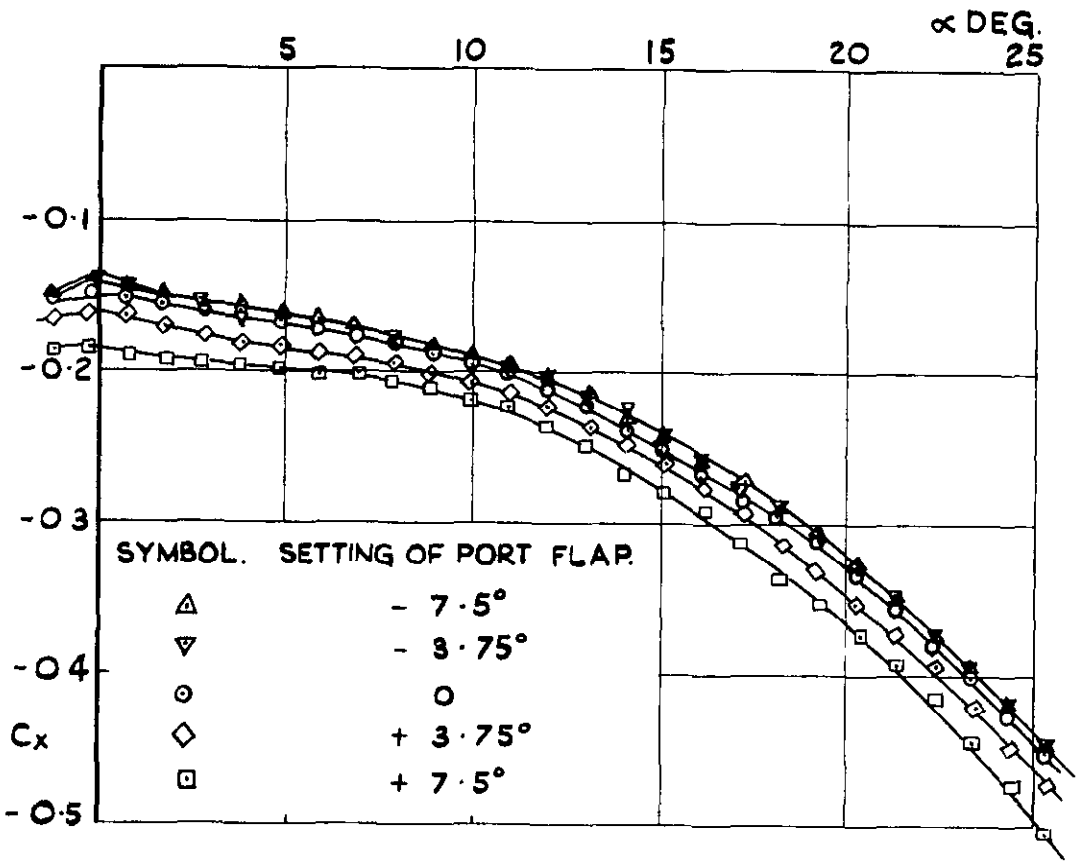

FIG.50. C_x vs α FOR MODEL WITH FLARE FLAP ACTING NORMAL TO THE INCIDENCE PLANE.

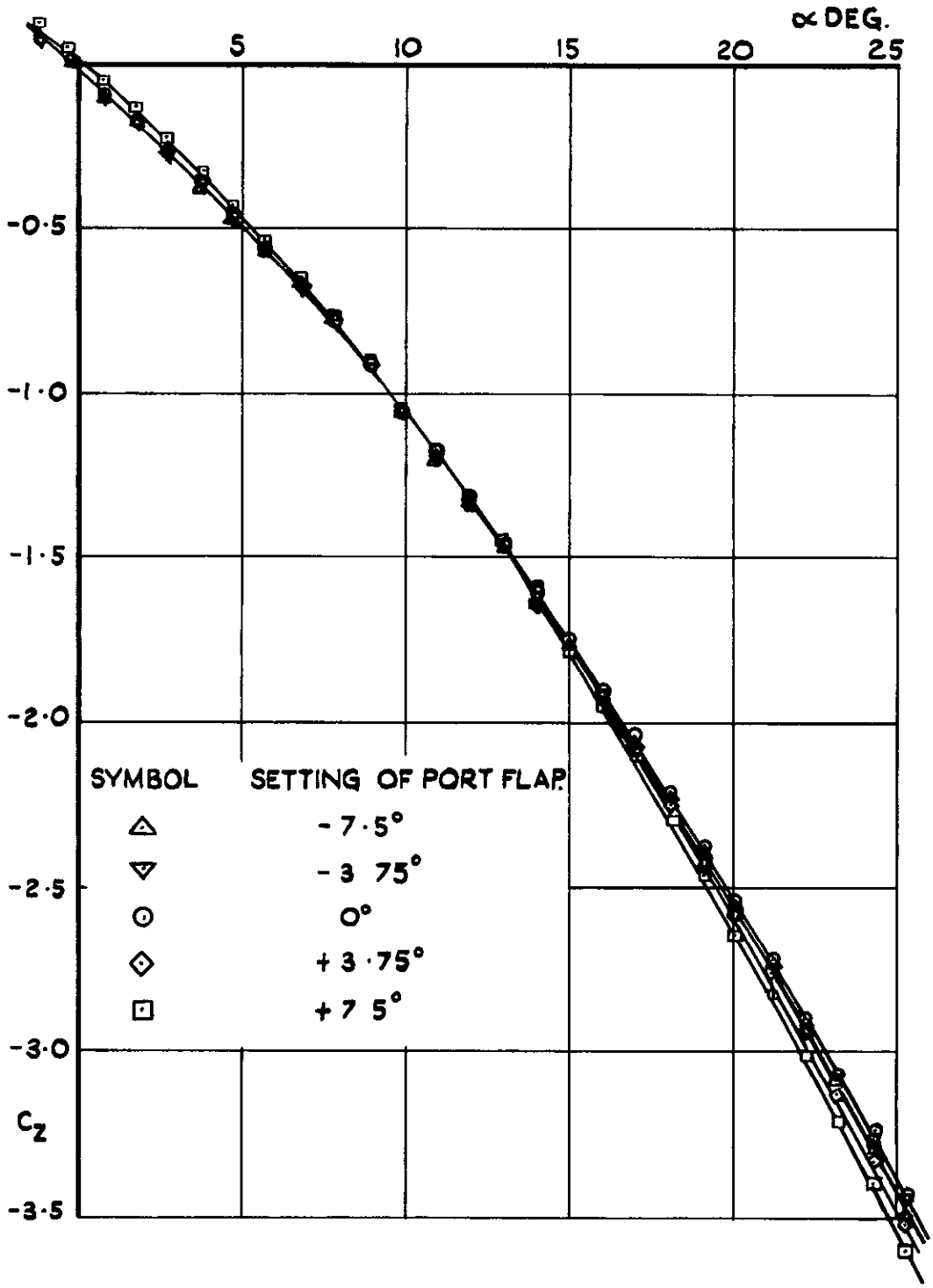

FIG. 51. C_z vs α FOR MODEL WITH FLARE FLAP ACTING NORMAL TO INCIDENCE PLANE.

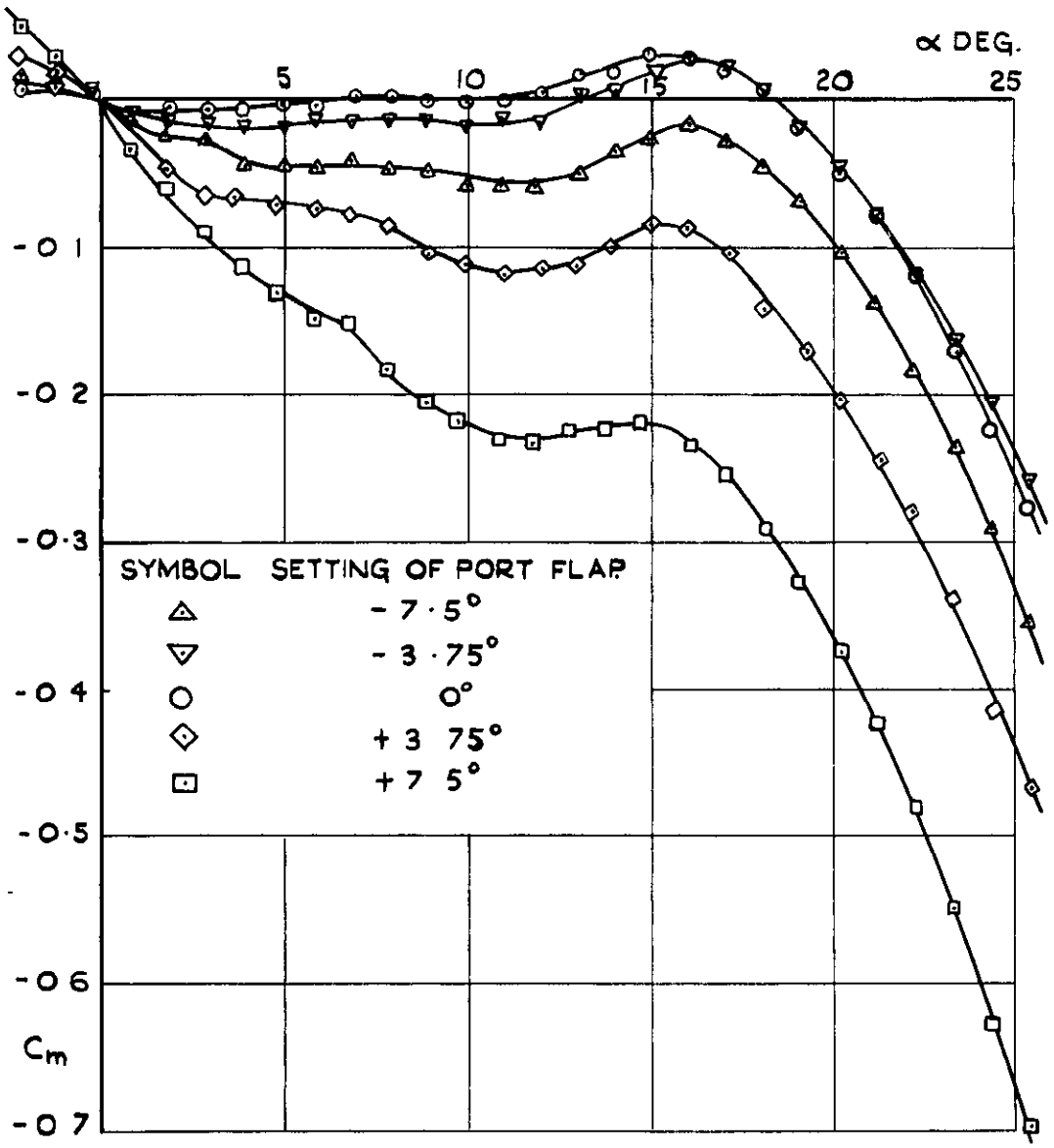

FIG. 52. C_m vs α FOR MODEL WITH FLARE FLAP ACTING NORMAL TO INCIDENCE PLANE

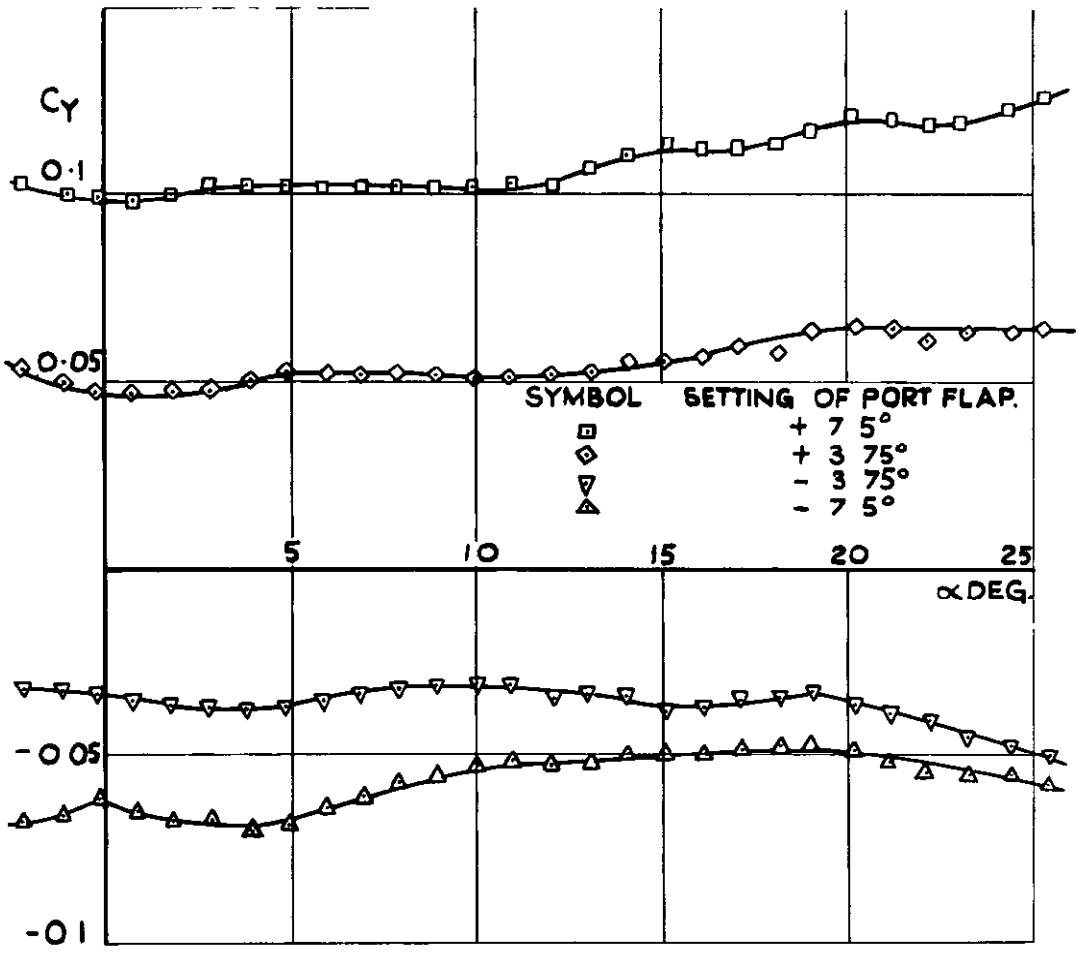

FIG. 53. C_y vs ∝ FOR MODEL WITH FLARE FLAP ACTING NORMAL TO INCIDENCE PLANE.

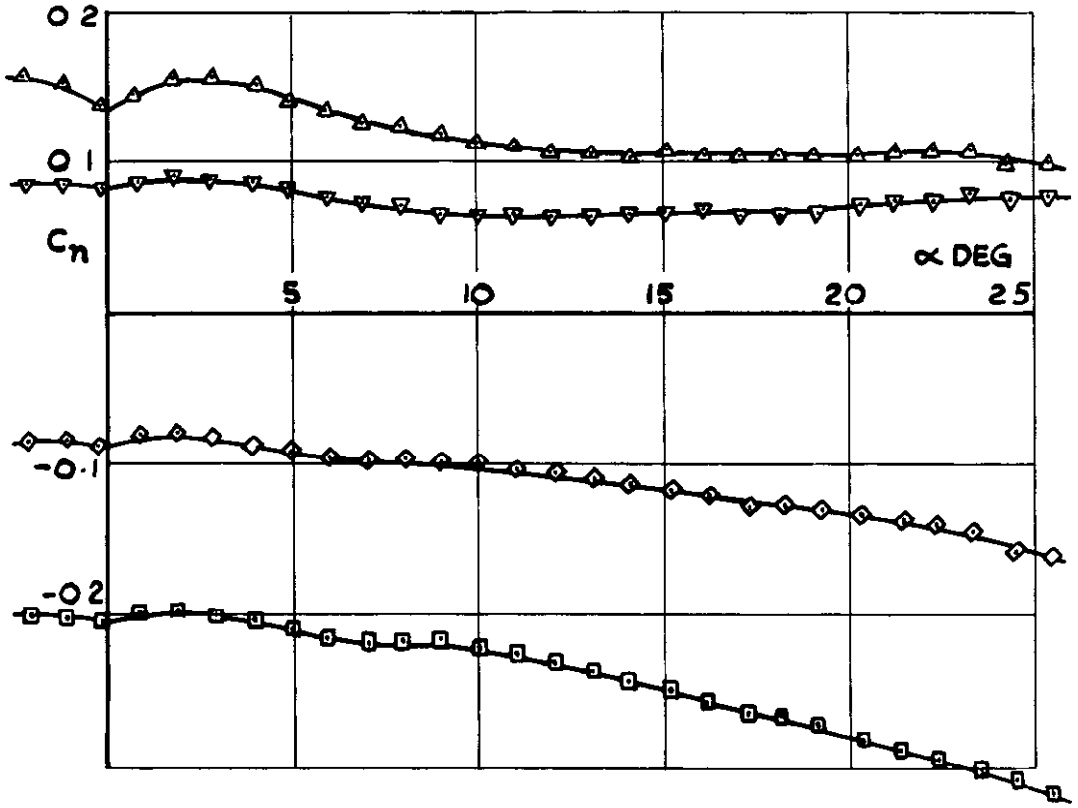

FIG. 54. C_n vs ∝ FOR MODEL WITH FLARE FLAP ACTING NORMAL TO INCIDENCE PLANE.

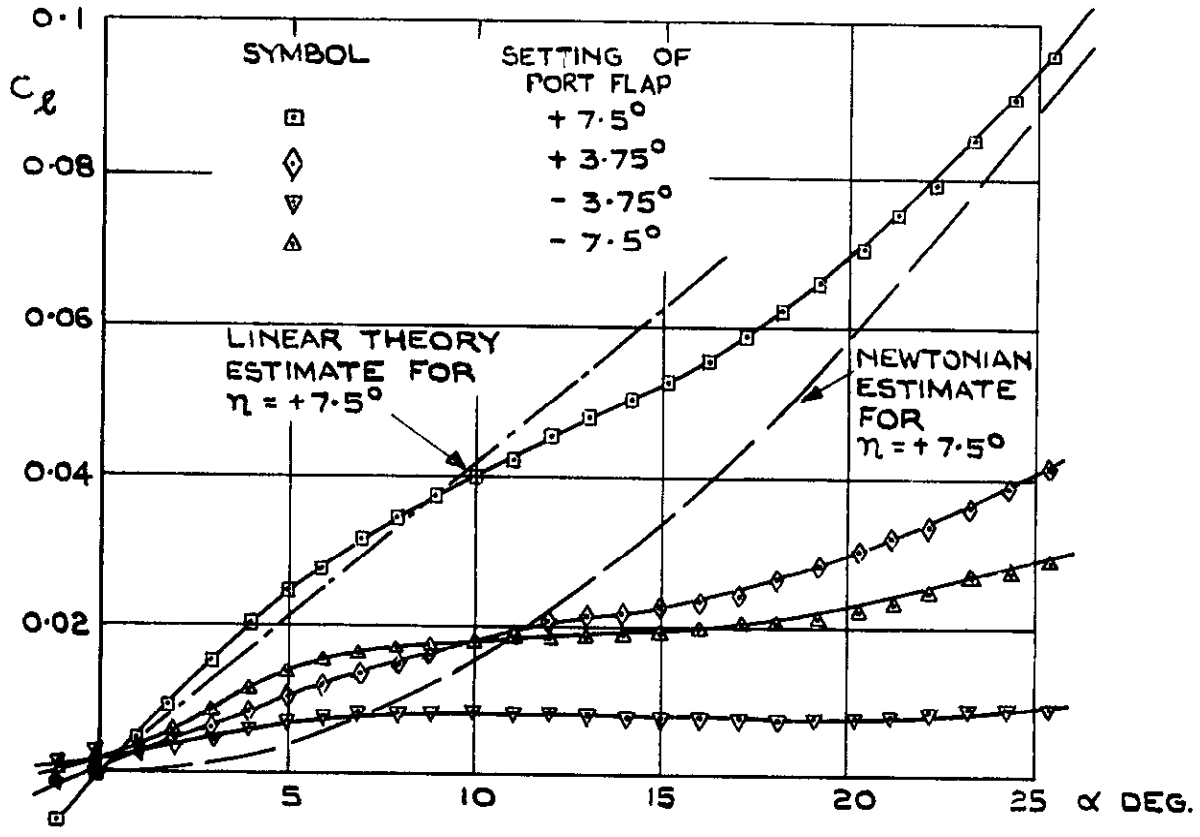

FIG. 55 C_ℓ vs α FOR MODEL WITH FLARE FLAP ACTING NORMAL TO INCIDENCE PLANE

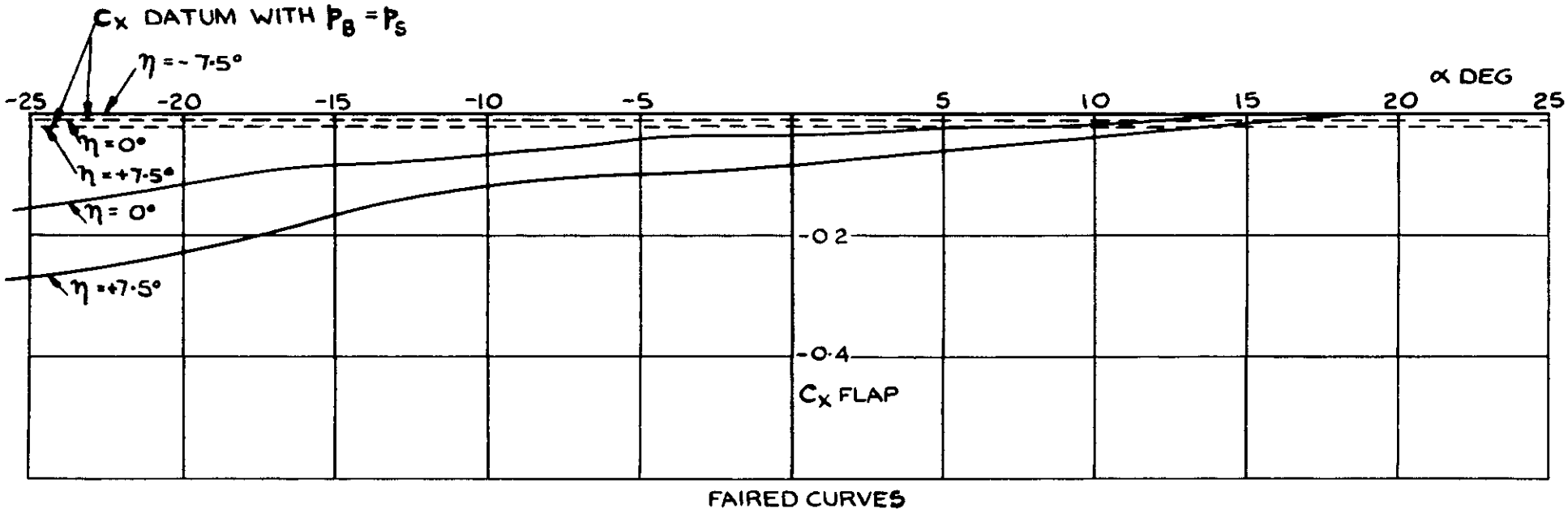

FIG. 56. VARIATION OF FLARE FLAP X FORCE COEFFICIENT WITH INCIDENCE FOR DEFLECTIONS IN INCIDENCE PLANE (BASED ON $P_b = 0$)

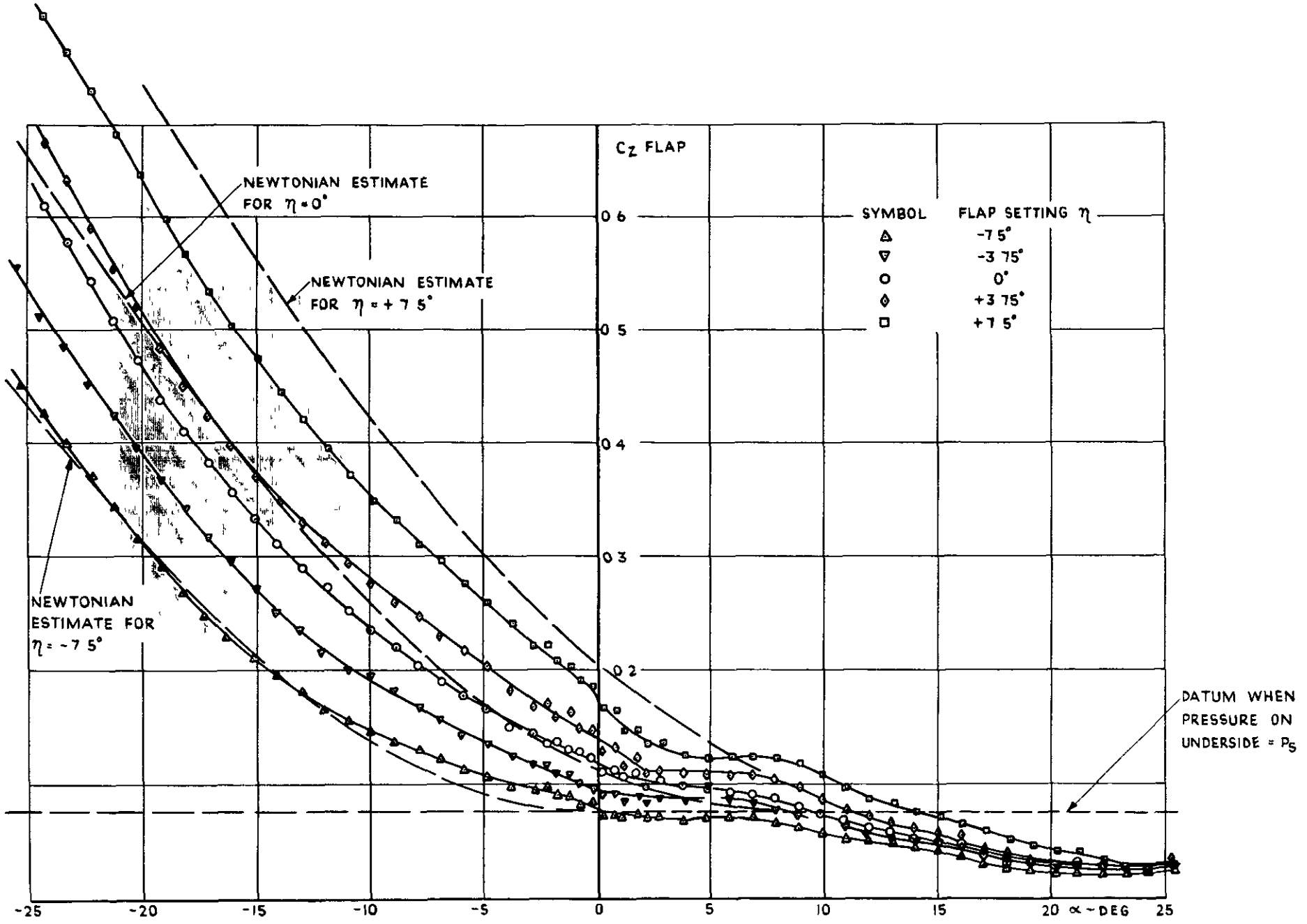

FIG. 57 VARIATION OF FLARE FLAP Z FORCE COEFFICIENT WITH INCIDENCE FOR DEFLECTIONS IN INCIDENCE PLANE (BASED ON $p = 0$ ON UNDERSIDE)

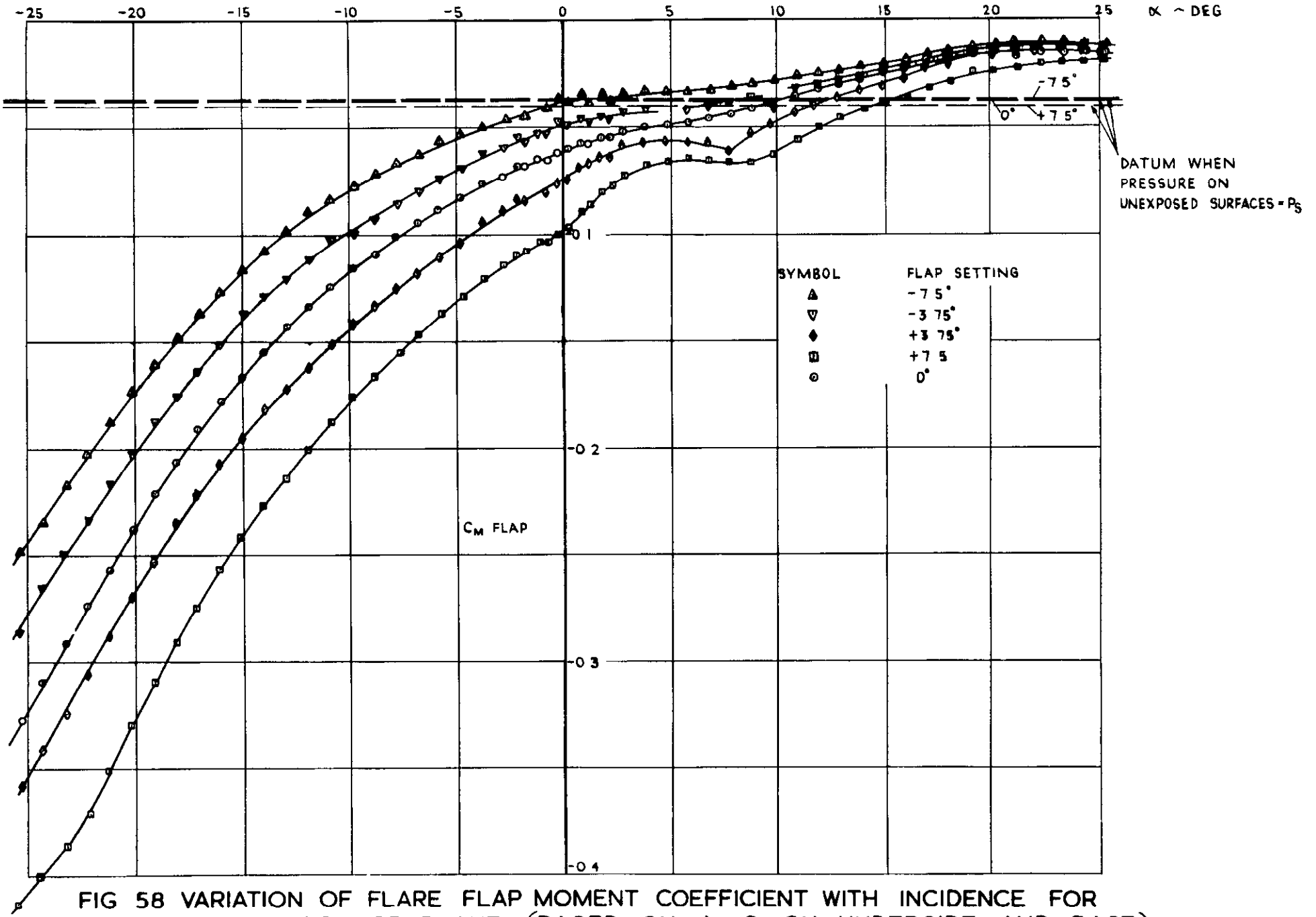

FIG 58 VARIATION OF FLARE FLAP MOMENT COEFFICIENT WITH INCIDENCE FOR DEFLECTIONS IN INCIDENCE PLANE (BASED ON $p = 0$ ON UNDERSIDE AND BASE.)

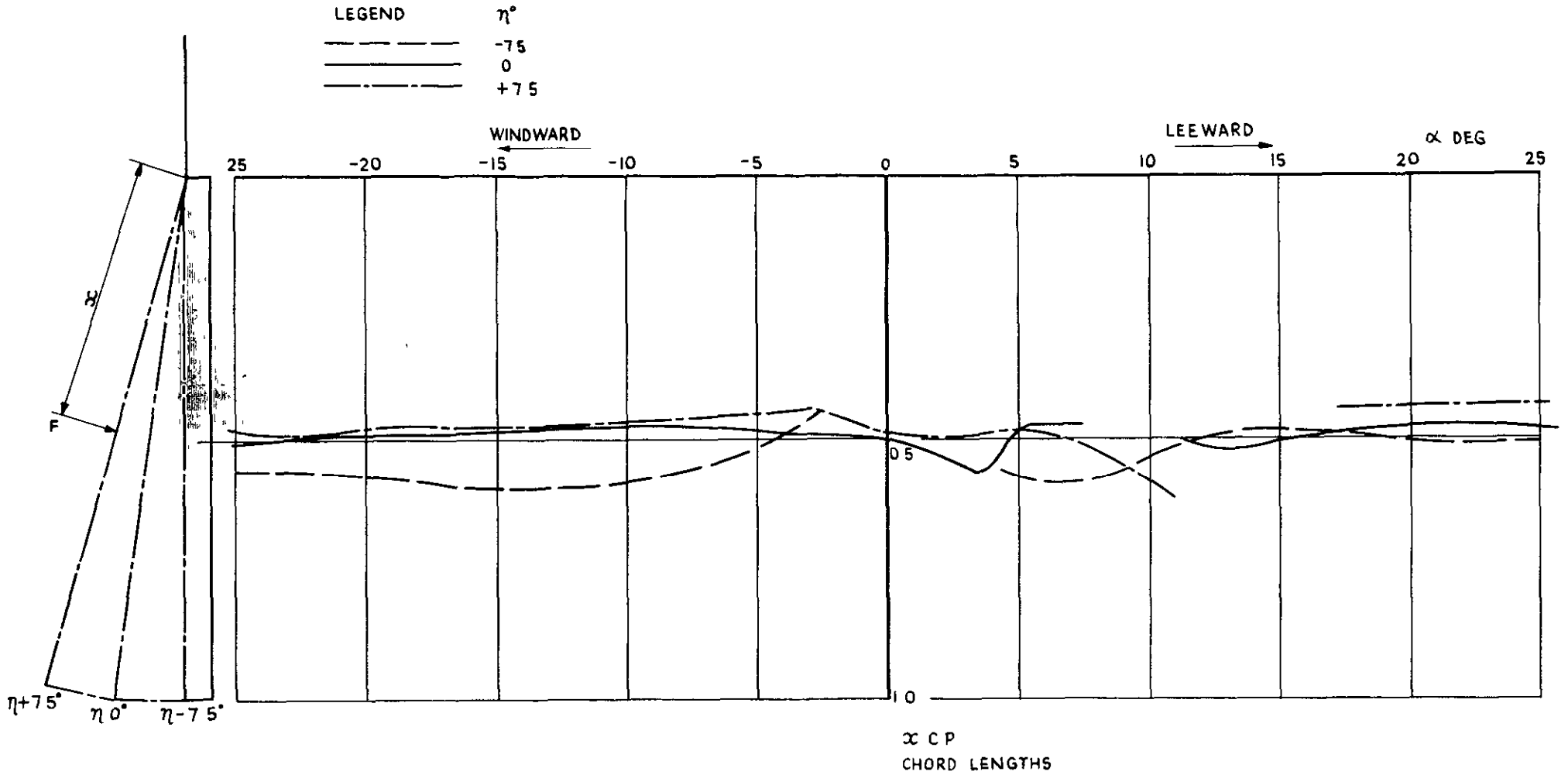

FIG. 59. VARIATION OF C.P. OF EXPOSED SURFACE OF FLARE FLAP WITH INCIDENCE.

SYMBOL	FLAP SETTING
△	+ 7·5°
□	+ 3 75°
○	0°
▽	-3·75°
◇	-7·5°

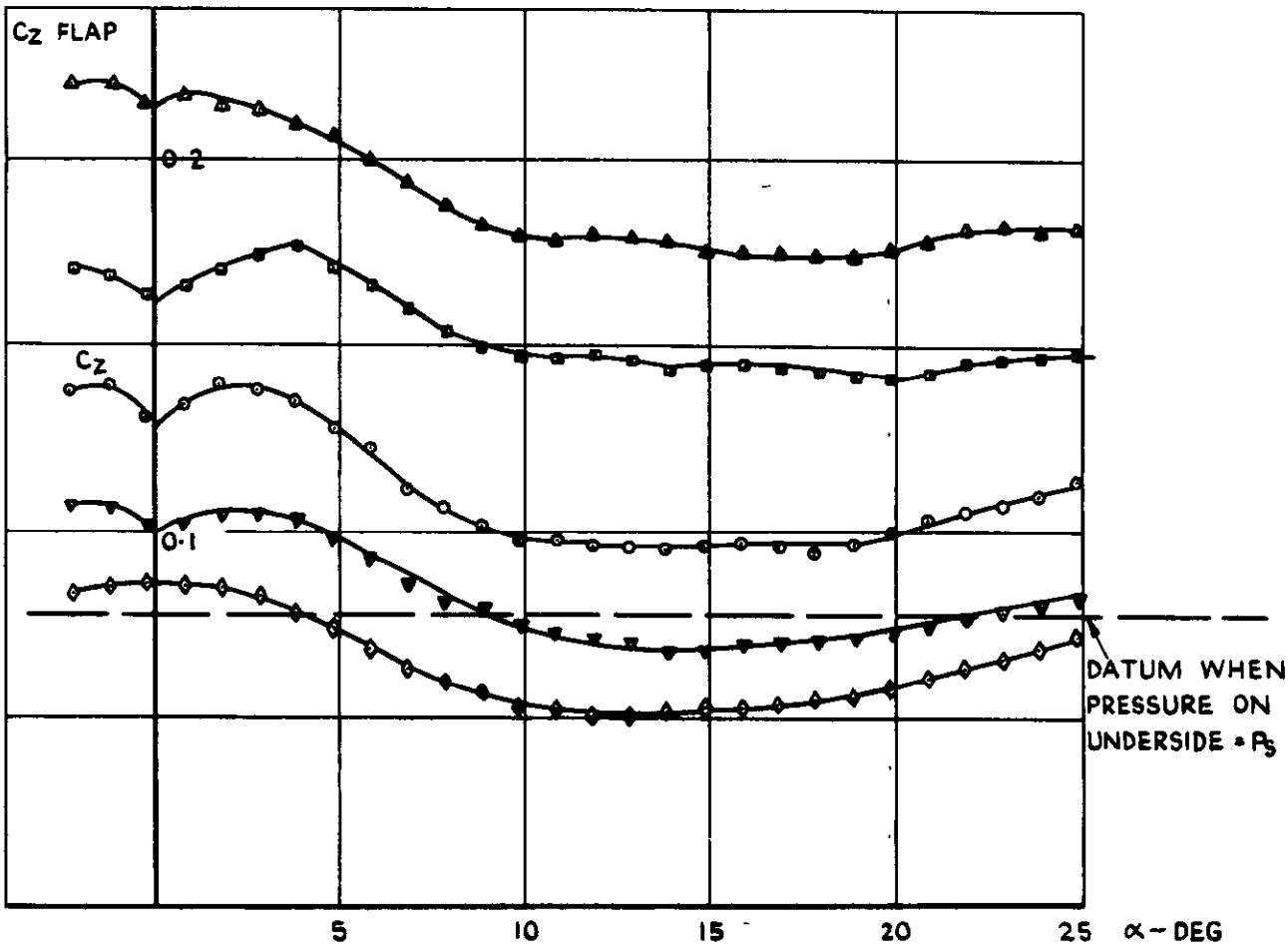

FIG. 60. VARIATION OF FLARE FLAP Z FORCE COEFFICIENT WITH INCIDENCE FOR DEFLECTIONS NORMAL TO INCIDENCE PLANE (BASED ON p = 0 ON UNDERSIDE.)

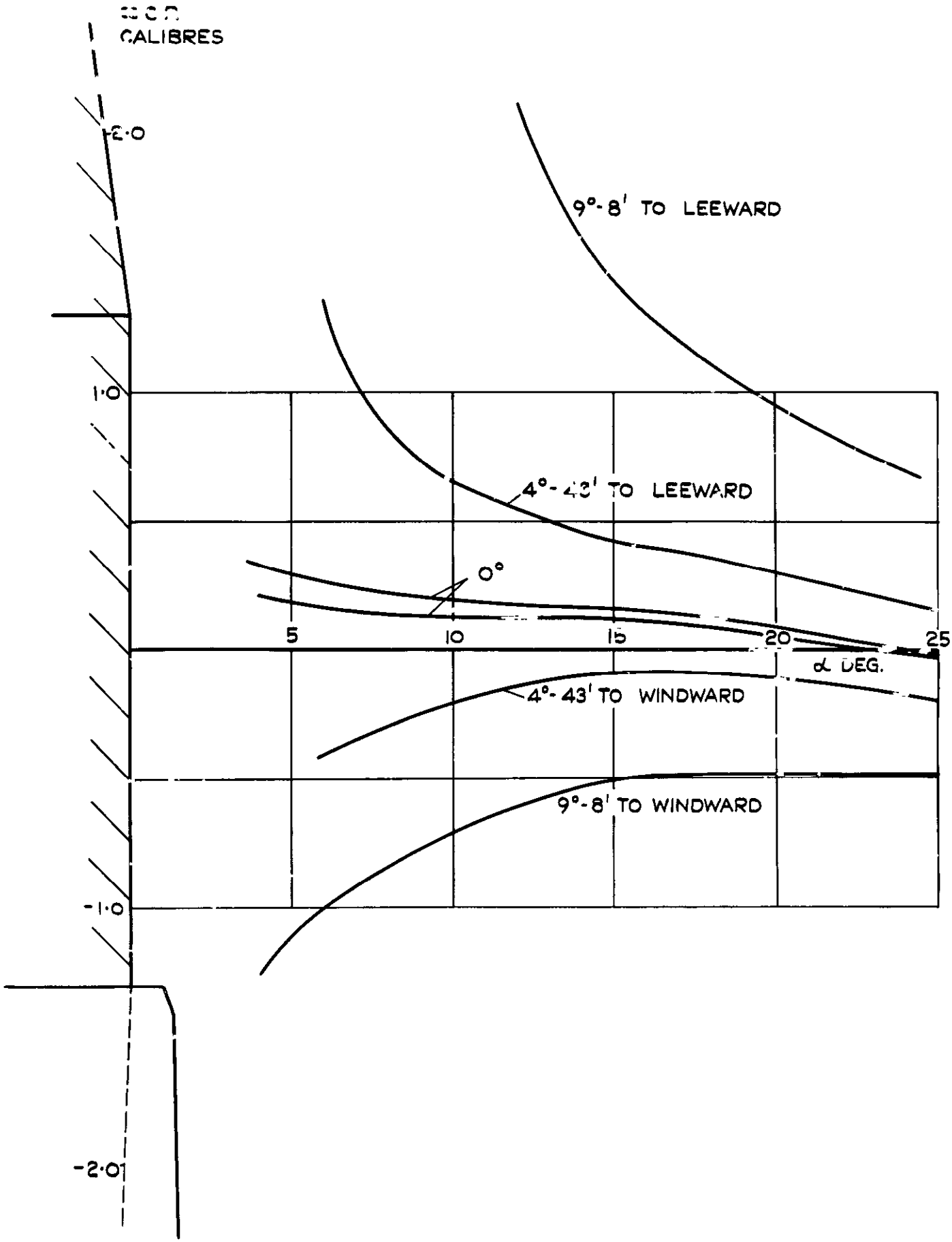

FIG. 133. C.P. VARIATION WITH INCIDENCE FOR MODEL WITH DEFLECTED RING CONTROL USED IN INCIDENCE PLANE.

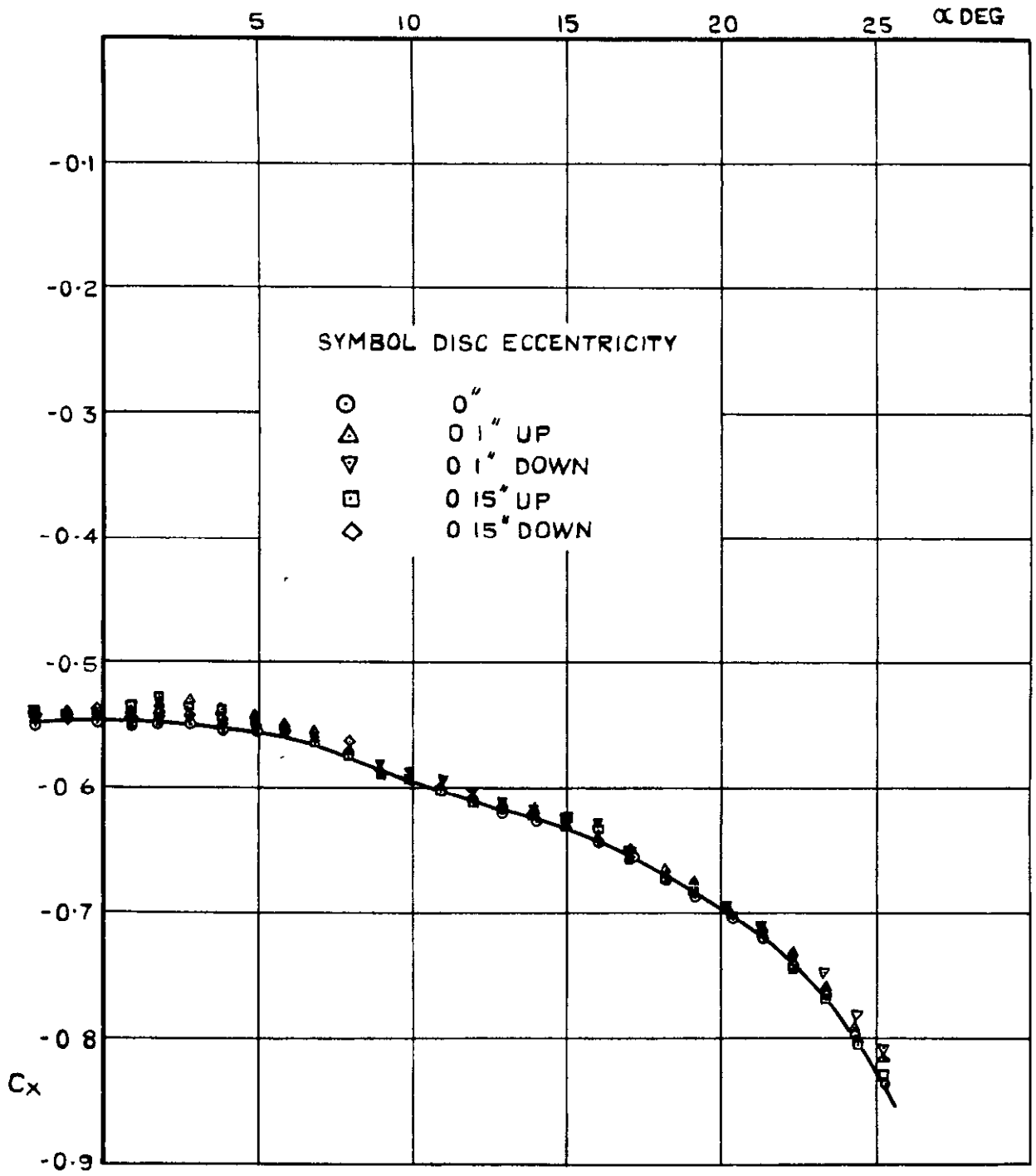

FIG.62. C_X vs α FOR MODEL WITH NOSE DISC TRANSLATED IN INCIDENCE PLANE.

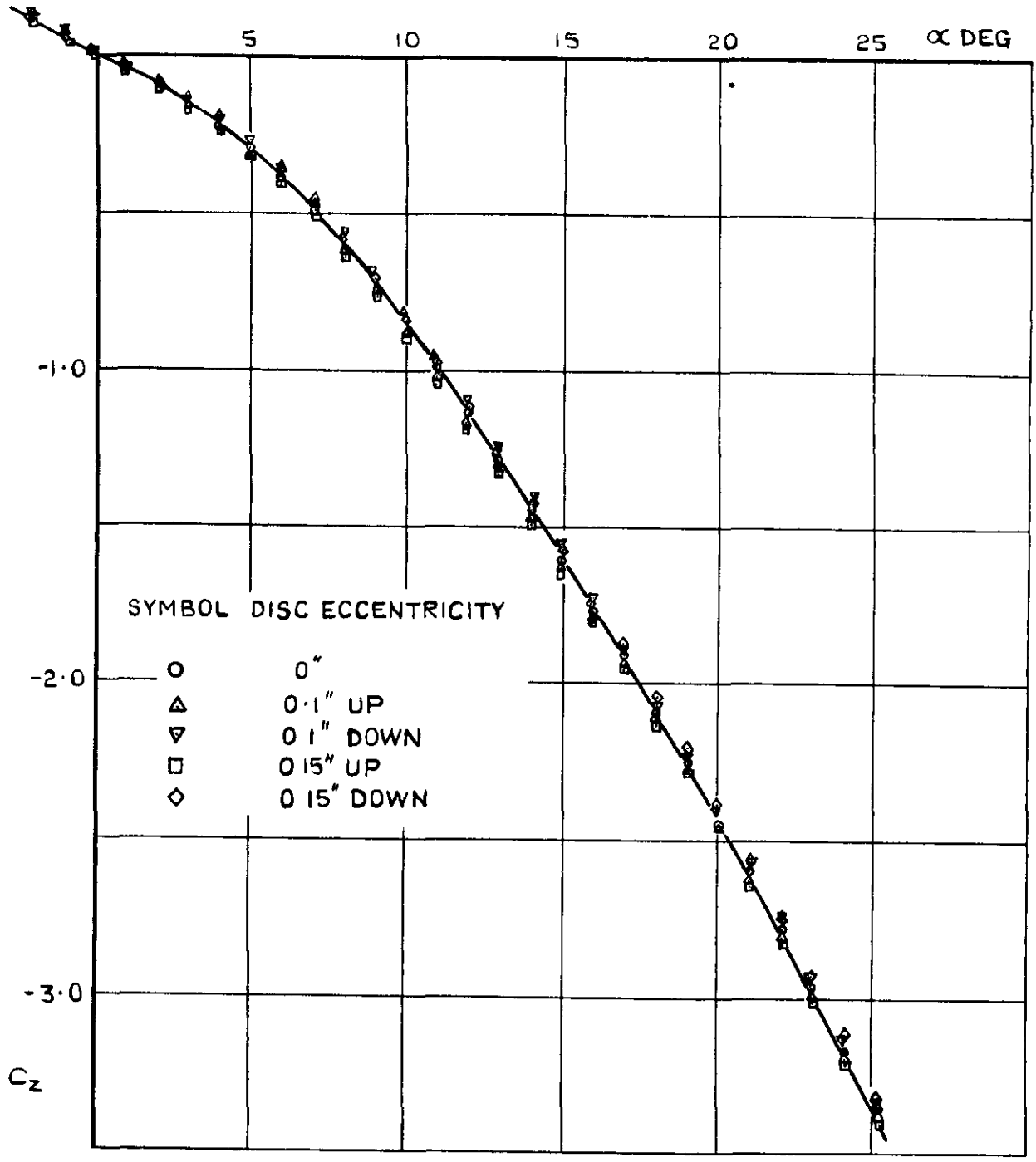

FIG.63 C_z vs α FOR MODEL WITH NOSE DISC TRANSLATED IN INCIDENCE PLANE.

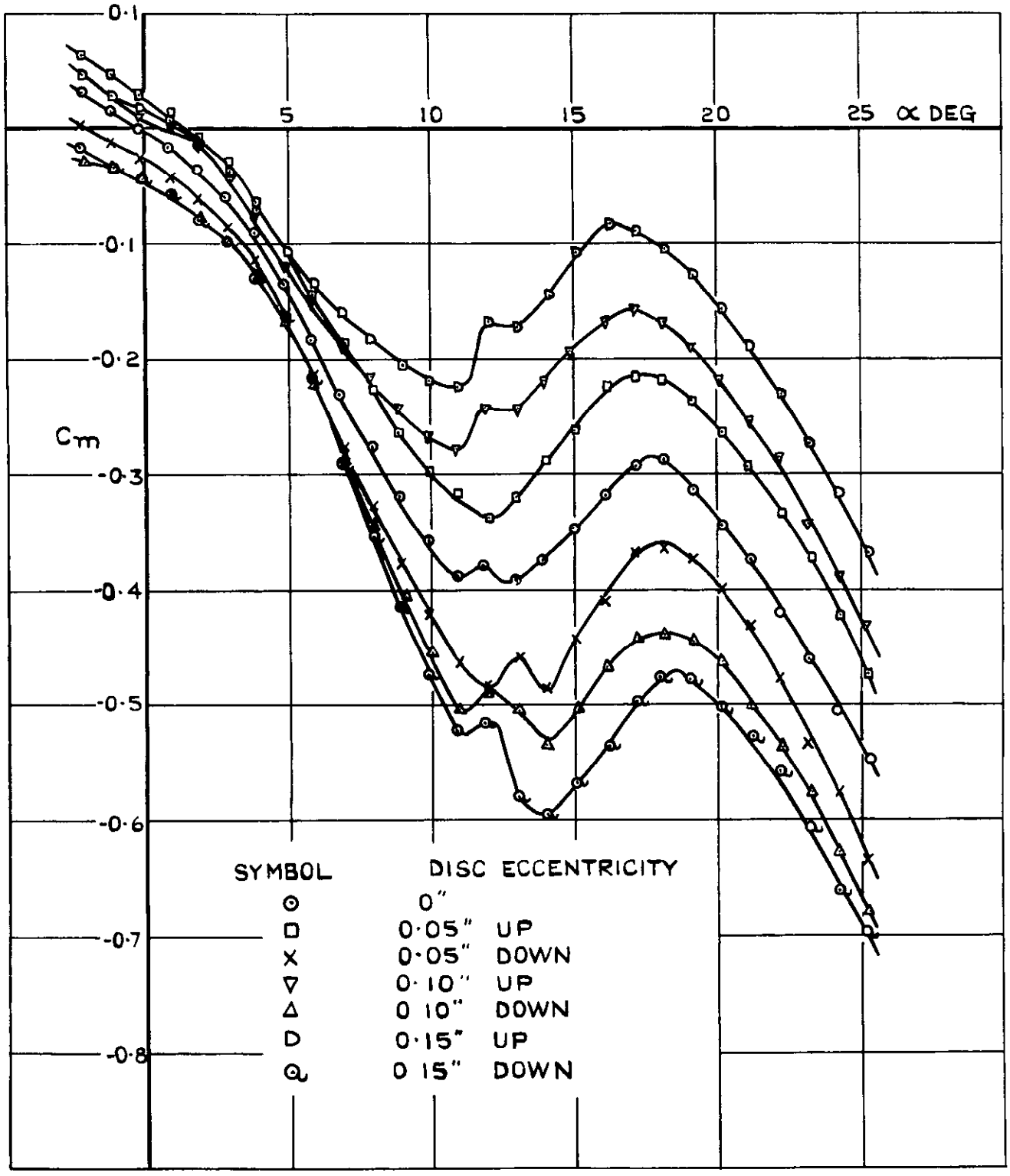

FIG.64. C_m vs α FOR MODEL WITH NOSE DISC TRANSLATED IN INCIDENCE PLANE.

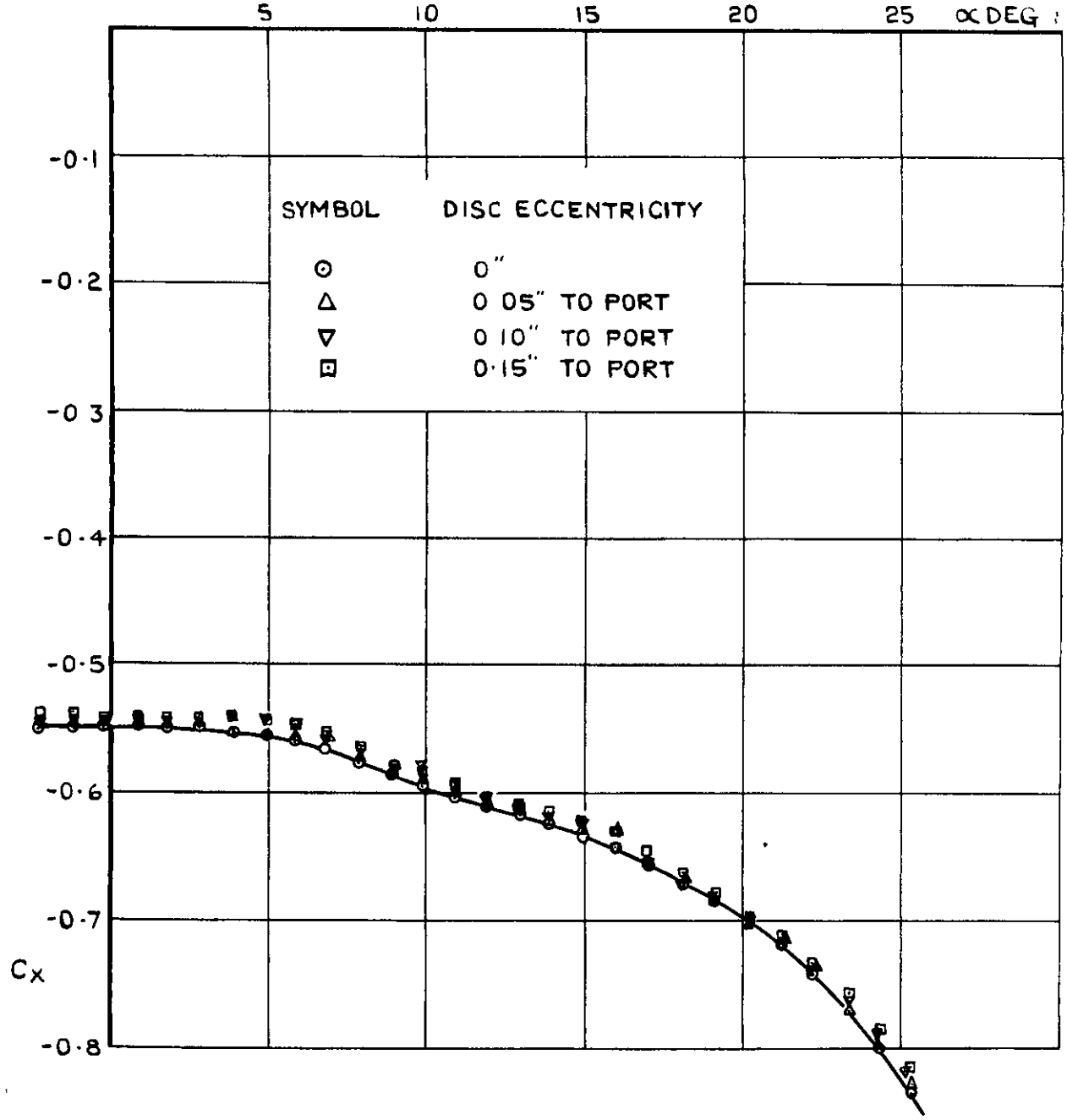

FIG.65. C_X VS α FOR MODEL WITH NOSE DISC TRANSLATED NORMAL TO THE INCIDENCE PLANE.

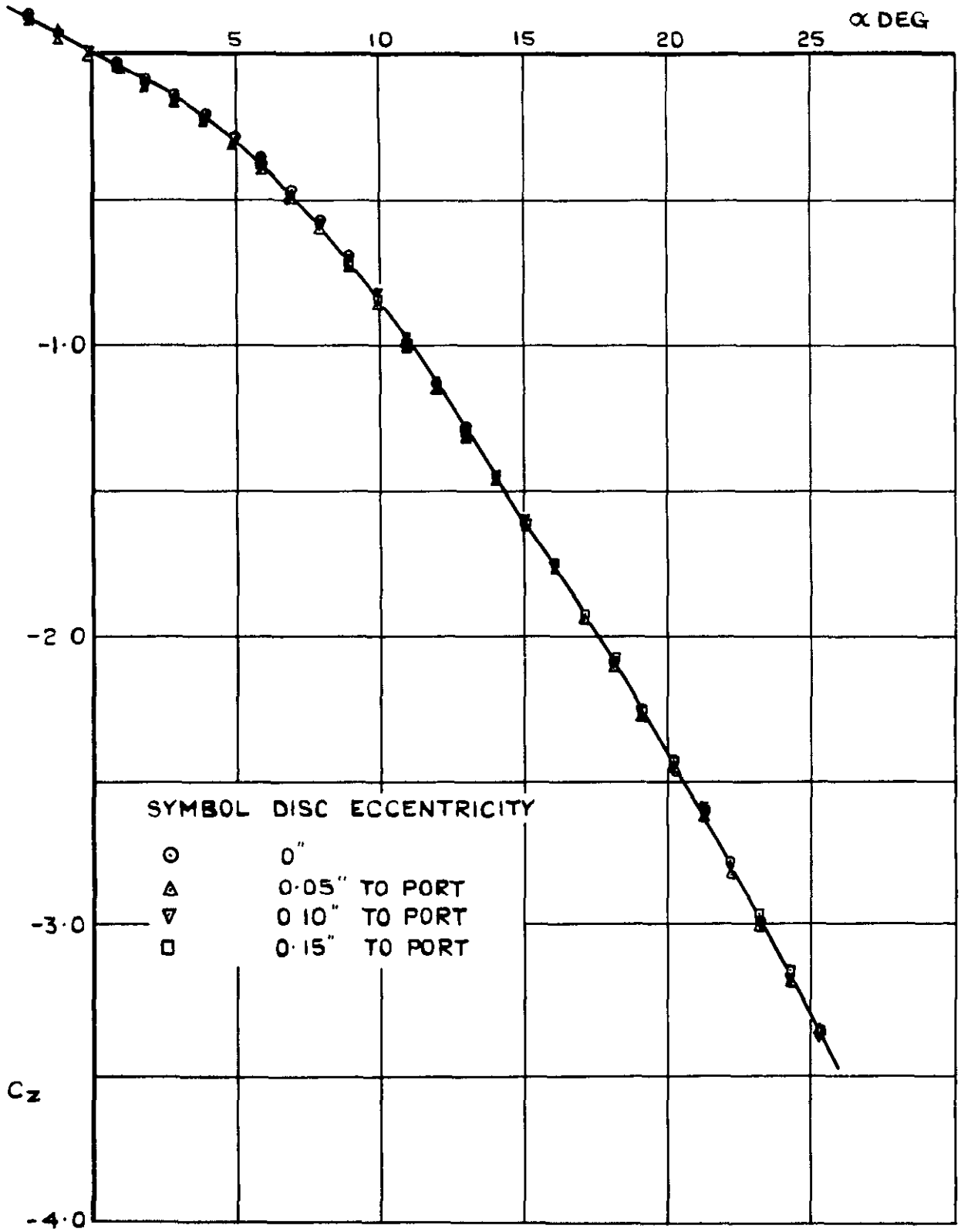

FIG.66. C_z VS α FOR MODEL WITH NOSE DISC TRANSLATED NORMAL TO INCIDENCE PLANE.

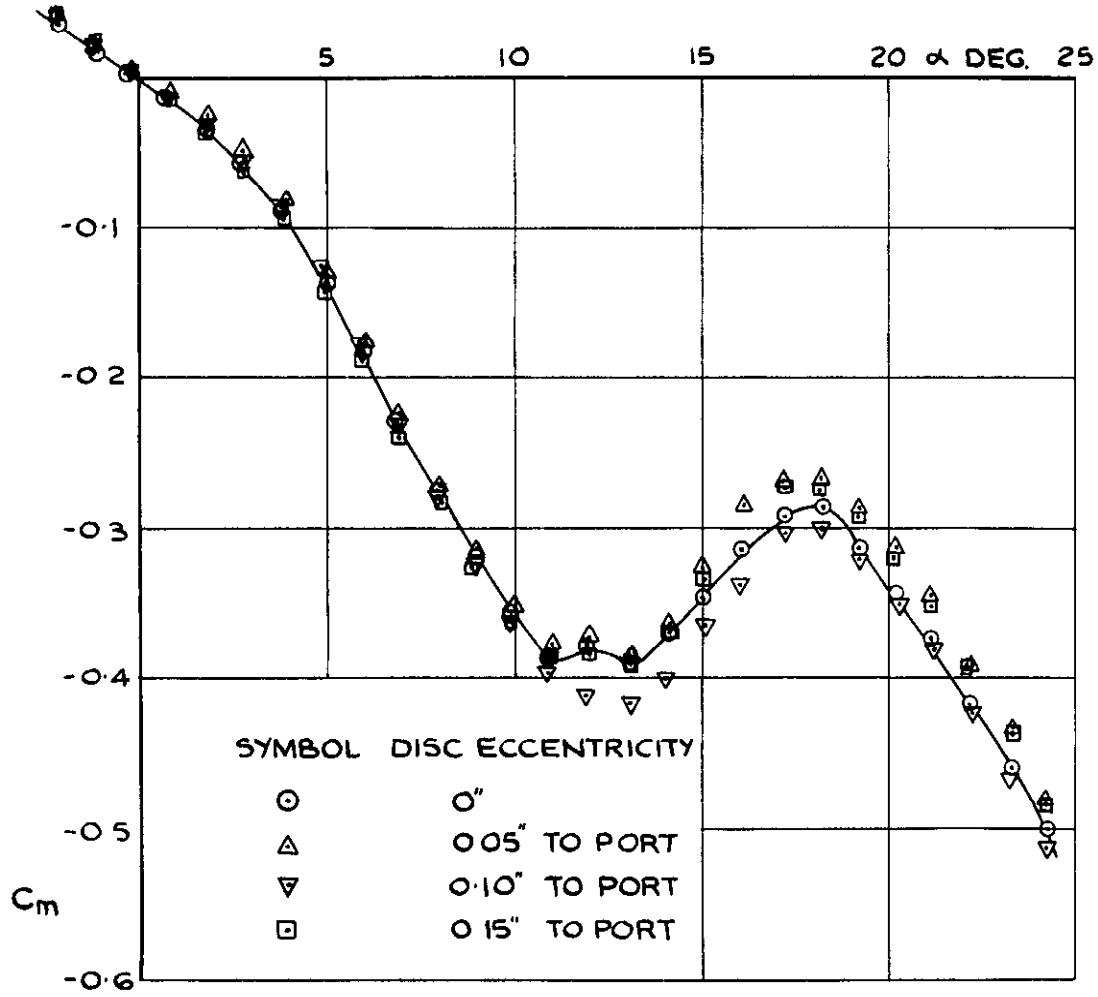

FIG. 67. C_m vs α FOR MODEL WITH NOSE DISC TRANSLATED NORMAL TO INCIDENCE PLANE.

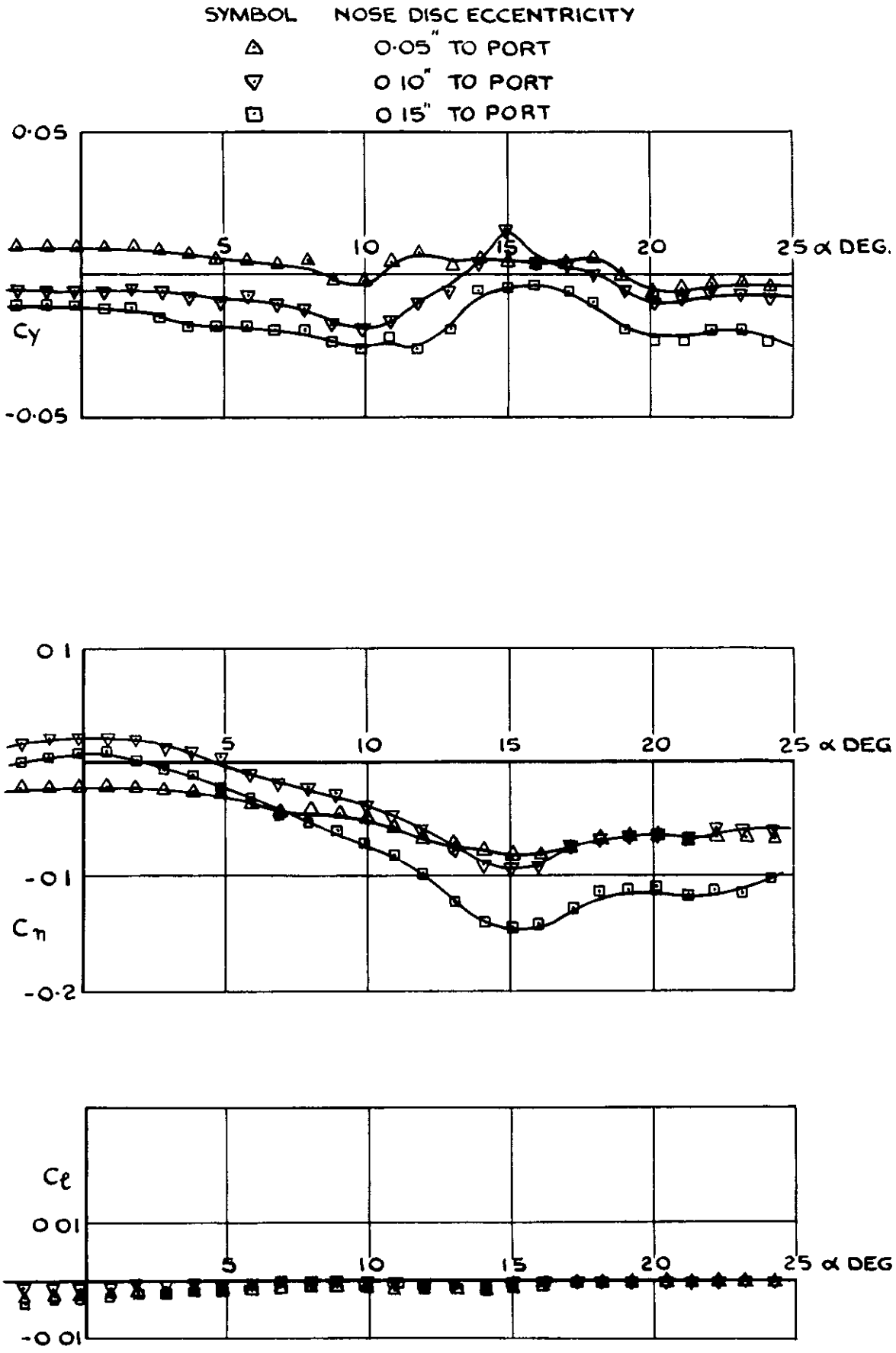

FIG. 68 VARIATION OF DIRECTIONAL & LATERAL COMPONENTS WITH α FOR MODEL WITH NOSE DISC TRANSLATED NORMAL TO INCIDENCE PLANE.

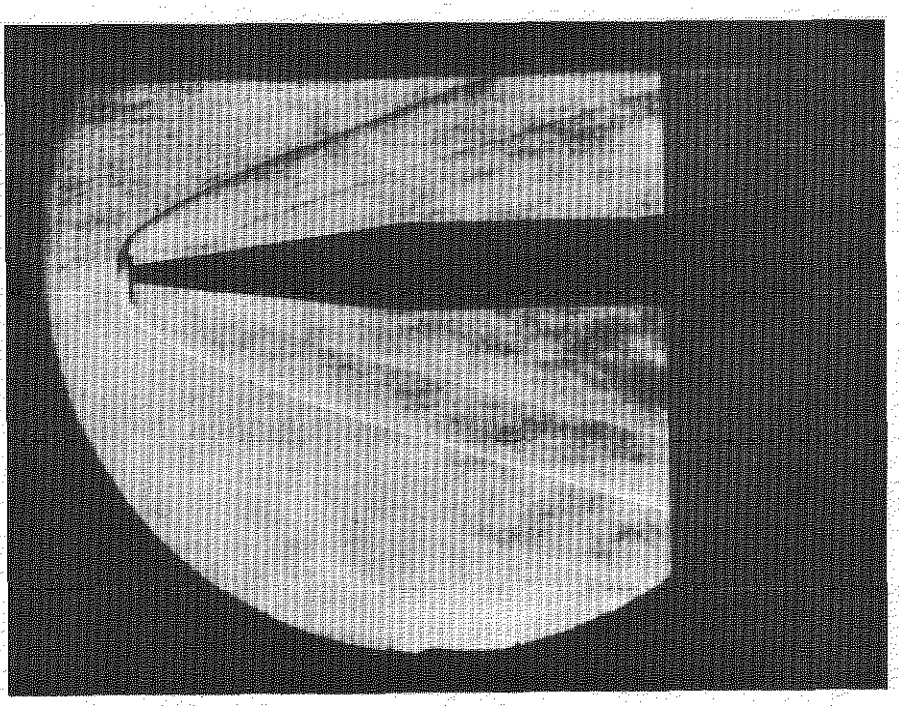

(a) η = 0.1"

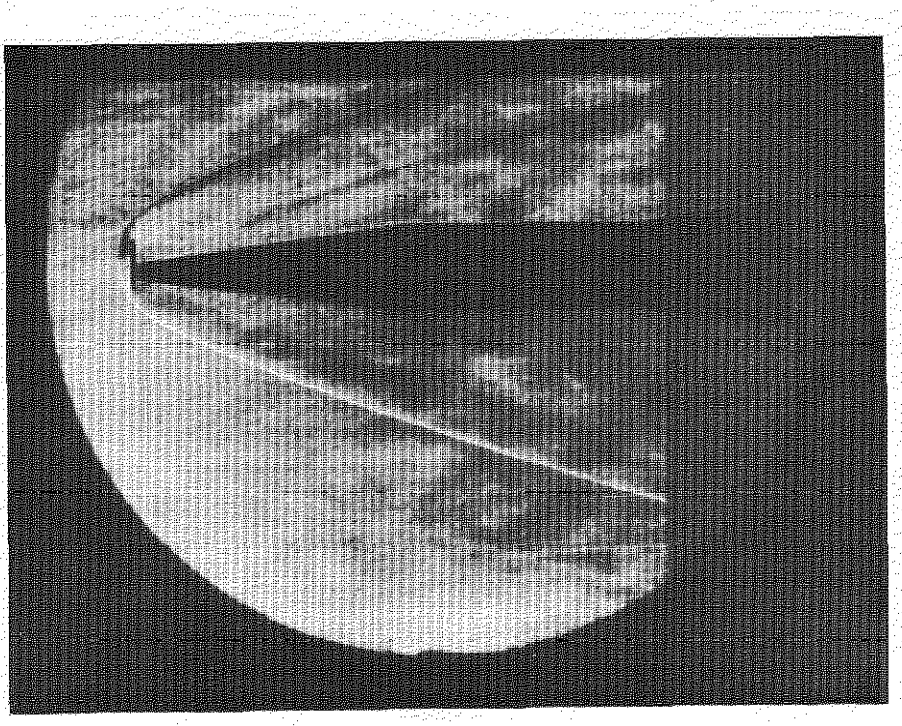

(b) η = 0.15"

FIG.69 SCHLIEREN PHOTOGRAPHS OF MODEL WITH ECCENTRIC NOSE DISC AT $\alpha = 0^{\circ}$

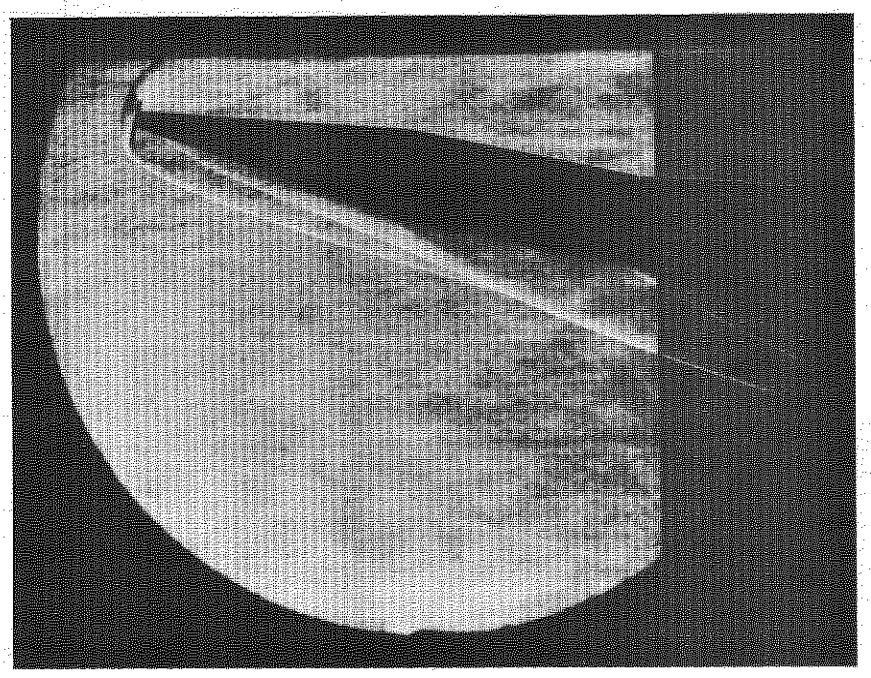

(a) $\alpha = 12^{\circ}$

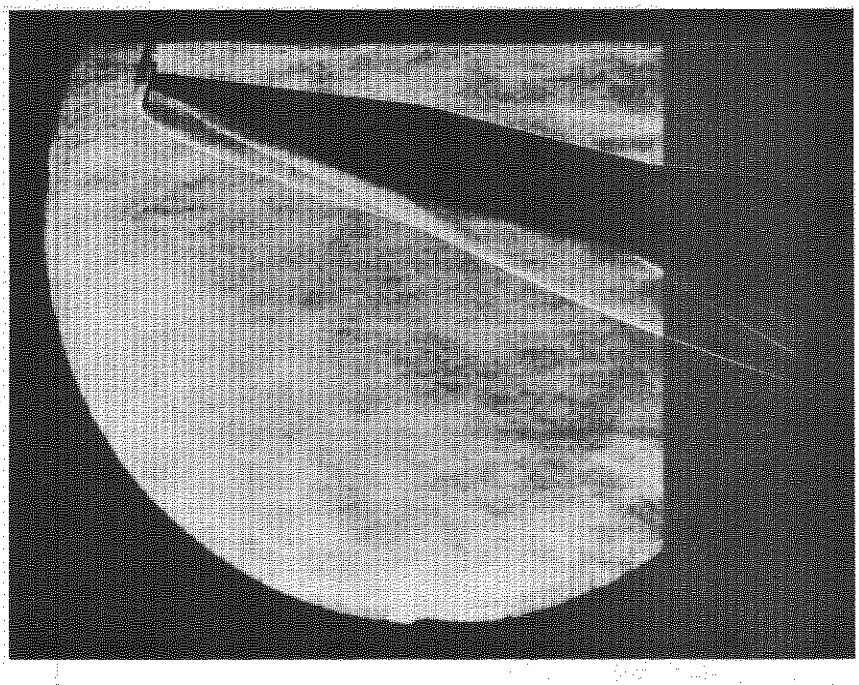

(b) $\alpha = 14^{\circ}$

FIG.70 SCHLIEREN PHOTOGRAPHS OF MODEL WITH ECCENTRIC NOSE DISC AT $\alpha = 12^{\circ}$ AND 14°

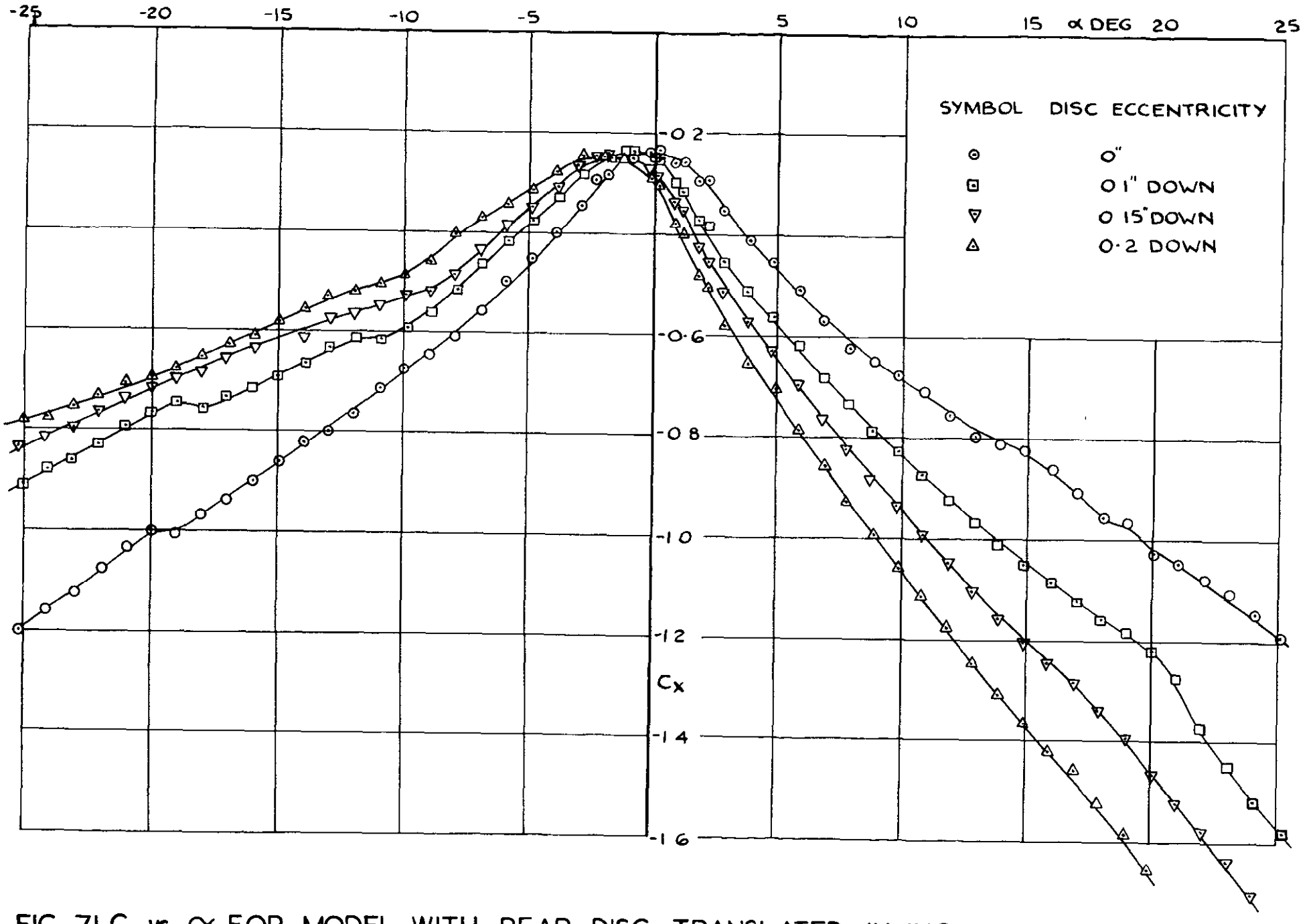

FIG 71 C_x vs α FOR MODEL WITH REAR DISC TRANSLATED IN INCIDENCE PLANE.

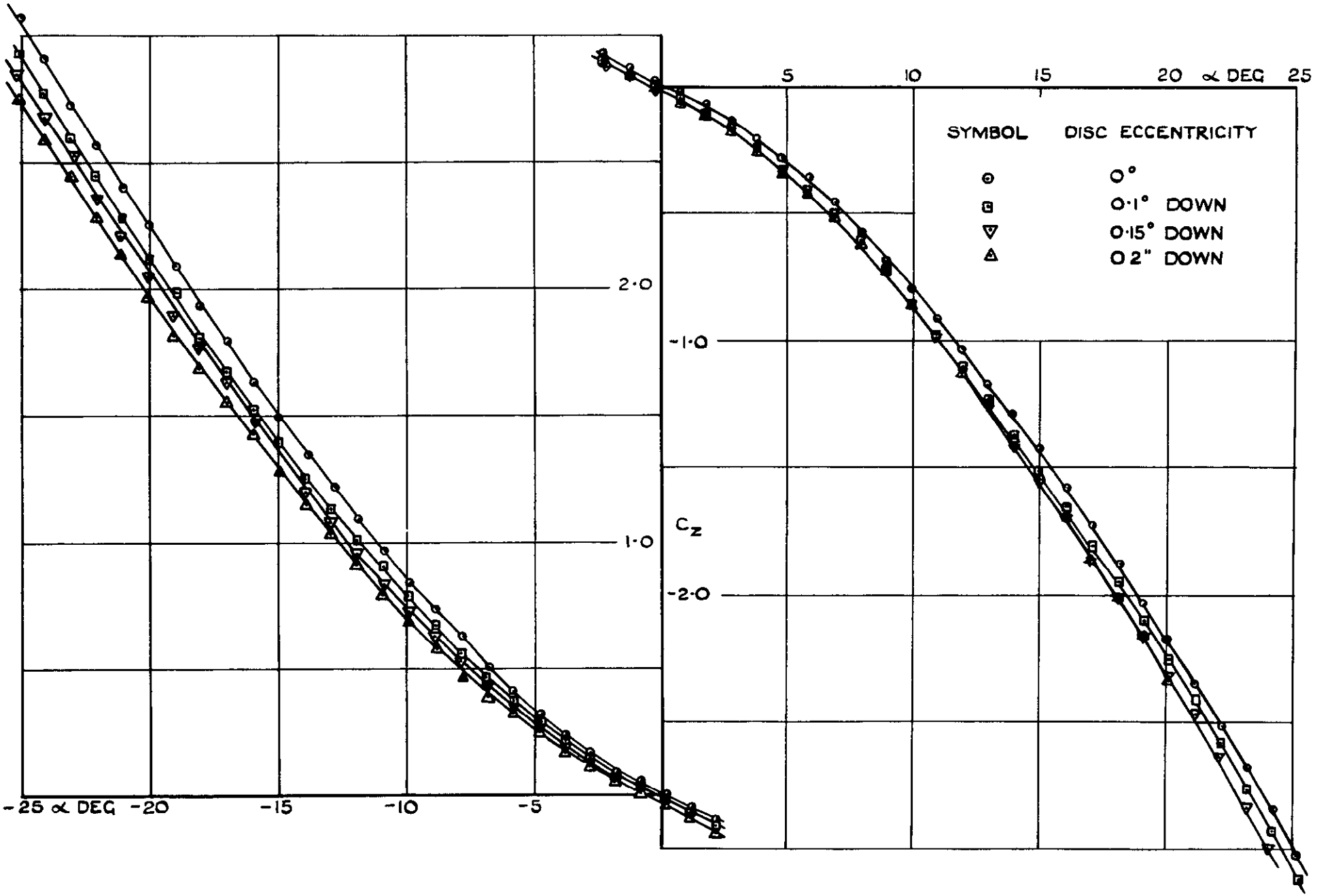

FIG. 72. C_z vs α FOR MODEL WITH REAR DISC TRANSLATED IN INCIDENCE PLANE.

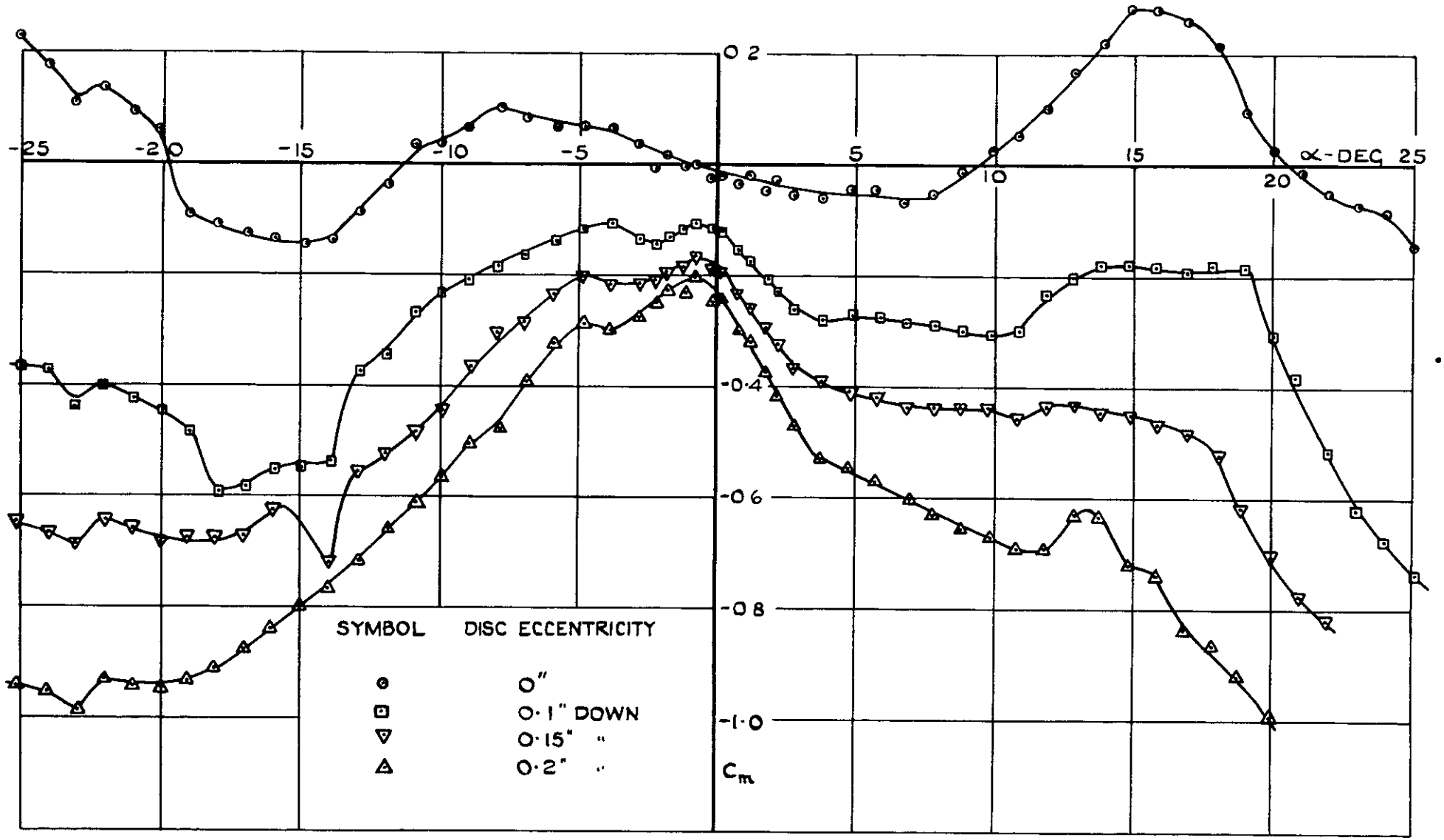

FIG. 73 C_m vs α FOR MODEL WITH REAR DISC TRANSLATED IN INCIDENCE PLANE

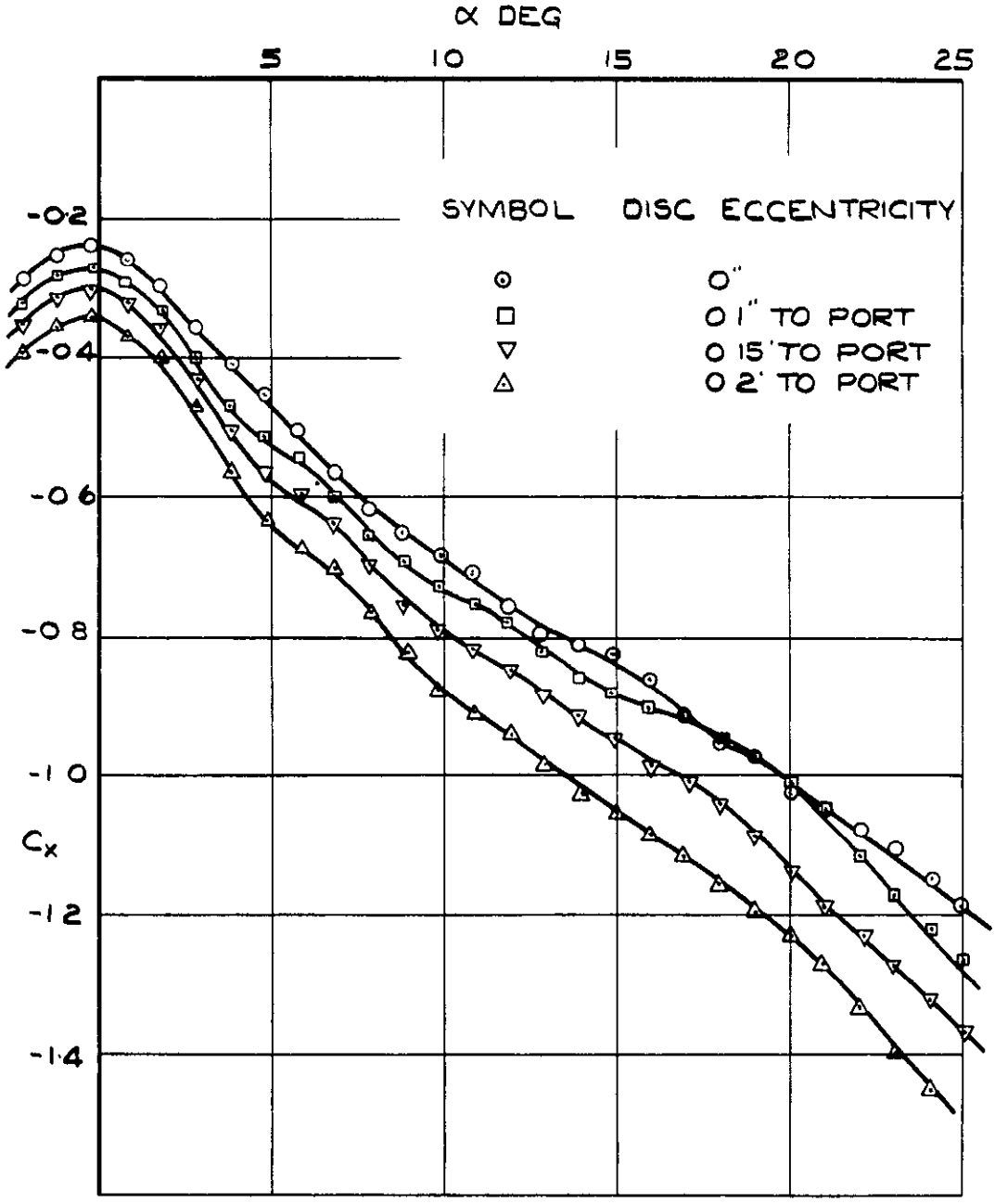

FIG.74. C_x vs α FOR MODEL WITH REAR DISC TRANSLATED NORMAL TO INCIDENCE PLANE

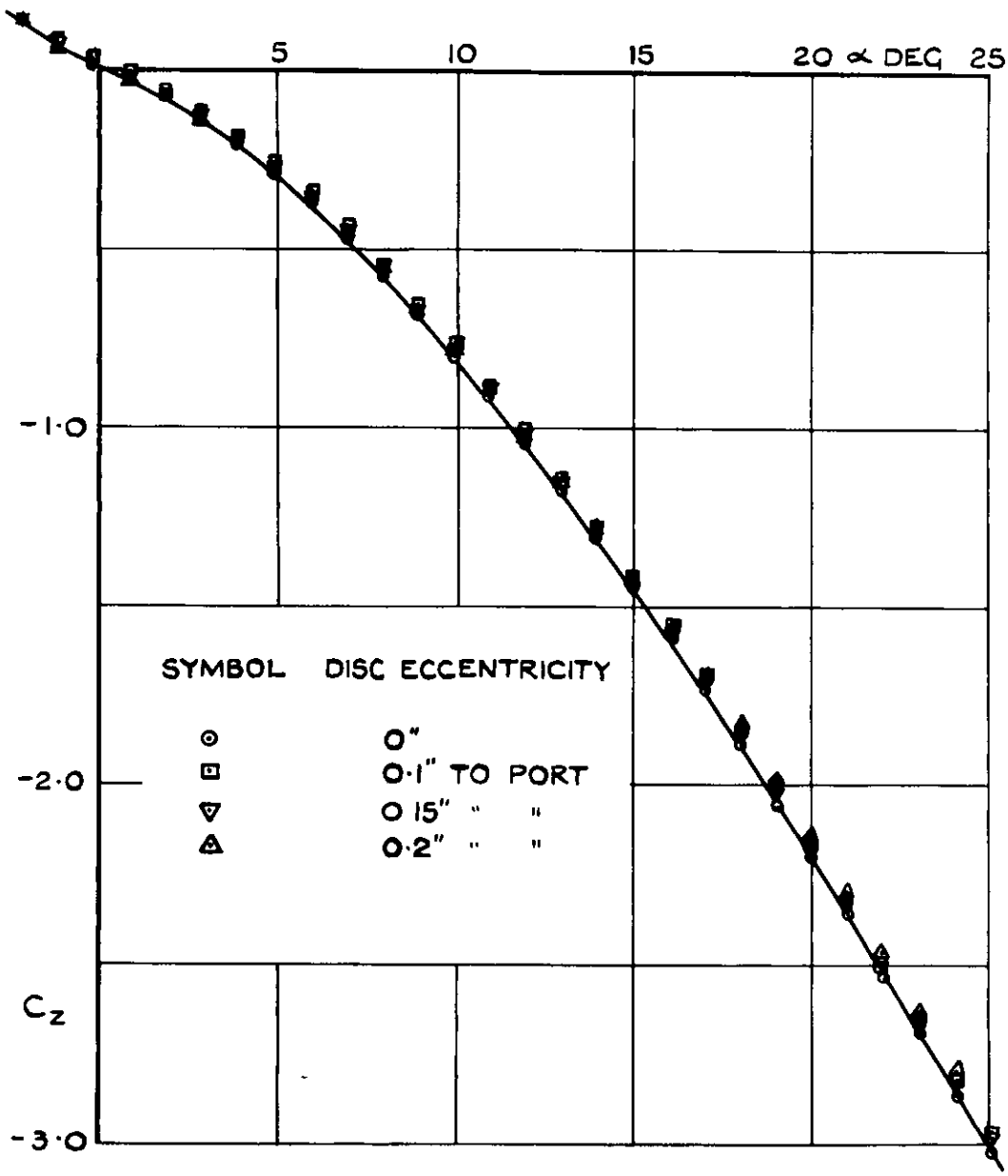

FIG. 75. C_z vs $\propto$ FOR MODEL WITH REAR DISC TRANSLATED NORMAL TO INCIDENCE PLANE.

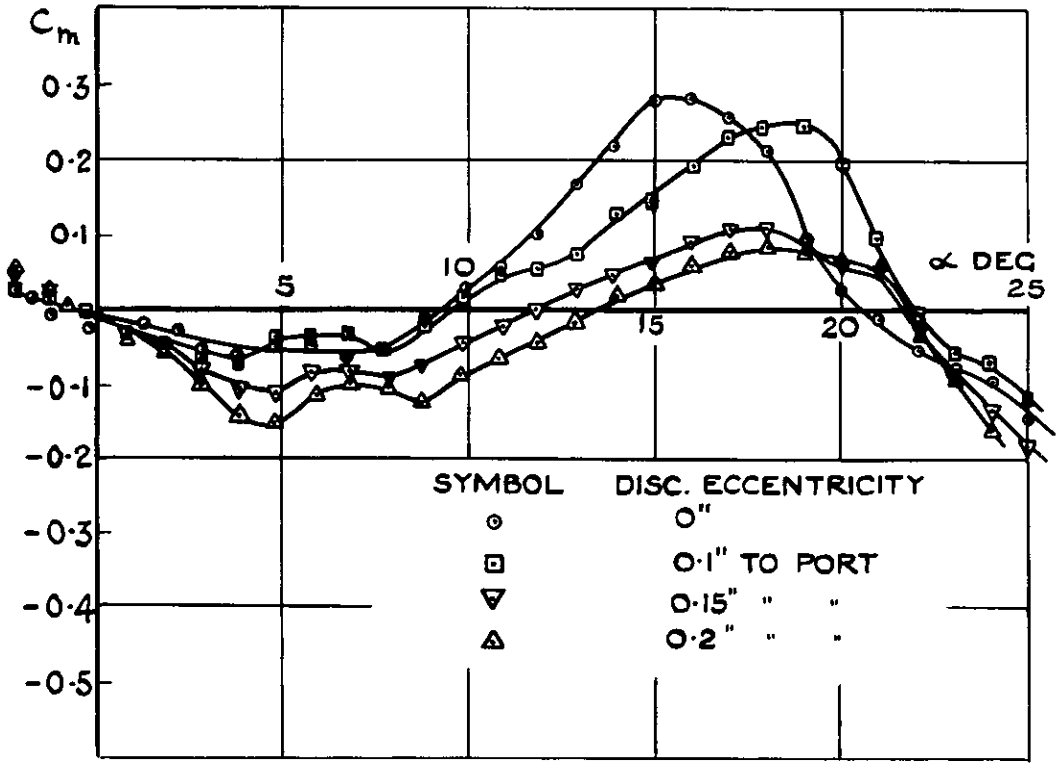

FIG. 76. C_m vs α FOR MODEL WITH REAR DISC TRANSLATED NORMAL TO INCIDENCE PLANE.

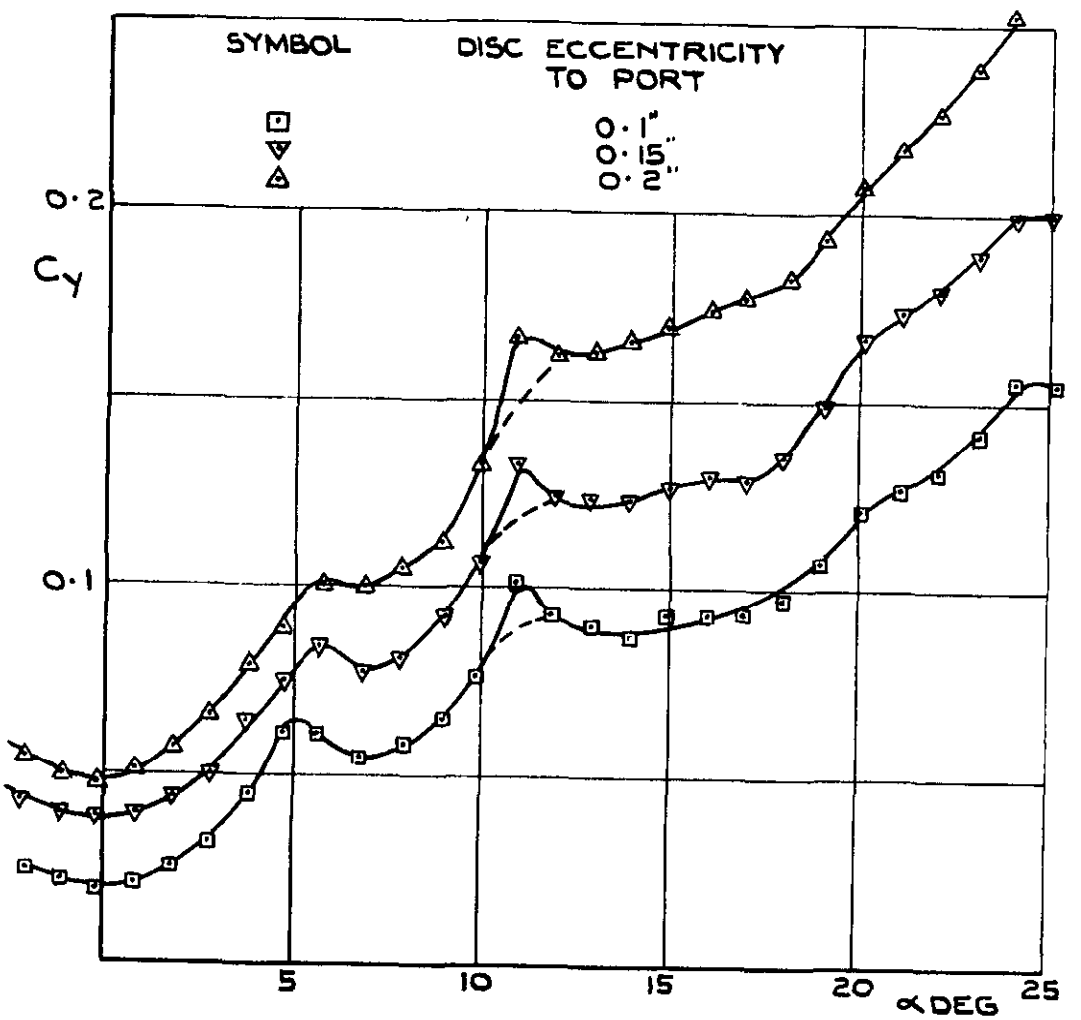

FIG. 77. C_y vs ∝ FOR MODEL WITH REAR DISC TRANSLATED NORMAL TO INCIDENCE PLANE

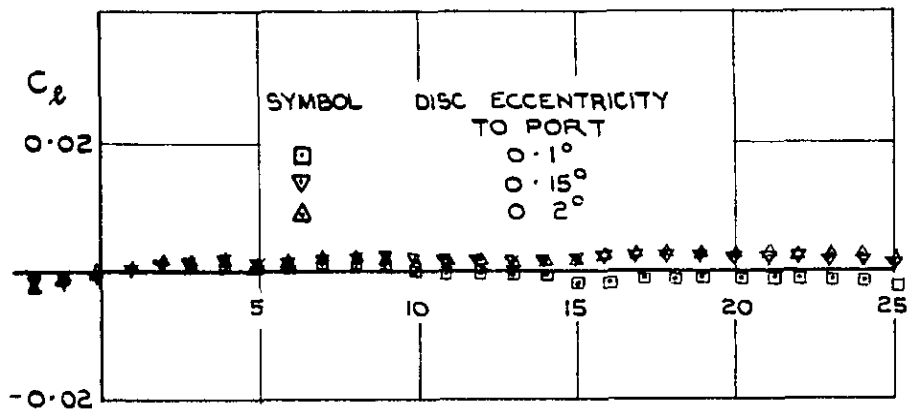

FIG. 78. C_ℓ vs α FOR MODEL WITH REAR DISC TRANSLATED NORMAL TO INCIDENCE PLANE

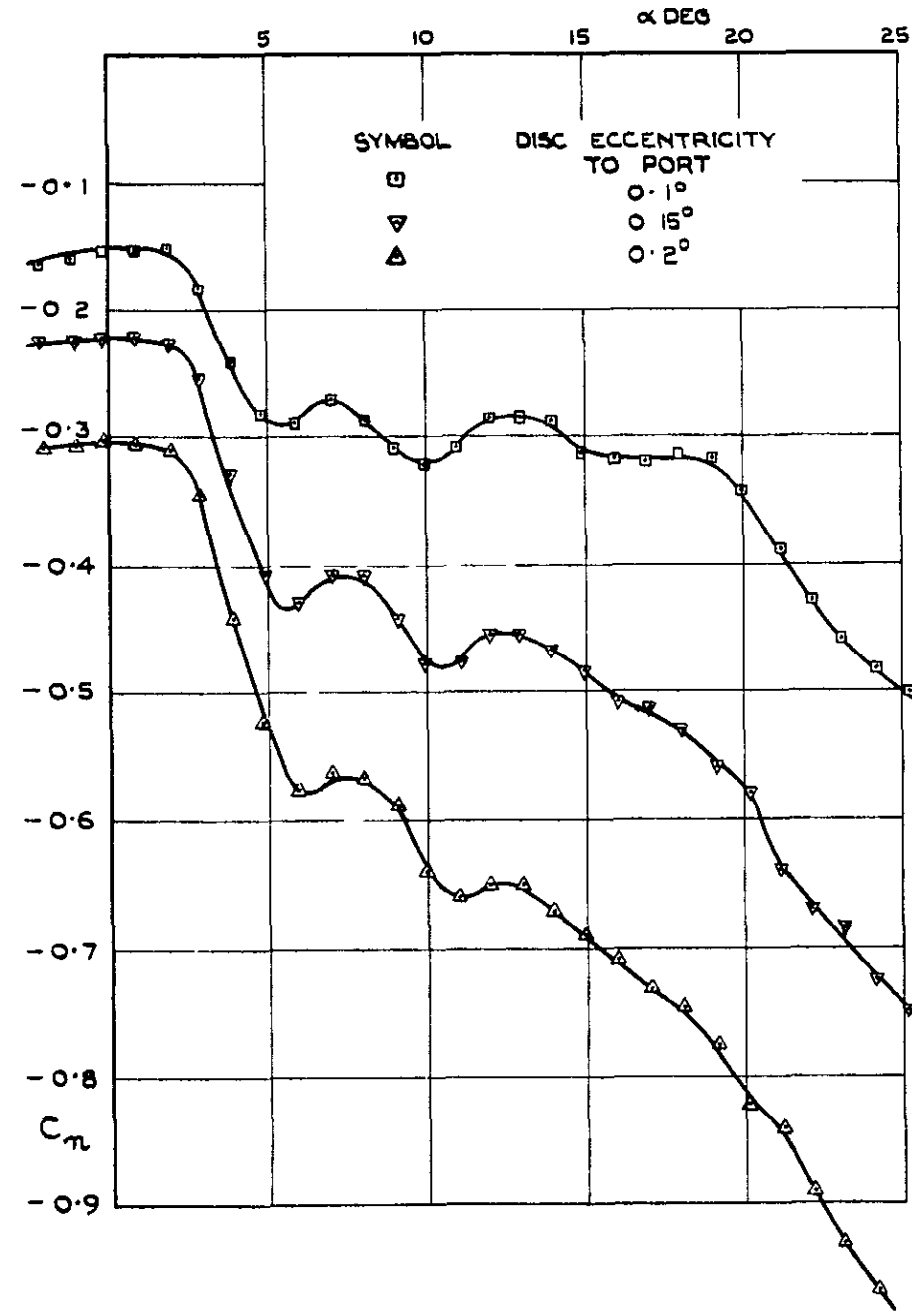

FIG. 79. C_n vs α FOR MODEL WITH REAR DISC TRANSLATED NORMAL TO INCIDENCE PLANE

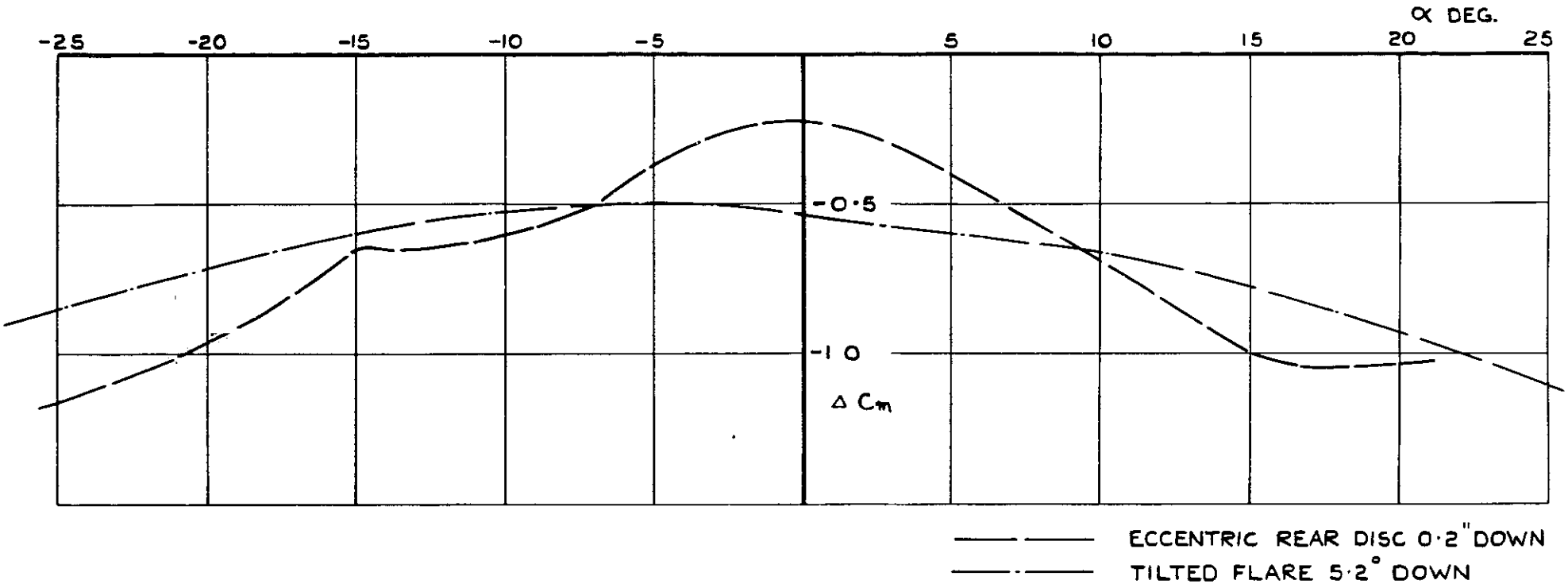

FIG. 80. COMPARISON OF ΔC_m VARIATION WITH α BETWEEN ECCENTRIC REAR DISC AND TILTED FLARE AT CORRESPONDING SETTINGS

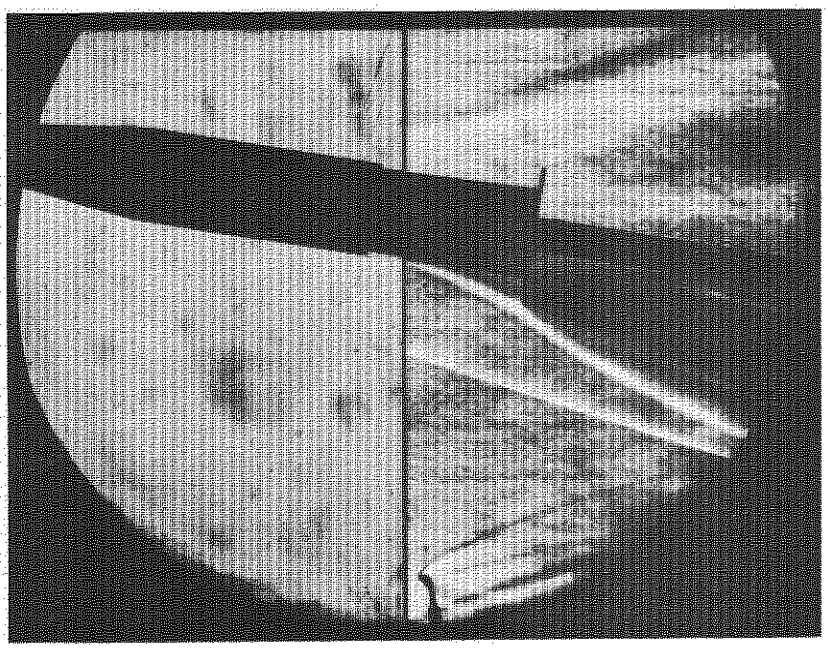

(a) $\alpha = 8^{\circ}$

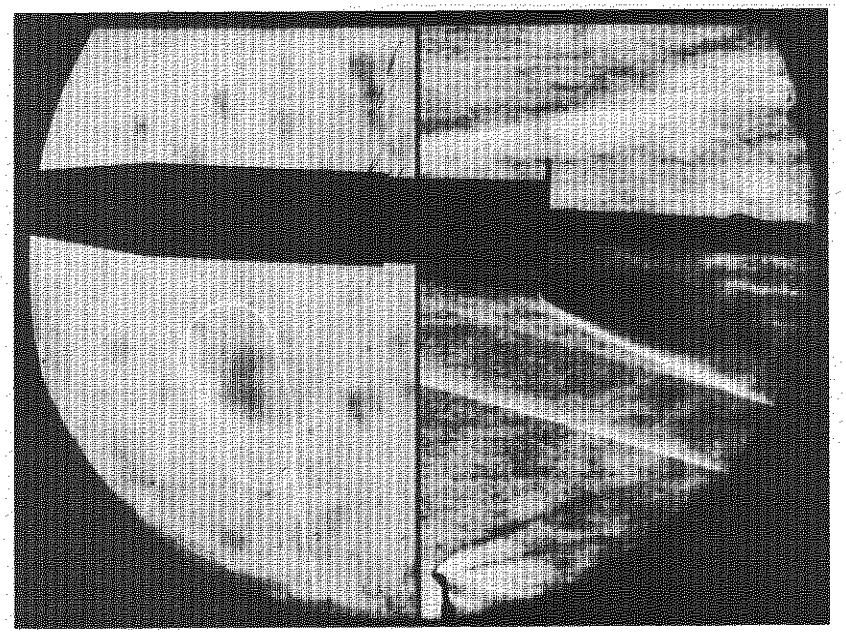

(b) $\alpha = 2^{\circ}$

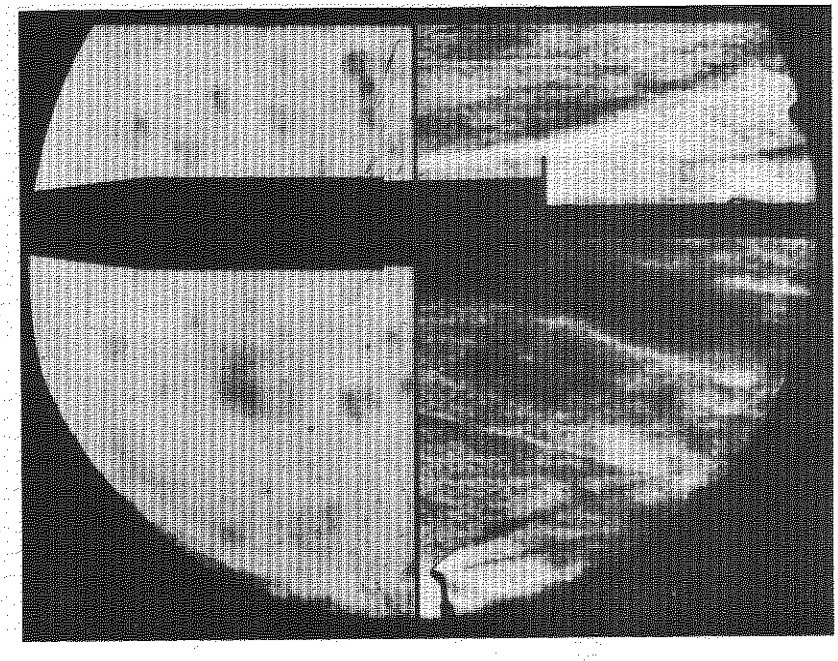

(c) $\alpha = 0^{\circ}$

FIG.81 SCHLIEREN PHOTOGRAPHS OF MODEL WITH REAR DISC CONTROL AT $\alpha = 0^{\circ}$, 2° AND 8°

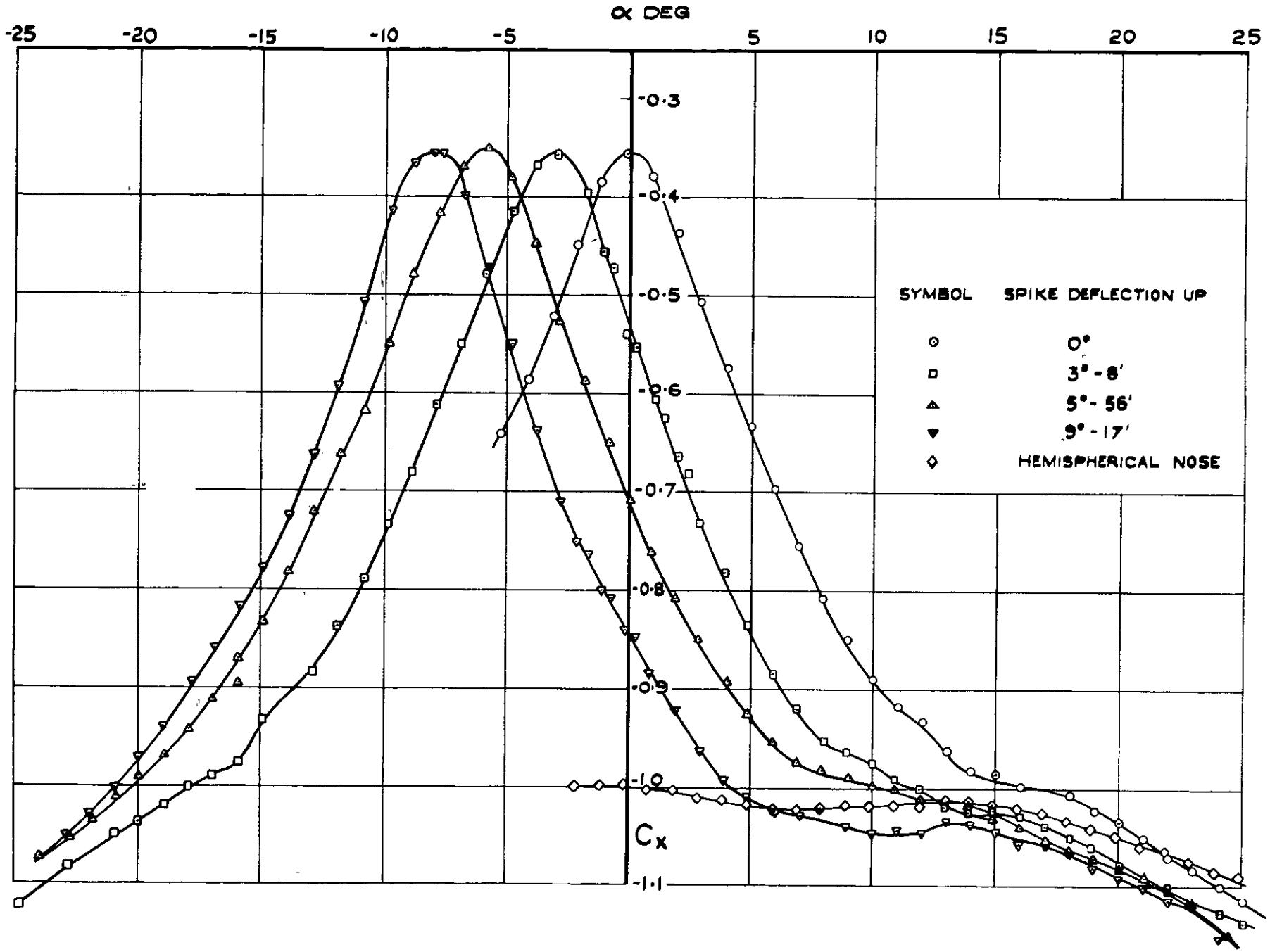

FIG 82 Cx vs α FOR MODEL WITH SPIKE DEFLECTED IN INCIDENCE PLANE.

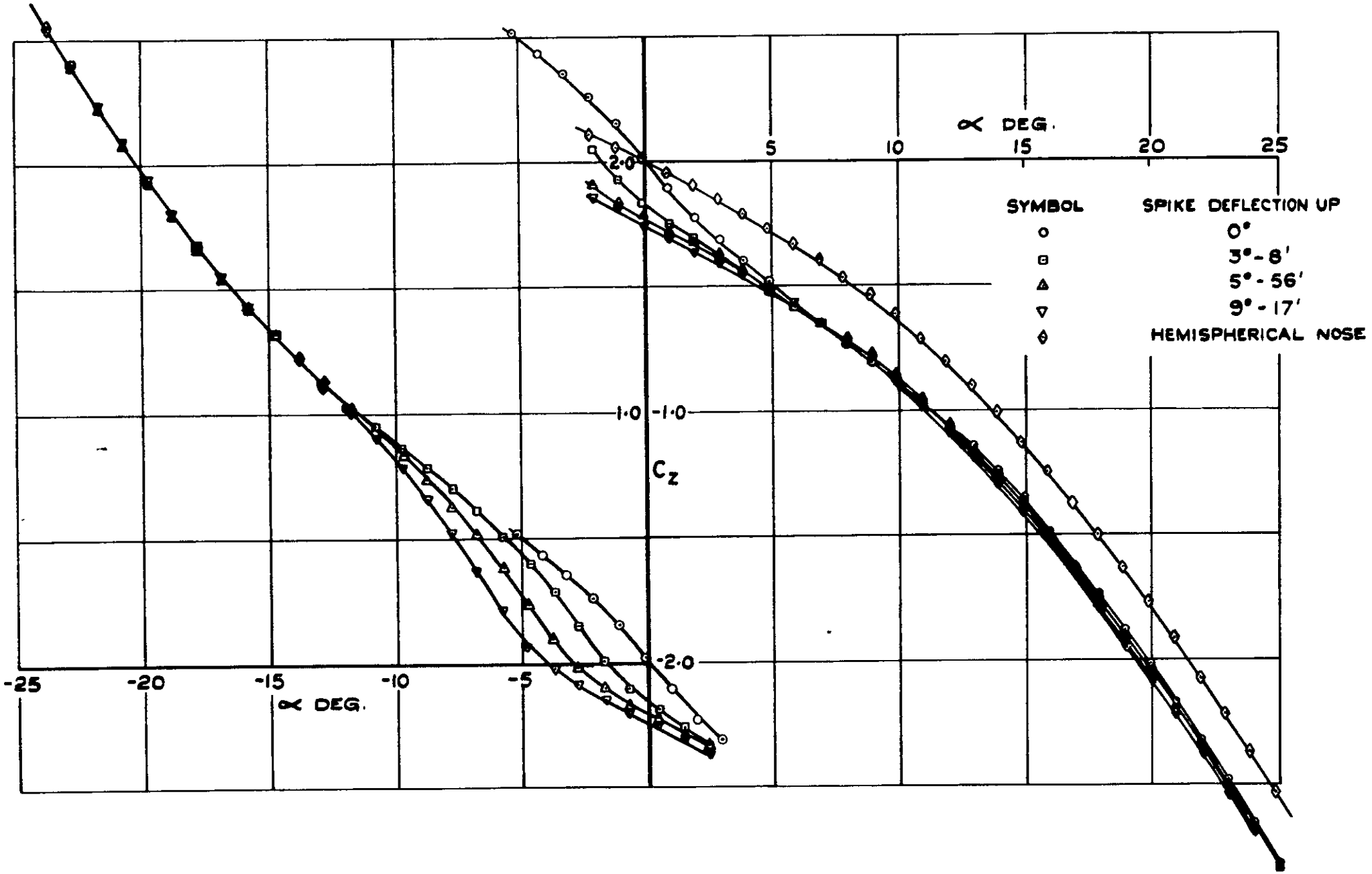

FIG. 83. Cz vs α FOR MODEL WITH SPIKE DEFLECTED IN INCIDENCE PLANE.

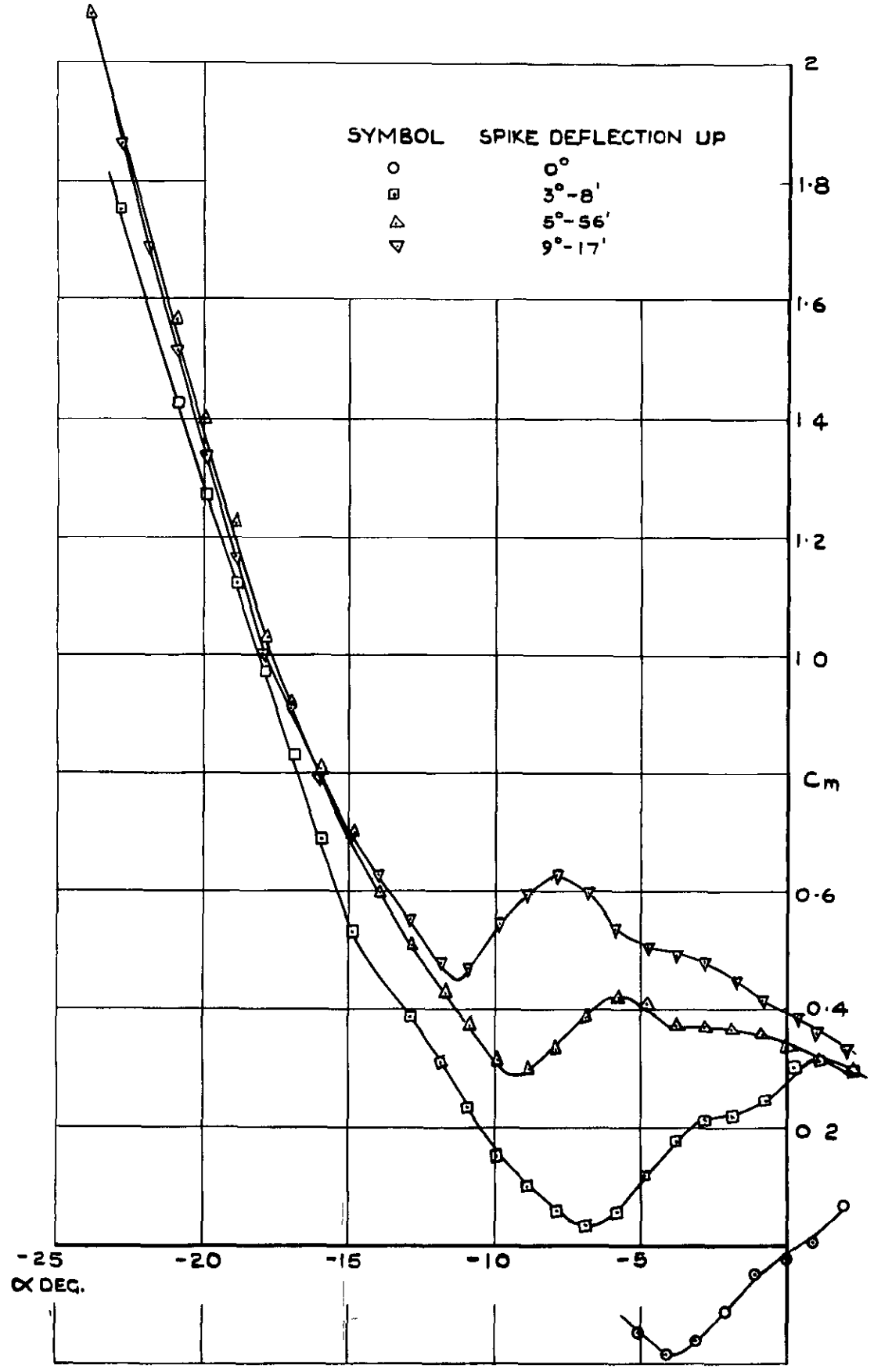

FIG. 84. Cm vs ∝ FOR MODEL WITH SPIKE DEFLECTED IN INCIDENCE PLANE (a) ∝ -VE.

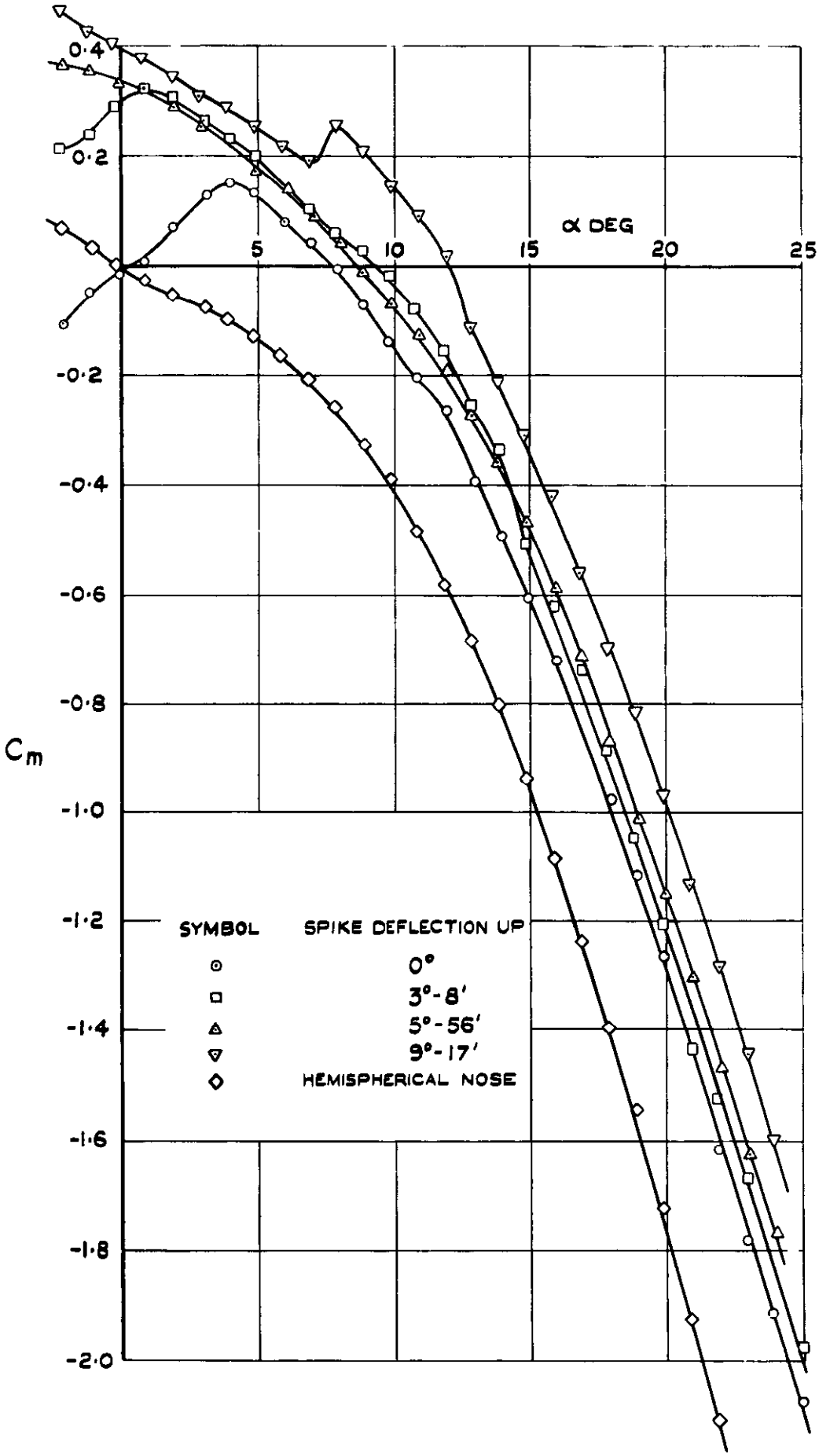

FIG. 84. (contd) C_m vs α FOR MODEL WITH SPIKE DEFLECTED IN INCIDENCE PLANE (b) α + VE.

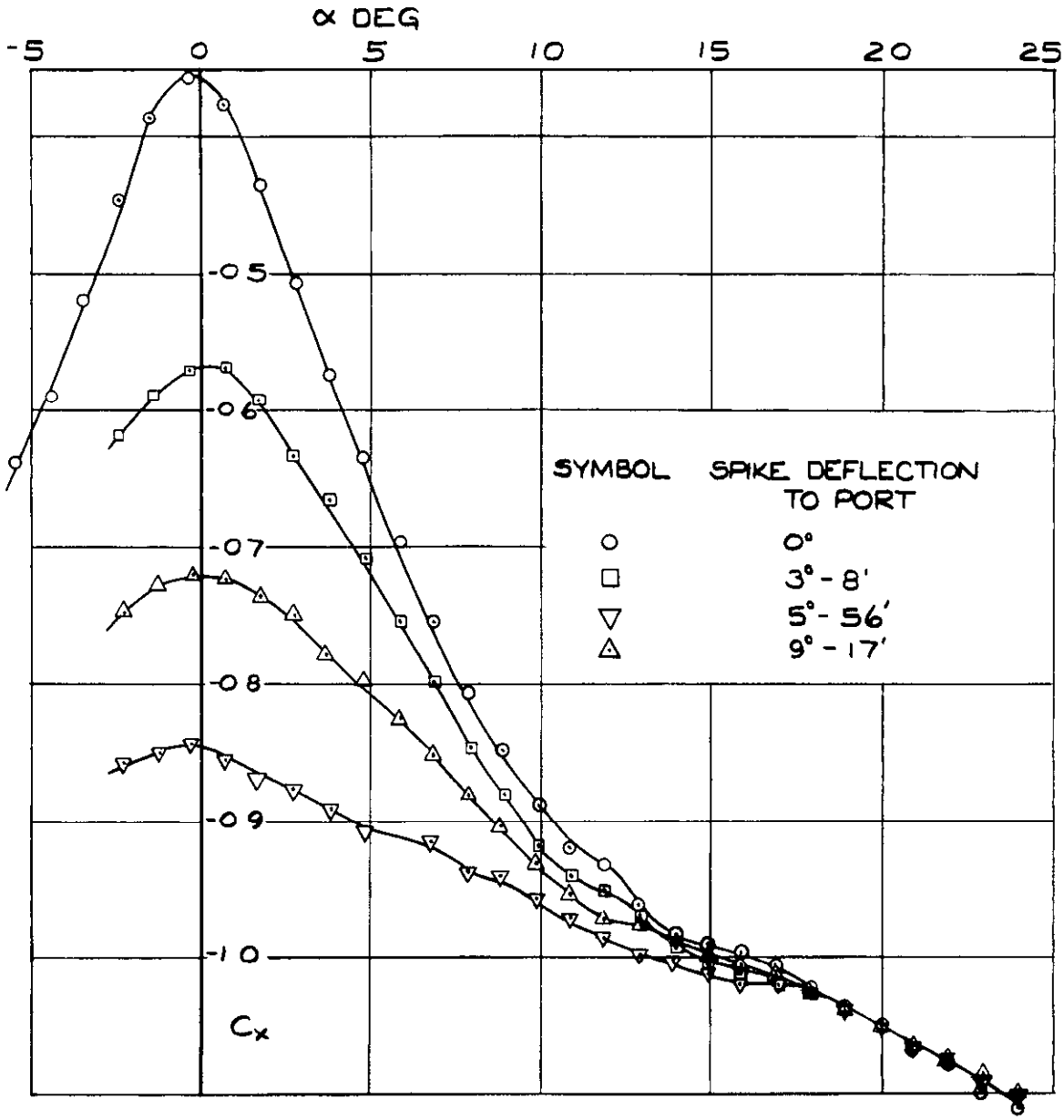

FIG.85. C_X vs α FOR MODEL WITH SPIKE DEFLECTED NORMAL TO INCIDENCE PLANE

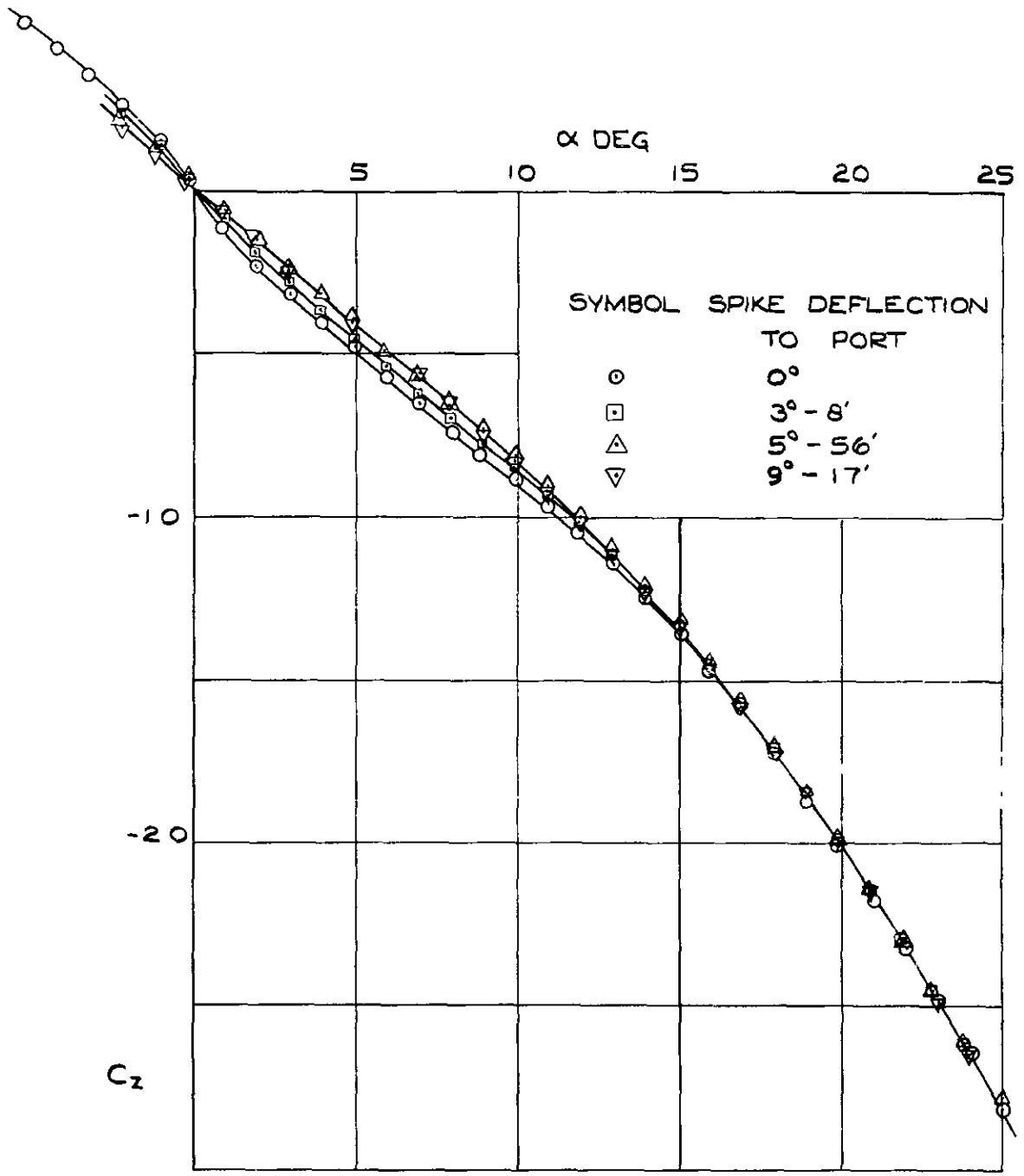

FIG. 86. C_z vs α FOR MODEL WITH SPIKE DEFLECTED NORMAL TO INCIDENCE PLANE

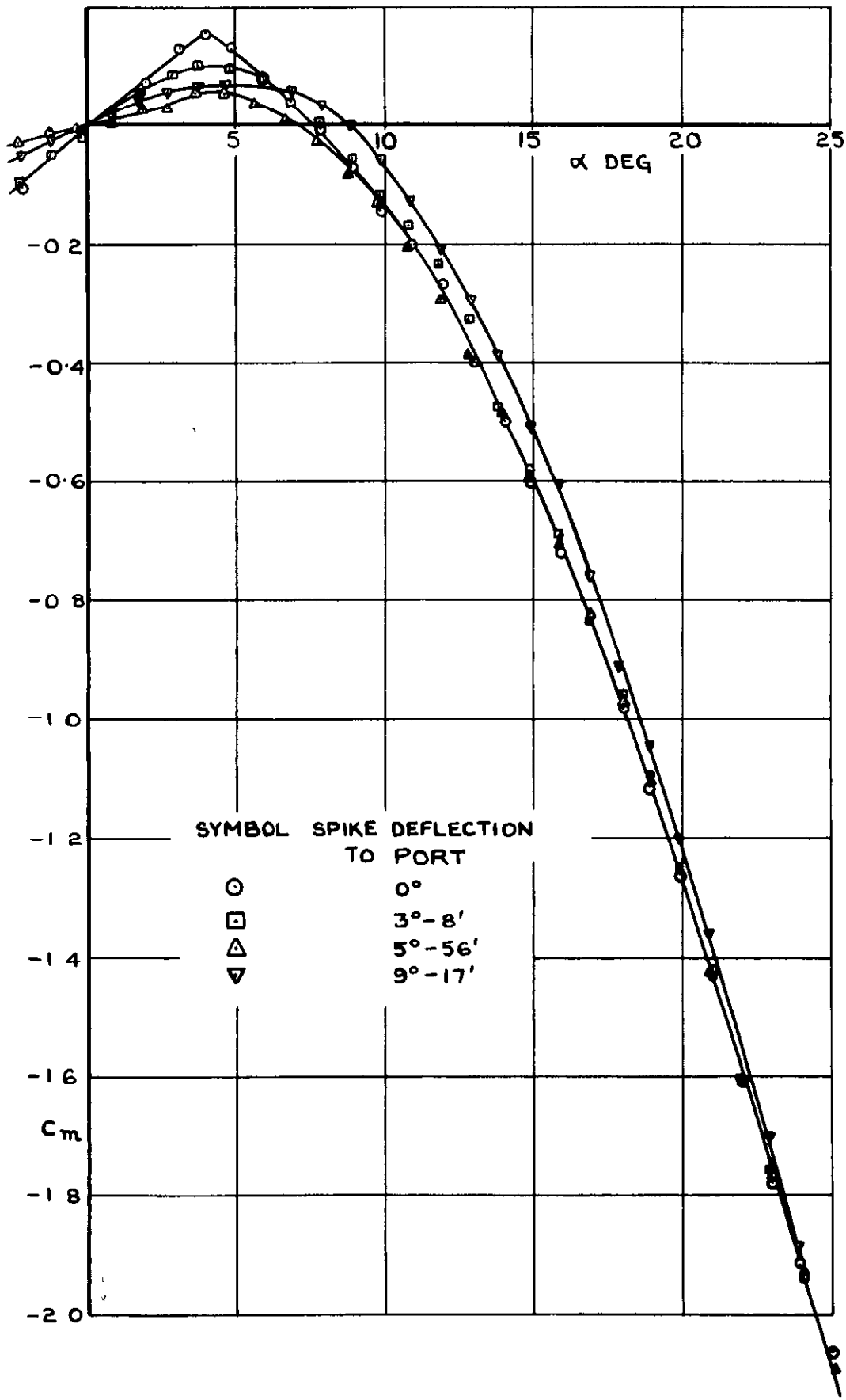

FIG. 87. C_m vs α FOR MODEL WITH SPIKE DEFLECTED NORMAL TO INCIDENCE PLANE.

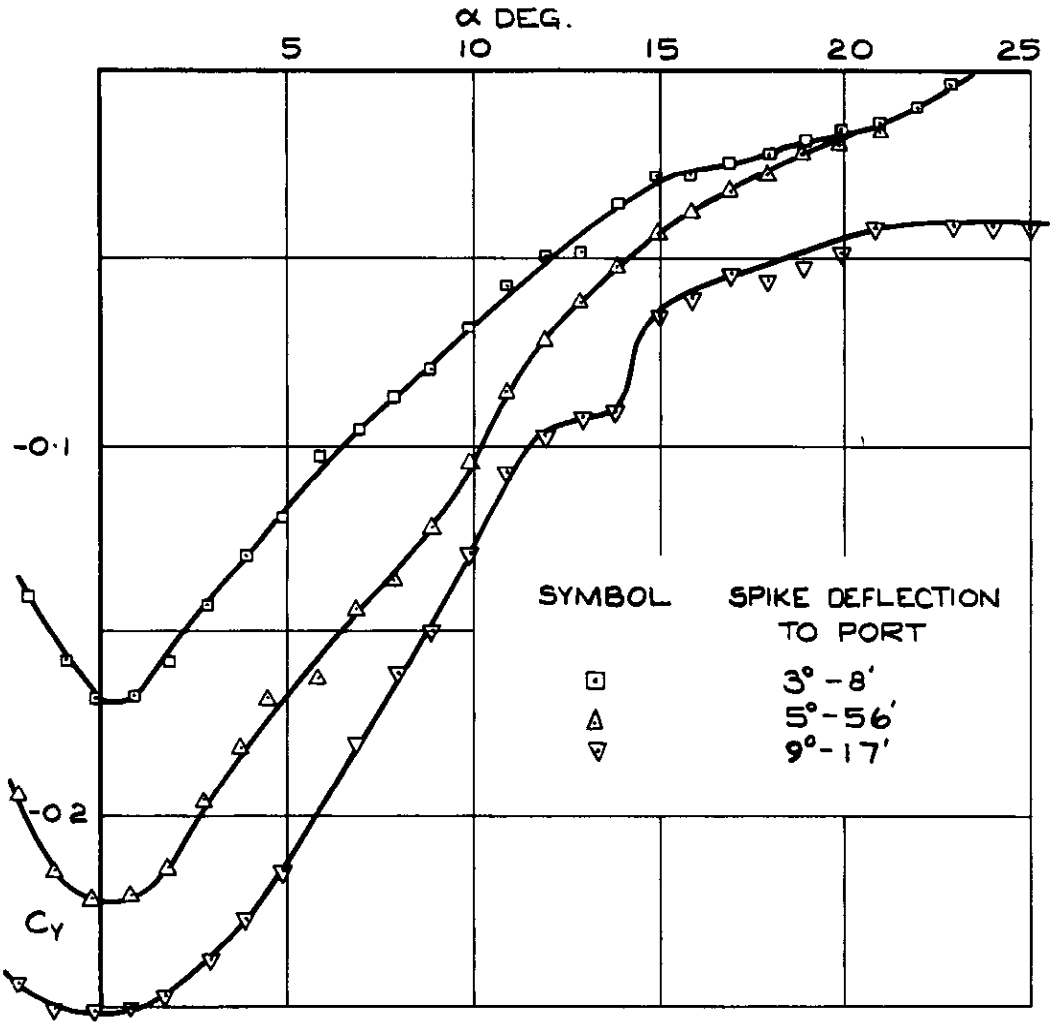

FIG.88. Cy vs α FOR MODEL WITH SPIKE DEFLECTED NORMAL TO INCIDENCE PLANE

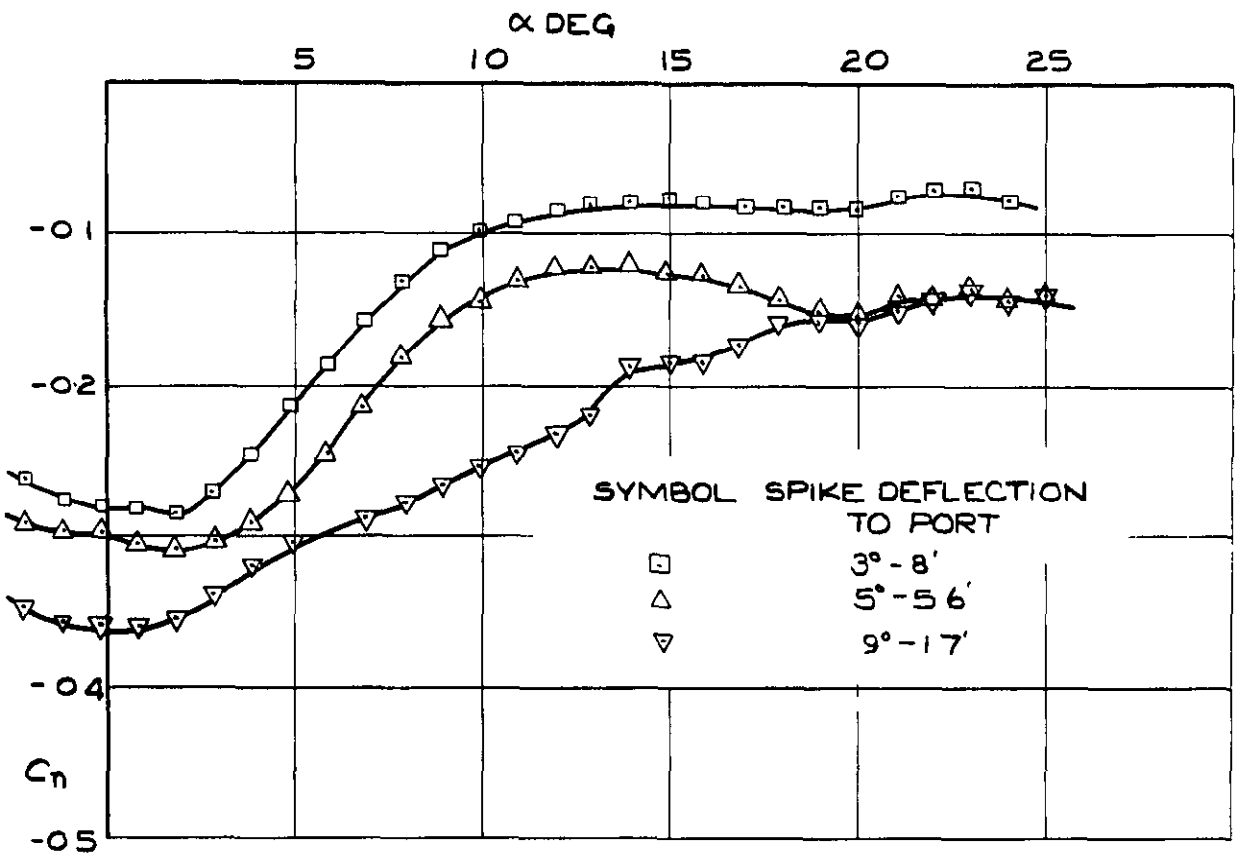

FIG. 89. C_n vs α FOR MODEL WITH SPIKE DEFLECTED NORMAL TO INCIDENCE PLANE

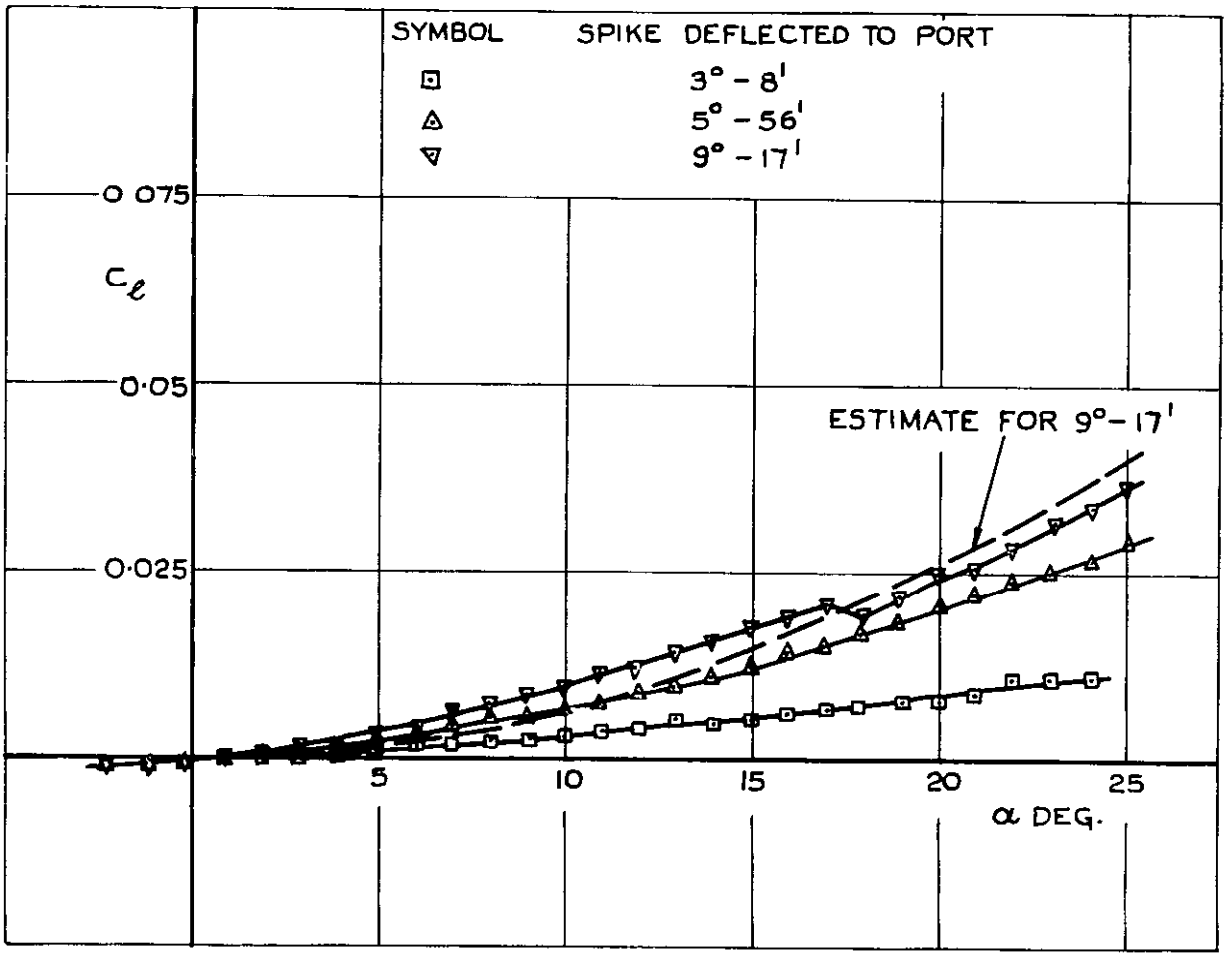

FIG. 90. C_ℓ vs α FOR MODEL WITH SPIKE DEFLECTED NORMAL TO INCIDENCE PLANE.

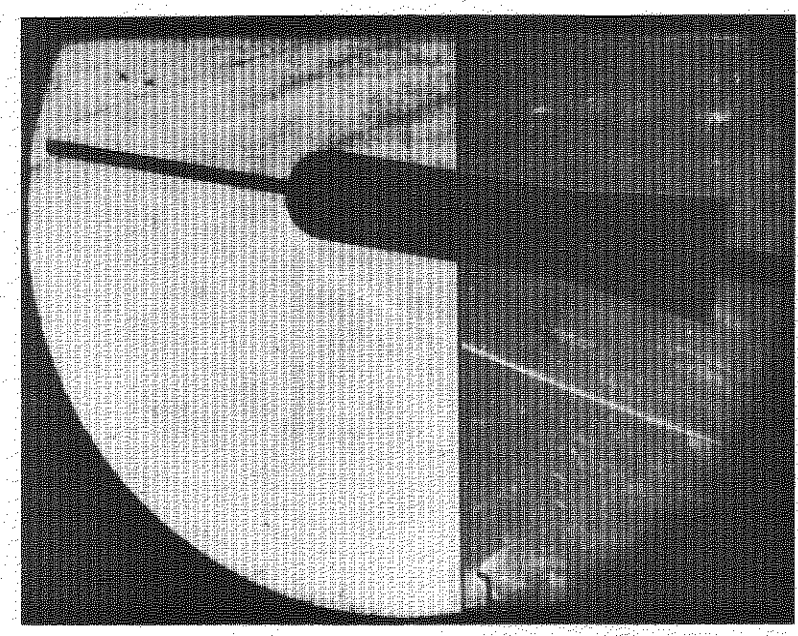

(a) $\alpha = 10^{\circ}$

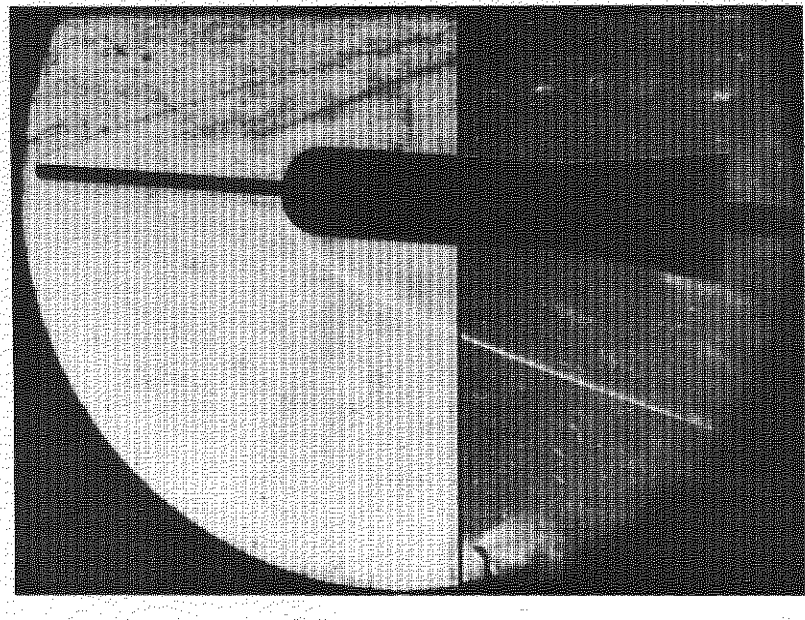

(b) $\alpha = 4^{\circ}$

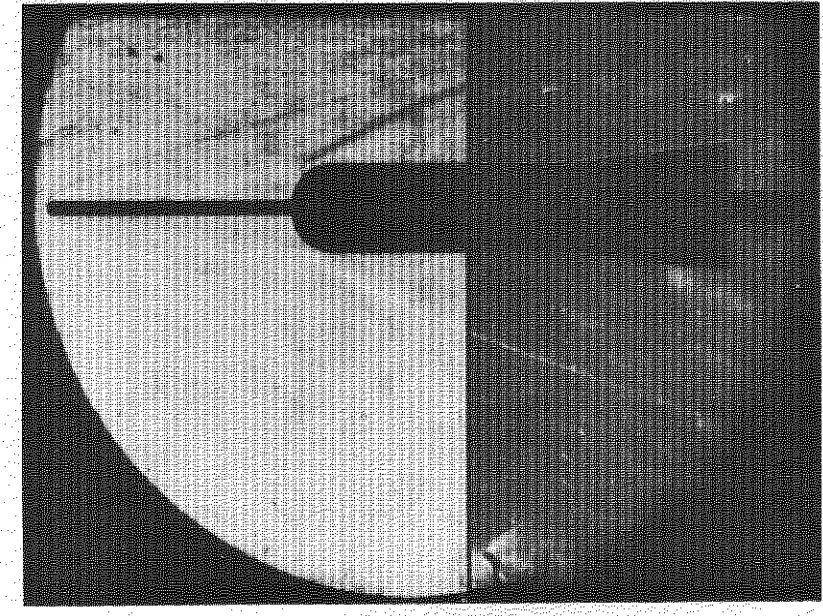

(c) $\alpha = 0^{\circ}$

FIG. 91 SCHLIEREN PHOTOGRAPHS OF SPIKE NOSED MODEL AT $\alpha = 0^{\circ}$, 4° AND 10°, $\eta = 0^{\circ}$

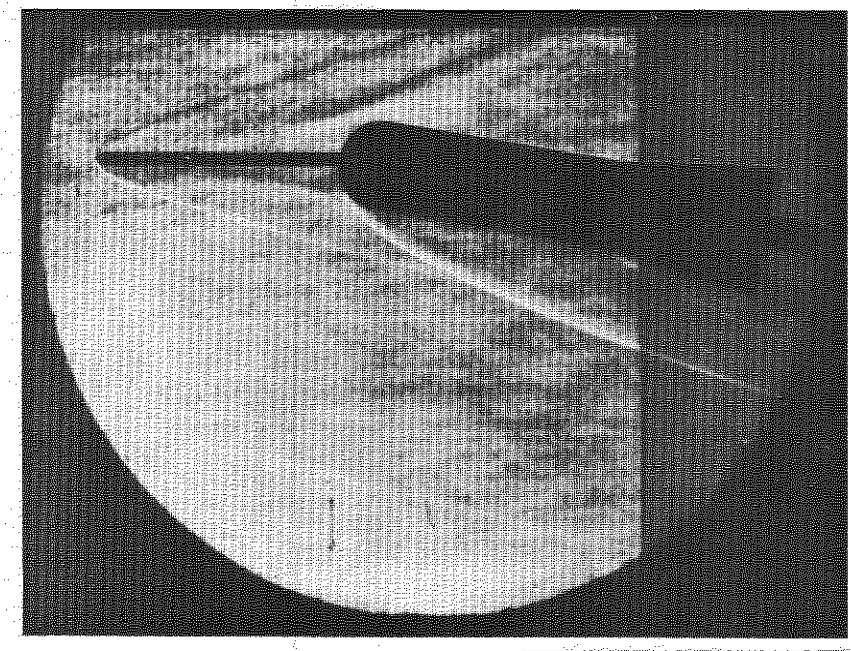

(a) $\eta = -9^{o}\ -17'$, $\alpha = 10^{o}$

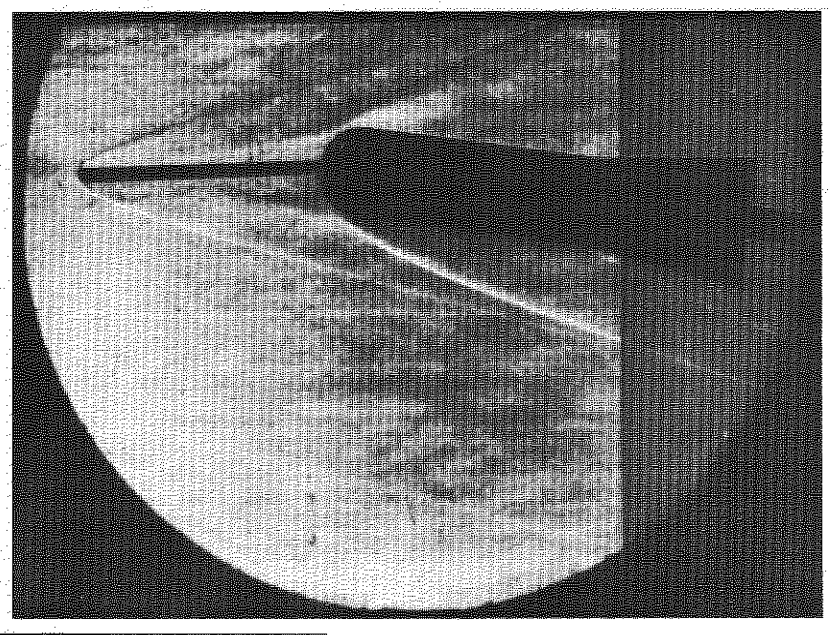

(b) $\eta = -9^{o}\ -17'$, $\alpha = 8^{o}$

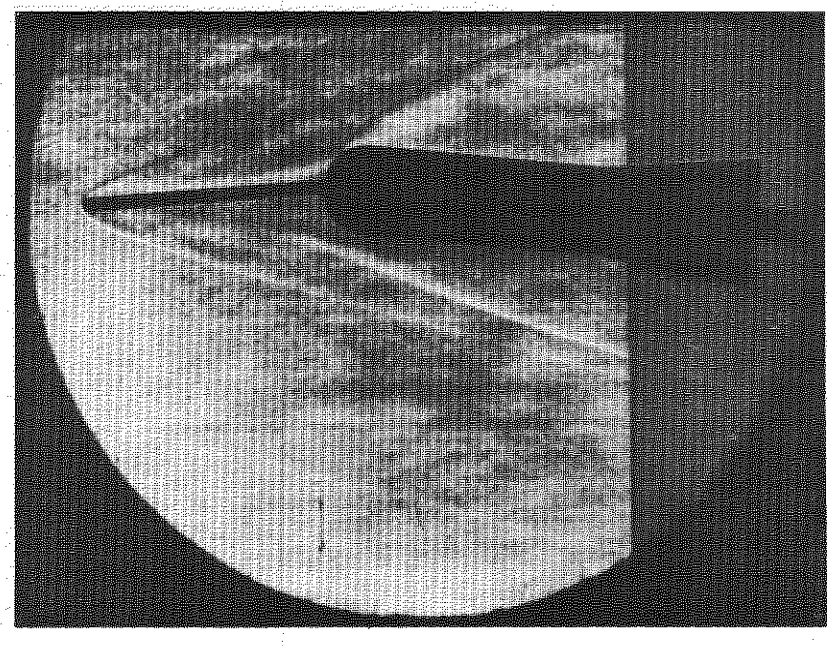

(c) $\eta = -9^{o}\ -17'$, $\alpha = 6^{o}$

FIG.92 SCHLIEREN PHOTOGRAPHS OF MODEL WITH SPIKE AT $\eta = -9^{o}\ -17'$, $\alpha = 6^{o}$, 8^{o} AND 10^{o}

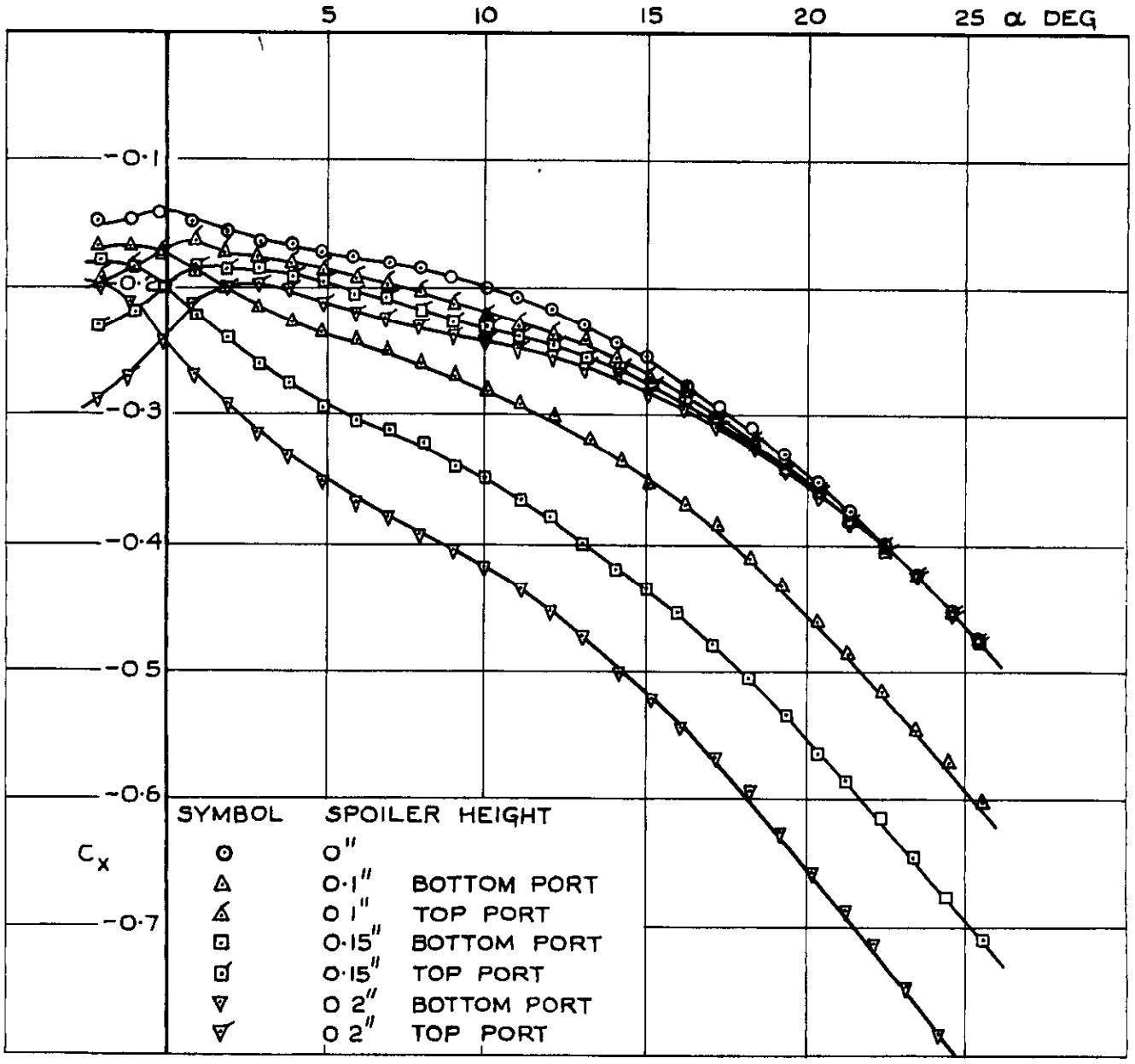

FIG.93. C_x vs α FOR MODEL WITH SWEPT SPOILER EXTENDED IN INCIDENCE PLANE.

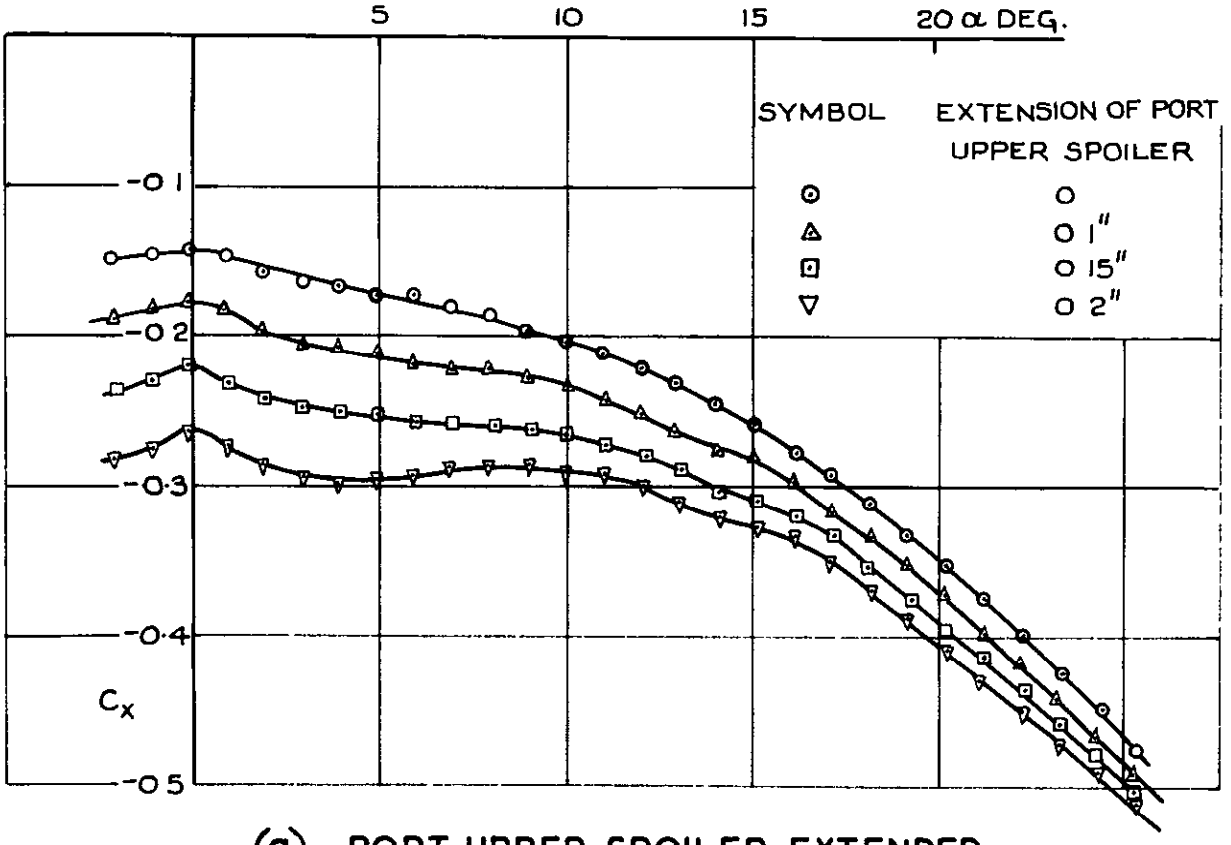

(a) PORT UPPER SPOILER EXTENDED.

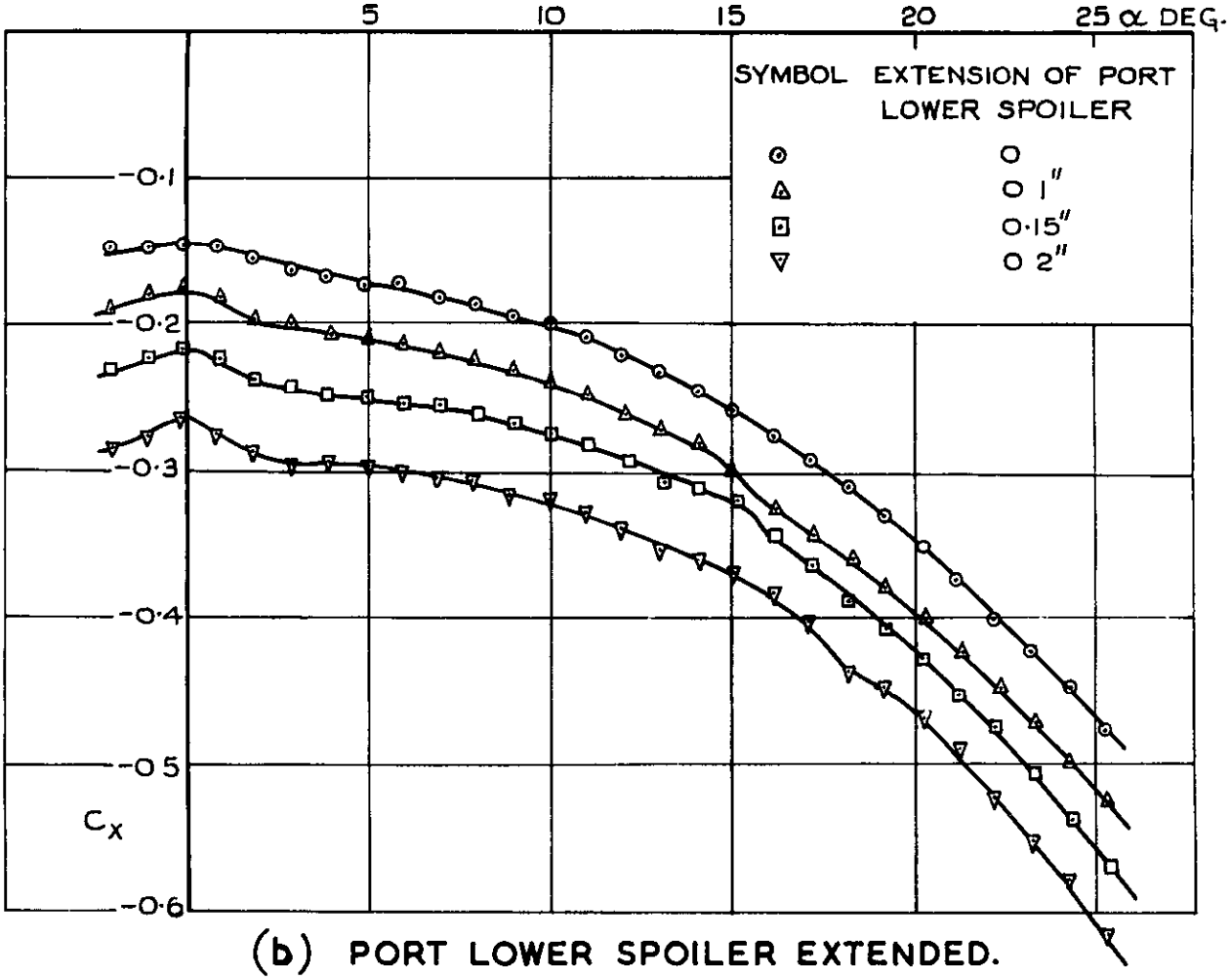

(b) PORT LOWER SPOILER EXTENDED.

FIG.94. C_x vs α FOR MODEL WITH SWEPT SPOILER EXTENDED NORMAL TO INCIDENCE PLANE.

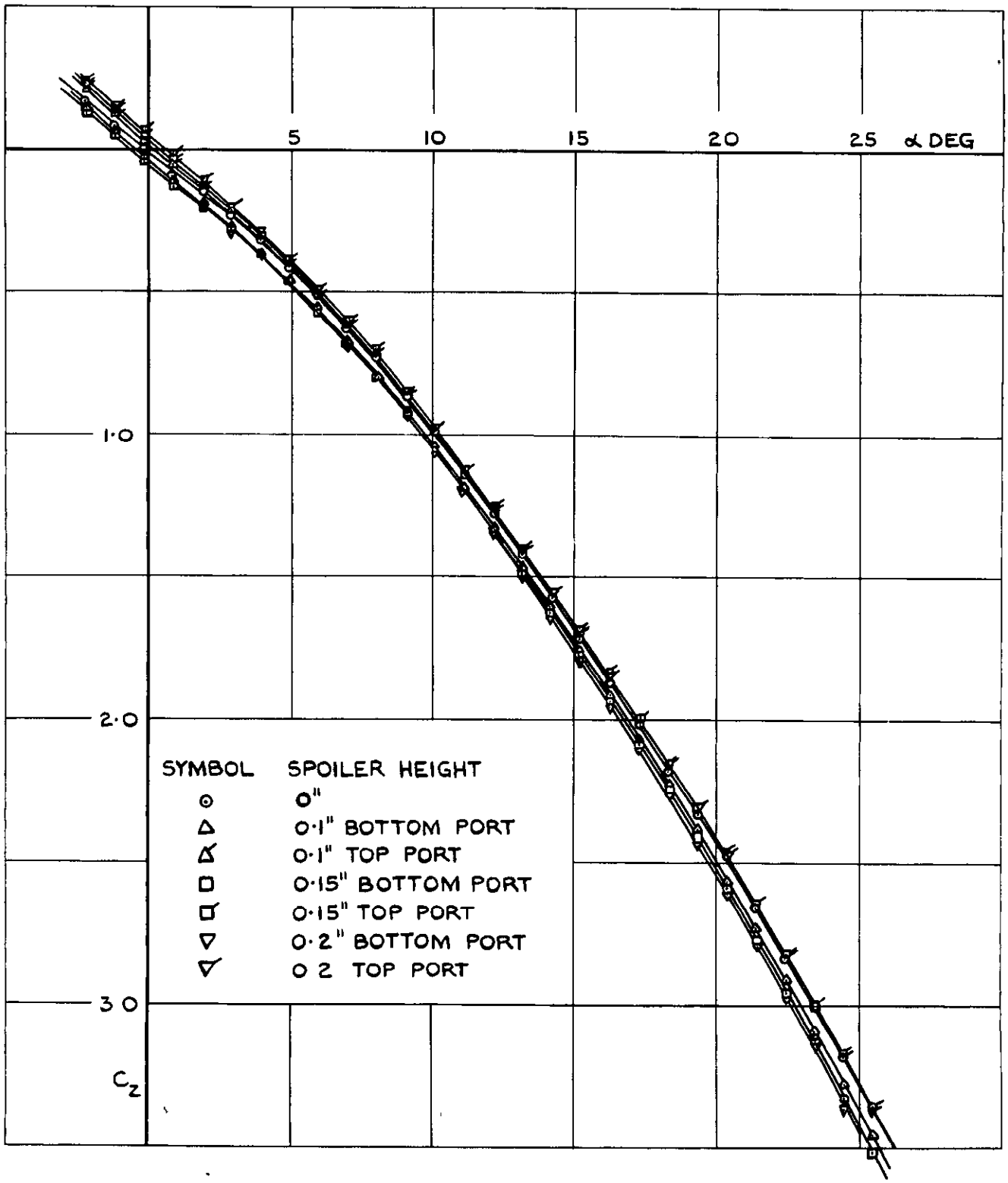

FIG.95. C_z vs α FOR MODEL WITH SWEPT SPOILER EXTENDED IN INCIDENCE PLANE.

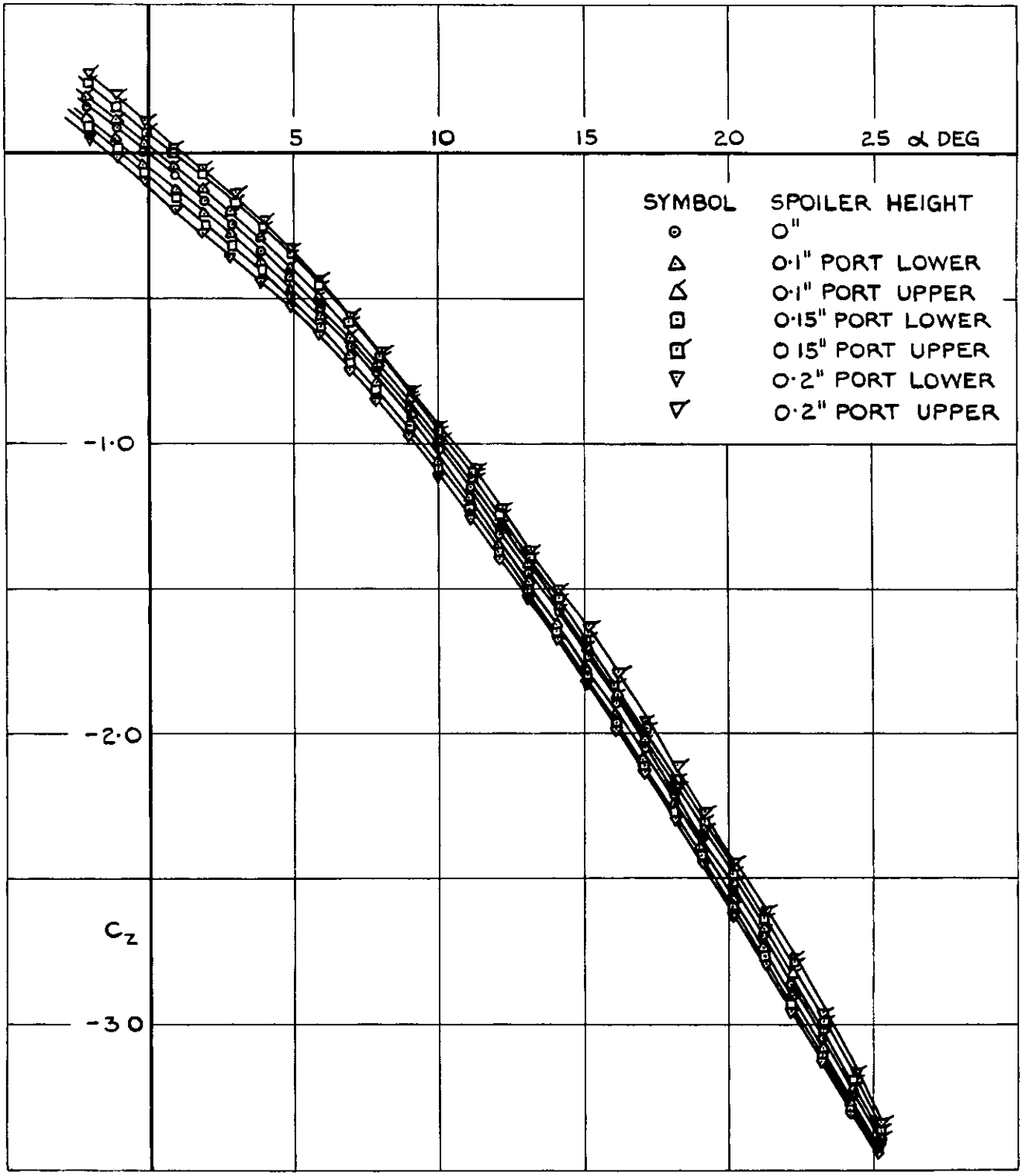

FIG.96. C_z vs α FOR MODEL WITH SWEPT SPOILER EXTENDED NORMAL TO INCIDENCE PLANE.

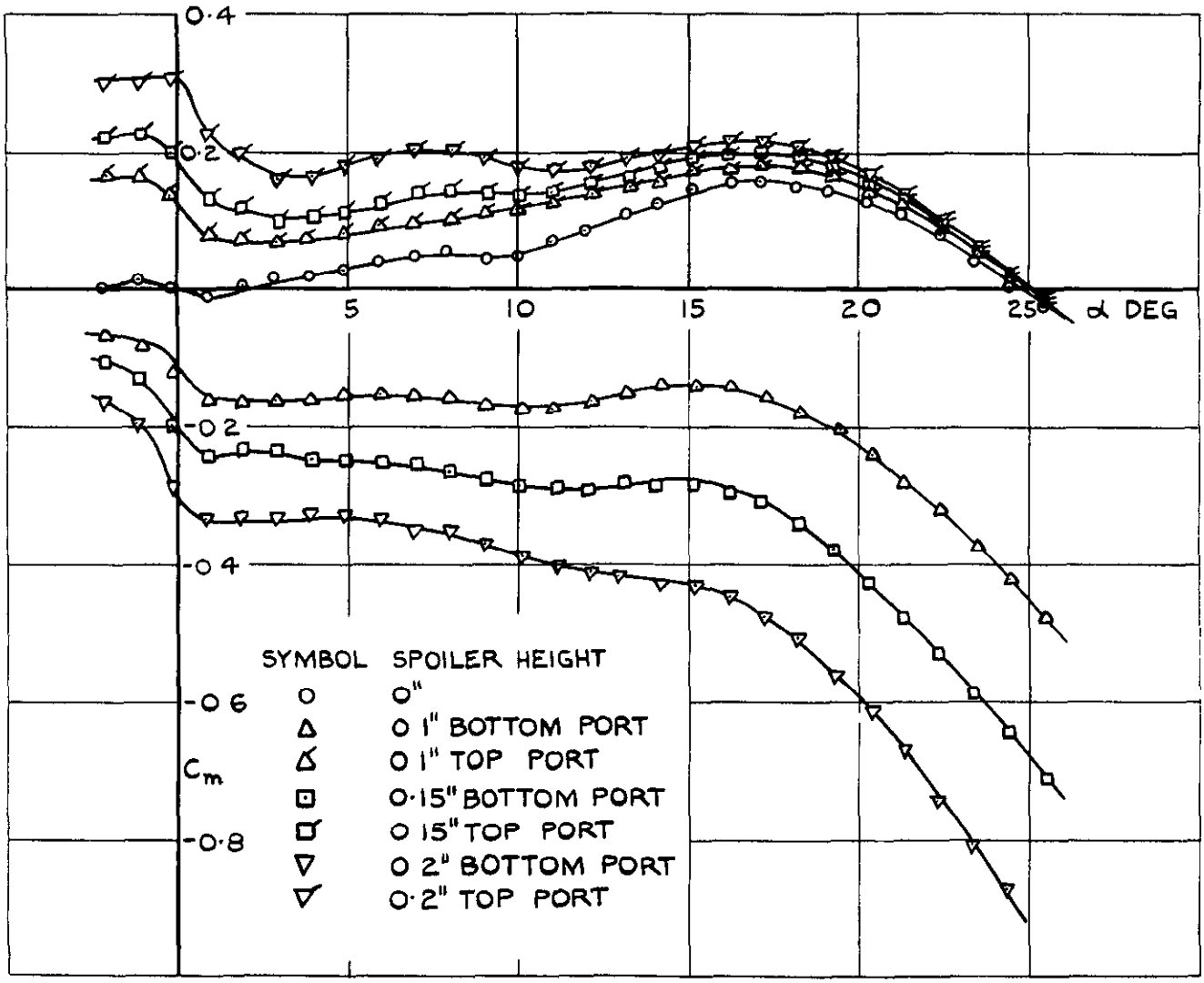

FIG. 97. C_m vs α FOR MODEL WITH SWEPT SPOILER EXTENDED IN INCIDENCE PLANE.

SYMBOL	SPOILER HEIGHT
○	0"
△	0·1" PORT LOWER
◁	0·1" PORT UPPER
□	0·15" PORT LOWER
◻	0·15" PORT UPPER
▽	0·2" PORT LOWER
▽	0·2" PORT UPPER

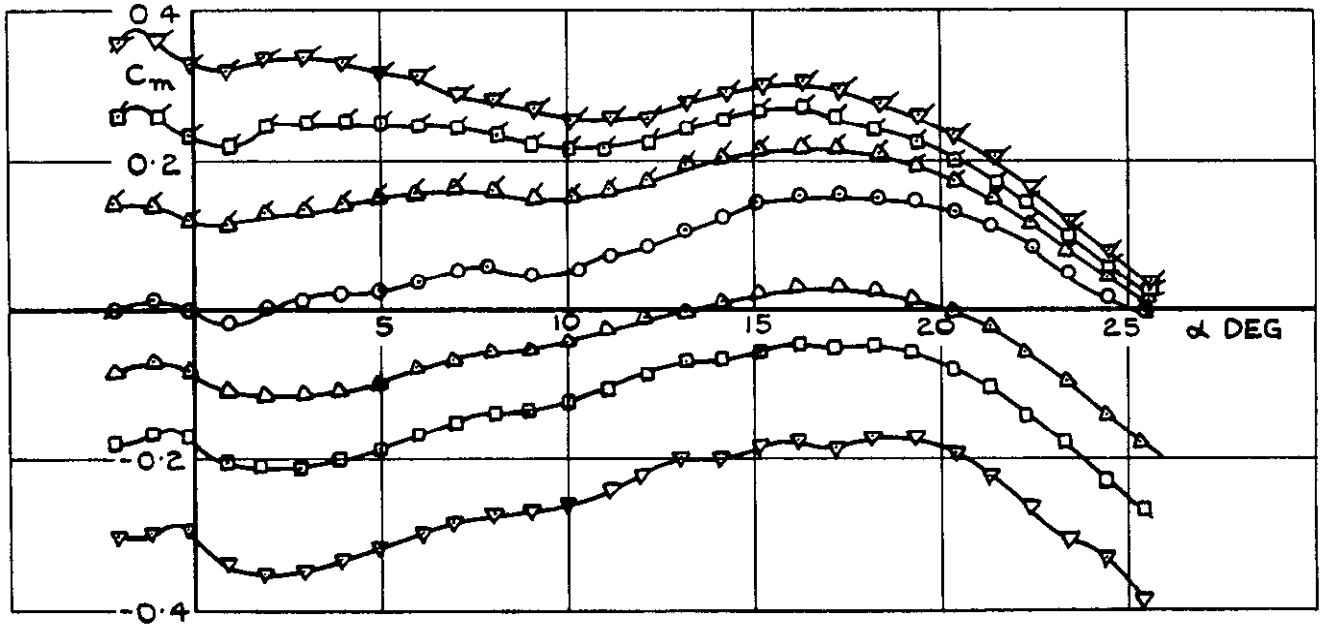

FIG.98 C_m vs α FOR MODEL WITH SWEPT SPOILER EXTENDED NORMAL TO INCIDENCE PLANE.

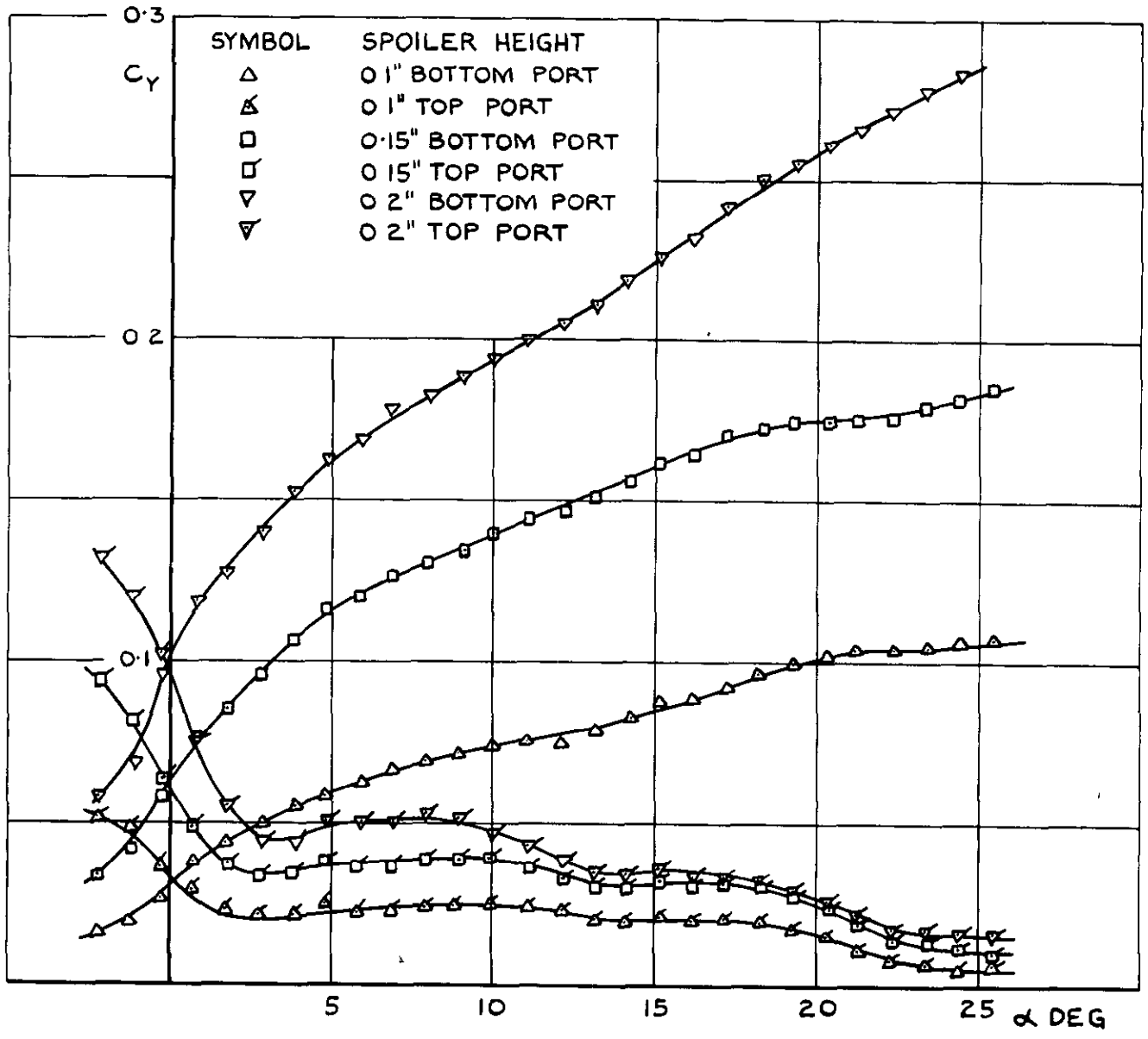

FIG. 99. C_Y vs α FOR MODEL WITH SWEPT SPOILER EXTENDED IN INCIDENCE PLANE.

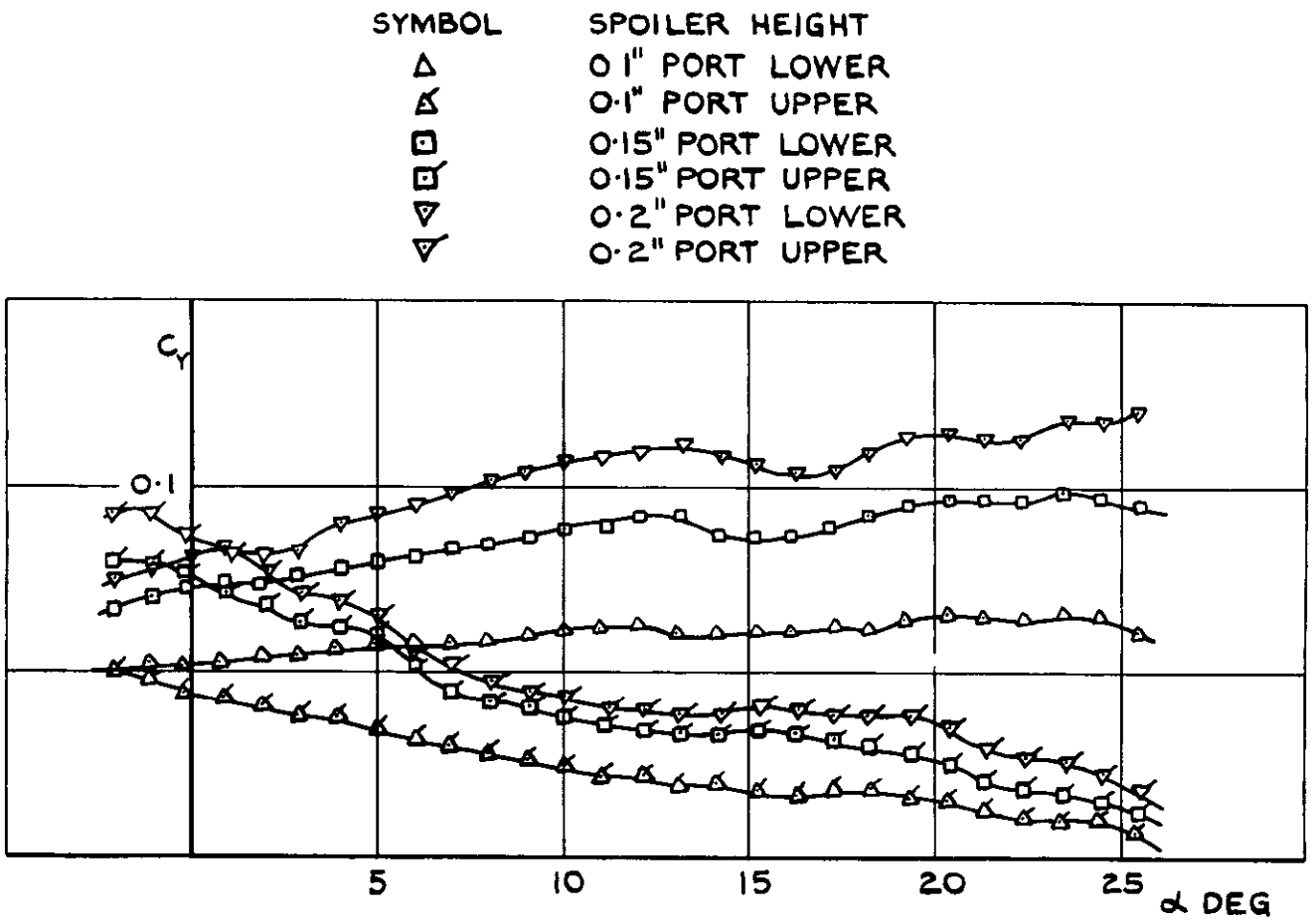

FIG. 100. C_Y vs α FOR MODEL WITH SWEPT SPOILER EXTENDED NORMAL TO INCIDENCE PLANE.

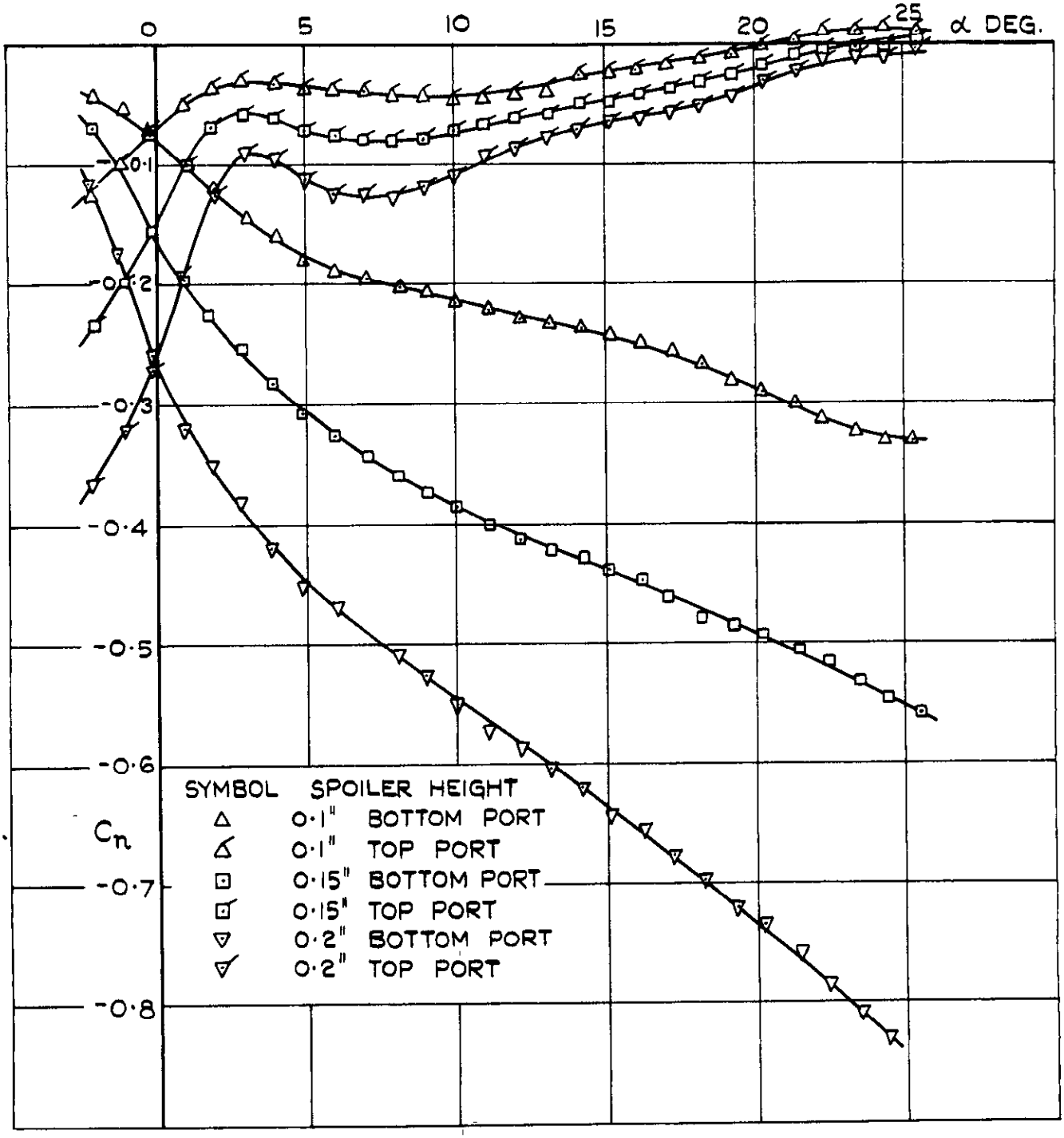

FIG. 101. C_n vs α FOR MODEL WITH SWEPT SPOILER EXTENDED IN INCIDENCE PLANE.

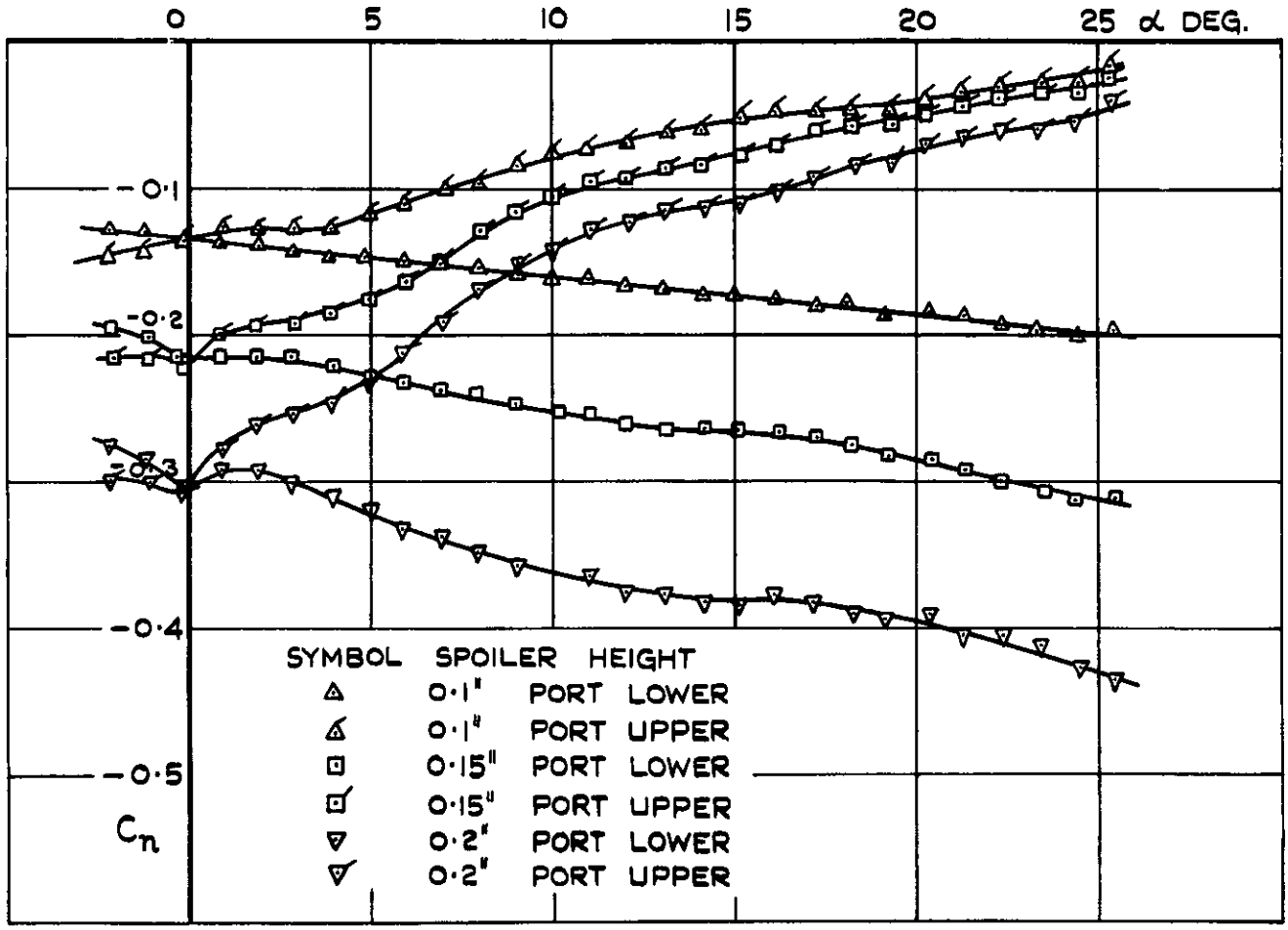

FIG. 102. C_n vs α FOR MODEL WITH SWEPT SPOILER EXTENDED NORMAL TO INCIDENCE PLANE.

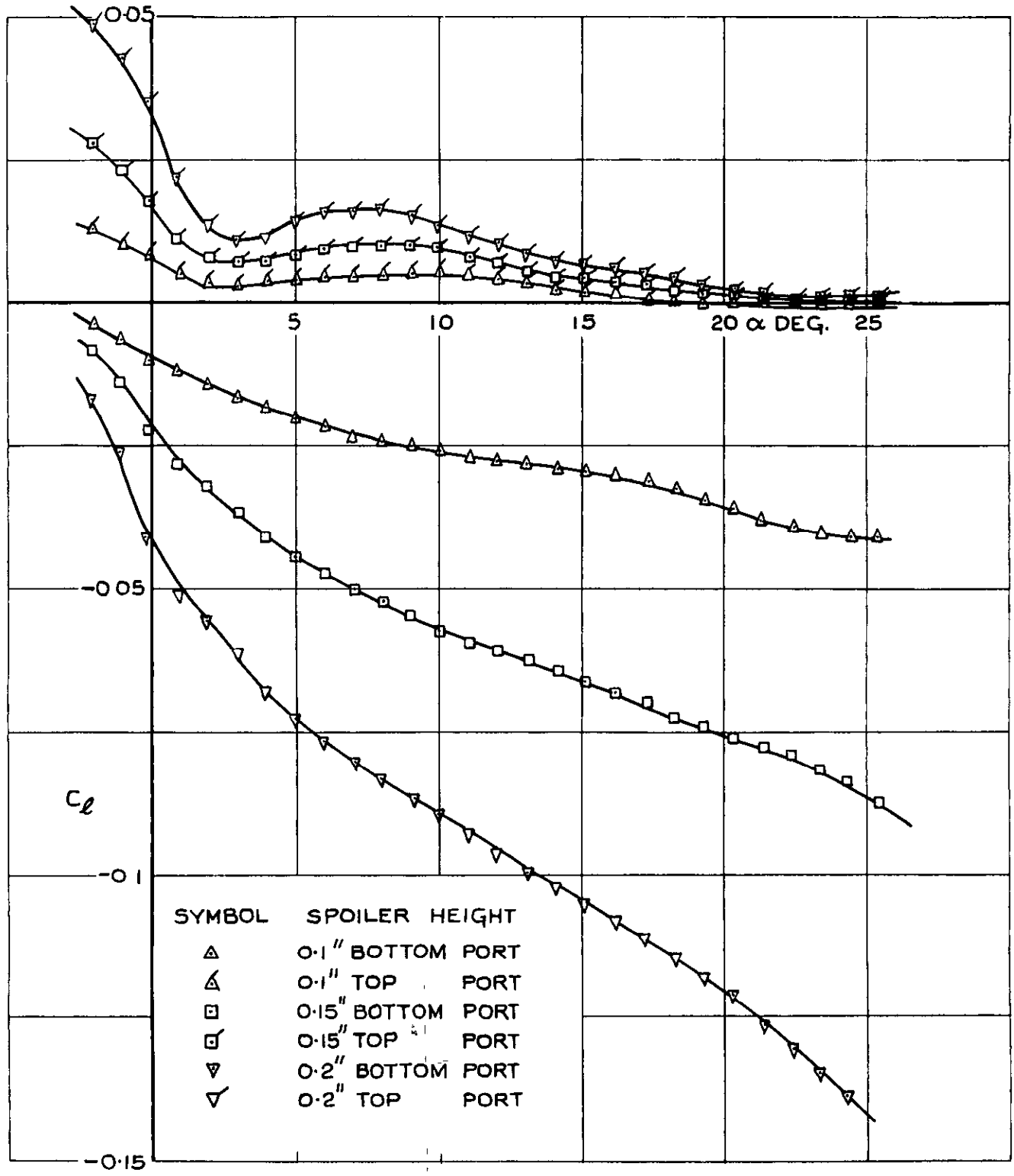

FIG.103. C_ℓ vs α FOR MODEL WITH SWEPT SPOILER EXTENDED IN INCIDENCE PLANE.

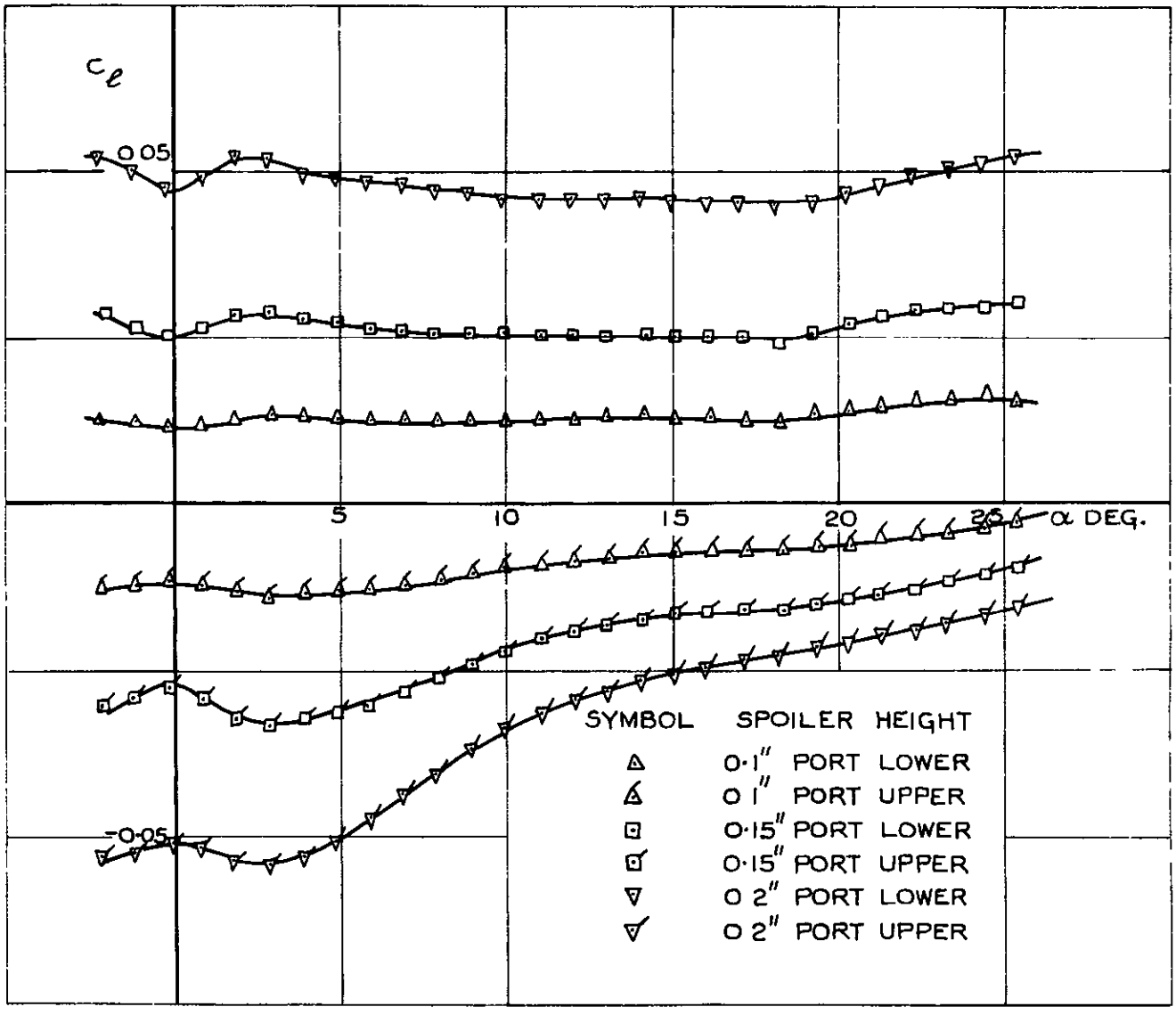

FIG.104. C_ℓ vs α FOR MODEL WITH SWEPT SPOILER EXTENDED NORMAL TO INCIDENCE PLANE.

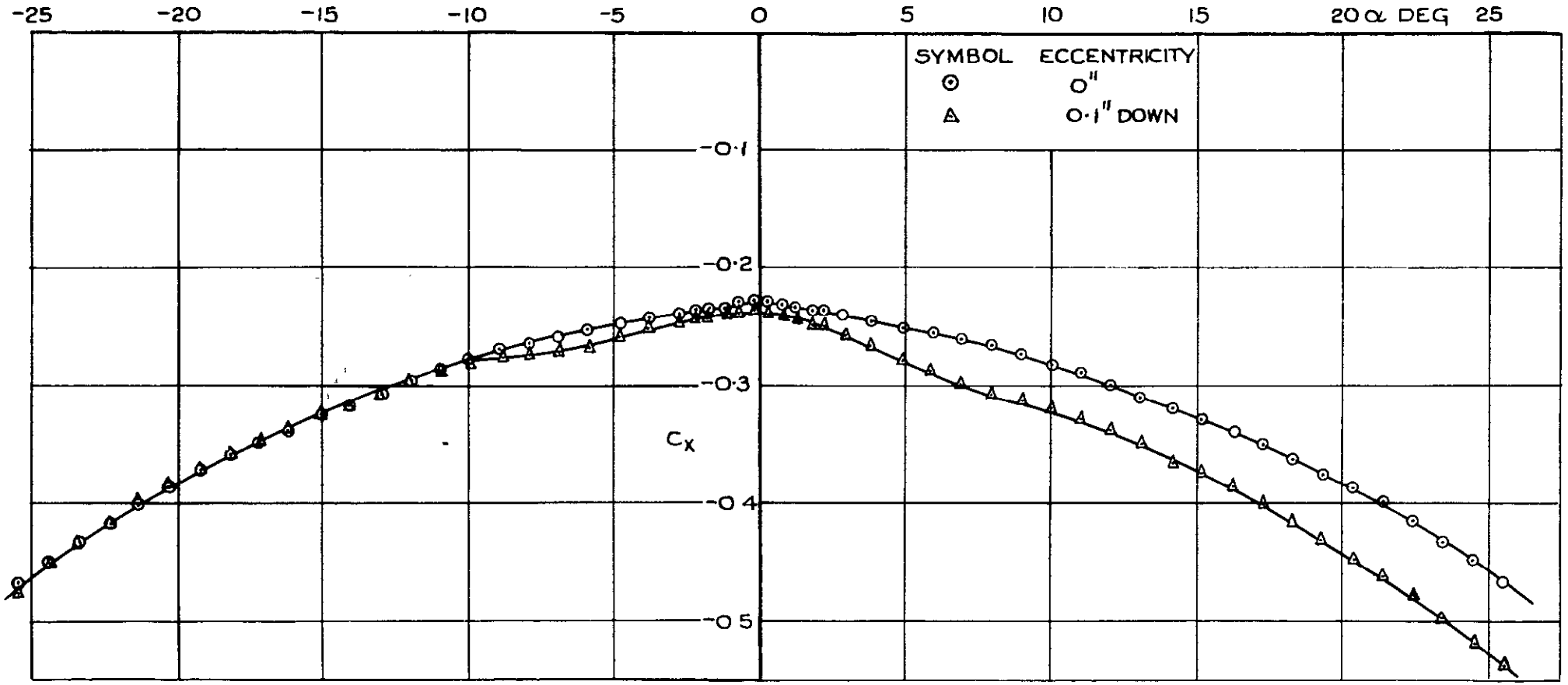

FIG.105. C_X vs α FOR MODEL WITH ECCENTRIC RING CONTROL ACTING IN INCIDENCE PLANE.

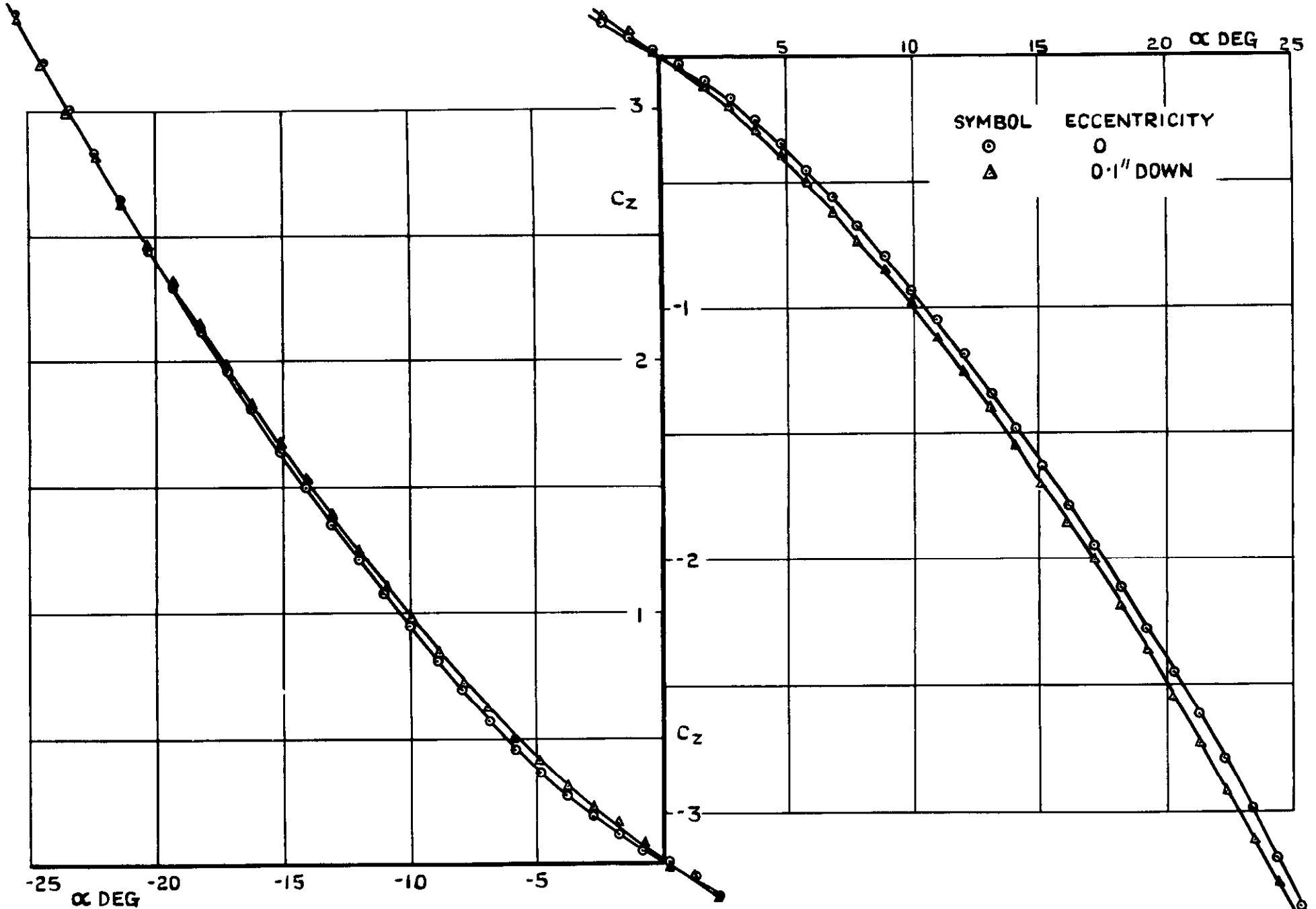

FIG.106. C_Z VS α FOR MODEL WITH ECCENTRIC RING CONTROL ACTING IN INCIDENCE PLANE.

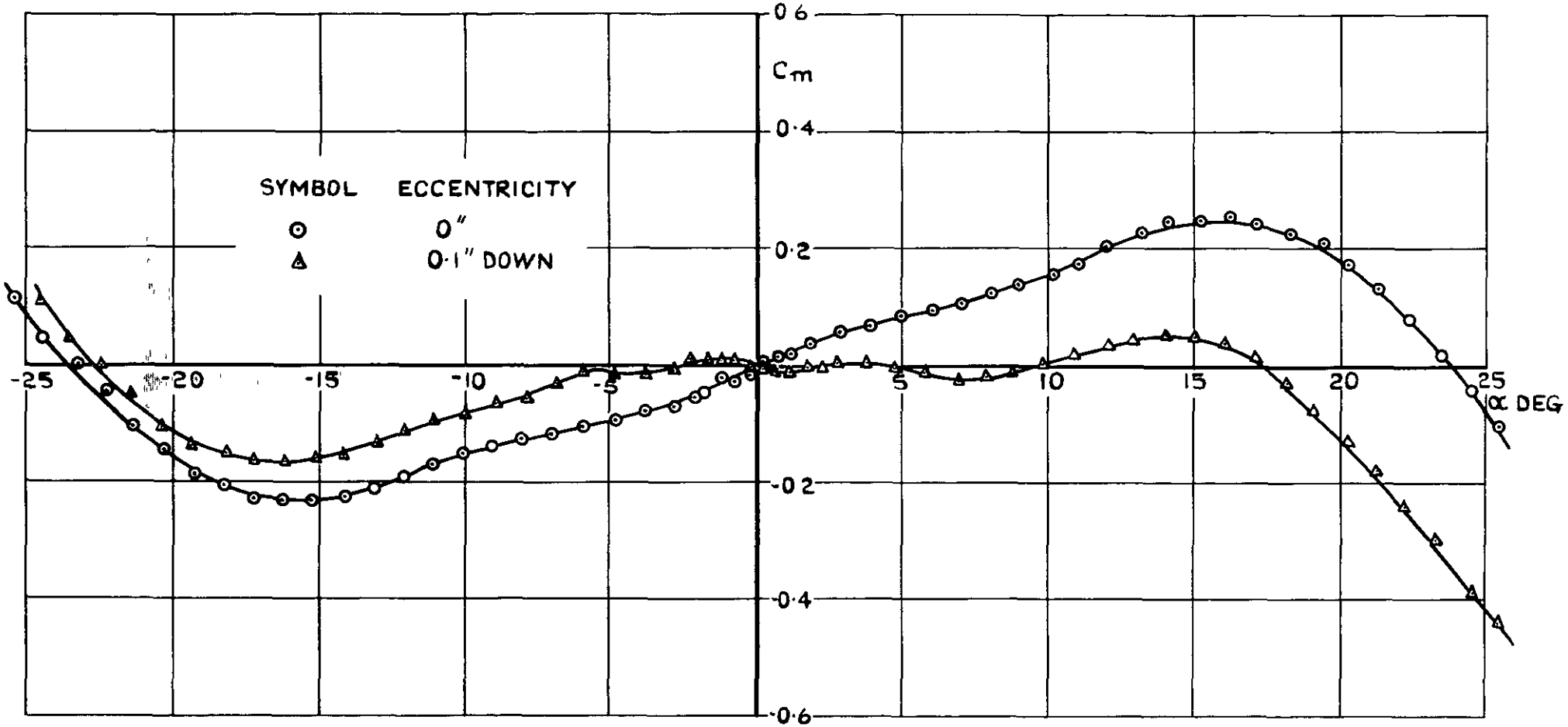

FIG. 107. C_m vs α FOR MODEL WITH ECCENTRIC RING CONTROL ACTING IN INCIDENCE PLANE.

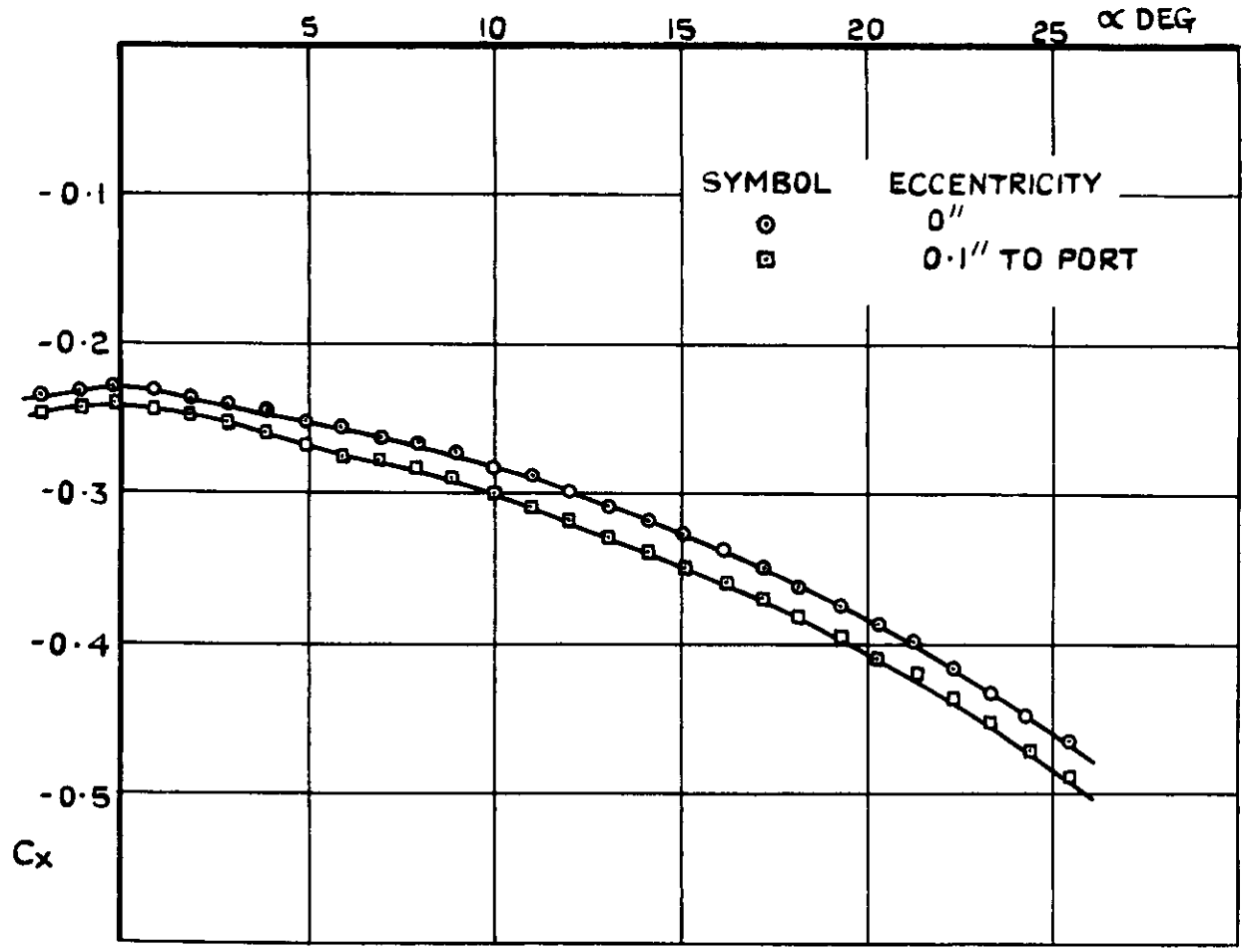

FIG.108. C_X VS α FOR MODEL WITH ECCENTRIC RING CONTROL ACTING NORMAL TO INCIDENCE PLANE.

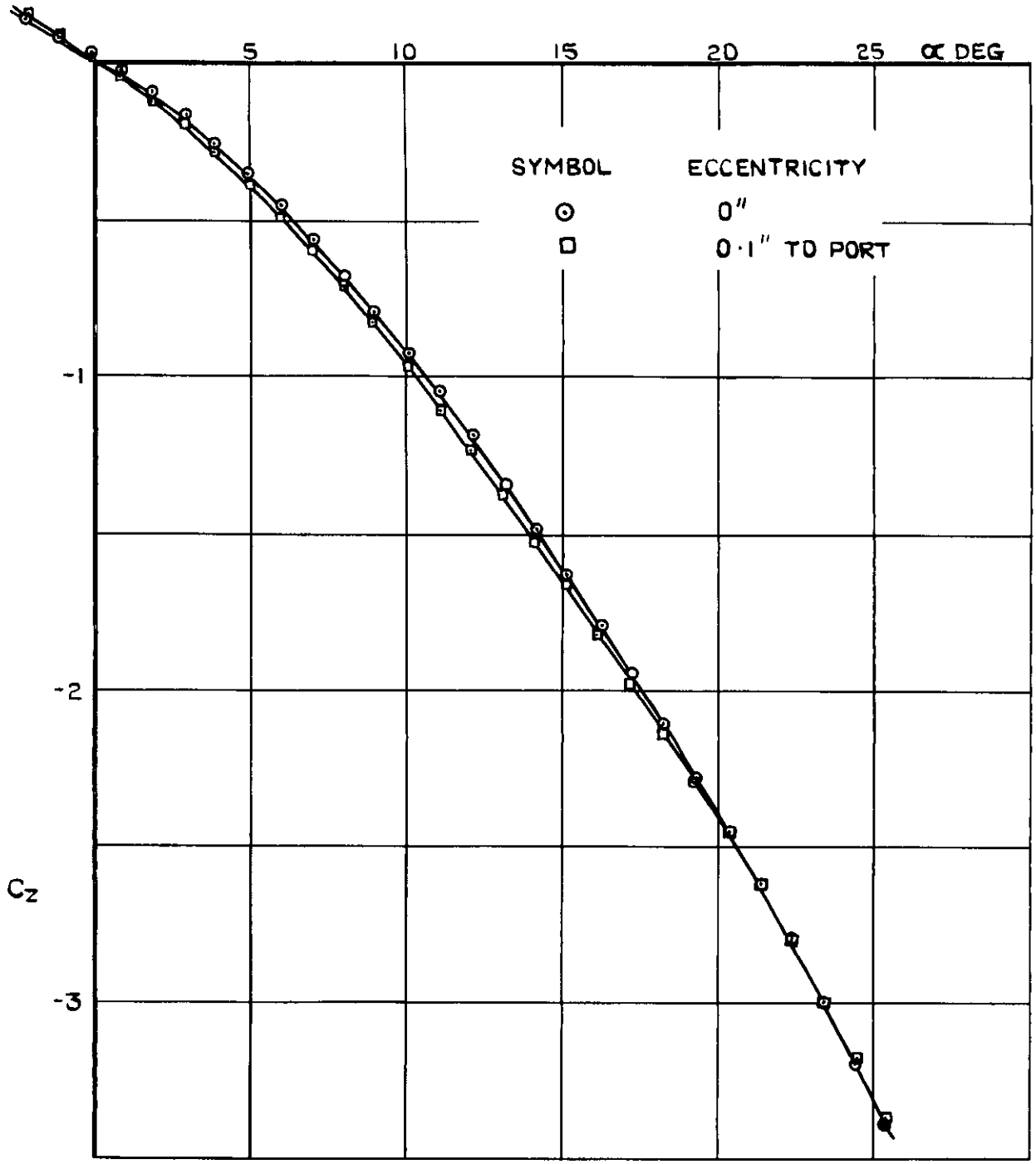

FIG.109. C_Z vs α FOR MODEL WITH ECCENTRIC RING CONTROL ACTING NORMAL TO INCIDENCE PLANE.

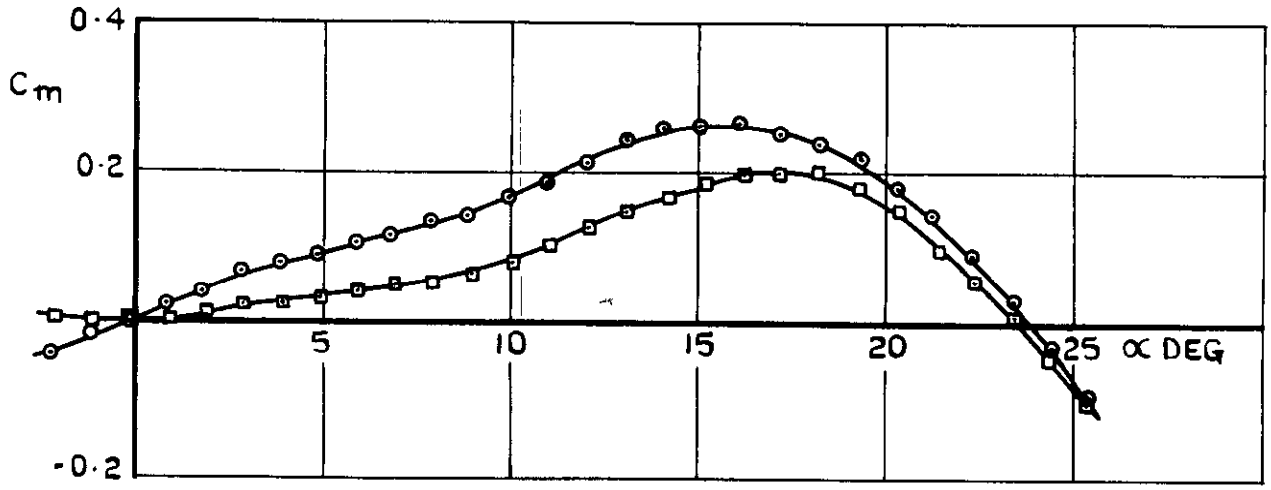

FIG.110. C_m vs α FOR MODEL WITH ECCENTRIC RING CONTROL ACTING NORMAL TO INCIDENCE PLANE.

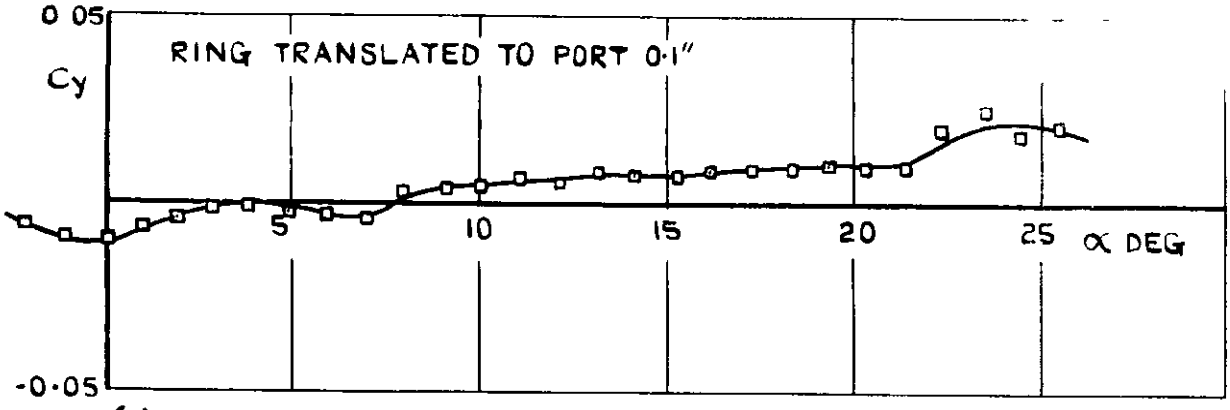

(a) C_y vs α

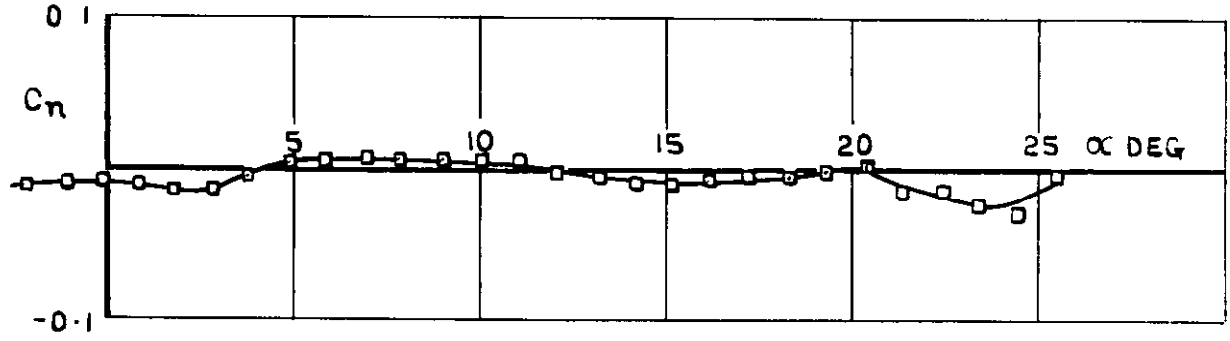

(b) C_n vs α

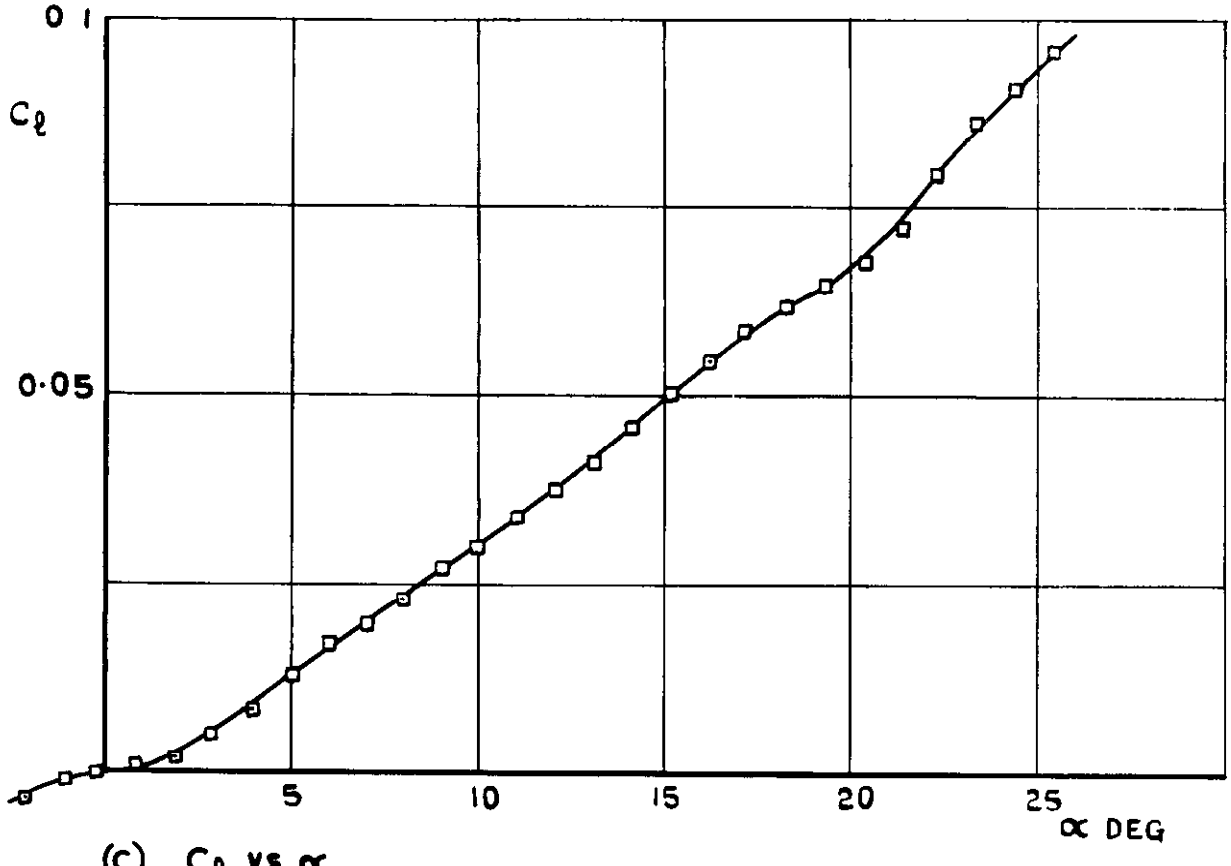

(c) C_ℓ vs α

FIG. 111. a, b & c. VARIATION OF DIRECTIONAL AND LATERAL COMPONENTS WITH α FOR MODEL WITH ECCENTRIC RING CONTROL ACTING NORMAL TO INCIDENCE PLANE.

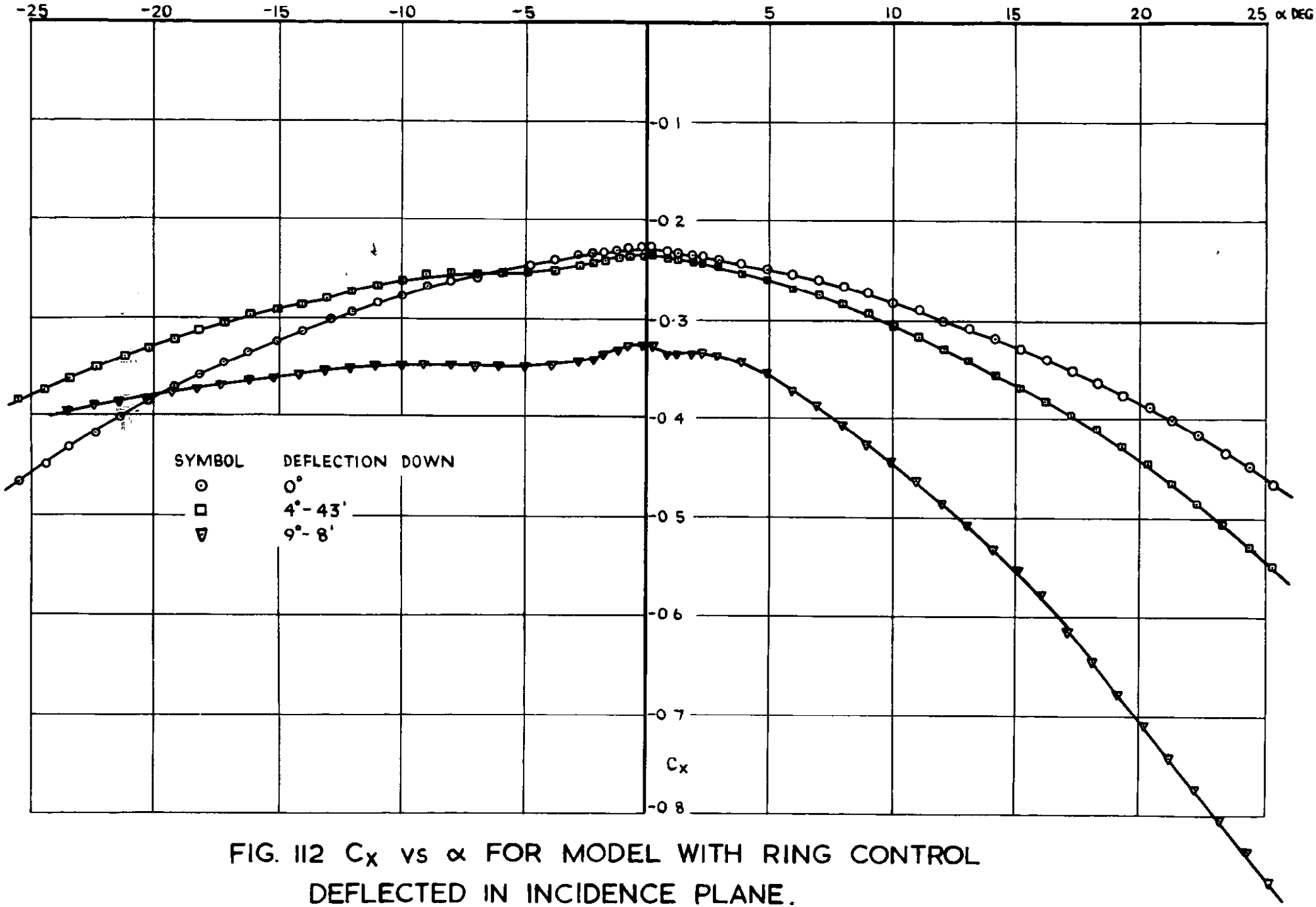

FIG. 112 C_x vs α FOR MODEL WITH RING CONTROL DEFLECTED IN INCIDENCE PLANE.

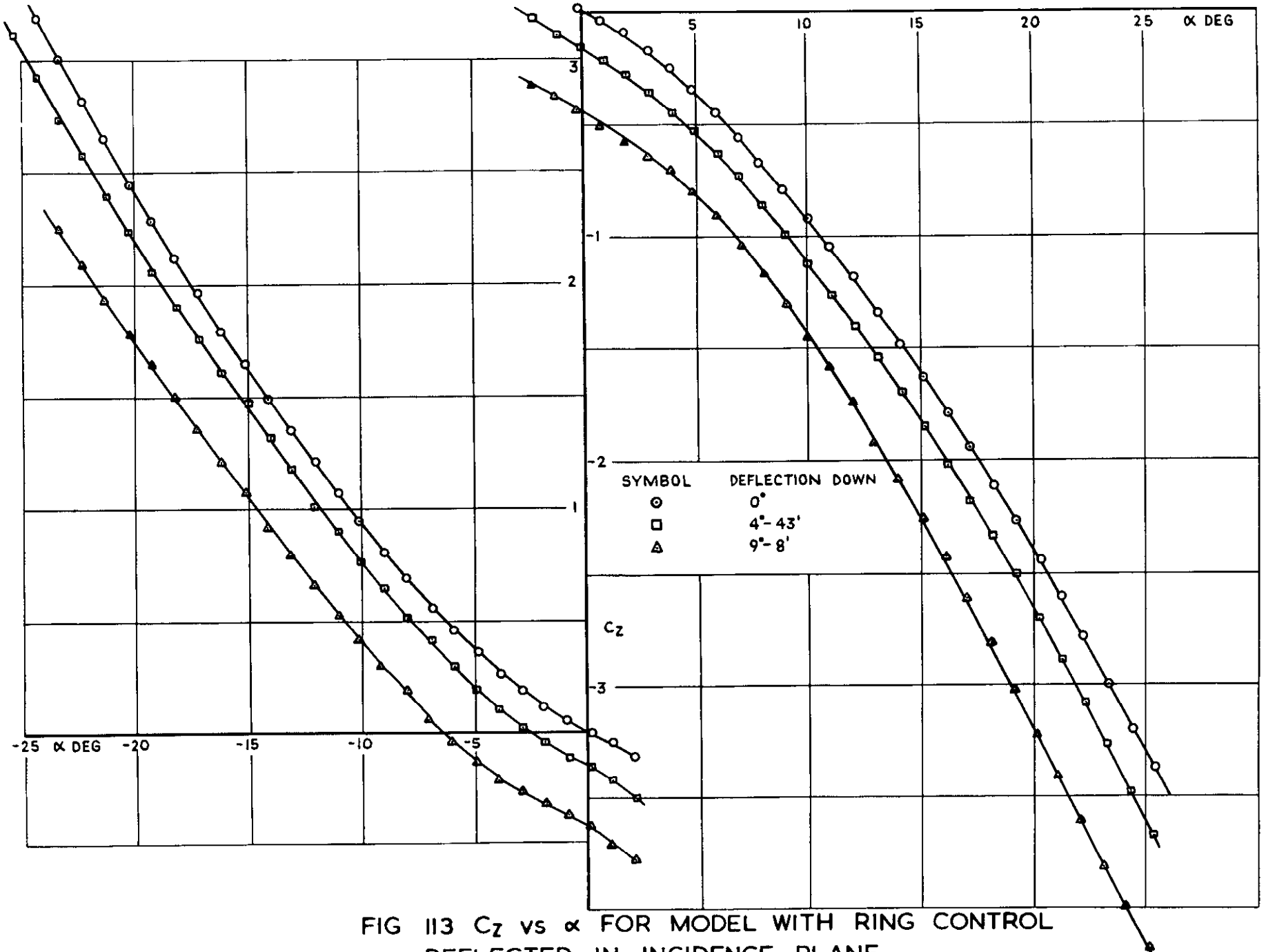

FIG 113 C_Z vs α FOR MODEL WITH RING CONTROL DEFLECTED IN INCIDENCE PLANE

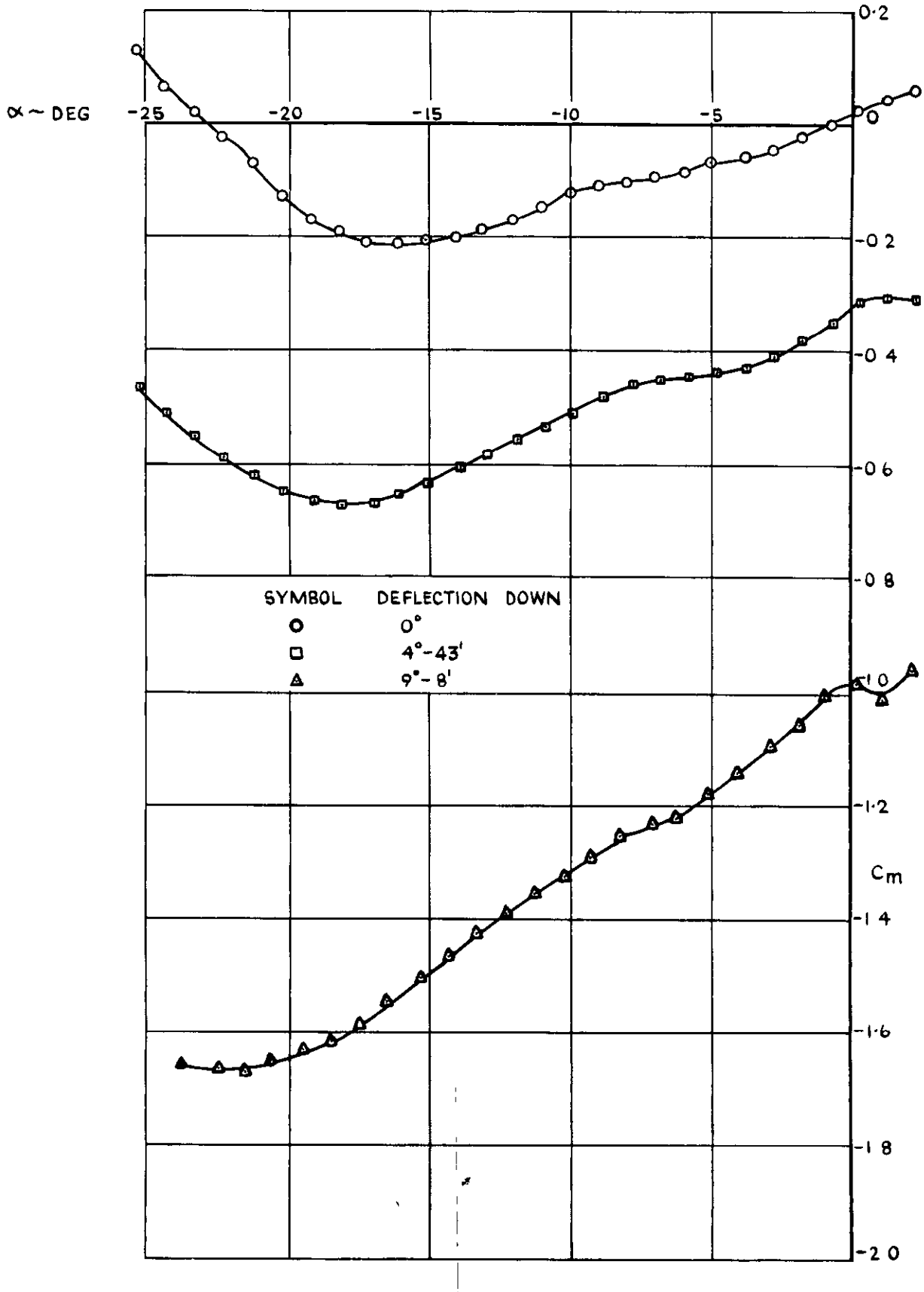

FIG. 114.(a) C_m vs α FOR MODEL WITH RING CONTROL DEFLECTED IN INCIDENCE PLANE ~ α - VE.

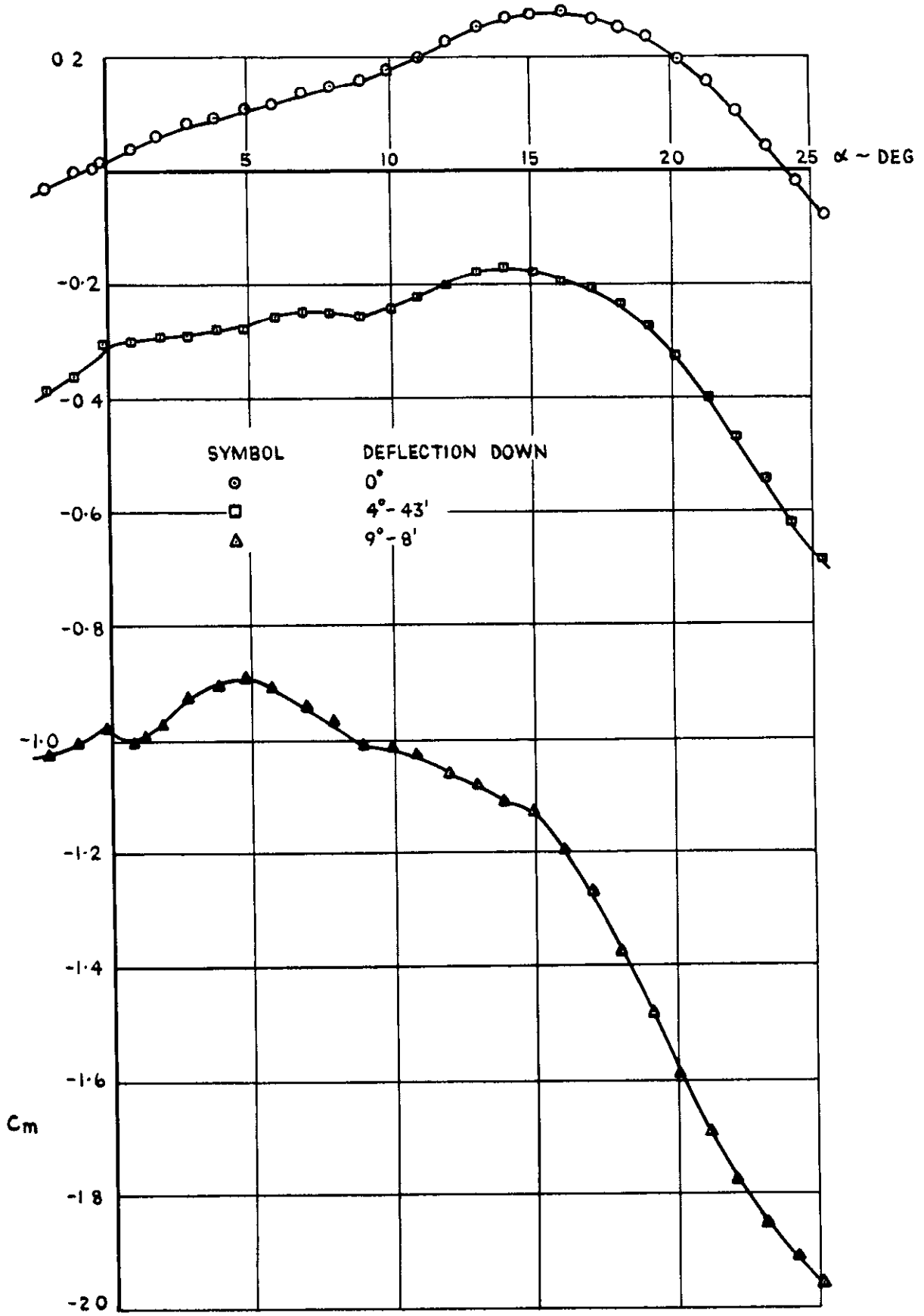

FIG. 114.(b.) Cm vs α FOR MODEL WITH RING CONTROL DEFLECTED IN INCIDENCE PLANE.

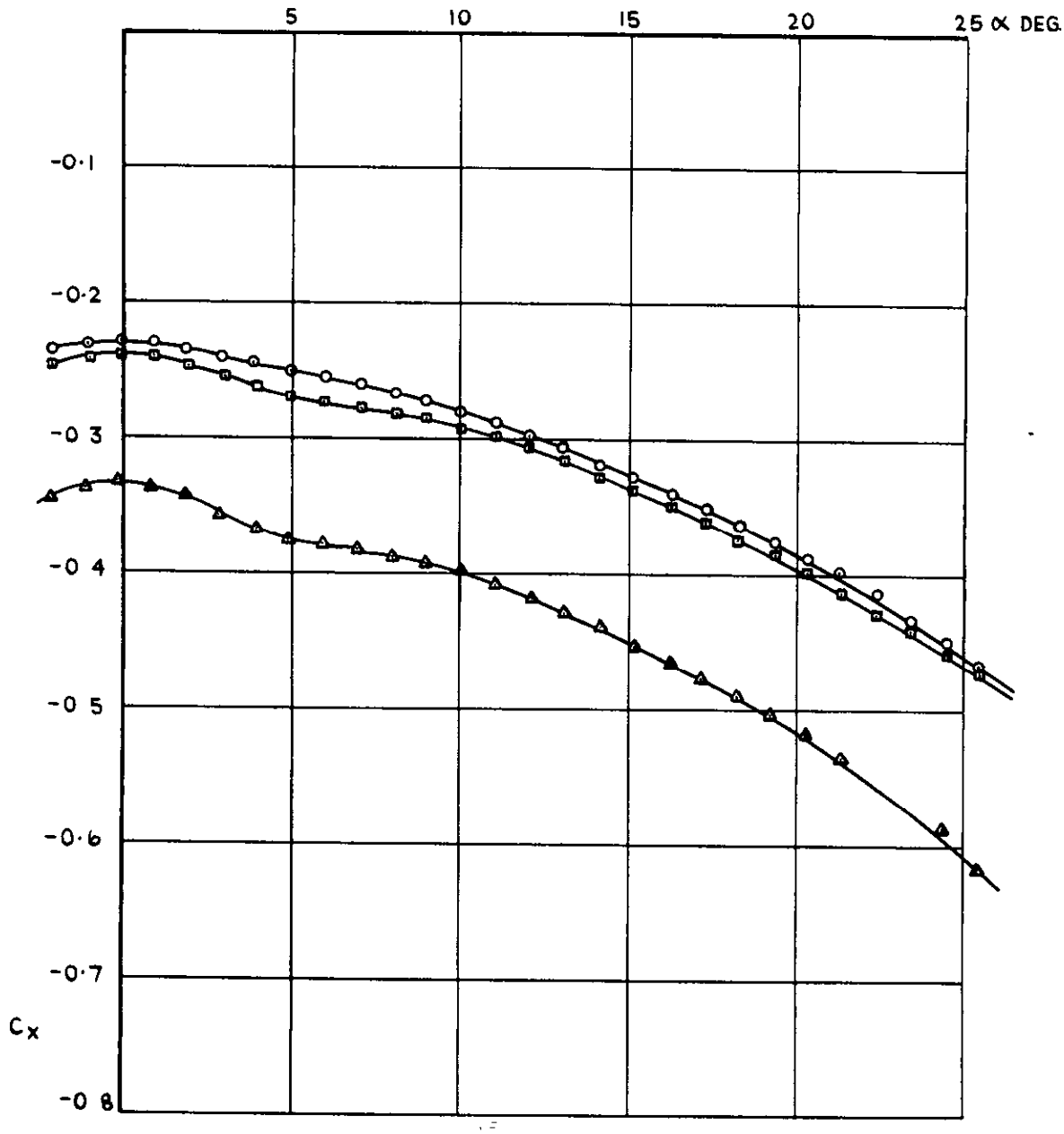

FIG. 115. C_X vs α FOR MODEL WITH RING CONTROL DEFLECTED NORMAL TO INCIDENCE PLANE.

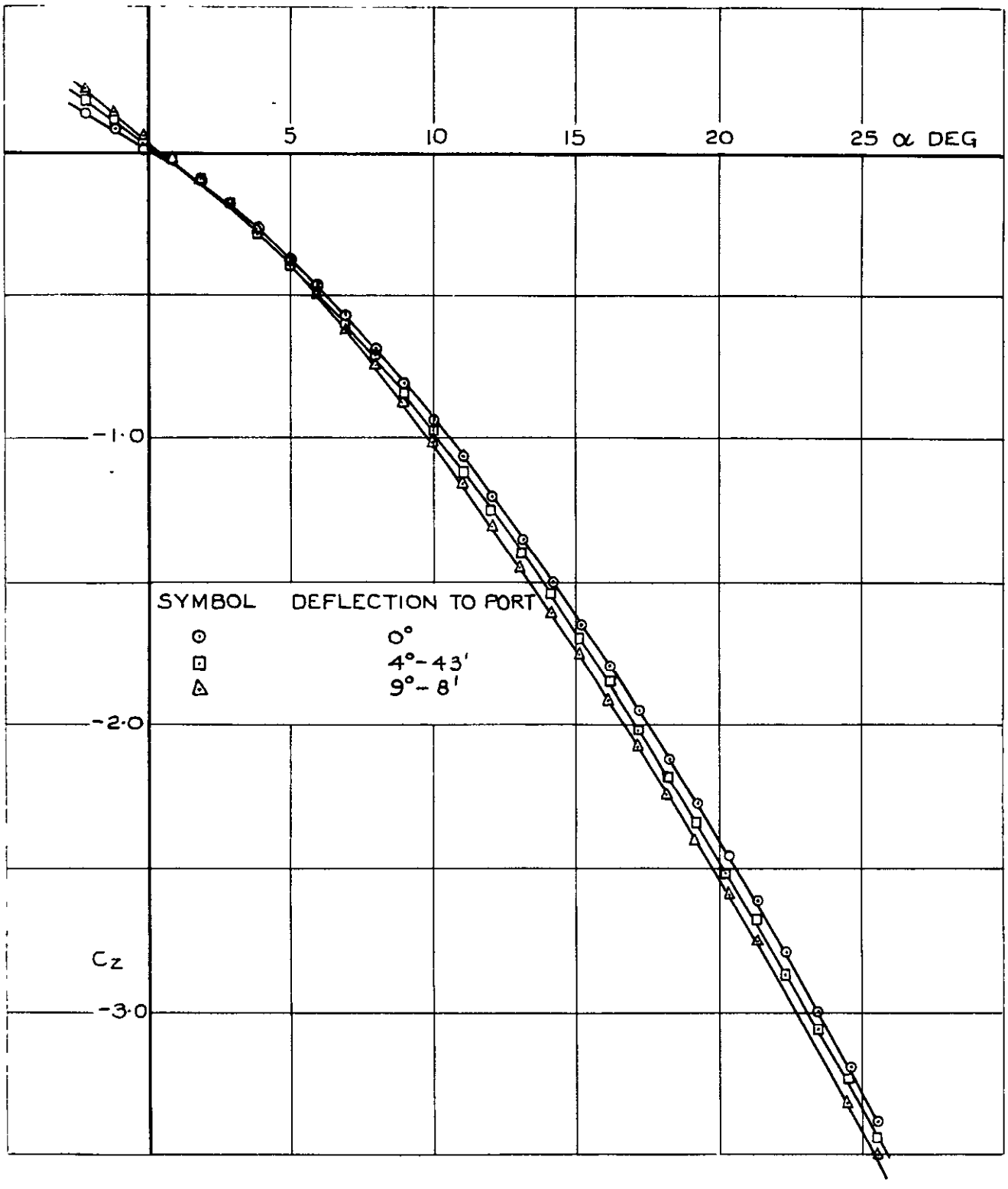

FIG. 116. C_z vs α FOR MODEL WITH RING CONTROL DEFLECTED NORMAL TO INCIDENCE PLANE.

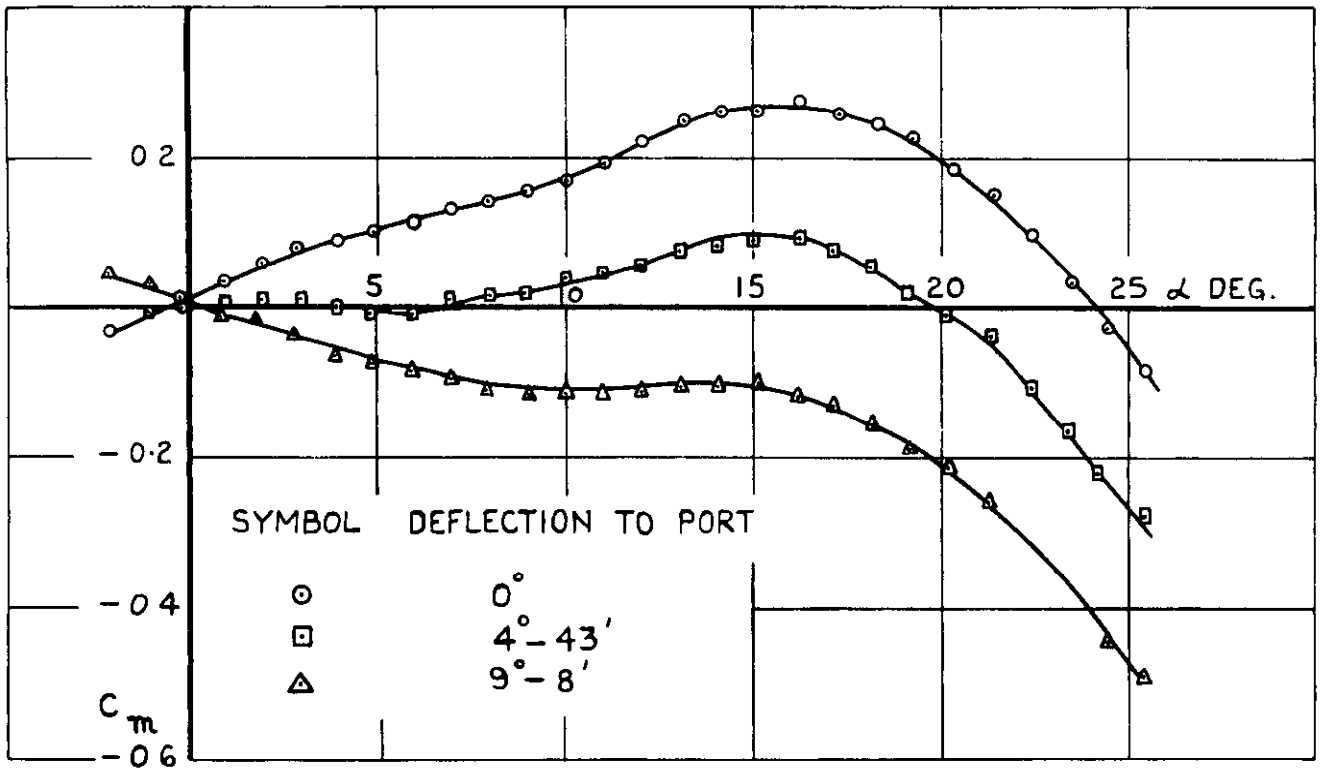

FIG. 117. C_m vs α FOR MODEL WITH RING CONTROL DEFLECTED NORMAL TO INCIDENCE PLANE.

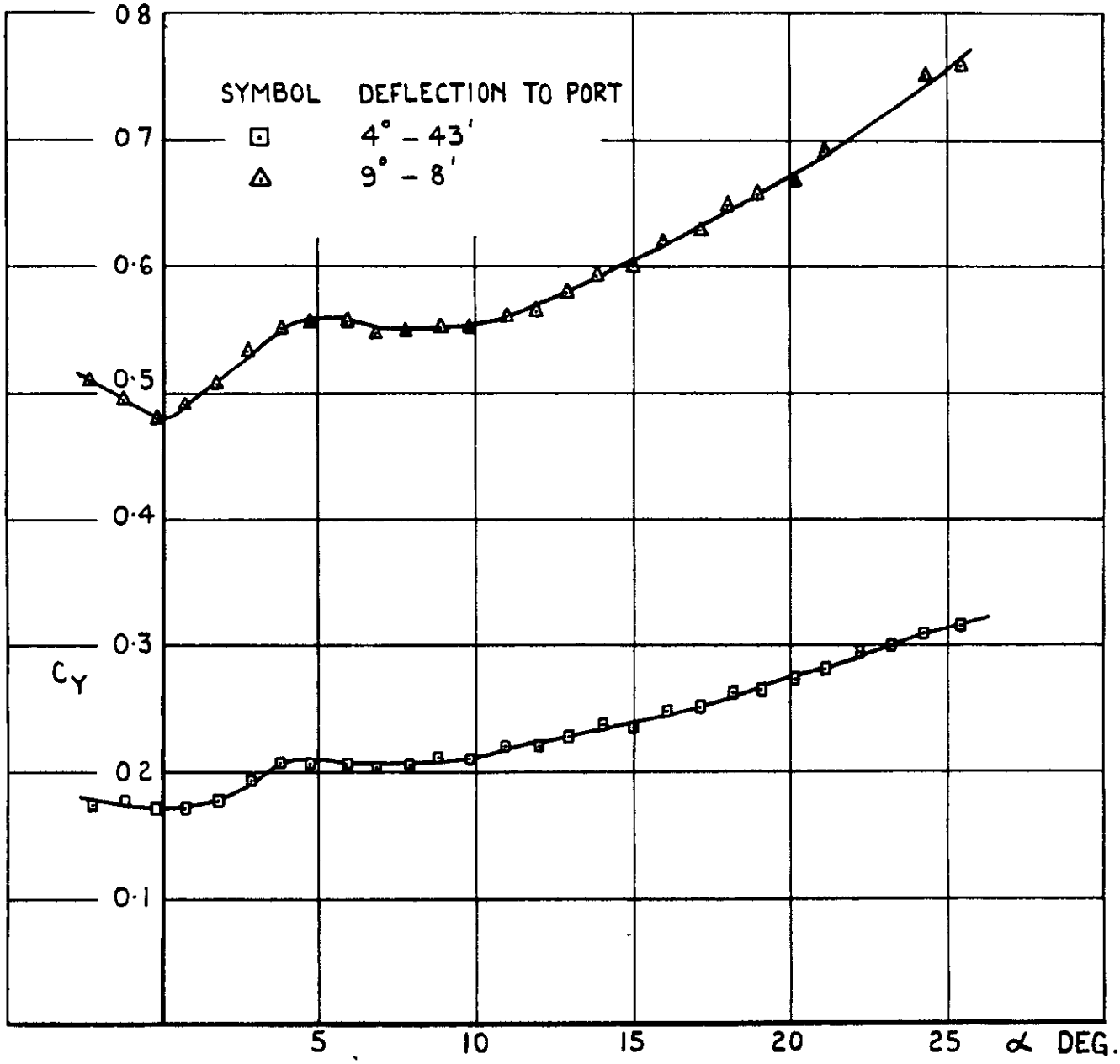

FIG. 118. C_y vs α FOR MODEL WITH RING CONTROL DEFLECTED NORMAL TO INCIDENCE PLANE.

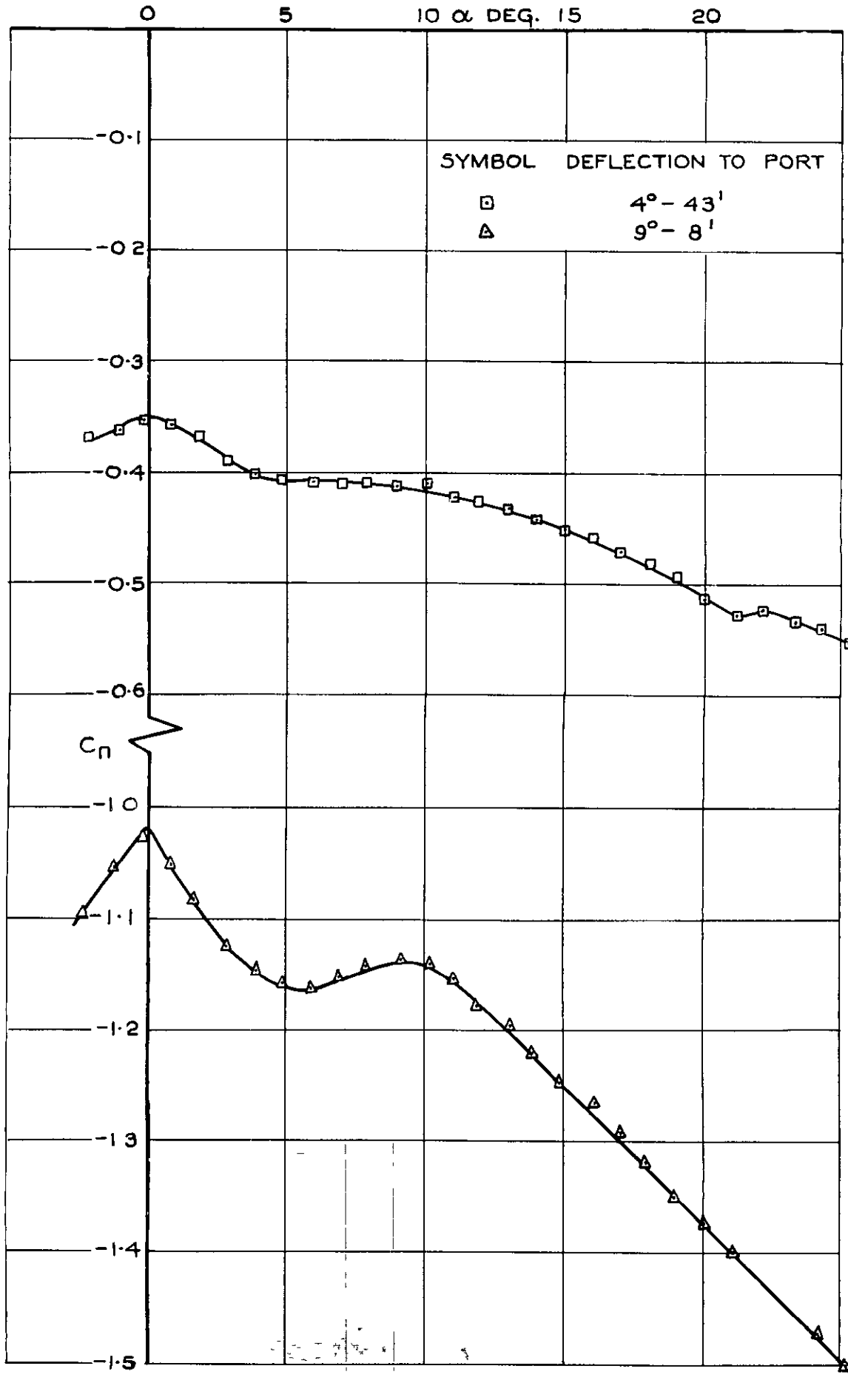

FIG.119. C_n vs α FOR MODEL WITH RING CONTROL DEFLECTED NORMAL TO INCIDENCE PLANE.

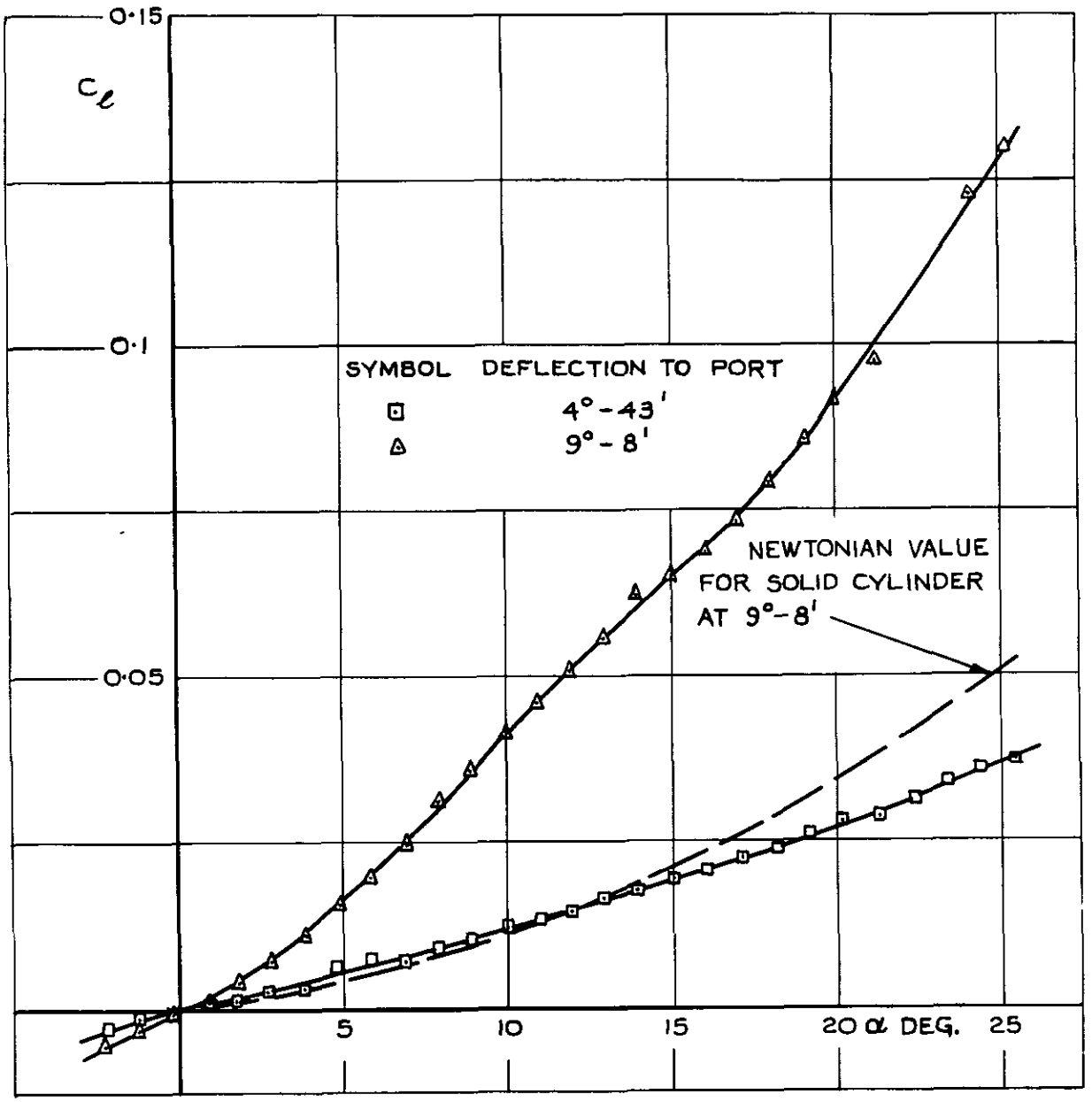

FIG.120. C_ℓ vs α FOR MODEL WITH RING CONTROL DEFLECTED NORMAL TO INCIDENCE PLANE.

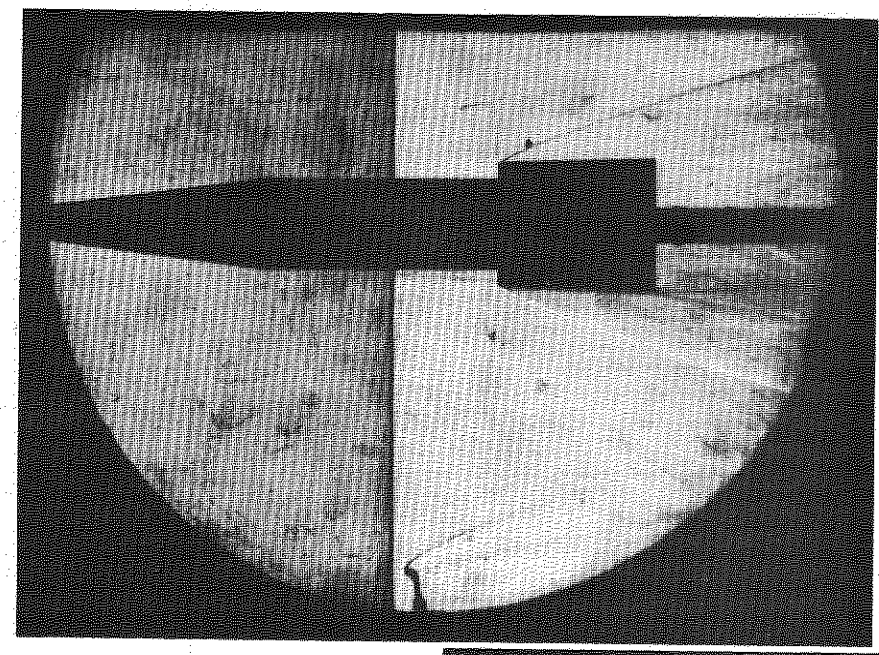

(a) $\alpha = 0^{\circ}$, $\eta = 0^{\circ}$

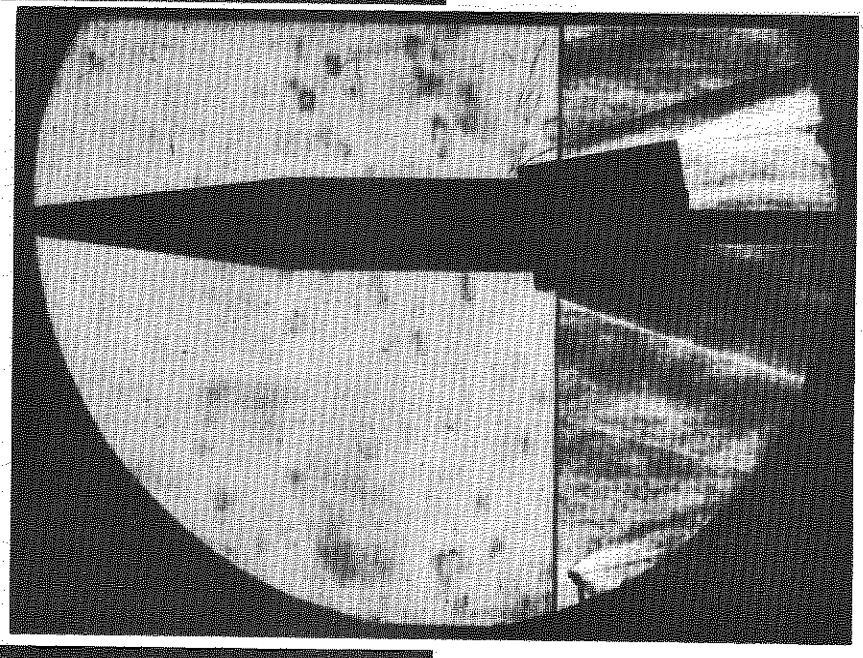

(b) $\alpha = 0^{\circ}$, $\eta = -9^{\circ}\ -8'$

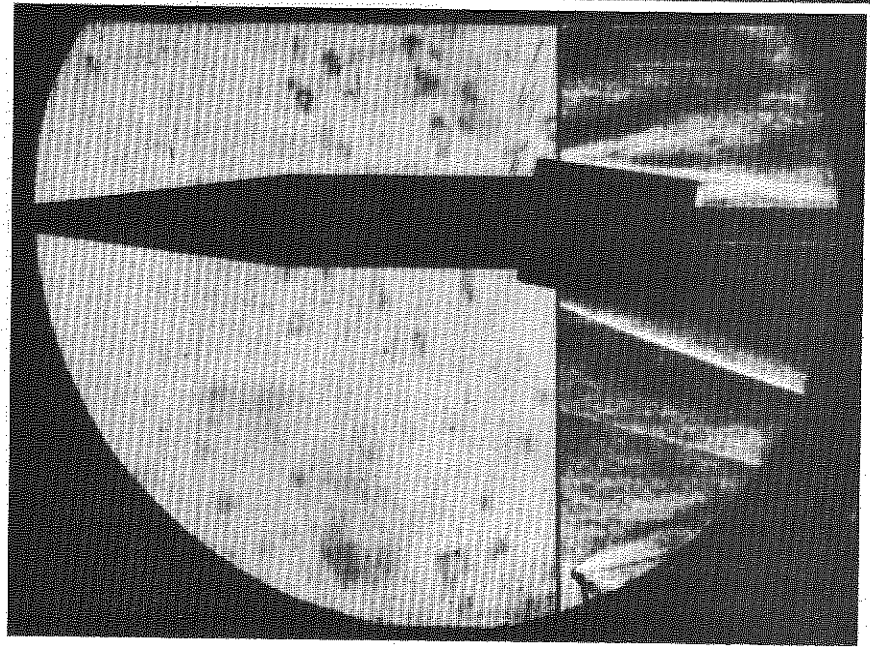

(c) $\alpha = 0^{\circ}$, $\eta = +9^{\circ}\ -8'$

FIG.121 SCHLIEREN PHOTOGRAPHS OF MODEL WITH RING CONTROL AT $\eta = 0^{\circ}$ AND $\pm 9^{\circ}\ -8'$

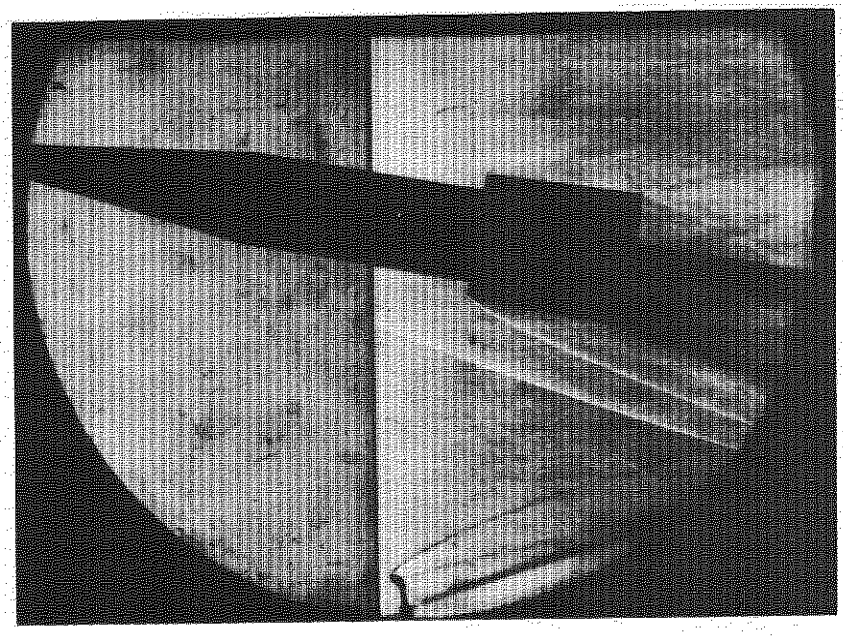

(d) $\alpha = 10^{o}$, $\eta = 0^{o}$

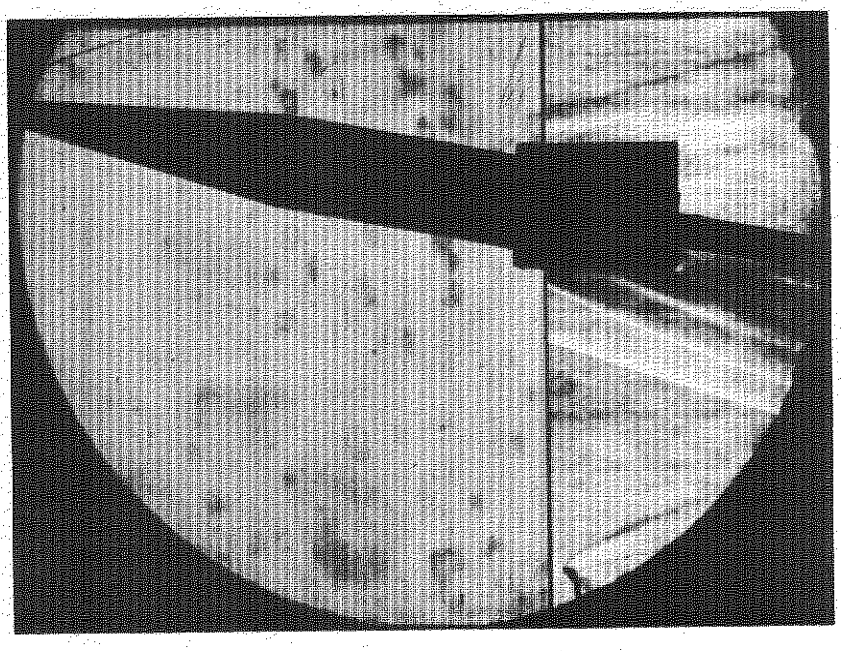

(e) $\alpha = 11^{o}$, $\eta = -9^{o}\ -8'$

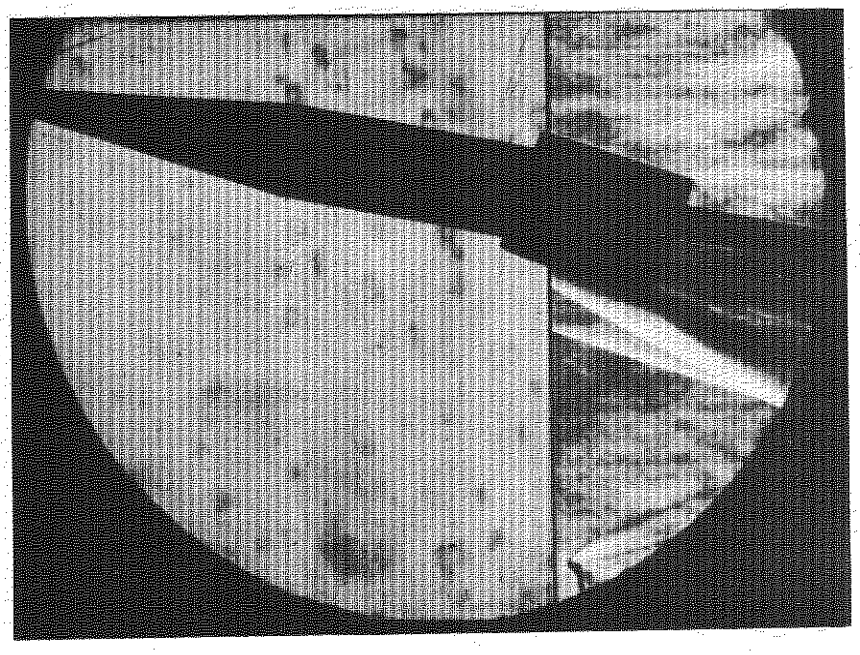

(f) $\alpha = 11^{o}$, $\eta = +9^{o}\ -8'$

FIG.121 (CONT.)

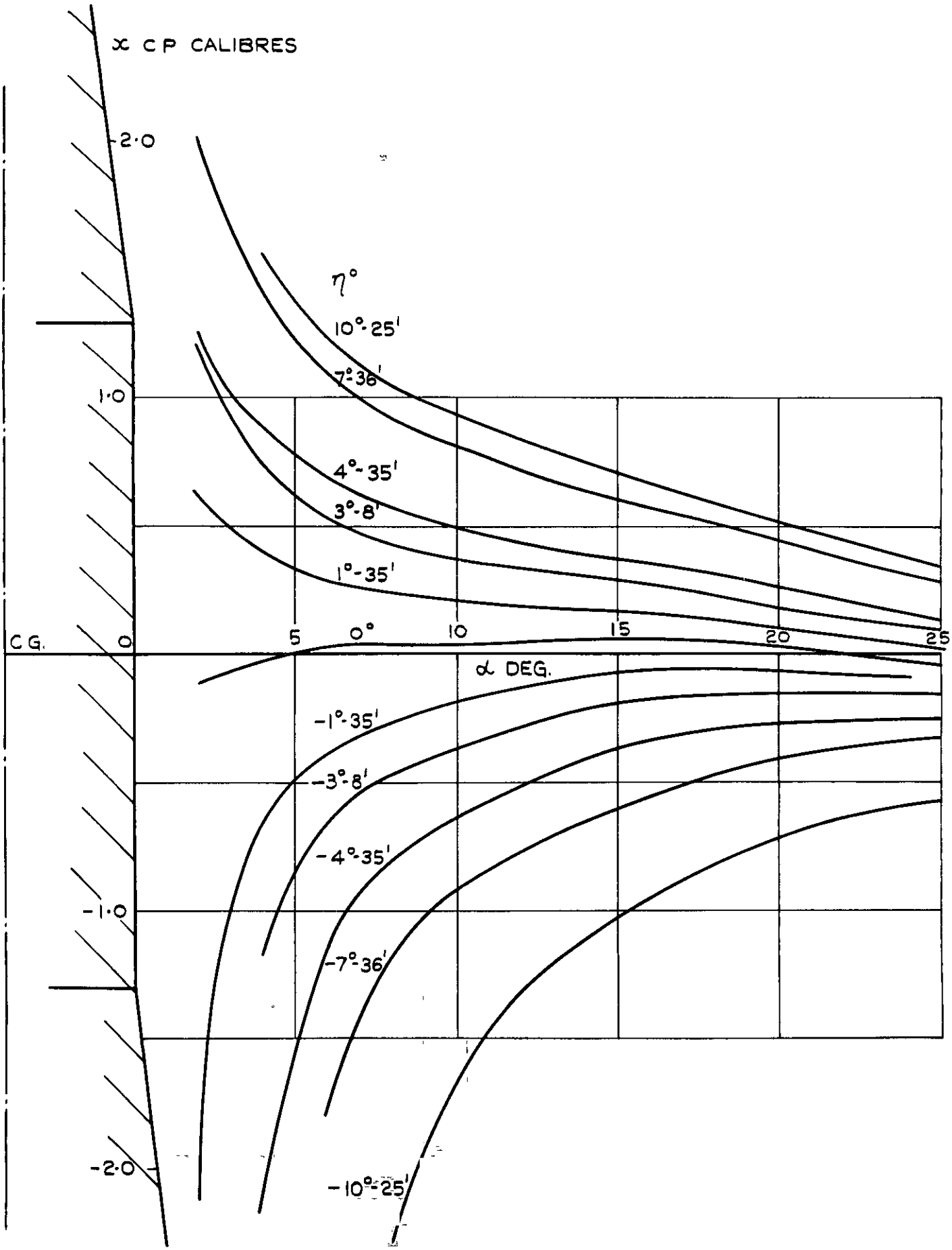

FIG. 122. C.P. POSITION VARIATION WITH INCIDENCE FOR MODEL WITH NOSE DEFLECTED IN INCIDENCE PLANE.

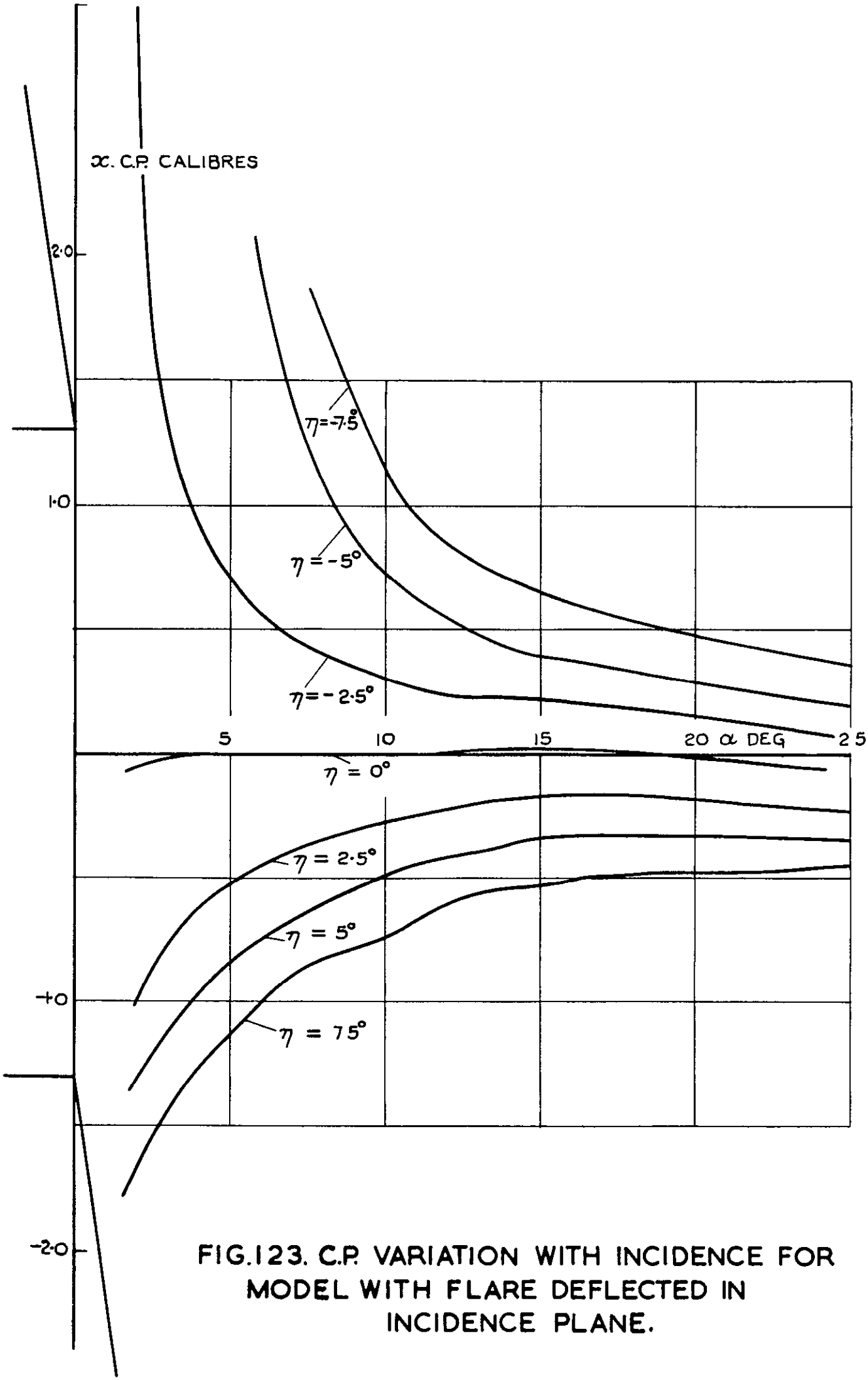

FIG.123. C.P. VARIATION WITH INCIDENCE FOR MODEL WITH FLARE DEFLECTED IN INCIDENCE PLANE.

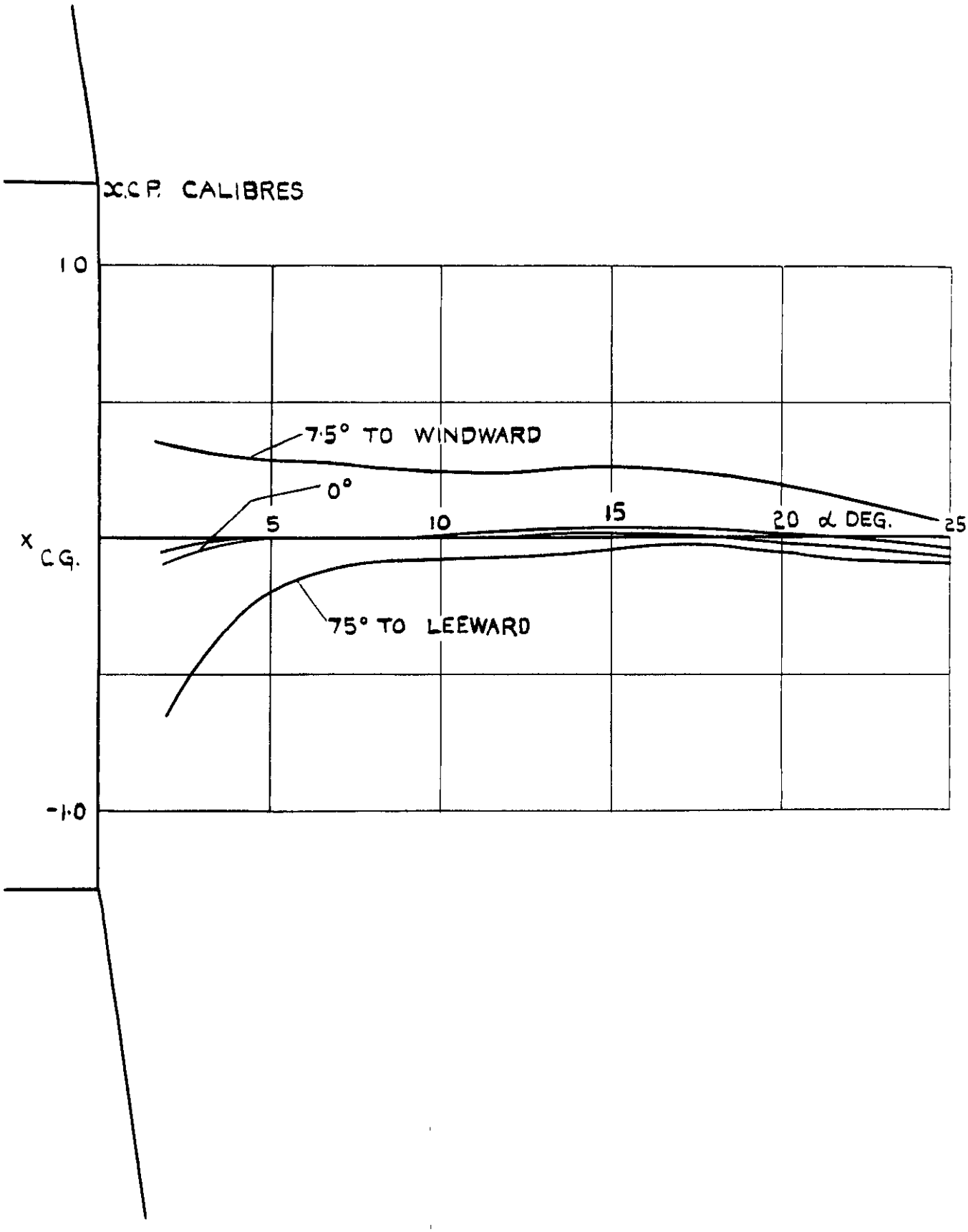

FIG.124. C. P. VARIATION WITH INCIDENCE FOR MODEL WITH NOSE FLAP CONTROL ACTING IN INCIDENCE PLANE.

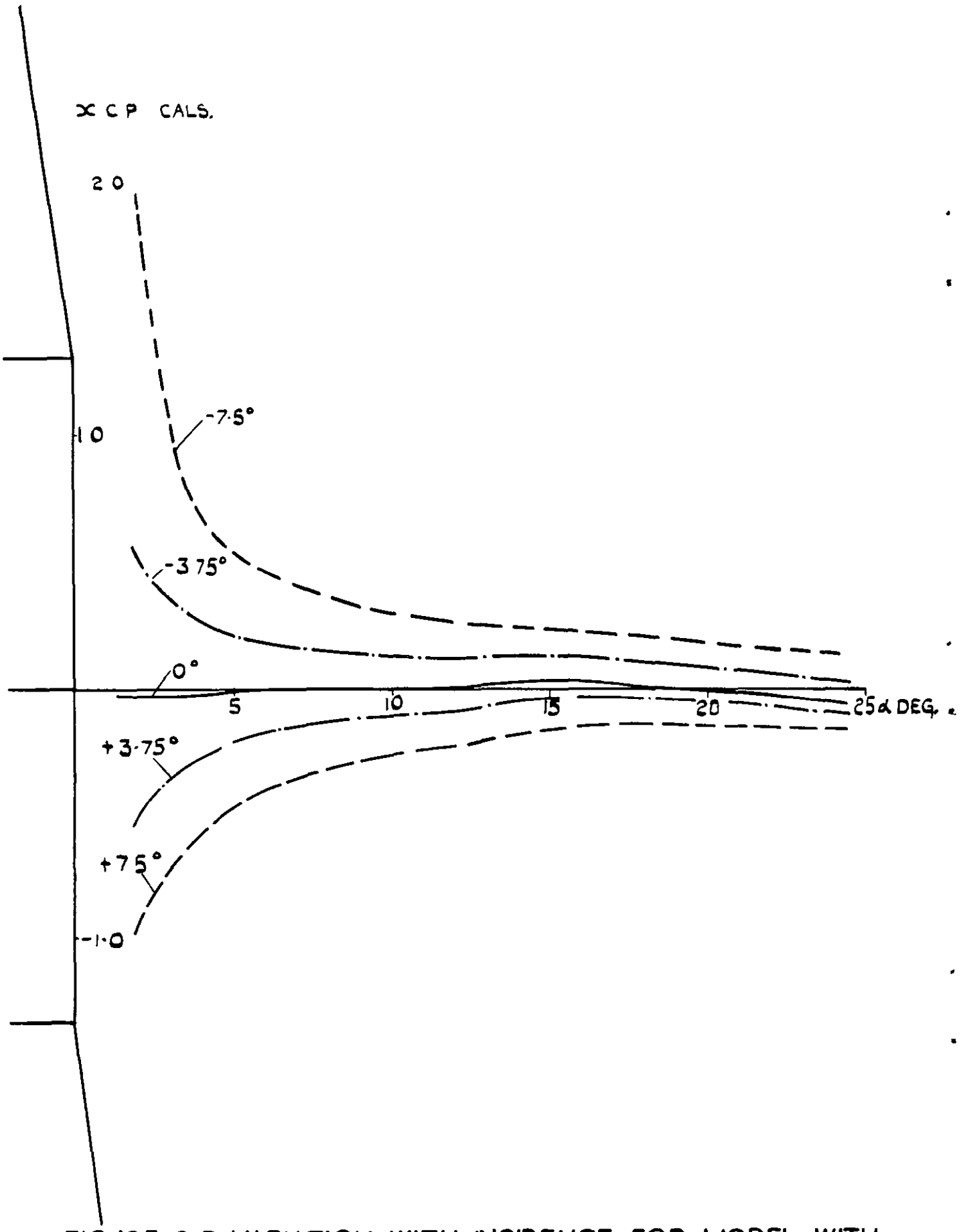

FIG.125. C.P. VARIATION WITH INCIDENCE FOR MODEL WITH FLARE FLAP CONTROL ACTING IN INCIDENCE PLANE FLAP ON WINDWARD SIDE.

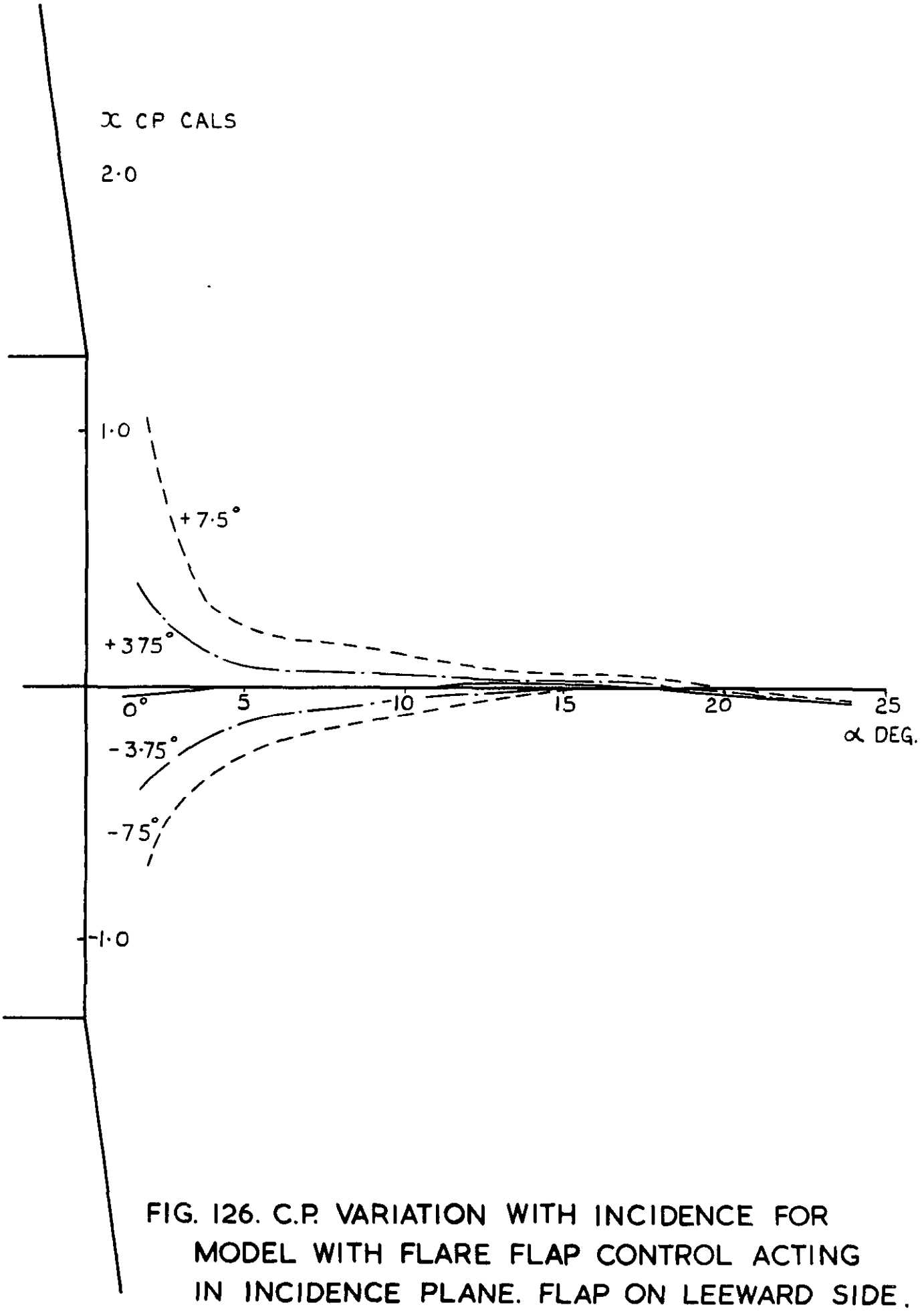

FIG. 126. C.P. VARIATION WITH INCIDENCE FOR MODEL WITH FLARE FLAP CONTROL ACTING IN INCIDENCE PLANE. FLAP ON LEEWARD SIDE.

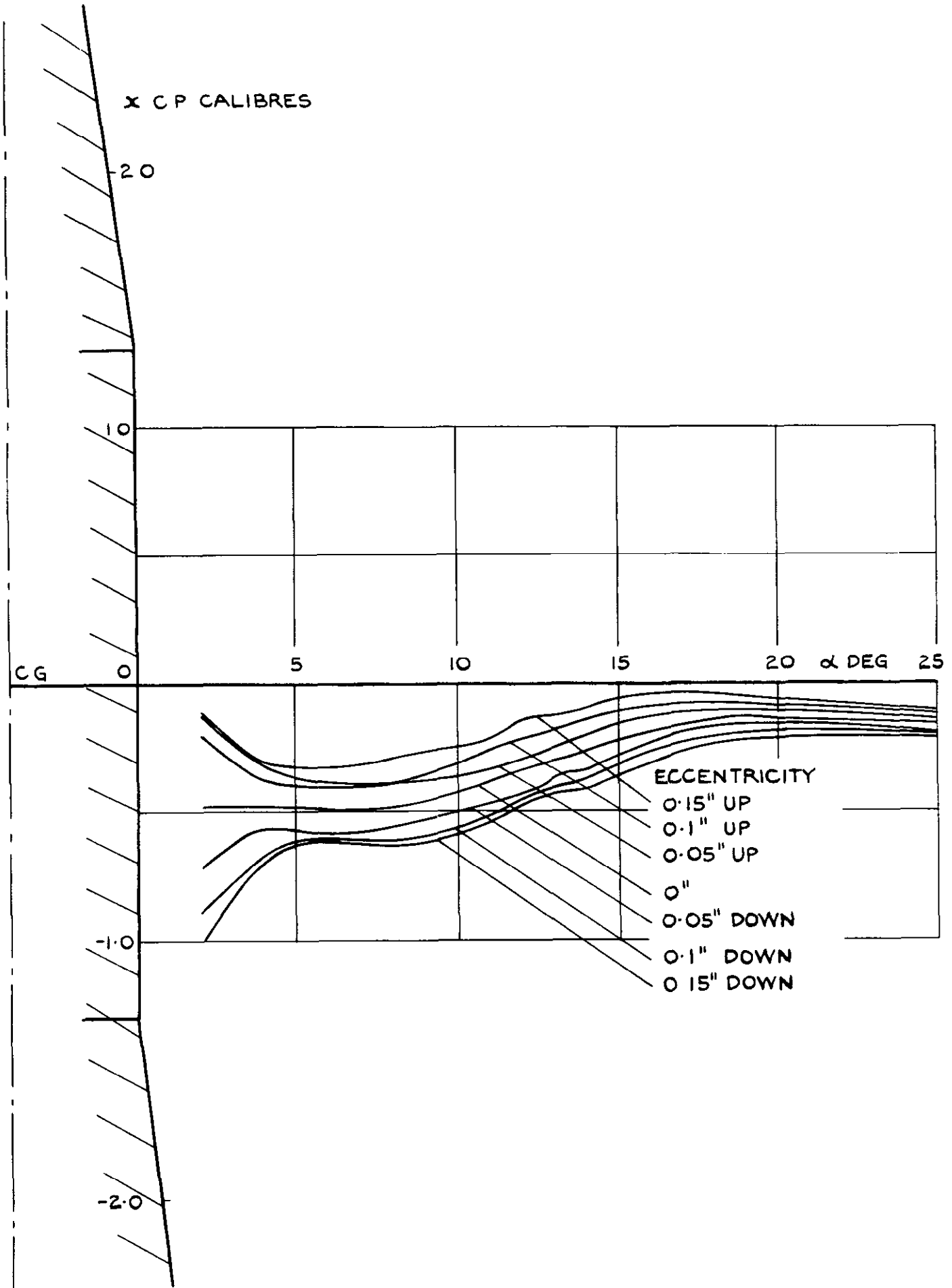

FIG. 127. C P VARIATION WITH INCIDENCE FOR MODEL WITH NOSE DISC TRANSLATED IN INCIDENCE PLANE.

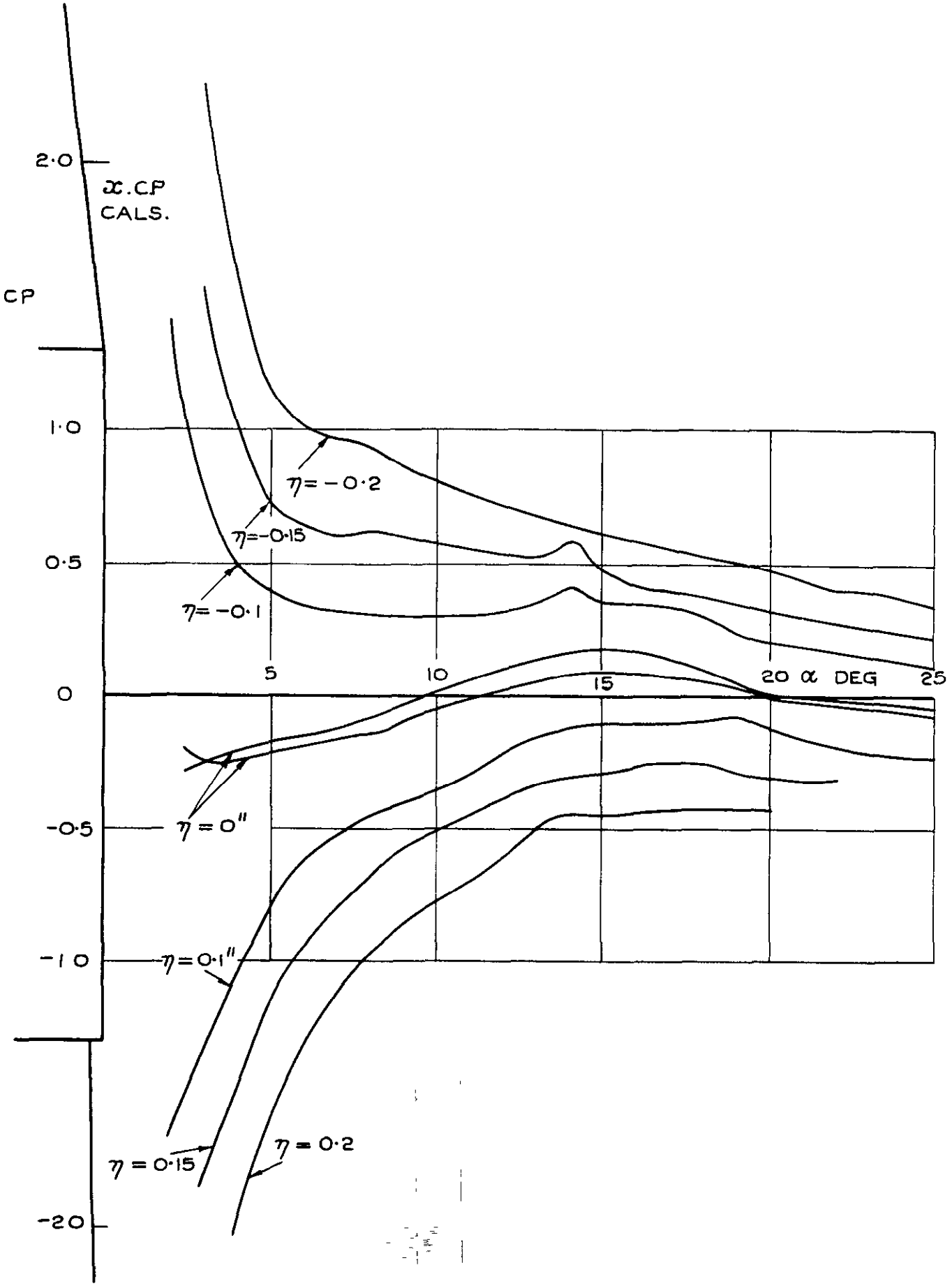

FIG.128. C.P VARIATION WITH INCIDENCE FOR MODEL WITH REAR DISC CONTROL USED IN INCIDENCE PLANE.

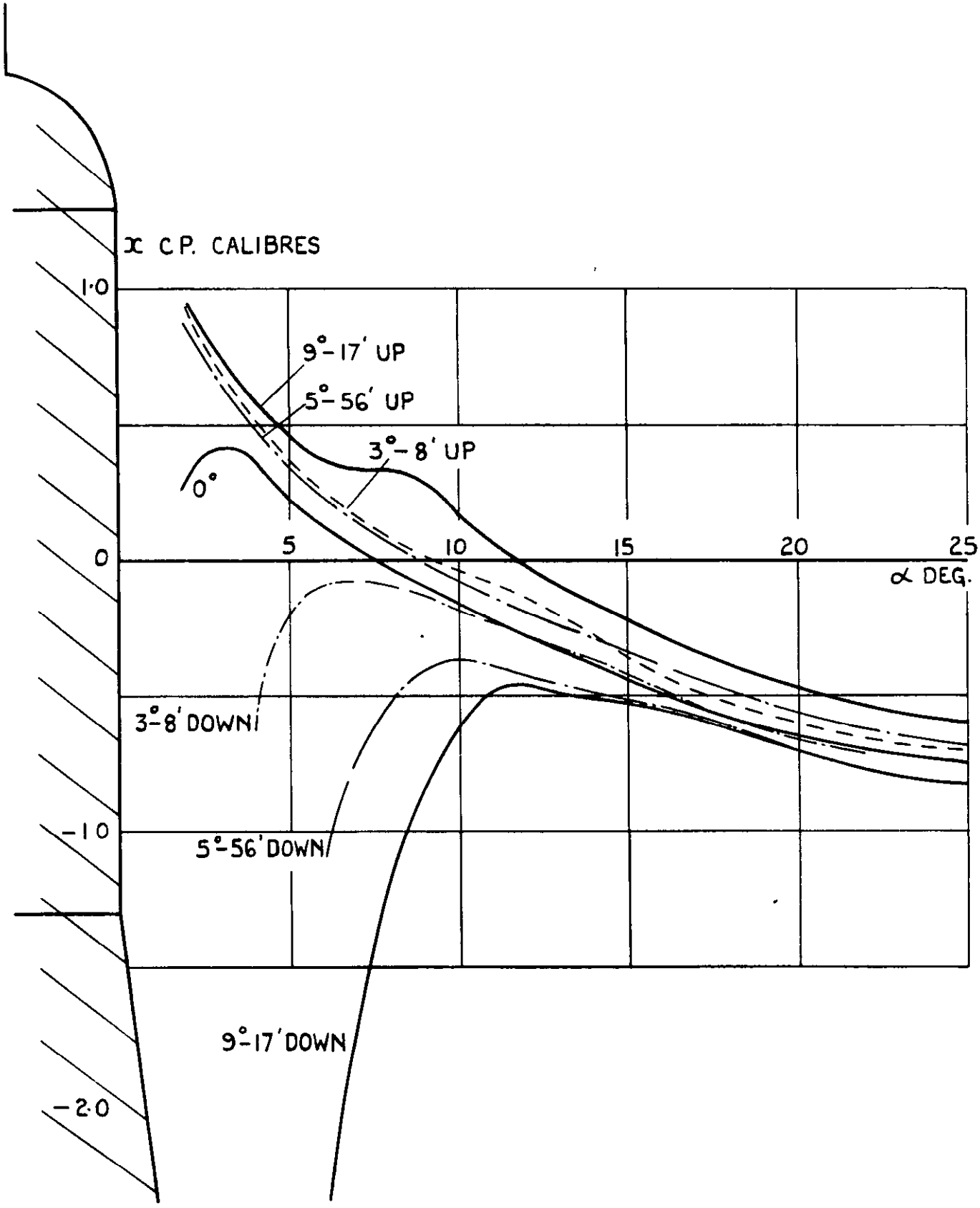

FIG. 129. C. P. VARIATION WITH INCIDENCE FOR MODEL WITH SPIKE DEFLECTED IN INCIDENCE PLANE.

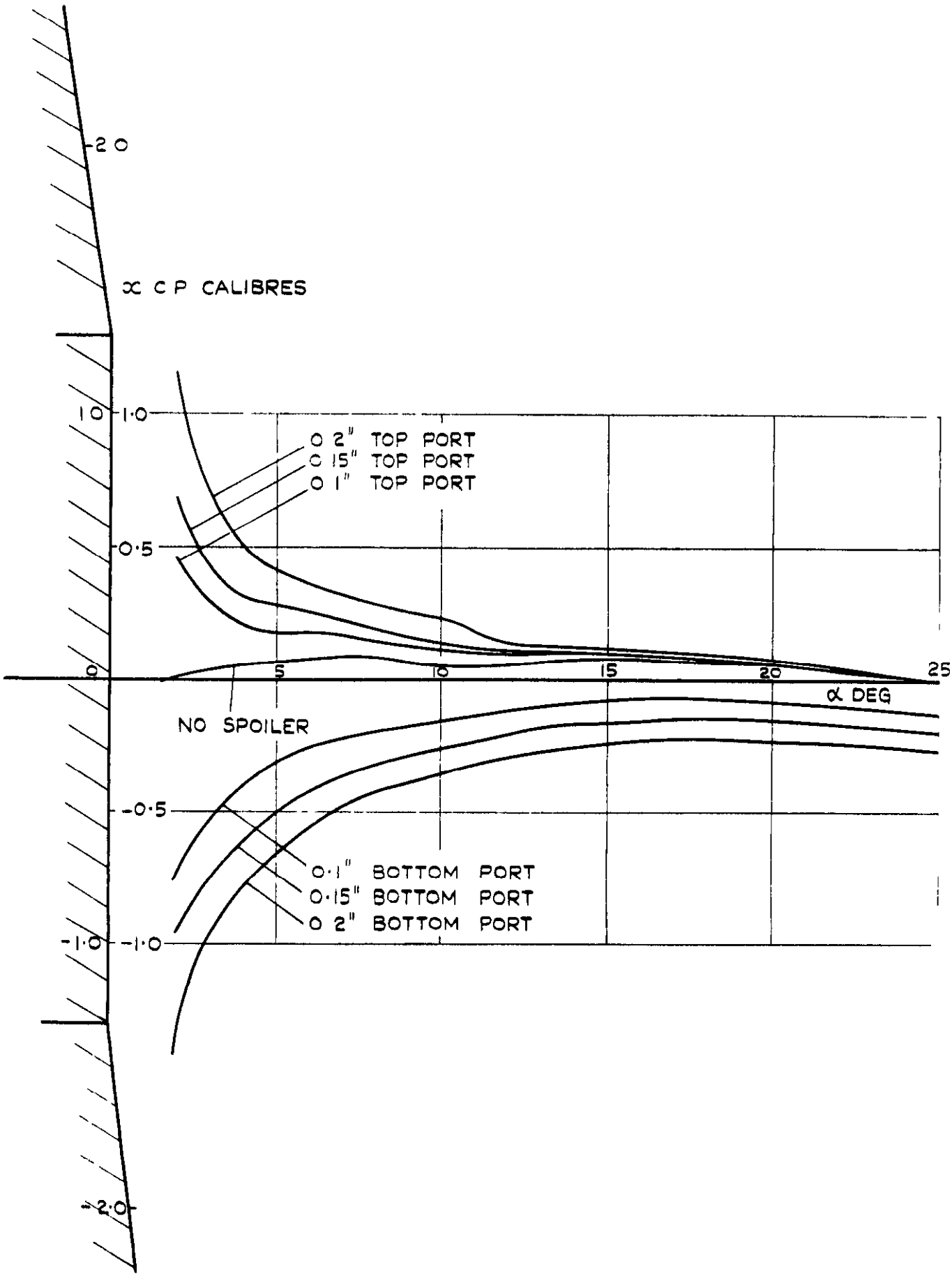

FIG. 130. C.P. VARIATION WITH INCIDENCE FOR MODEL WITH A SWEPT SPOILER EXTENDED IN THE INCIDENCE PLANE.

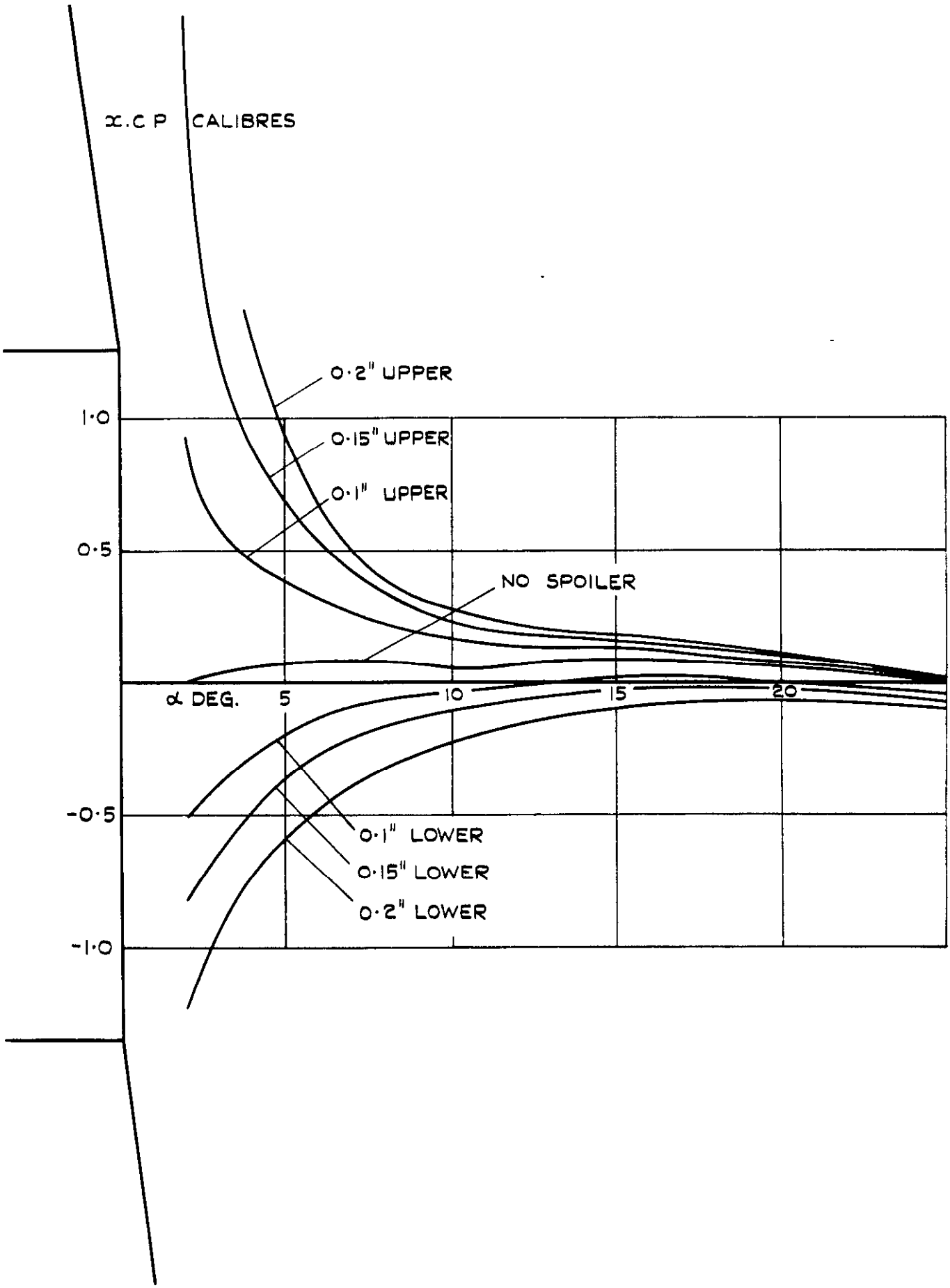

FIG. 131. VARIATION OF C.P. WITH SPOILER HEIGHT AND INCIDENCE - MODEL WITH SWEPT SPOILER EXTENDED NORMAL TO INCIDENCE PLANE.

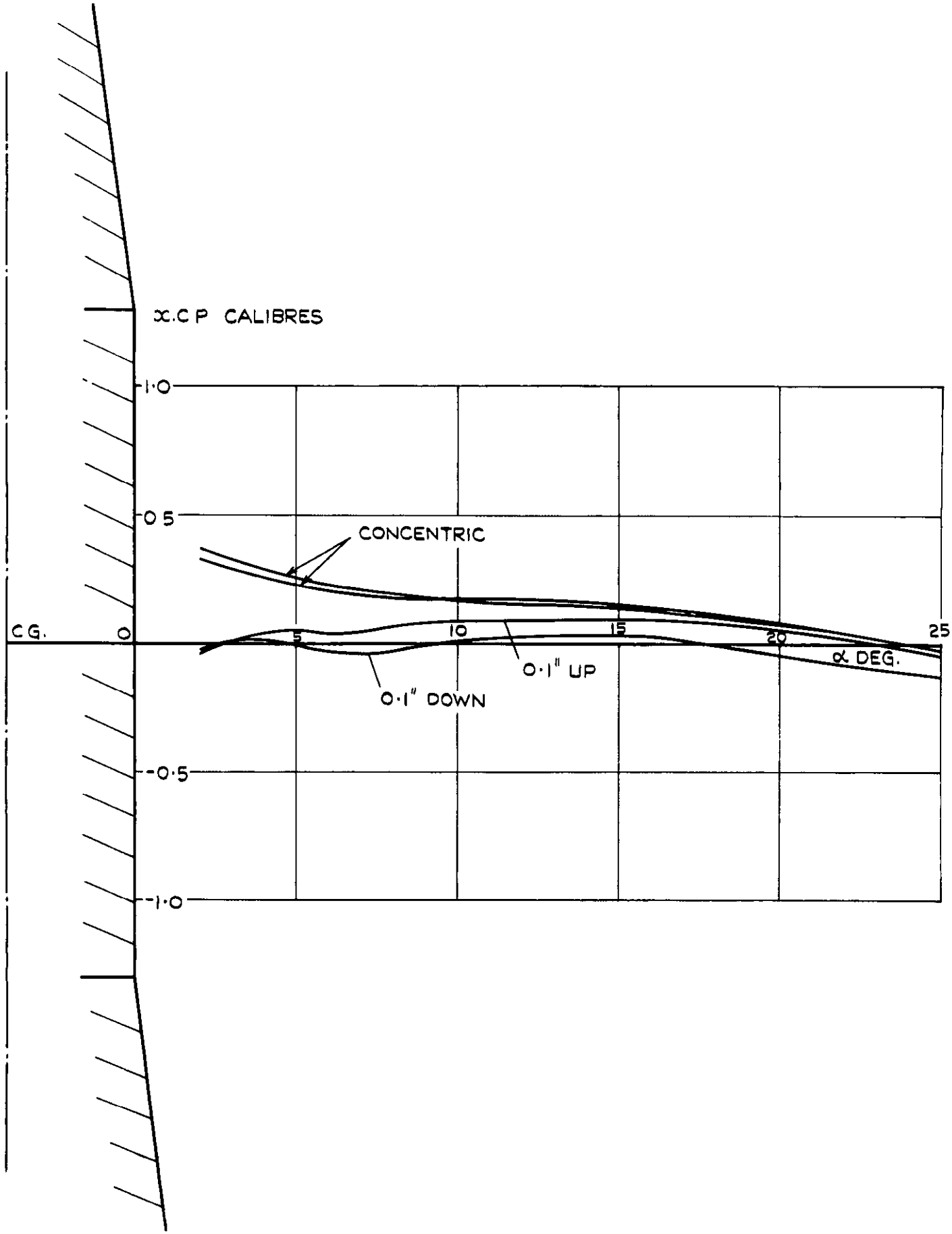

FIG. 132. C.P. VARIATION WITH INCIDENCE FOR MODEL WITH ECCENTRIC RING CONTROL USED IN INCIDENCE PLANE.

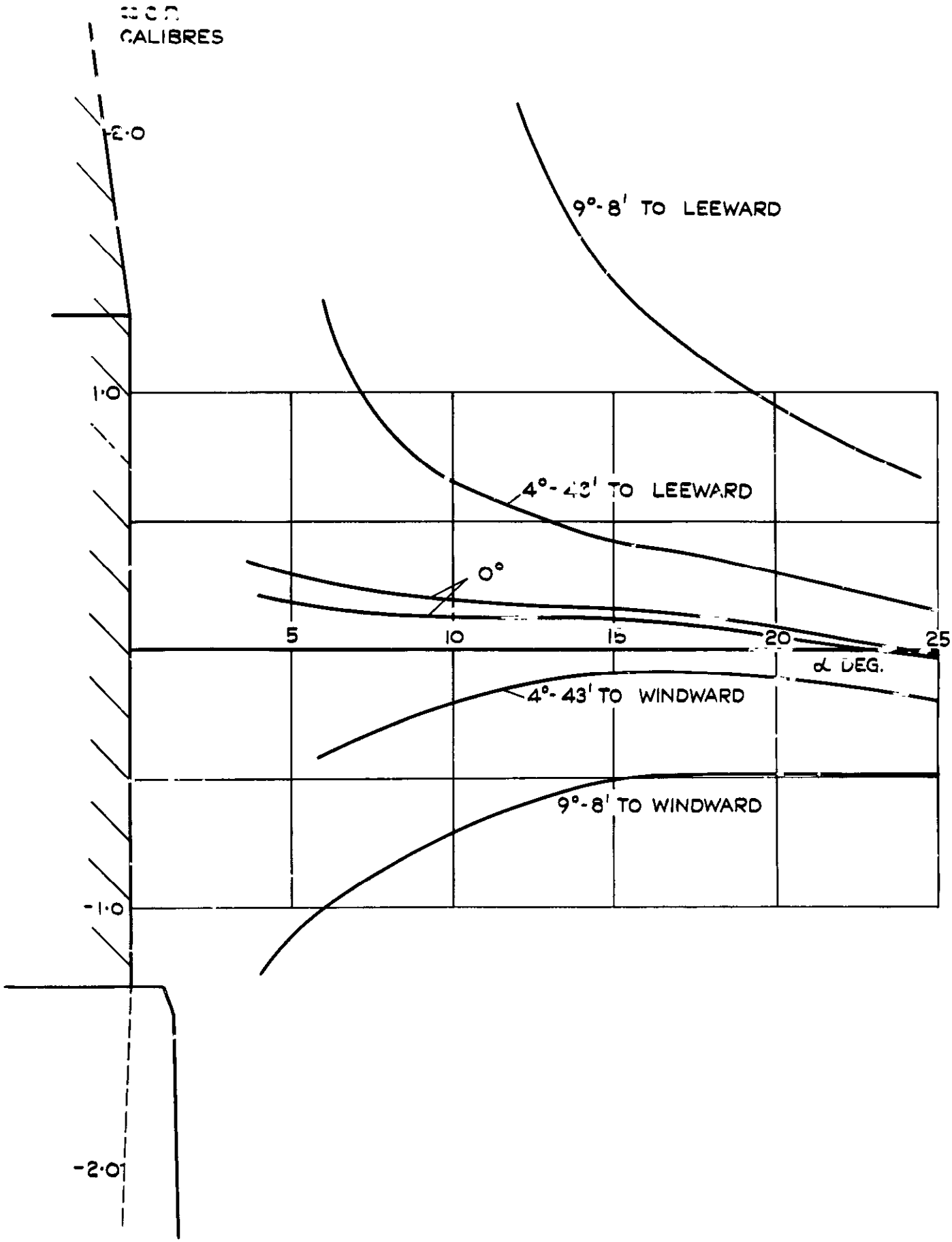

FIG. 133. C.P. VARIATION WITH INCIDENCE FOR MODEL WITH DEFLECTED RING CONTROL USED IN INCIDENCE PLANE.

A.R.C. C.P. No. 745

533.696.3/4 :
533.694 :
533.6.013.1 :
533.6.011.5

WIND TUNNEL FORCE AND MOMENT INVESTIGATION AT M = 4.3 INTO THE APPLICATION OF VARIOUS DEVICES FOR THE CONTROL OF A CONE-CYLINDER-FLARE CONFIGURATION. Pecover, B.E. January 1963.

Measurements have been made in the R.A.E. No.6 (11" x 6") wind tunnel of the six components of force and moment on a basic cone-cylinder-flare configuration fitted individually with ten different devices to produce aerodynamic control. In addition, some measurements of three components of force and moment on a flap or panel in the flare tail are given.

P.T.O.

A.R.C. C.P. No. 745

533.696.3/4 :
533.694 :
533.6.013.1 :
533.6.011.5

WIND TUNNEL FORCE AND MOMENT INVESTIGATION AT M = 4.3 INTO THE APPLICATION OF VARIOUS DEVICES FOR THE CONTROL OF A CONE-CYLINDER-FLARE CONFIGURATION. Pecover, B.E. January 1963.

Measurements have been made in the R.A.E. No.6 (11" x 6") wind tunnel of the six components of force and moment on a basic cone-cylinder-flare configuration fitted individually with ten different devices to produce aerodynamic control. In addition, some measurements of three components of force and moment on a flap or panel in the flare tail are given.

P.T.O.

A.R.C. C.P. No. 745

533.696.3/4 :
533.694 :
533.6.013.1 :
533.6.011.5

WIND TUNNEL FORCE AND MOMENT INVESTIGATION AT M = 4.3 INTO THE APPLICATION OF VARIOUS DEVICES FOR THE CONTROL OF A CONE-CYLINDER-FLARE CONFIGURATION. Pecover, B.E. January 1963.

Measurements have been made in the R.A.E. No.6 (11" x 6") wind tunnel of the six components of force and moment on a basic cone-cylinder-flare configuration fitted individually with ten different devices to produce aerodynamic control. In addition, some measurements of three components of force and moment on a flap or panel in the flare tail are given.

The controls tested consisted of a tilting nose, tilting flare, nose flap, flare flap, eccentric nose disc, eccentric rear disc, tilting spike, swept spoiler, eccentric ring and tilting ring. The measurements were made at $M = 4.3$ and Reynolds number from 1.4×10^6 to 5×10^6 depending on the configuration.

Results are discussed and compared with simple estimates and finally the controls are compared with each other. No single device had completely acceptable characteristics. Many, including the tilting nose and flare, were quite effective but only the swept spoiler arrangement could eliminate cross coupling.

The controls tested consisted of a tilting nose, tilting flare, nose flap, flare flap, eccentric nose disc, eccentric rear disc, tilting spike, swept spoiler, eccentric ring and tilting ring. The measurements were made at $M = 4.3$ and Reynolds number from 1.4×10^6 to 5×10^6 depending on the configuration.

Results are discussed and compared with simple estimates and finally the controls are compared with each other. No single device had completely acceptable characteristics. Many, including the tilting nose and flare, were quite effective but only the swept spoiler arrangement could eliminate cross coupling.

The controls tested consisted of a tilting nose, tilting flare, nose flap, flare flap, eccentric nose disc, eccentric rear disc, tilting spike, swept spoiler, eccentric ring and tilting ring. The measurements were made at $M = 4.3$ and Reynolds number from 1.4×10^6 to 5×10^6 depending on the configuration.

Results are discussed and compared with simple estimates and finally the controls are compared with each other. No single device had completely acceptable characteristics. Many, including the tilting nose and flare, were quite effective but only the swept spoiler arrangement could eliminate cross coupling.

Published by
HER MAJESTY'S STATIONERY OFFICE

To be purchased from
York House, Kingsway, London W.C.2
423 Oxford Street, London W.1
13A Castle Street, Edinburgh 2
109 St. Mary Street, Cardiff
39 King Street, Manchester 2
50 Fairfax Street, Bristol 1
35 Smallbrook, Ringway, Birmingham 5
80 Chichester Street, Belfast 1
or through any bookseller

S.O. CODE No. 23-9015-45